MATERIAL DEPOSITION AND LASER ANNEALING OF METAL OXIDE THIN FILMS FOR ELECTRONICS FABRICATED AT LOW TEMPERATURE

SALEM OMAR ELHAMALI

A thesis submitted in partial fulfilment of the requirements of Nottingham Trent University for the degree of Doctor of Philosophy

School of Science and Technology

Nottingham Trent University

October 2016

Copyright Statement

This work is the intellectual property of the author, and may also be owned by the research sponsor(s) and/or Nottingham Trent University. You may copy up to 5% of this work for private study, or personal, non-commercial research. Any re-use of the information contained within this document should be fully referenced, quoting the author, title, university, degree level and pagination. Queries or requests for any other use, or if a more substantial copy is required, should be directed in the first instance to the author.

Abstract

With an aim to investigate methods to realise low thermal-budget fabrication of aluminium doped zinc oxide (AZO) and indium gallium zinc oxide (IGZO) thin films, a dual step fabrication process was studied in this research. Initially, an experimental programme was undertaken to deposit AZO and IGZO films by radio frequency (RF) magnetron sputtering with no external substrate heating and at a wide range of deposition parameters including oxygen to argon ratio, RF power, and sputtering pressure. Thereafter, the samples were subjected to post-depositing annealing in air at ambient temperature utilising the advantages of excimer laser annealing (ELA) with a pulsed krypton fluoride (KrF) excimer laser at different laser fluences and number of pulses. The electrical, structural, compositional, and optical properties of the fabricated samples were systematically investigated as a function of the fabrication (deposition and annealing) conditions. A range of thin film characterisation techniques was used including 4-point probe (4PP), Van der Pauw (VDP), Hall Effect, X-ray diffraction (XRD), X-ray photoelectron spectroscopy (XPS), Atomic-force microscopy (AFM), Energy-dispersive X-ray spectroscopy (EDX), and optical transmittance and reflectance spectroscopy.

Sputter-deposition of AZO and IGZO at room temperature revealed that the electrical properties of the deposited films are profoundly controlled by the deposition conditions applied. Low sputtering pressure of 2 mTorr is desired to obtain the best quality materials. However, high RF power of 180 W (4 W/cm^2) is required to produce AZO with enhanced crystallinity, high electron density, and thus low resistivity. While, moderate RF power of 50 W (1.1 W/cm^2) is applied to produce amorphous IGZO films with moderate-to-high resistivity suitable for thin film transistors (TFTs). The oxygen to argon ratio is found to have the most significant impact on defining the electrical properties for both AZO and IGZO. The resistivity of IGZO films was dependant on their metallic composition which in turn is controlled by the deposition conditions. TFTs were fabricated on silicon substrates with 40 nm thick IGZO as the active layer deposited at room temperature and different growth conditions. TFT performance was largely affected by the active layer deposition conditions. TFTs with the optimised IGZO, deposited at 50 W and 2 mTorr of 2% oxygen to argon ratio, exhibited a field effect mobility of 0.67 cm^2/Vs, an on/off current ratio of 5x10^5, a turn on voltage of -0.15 V, and a subthreshold swing S of 0.28 V/decade.

Upon ELA, AZO showed a resistivity reduction which is shown to result from increasing both the free electron density and mobility. When the optimised as-deposited AZO, 180 nm thick deposited at 180 W and 2 mTorr of 0.2% oxygen to argon ratio, annealed with 5 pulses at 125 mJ/cm^2, a 50% resistivity reduction to 5x10^{-4} Ω.cm was obtained. It was demonstrated that average grain size increase, oxygen related defects decrease, and aluminium activation in doped ZnO are the origin of the AZO resistivity reduction upon ELA. Rapid thermal annealing (RTA) was also examined on AZO; RTA in nitrogen at 300°C for 20s increased the AZO gain size and doping efficiency leading to similar resistivity reduction to that achieved by the optimised ELA. Both ELA and RTA enhanced the AZO visible transmission to > 85 %, while the near infrared transmission was degraded due to higher electron density after annealing. The electro-optical properties of the optimised AZO samples obtained by ELA and RTA, which are very close to those of standard tin doped indium oxide (ITO), demonstrate the viability of AZO as an attractive transparent conducting material for various electronic applications. The potential use of AZO for photovoltaics (PVs) as well as the AZO stability against damp heat exposure were also examined. PVs with optimised ELA and RTA treated AZO samples showed comparable power conversion efficiency (PCE) to that of PVs with high-quality commercial ITO. The damp heat stability of AZO samples was strongly dependant on the fabrication conditions.

In regard to IGZO, ELA increased the free electron density and mobility leading to better conductivity, while the amorphous structure is maintained. ELA with single pulse at a low energy density of 30 mJ/cm^2 resulted in an improved performance for IGZO TFTs on silicon substrates achieving a field effect mobility of 3.33 cm^2/Vs, an on/off current ratio of 3x10^7, a turn on voltage of +0.35 V, and a subthreshold swing S of 0.27 V/decade. Moreover, ELA was successfully applied to IGZO TFTs on polymer flexible PEN leading to TFTs with enhanced performance.

Hence, a combination of RF magnetron sputtering at room temperature and ELA, which are both efficiently applicable to thin films mass production, has been demonstrated to provide a low thermal budget fabrication route for functional materials including AZO, as the most promising substitute to ITO in a wide range of applications, and IGZO as the most attractive material for TFT applications. This combination is an alternative thin film fabrication route to using elevated substrate temperature or post-deposition thermal annealing typically applied in the dominant literature reports, to obtain thin films with suitable characteristics.

Acknowledgements

First and foremost, all praise and thanks to ALLAH the Almighty, for His showers of blessing during my study, and for giving me the ability and strength to conduct this research.

I would like to express my sincere gratitude to my Director of Studies Dr. Demosthenes Koutsogeorgis for his invaluable guidance, continued support, stimulating discussions, and great contribution of time and effort to make my research experience successful and productive. Words are powerless and will never express my gratitude to him for his support that goes far beyond the role of Director of Studies. I have been most fortunate to have Prof. Wayne Cranton in the supervisory team, I am indebted to him for his guidance, encouragement, and support. Although Prof. Wayne Cranton left Nottingham Trent University, he continued to contribute to the research. I am proud and grateful for having Dr. Demosthenes Koutsogeorgis and Prof. Wayne Cranton in the supervision team of my study. Thanks also to Dr. Robert Ranson for his encouragement during the research.

Besides the supervision team, I would like to thank the Ministry of Higher Education and Scientific Research-Libya and the Libyan Cultural Attaché-London for the financial support of this research.

My gratitude is also extended to Dr. Xianghui Hou at the University of Nottingham – UK and Prof. Panos Patsalas at the Aristotle University of Thessaloniki – Greece, who provided me an opportunity to use their LAB facilities. Also, I would like to thank Dr. Peter Downs and all people from PragmatIC Printing Ltd for their invaluable contributions on this work.

I sincerely thank my research colleagues (current and ex) at iSMART facility –Nottingham Trent University, Dr. Nikolaos Kalfagiannis, Dr. Neranga Abeywickrama, Dr. Khairi Abusabee, Mr. Jacob Spear, and Mr. Christopher Mutton, for their assistance and helpful discussions.

Last but not least, I am extremely grateful to my parents and my extended family in Libya for their love, prayers, and sacrifices they have had to make for my future and personal career. I am very much thankful to my wife Mrs. Fatima Frhat for her understanding and continuing encouragement and support to complete my research. Also, I should thank my sons Omar and Assem, and I hope that in the future they would understand and appreciate why I was not able to spend enough time with them during my study.

List of Publications

List of Journal Papers

1. M. Wang, X. Hou, J. Liu, K. Choy, P. Gibson, **S. O. Elhamali**, D. Koutsogeorgis and W. Cranton, "An alternative non- vacuum and low cost ESAVD method for the deposition of Cu (In, Ga) Se2 absorber layers", **Physica Status Solidi (a), 2014.**
2. **S. O. Elhamali**, W. Cranton, N. Kalfagiannis, X. Hou, R. Ranson and D. Koutsogeorgis, "Enhanced electrical and optical properties of room temperature deposited Aluminium doped Zinc Oxide (AZO) thin films by excimer laser annealing", **Optics and Lasers in Engineering, vol. 80, pp. 45-51, 2016.**
3. **S. O. Elhamali**, W. Cranton, P. Patsalas, R. Ranson, and D. Koutsogeorgis, "Electrical, structural, and compositional properties evolution of Al-doped zinc oxide upon different deposition conditions, excimer laser annealing, and rapid thermal annealing", ***in preparation* to be submitted to Journal of Solar Energy Materials & Solar Cells.**
4. **S. O. Elhamali**, W. Cranton, R. Ranson, S. Dellis, N. Kalfagiannis, and D. Koutsogeorgis, "Excimer laser annealing of In-Ga-Zn-O for thin film transistors fabrication at low thermal budget on flexible substrates", ***in preparation* to be submitted to Science and Technology of Advanced Materials.**

List of Conference Presentations

1. **S. O. Elhamali**, W. Cranton, R. Ranson, D. Koutsogeorgis, "Material Deposition and Photonic Processing of Metal Oxide Thin Films for Low Temperature Electronics". **An oral and a poster presentation at School of Science & Technology 8th Annual Research (STAR) Conference, 07-08 May 2014 (Nottingham Trent University, Nottingham – UK).**
2. **S. O. Elhamali**, W. Cranton, R. Ranson, S. Kassavetis, G. Vourlias, P. Patsalas, D. Koutsogeorgis, "Enhancements of electrical and optical properties of low-temperature deposited Aluminium doped Zinc Oxide (AZO) thin films by photonic processing". **A poster presentation at 11th International Conference on Nanosciences & Nanotechnologies (NN14), 08-11 July 2014 (Thessaloniki – Greece).**
3. **S. O. Elhamali**, W. Cranton, P. Patsalas, S. Kassavetis, G. Vourlias, R. Ranson, D. Koutsogeorgis, "Room-temperature fabrication of highly conductive and transparent aluminium-doped Zinc Oxide (AZO) films by RF magnetron sputtering and photonic processing". **An oral presentation at 5th International Symposium on Transparent Conductive Material (TCM), 12 - 17 October 2014 (Crete – Greece).**

4. D. Mohammed, J. Phillips, D. Furze, **S. O. Elhamali**, D. Koutsogeorgis, W. Cranton, S. Kukureka, “Mechanical and tribological properties of Al-ZnO coated polymers for flexible devices”. **A poster presentation at 5th International Symposium on Transparent Conductive Material (TCM), 12 - 17 October 2014 (Crete – Greece).**
5. D. Mohammed, **S. O. Elhamali**, D. Koutsogeorgis, B. James, S. Kukureka, “Failure behaviour of AZO/Ag/AZO multilayers on PEN substrates for flexible electronic devices”. **An oral presentation at 42nd International Conference on Metallurgical Coatings and Thin Films (ICMCTF), 20-24 April 2015 (San Diego – USA).**
6. **S. O. Elhamali**, W. Cranton, N. Kalfagiannis, X. Hou, R. Ranson, D. Koutsogeorgis, “Room temperature Fabrication of Highly Conductive and Transparent Aluminium doped Zinc Oxide Films by RF Magnetron Sputtering and Excimer Laser Annealing”. **A poster presentation at the European Materials Research Society (E-MRS) Spring Meeting, 11-15 May 2015 (Lille – France).**
7. **S. O. Elhamali**, P. Downs, N. Kalfagiannis, W. Cranton, C. Ramsdale, R. Price, R. Ranson, D. Koutsogeorgis, “Material Deposition and Excimer Laser Annealing of Indium Gallium Zinc Oxide for Thin Film Transistors Fabrication at Low Thermal Budget”. **A poster presentation at the Materials Research Society (MRS) Fall Meeting & Exhibit, 29 November- 04 December, 2015 (Boston, Massachusetts – USA).**
8. **S. O. Elhamali**, P. Downs, N. Kalfagiannis, W. Cranton, C. Ramsdale, R. Price, R. Ranson, D. Koutsogeorgis, “Excimer Laser Annealing of In-Ga-Zn-O for Thin Film Transistors Fabrication at Low Thermal Budget on Flexible Substrates”. **A poster presentation at the European Materials Research Society (E-MRS) Spring Meeting, 02-06 May 2015 (Lille – France).**
9. **S. O. Elhamali,** N. Pliatsikas, W. Cranton, R. Ranson, P. Patsalas, D. Koutsogeorgis, “Electrical, structural, and compositional properties evolution of Al-doped zinc oxide upon excimer laser annealing, rapid thermal annealing, and damp heat exposure”. **An abstract submitted for an oral presentation at 6th International Symposium on Transparent Conductive Material (TCM), 0 9 - 13 October 2016 (Crete – Greece).**

List of Abbreviations

4PP	Four-Point Probe
AFM	Atomic-force microscopy
ALD	Atomic layer deposition
a-Si:H	Amorphous hydrogenated silicon
AZO	Aluminium doped zinc oxide
BBXRD	Bragg Brentano X-ray diffraction
BE	Binding energy
CBM	Conduction band minimum
CFA	Conventional furnace annealing
CIGS	Copper indium gallium selenide
cps	Counts per second
CVD	Chemical vapour deposition
DC	Direct current
DH	Damp heat
EDX	Energy-dispersive X-ray spectroscopy
ELA	Excimer laser annealing
FCC	Federal communication commission
FPD	Flat panel display
FWHM	Full width at half maximum
GIXRD	Grazing incidence X-ray diffraction
GZO	Gallium doped zinc oxide
IGZO	Indium gallium zinc oxide
iSMART	innovations in surfaces, materials and related technologies
IR	Infrared
ITO	Indium tin oxide (Tin doped indium oxide)
IZO	Indium zinc oxide
KE	Kinetic energy
KrF	Krypton fluoride
LTPS	Low-temperature polycrystalline silicon

Nd:YAG	Neodymium-doped yttrium aluminium garnet
Nd:YVO_4	Neodymium-doped yttrium orthovanadate
NIR	Near infrared
NTU	Nottingham Trent University
OPV	Organic photovoltaic
PECVD	Plasma-enhanced chemical vapor deposition
PEDOT:PSS	poly(3,4-ethylenedioxythiophene) polystyrene sulfonate
PET	Polyethylene terephthalate
PEN	Polyethylene Naphthalate
PLD	Pulsed laser deposition
PPL	Pragmatic printing ltd
PVD	Physical vapor deposition
PV	Photovoltaic
P3HT:PCBM	Poly 3-hexylthiophene: phenyl-C61-butyric acid methyl ester
RF	Radio frequency
RH	Relative Humidity
RT	Room Temperature
RTA	Rapid thermal annealing
sccm	Standard cubic centimetres per minute
SDD	Silicon drift detector
SEM	Scanning electron microscope
TCM	Transparent Conducting material
TCO	Transparent Conducting Oxide
TEM	Transmission electron microscopy
TFT	Thin film transistor
TOF-SIMS	Time-of-flight secondary ion mass spectrometry
TSO	Transparent Semiconducting Oxide
UHV	Ultra high vacuum
UV	Ultra violet
VBM	Valence band maximum

VDP	Van der Pauw
VIS	Visible
WCD	Wet chemical deposition
XeCl	Xenon Chloride
XPS	X-ray photoelectron spectroscopy
XRD	X-ray diffraction
XRR	X-ray reflectivity
Yb:YAG	Ytterbium doped yttrium aluminum garnet

List of Symbols

A	Optical absorbance, or Cross-sectional area
B	Magnetic field
c	Speed of light (3.00×10^{8} m/s)
C(T)	Material specific heat
Ci	Gate capacitance per unit area in thin film transistors
D	Average grain size, or Drain terminal in thin film transistors
d	inter-planar spacing
D_h	Thermal diffusivity
e	Electron
E	Electric field
E_f	Fermi level
E_g	Bandgap
F_e	Electrostatic force
F_L	Lorentz force
G	Gate terminal in thin film transistors
g_m	The maximum transconductance for transfer curves for thin film transistors
h	Planck's constant (4.135×10^{-15} eV. s)
I	Current
I_D	Drain current in thin film transistors
K(T)	Material thermal conductivity
L	Channel length in thin film transistors
l	Sample length
L_{th}	Heat diffusion length
m_{eff}	Carrier effective mass
N	Free carrier density
q	Elementary charge for a carrier (1.602×10^{-19} coulombs for an electron)
R	Resistance, or Optical reflectance
r	Carrier scattering factor

Ra	Arithmetic roughness
r_{CH}	Channel resistance per channel length unit in thin film transistors
R_H	Hall coefficient
R_{ON}	On-resistance in thin film transistors
R_{RMS}	Root mean square roughness
R_{sh}	Sheet resistance
S	Subthreshold swing in thin film transistors
S	Source terminal in thin film transistors
t	The thickness of a film sample
T	Optical transmittance
V	Voltage
v	Carrier drift velocity
V_D	Drain voltage in thin film transistors
V_G	Gate voltage in thin film transistors
V_H	Hall voltage
V_o	Oxygen vacancy
V_{ON}	Turn-on voltage in thin film transistors
V_{TH}	threshold voltage in thin film transistors
W	Channel width in thin film transistors
w	The width of a film sample
Zn_i	Zinc interstitial atom
α	Optical absorption coefficient
β	Diffraction peak broadening defined as FWHM
θ	Bragg angle
λ	Wavelength
λ_{gap}	Bandgap wavelength
λ_{pl}	Plasma wavelength
μ	Free carrier mobility
μ_{FE}	Field-effect mobility in thin film transistors
μ_{lin}	Linear mobility in thin film transistors

μ_{sat}	Saturation mobility in thin film transistors
ρ	Electrical resistivity
ρ (T)	Material density
σ	Electrical conductivity
τ	Diffraction peak broadening defined as the total area under the peak divided by the peak height
τ_{relx}	Carrier relaxation time
φ	Work function
Φb	Potential barrier between grains in polycrystalline thin films

List of Contents

Copyright Statement ii

Abstract iii

Acknowledgements v

List of Publications vi

List of Abbreviations viii

List of Symbols xi

List of Contents xiv

List of Figures xix

List of Tables xxvi

1 Introduction 1-1

1.1 Overview 1-1

1.2 Motivation of the present work 1-1

1.3 Research aim 1-2

1.4 Research objectives 1-2

1.5 Overview of research methodology 1-3

1.6 Significant contribution to the field of oxide-based electronics 1-4

1.7 Structure of the thesis 1-4

2 Background and Literature Review 2-1

2.1 Introduction 2-1

2.2 Introduction to transparent conducting oxides (TCOs) 2-1

2.3 Zinc oxide-based TCOs 2-3

2.4 Zinc oxide crystal structure: 2-3

2.5 Electronic band structure and optical bandgap 2-4

2.6 Electrical properties 2-6

2.6.1 Grain boundaries scattering 2-7

2.6.2 Ionised impurity scattering 2-8

2.7 Optical properties 2-8

2.8 Introduction to transparent semiconducting oxides (TSOs) 2-9

2.9 Thin-Film Transistors (TFTs) 2-9
2.9.1 TFT structures and classifications 2-10
2.9.2 Basic TFT operation 2-11
2.9.3 TFT Electrical Characterisation 2-12
2.9.4 Materials used as the active layer in TFTs 2-14
2.9.5 Conduction mechanism of amorphous TSOs 2-15
2.9.6 Amorphous TSOs for TFT active layer 2-16
2.10 Fabrication of TCOs and TSOs 2-17
2.10.1 Previous publications on sputter-deposition of AZO 2-17
2.10.2 Previous publications on laser annealing of AZO 2-19
2.10.3 Previous publications on sputter-deposition of a-IGZO 2-23
2.10.4 Previous publications on laser annealing of a-IGZO 2-25
3 Thin Film Fabrication and Characterisation Techniques 3-1
3.1 Introduction 3-1
3.2 Thin film technology 3-1
3.3 Thin film sputter-deposition 3-2
3.3.1 Physics of thin film sputter-deposition 3-2
3.3.2 Experimental RF magnetron sputtering system 3-5
3.4 Post-deposition annealing 3-8
3.5 Excimer laser Annealing (ELA) 3-8
3.5.1 Basic concept of excimer laser annealing (ELA) 3-9
3.5.2 Experimental ELA system 3-10
3.6 Rapid Thermal Annealing (RTA) 3-12
3.7 Thin-film materials characterisation techniques 3-13
3.7.1 X-Ray Diffraction (XRD) 3-13
3.7.2 X-ray Photoelectron Spectroscopy (XPS) 3-18
3.7.3 Energy Dispersive X-ray Spectroscopy (EDX) 3-21
3.7.4 Resistivity measurements by four-point probe (4PP) technique 3-22
3.7.5 Resistivity measurements by Van der Pauw (VDP) technique 3-24
3.7.6 Hall Effect measurement 3-25
3.7.7 Atomic Force Microscopy (AFM) 3-28

3.7.8 Optical transmittance and reflectance spectra 3-31

4 Room Temperature Sputter-deposition of AZO Films 4-1

4.1 Introduction 4-1

4.2 Experimental investigation of AZO deposition parameters 4-1

4.2.1 Oxygen to argon ratio optimisation 4-3

4.2.2 The applied RF power and sputtering pressure optimisation . 4-4

4.3 Sputter-deposition results and discussion 4-4

4.3.1 Growth rate 4-4

4.3.2 Influence of oxygen to argon ratio on the AZO microstructure characteristics 4-6

4.3.3 Influence of oxygen to argon ratio on the AZO conductivity and transparency 4-7

4.3.4 Influence of the RF power on the AZO microstructure characteristics 4-9

4.3.5 Influence of the sputtering pressure on the AZO microstructure characteristics 4-10

4.3.6 Influence of the RF power on the AZO stoichiometry 4-12

4.3.7 Influence of the sputtering pressure on the AZO stoichiometry 4-18

4.3.8 Influence of the RF power on the AZO electrical properties . 4-22

4.3.9 Influence of the sputtering pressure on the AZO electrical properties 4-24

4.3.10 Resistivity lateral distribution across the substrate 4-26

4.3.11 Influence of the RF power and sputtering pressure on the AZO optical properties 4-28

4.4 Concluding remarks 4-30

5 Annealing Studies on AZO Films Sputter-deposited at Room Temperature 5-1

5.1 Introduction 5-1

5.2 Post-deposition ELA optimisation 5-1

5.3 Post-deposition RTA optimisation 5-2

5.4 Combined post-deposition annealing with ELA and RTA 5-3

5.5 Post-deposition annealing results and discussion 5-3

5.5.1 Influence of ELA and RTA on the AZO microstructure characteristics 5-3

5.5.2 Influence of ELA and RTA on the AZO stoichiometry 5-14

5.5.3 Influence of ELA and RTA on the AZO electrical properties. 5-18

5.5.4 Influence of ELA and RTA on the AZO optical properties 5-28

5.6 International Electrotechnical Commission (IEC) test 61646 on AZO 5-30

5.7 AZO films for potential application in photovoltaics 5-35

5.8 Concluding remarks 5-36

6 Low Thermal Budget Fabrication of IGZO Thin Film Transistors .. 6-1

6.1 Introduction 6-1

6.2 IGZO thin films sputter-deposition investigation 6-1

6.3 IGZO thin films ELA investigation 6-2

6.4 TFT devices fabrication and ELA treatment investigation 6-3

6.5 IGZO thin films sputter deposition and ELA results and discussion 6-4

6.5.1 Dependence of the growth rate on the deposition parameters.. 6-4

6.5.2 Dependence of the IGZO films metallic composition on the deposition parameters 6-6

6.5.3 Dependence of the IGZO films resistivity on the deposition parameters 6-9

6.5.4 The effect of ELA in IGZO thin films electrical characteristics 6-13

6.6 IGZO TFT sputter deposition and ELA results and discussion 6-15

6.6.1 Dependence of the IGZO TFT performance on the IGZO layer deposition parameters 6-15

6.6.2 Effect of ELA on the performance of IGZO TFTs on Silicon substrates 6-20

6.6.3 Effect of ELA on the performance of IGZO TFTs on flexible PEN substrates 6-27

6.7 Concluding remarks 6-29

7 Conclusions and Future Perspectives 7-1

7.1 Introduction 7-1

7.2 Conclusions 7-1

7.3 Key outcomes of the research 7-4
7.4 Future perspectives 7-4
7.4.1 Future work for AZO 7-4
7.4.2 Future work for IGZO 7-6
8 References 8-1
9 Appendices 9-1
Appendix A. Reproducibility test of the deposition and annealing parameters for AZO 9-1
Appendix B. ELA parameters effect on the resistivity of AZO of different deposition conditions. 9-3
Appendix C. Publications copies 9-8

List of Figures

Fig. 2-1 The commonly used transparent conducting materials TCMs in FPDs and PVs industries with their value in 2012 [21]. 2-2

Fig. 2-2 (a) The ZnO wurtzite structure, (b) an Al atom introduced to the ZnO lattice. Adopted from [15]. 2-3

Fig. 2-3. Schematic representation of the electronic band structure (a) undoped ZnO, (b) doped ZnO in the case of Burstein Moss effect, and (c) doped ZnO in the case of bandgap renormalisation effect [31]... 2-5

Fig.2-4. Schematic representation illustrates the band bending due to the grain boundaries impact on the carrier transport in an n-type polycrystalline material. Adopted from [15, 43]. 2-7

Fig. 2-5. Absorption, Transmission, and Reflection spectra for ZnO thin film [12]. 2-8

Fig. 2-6. Schematics showing the most common TFT structures, (a) bottom-gated-coplanar structure, (b) top-gated-coplanar structure, (c) bottom-gated-staggered structure, and (d) top-gated-staggered structure. Adopted from [48]……… 2-10

Fig. 2-7. Energy band diagram for a semiconductor-insulator-metal stack representing n-type TFT- enhancement mode, (a) Vg=0 V (equilibrium), (b) Vg<0 V (depletion), and (c) Vg>0 V (accumulation). Adopted from [48]. 2-11

Fig. 2-8. Schematics represent TFT operation regimes, (a) linear regime, and (b) saturation regime. Adopted from [48]. 2-12

Fig. 2-9 Typical transfer characteristics curve for n-type semiconductor TFT.......... 2-13

Fig. 2-10. Schematic representation for “the carrier transport paths” in the CBM for ionic semiconductors (a) crystal, (b) amorphous, and in covalent semiconductor (c) crystal, (d) amorphous. Adapted from [6] 2-15

Fig. 3-1. Commonly used thin film deposition methods, adapted from [9, 117].......... 3-1

Fig. 3-2. Phenomena arising from interactions of argon ions with the sputtering target [86, 118, 120].. 3-3

Fig. 3-3. Illustration of the experimental RF magnetron sputtering system, and the sputter-deposition mechanism.. 3-7

Fig. 3-4. Schematic diagram of NTU Excimer Laser Annealing system. 3-11

Fig. 3-5. Beam homogenizer (Exitech Ltd., type EX-HS-700D)............................... 3-11

Fig.3-6. The concept of Bragg’s law for interaction between X-ray beam and crystallographic planes. Adapted from [126]. 3-14

Fig. 3-7. A schematic representation of XRD measurements in θ/2θ scan mode (Bragg-Brentano XRD. Adopted from [126]... 3-15

Fig. 3-8. Schematic diagram of photoelectron emission, energy level diagram for photoelectron effect, and XPS measurement. Adopted from [137]. 3-19
Fig. 3-9. Wide scan of XPS measurement for an AZO thin film. 3-20
Fig. 3-10. Schematic of an EDX system and the types of X-ray lines observed in generated x-ray spectra. Adopted from [137]. 3-21
Fig.3-11. Schematic drawing of the linear four-point probe sheet resistance and resistivity measurement system. Adopted from [141]. 3-23
Fig. 3-12. A schematic drawing of van der Pauw method for resistivity measurement. Adopted from [141]. 3-25
Fig. 3-13. A schematic diagram of the Hall Effect concept and standard geometry. Adopted from [141]. 3-26
Fig. 3-14. A schematic representation of Hall Effect measurement in van der Pauw geometry. 3-28
Fig. 3-15. Schematic representation of the AFM concept. Adopted from [137]. 3-29
Fig. 3-16 Schematic illustration of optical transmittance and reflectance measurements set-up….. 3-31
Fig. 4-1. Growth rate and substrate temperature versus RF power. 4-5
Fig. 4-2. High-resolution XRD spectra for AZO samples as a function of the oxygen to argon ratio, deposited at RT, 120 W, and 2 mTorr. The inset graph shows the results of Voigt-function analysis. 4-7
Fig. 4-3. The electrical characteristics (ρ, μ, and N) for AZO as a function of the oxygen to argon ratio, deposited at RT, 120 W, and 2 mTorr. 4-8
Fig. 4-4. High-resolution XRD spectra for AZO as a function of the applied RF power, deposited at RT, 2 mTorr, and 0.2% O_2 in Ar %. The inset graph is the wide scan for the optimised AZO. 4-9
Fig. 4-5. XRD data analysis for AZO as a function of the applied RF power, deposited at RT, 2 mTorr, and 0.2% O_2 to Ar %. 4-10
Fig. 4-6. High-resolution XRD spectra for AZO samples as a function of the deposition pressure, deposited at RT, 180 W, and 0.2% O_2 to Ar %..... 4-11
Fig. 4-7. XRD data analysis for AZO samples as a function of the deposition pressure, deposited at RT, 180 W, and 0.2% O_2 to Ar %. 4-11
Fig. 4-8 . Wide XPS spectra of the optimised as-deposited AZO thin film before and after Ar etching. 4-12
Fig. 4-9. High resolution O1s XPS spectra for the optimised as-deposited AZO before and after Ar etching. 4-13

Fig. 4-10. The relative atomic concentration values for Zinc, Oxygen, and Aluminium obtained from the XPS measurements as a function of the applied RF power….. 4-14

Fig. 4-11. High resolution O1s XPS spectra of AZO films deposited at different RF power fitted into two peaks. 4-15

Fig. 4-12. (a) AFM plan view images, (b) 3-D images, and (c) roughness details, for AZO samples deposited at different RF power 4-16

Fig. 4-13. High resolution XPS spectra of Al2p in AZO films deposited at different RF power and fitted into two chemical states.. 4-17

Fig. 4-14. High resolution O1s XPS spectra of AZO films deposited at different sputtering pressure fitted into two peaks. 4-18

Fig. 4-15. (a) AFM plan view images, (b) 3-D images, and roughness details, and (c) for AZO samples deposited at different sputtering pressure. 4-20

Fig. 4-16. Schematic representation of Thornton structure zone model [174] to linking the deposited film microstructural properties to the substrate temperature and sputtering pressure. 4-20

Fig. 4-17. High resolution XPS spectra of Al2p in AZO films deposited at different sputtering pressure and fitted into two chemical states............................ 4-21

Fig. 4-18. The electrical characteristics (ρ, μ, and N) for AZO samples as a function of the applied RF power, deposited at room temperature, 2 mTorr, and 0.2% oxygen to argon. 4-22

Fig. 4-19. The correlation between the electrical characteristics and the XRD /XPS data for AZO samples deposited at different RF power. 4-23

Fig. 4-20 The electrical characteristics (ρ, μ, and N) for AZO samples as a function of the sputtering pressure, deposited at room temperature, 180 W, and 0.2% oxygen to argon ratio. 4-24

Fig. 4-21. The correlation between the electrical characteristics and the XRD /XPS data for AZO samples deposited at different sputtering pressure. 4-25

Fig. 4-22. The effect of the sputtering pressure on AZO resistivity at different RF power. ……………………………………………………………………….4-26

Fig. 4-23. Lateral electrical properties (ρ, μ, and N) distribution of AZO samples of different deposition parameters and as a function of the location on the substrate, (a) the optimised deposition condition 180 W and 2 mTorr, (b) 80 W and 2 mTorr, and (c)180 W and 5 mTorr. 4-28

Fig. 4-24. AZO films optical transmittance spectra (a) as a function of the applied RF power at 2 mTorr, and (b) as a function of the sputtering pressure at 180 W. The inset graphs show linear extrapolations of Tauc's plot for these films……….. 4-29

Fig. 5-1. The optimised RTA cycle for AZO samples. 5-3

Fig. 5-2. Wide XRD spectra for the optimised AZO samples (a) after ELA with 5 pulses at 125 mJ/cm^2 in air, and (b) after RTA at 300°C for 20s in nitrogen. 5-4

Fig. 5-3. High-resolution XRD spectra for the optimised as-deposited AZO samples ELA-treated at 125 mJ/cm^2 (a) with one pulse, and (b) with five pulses. 5-5

Fig. 5-4. Mechanism for stress state changes throughout the AZO sample thickness upon ELA. 5-6

Fig. 5-5. High resolution XRD data for the optimum as-deposited AZO180 nm thick resolved to two XRD peaks after ELA at 125 mJcm^2 (a) with one pulse, and (b) with five pulses. 5-7

Fig. 5-6. (a-c) XRD patterns for AZO samples of different thicknesses pre and post ELA, and (e-f) the XRD data upon ELA resolved to two peaks. 5-9

Fig. 5-7. The optimised AZO 180 nm-thick ELA treated with five pulses at 75 mJ/cm^2. 5-10

Fig. 5-8. The obtained results from resolving the XRD data for AZO of different thickness upon ELA, (a) the effect of ELA on the average grain size, and (b) the extent of the ELA effect over the sample thickness. 5-10

Fig. 5-9. TEM image showing the effect of KrF ELA on a 200 nm thick ZnO film. The upper layer of 135 nm was modified. Adapted from [187] 5-11

Fig. 5-10. High-resolution XRD data for AZO samples underwent RTA at different annealing temperatures and for a dwell time of 20s, the inset graph illustrates Voigt-function model results. 5-12

Fig. 5-11 High-resolution XRD data for AZO samples underwent RTA at the optimum annealing temperature (300°C) and for different dwell time, the inset graph illustrates Voigt-function model results. 5-13

Fig. 5-12 High-resolution XRD data for the optimised as-deposited AZO sample was that initially ELA-treated, followed by RTA-treatment. 5-14

Fig. 5-13. O1s XPS spectra for the optimised as-deposited and ELA-treated AZO samples resolved into two components. 5-15

Fig. 5-14 O1s XPS spectra for the optimised as-deposited and RTA-treated AZO samples resolved into two peaks. 5-17

Fig. 5-15. Al2p photoelectron spectra for AZO samples, (a) as-deposited resolved into two chemical states Al2p(I) and Al2p(II), (b) and (c) post ELA and RTA respectively resolved into one chemical state Al2p(I). 5-18

Fig. 5-16. The effect of ELA at different energy densities and number of pulses on AZO resistivity as a function of (a) the applied RF power at 2 mTorr, and (b) the sputtering pressure at 180 W. 5-19

Fig. 5-17. The effect of ELA at five pulses and different energy densities on the electrical characteristics for the optimised as-deposited AZO samples, the values at 0 mJ/cm^2 are for the as-deposited AZO sample. 5-20

Fig. 5-18. The effect of optimum ELA (5 pulses at 125 mJ/cm^2 in air) on the electrical properties of all the as-deposited AZO samples, (a) as a function of RF power, and (b) as a function of sputtering pressure. 5-20

Fig. 5-19. (a) AFM plan view images, (b) 3-D images, and (c) roughness details for AZO pre and post ELA. 5-21

Fig. 5-20. ELA effect on the electrical characteristics (ρ, N, and μ) of AZO samples of different thickness. 5-22

Fig. 5-21. The effect of ELA environment on the achieved electrical characteristics of AZO samples. 5-23

Fig. 5-22. Changes in the electrical characteristics of the optimised as-deposited AZO films upon RTA at different target annealing temperatures for 20 second… 5-24

Fig. 5-23. Changes in the electrical characteristics of the optimised as-deposited AZO films upon RTA at 300°C and for different dwell times. 5-25

Fig. 5-24. AFM plan view images, (b) 3-D images, and (c) roughness details for AZO pre and post RTA. 5-26

Fig. 5-25. The resistivity changes upon ELA and RTA combination, (a) AZO samples were initially RTA-treated followed by ELA at 125 mJ/cm^2 at different number of pulses, (b) AZO samples ELA-treated then RTA-treated at the optimised conditions. 5-27

Fig. 5-26. The optical transmittance of the optimised as-deposited AZO after ELA and RTA treatments. 5-28

Fig. 5-27. UV/VIS transmittance, reflectance, and absorptance spectra for the optimised AZO, (a) after ELA, (b) after RTA. The inset graphs show linear extrapolations of Tauc's plot for bandgap estimation. 5-29

Fig. 5-28. (a) The electrical resistivity changes for AZO samples of different growth conditions as a function of the (IEC) 61646 test time, and (b) the resistivity changes ratio. 5-31

Fig. 5-29. (a) The electrical resistivity changes for the optimised AZO samples and the ITO reference samples as a function of the (IEC) 61646 test time, and (b) the resistivity changes ratio. 5-33

Fig. 5-30. The electrical properties for the examined AZO and ITO samples pre and post the IEC 61646 test, (a) different AZO growth conditions, and (b) the optimised AZO samples and the ITO reference. 5-34

Fig. 5-31 Schematic illustration of cross section for the examined OPV devices 5-35

Fig. 6-1. (a-g) a process flow for IGZO TFTs fabrication, (h) top-view optical micrograph image, and (i) 3D schematic illustration and top view of the fabricated TFTs structure……………………………………………………………………….6-4

Fig. 6-2. The effect of the deposition parameters on IGZO films growth rate, (a) the RF power, (b) the O_2 in Ar %, (c) the sputtering pressure, and (d) the used target In-Ga-Zn at. % determined via EDX. 6-5

Fig. 6-3. In-Ga-Zn atomic concentrations for IGZO samples vs. applied RF power at 2 mTorr of 2% O_2 in Ar, determined via EDX. 6-7

Fig. 6-4. In-Ga-Zn atomic concentrations for IGZO samples vs. oxygen to argon ratios, at 50 W, and 2 mTorr, determined via EDX... 6-7

Fig. 6-5. In-Ga-Zn atomic concentrations for IGZO samples vs. sputtering pressure, at 50 W, and 2% O_2 in Ar, determined via EDX. 6-8

Fig. 6-6. In-Ga-Zn atomic concentrations for IGZO samples vs. the used IGZO target composition, IGZO films deposited at RT, 50 W, and 2mTorr of 2% O_2 in Ar, determined via EDX. 6-8

Fig. 6-7. IGZO thin films resistivity vs. applied RF power at RT, and 2 mTorr of 2% O_2 in Ar upon ELA with one pulse at different laser energy densities. 6-9

Fig. 6-8. IGZO thin films resistivity vs. O_2 to Ar % at RT, 50 W, and 2 mTorr upon ELA with one pulse at different laser energy densities. Dashed lines correspond to unmeasurable values by 4PP. 6-10

Fig. 6-9. IGZO thin films resistivity vs. sputtering pressure at RT, 50 W, and 2% O_2 in Ar upon ELA with one pulse at different laser energy densities. Dashed lines correspond to unmeasurable values by 4PP. 6-11

Fig. 6-10. IGZO films resistivity vs. the used IGZO target composition, 200 nm thick IGZO films deposited at RT, 50 W, and 2 mTorr of 2% O_2 in Ar. Dashed bar represents unmeasurable resistivity by 4PP. 6-12

Fig. 6-11. The dependence of the electrical characteristics on ELA laser energy density for 200 nm thick IGZO samples deposited at the optimised condition, (a) from IGZO (1:1:1), and (b) from IGZO (2:1:1). Dashed lines correspond to unmeasurable values.. 6-13

Fig. 6-12. Averaged transfer characteristics curves for as-deposited IGZO TFTs deposited at different RF power, RT, 2 mTorr of 2% O2 in Ar. 6-16

Fig. 6-13. Averaged transfer characteristics curves for as-deposited IGZO TFTs deposited at different O_2 in Ar%, RT, 50 W, and 2 mTorr. 6-17

Fig. 6-14. Averaged transfer characteristics curves for as-deposited IGZO TFTs deposited at different sputtering pressure at RT, 50 W, and 2% O_2 in Ar. 6-18

Fig. 6-15. Averaged transfer characteristics curves for the optimised as-deposited IGZO TFTs upon ELA with one pulse at different energy densities. 6-20

Fig. 6-16 The effect of ELA laser energy density on IGZO TFTs on resistance R_{ON}………..6-22

Fig. 6-17. The dependence of the electrical characteristics on ELA laser energy density for 40 nm thick IGZO samples deposited at the optimised condition, (a) from IGZO (1:1:1), and (b) from IGZO (2:1:1). Dashed lines correspond to unmeasurable values...6-23

Fig. 6-18. XRD patterns for the optimised IGZO (1:1:1) samples pre and post ELA at different energy densities. The XRD pattern for the used substrates (Al_2O_3/Si) is also included as a reference. 6-24

Fig. 6-19. Atomic concentrations of the contained metals in the optimised as-deposited IGZO samples examined for TFTs before and after ELA with one pulse at 30 mJ/cm^2 obtained by XPS vs. EDX. 6-25

Fig. 6-20. The Effect of ELA with one pulse at 30 mJ/cm^2 on the photoelectron spectra of the contained elements for the optimised as-deposited IGZO samples examined for TFTs..6-26

Fig. 6-21. Averaged transfer characteristics curves for IGZO TFTs on PEN upon ELA with one pulse at different energy densities. Two wafers were tested for reproducibility test..6-28

List of Tables

Table 2-1. Summaries the most common TFT technologies [14, 48, 64] 2-15

Table 2-2. A summary of previous reports on laser annealing of AZO thin films. Results of rapid thermal annealing RTA [102] are included for comparison. The ref. [101] is from the results of this PhD study. 2-22

Table 2-3. A summary of previous reports on laser annealing of IGZO thin films. ... 2-29

Table 3-1. The absorption coefficient and penetration depth for AZO and IGZO thin film at the wavelength of KrF laser (248 nm). 3-10

Table 4-1. A summary of the investigated deposition parameters for AZO samples. 4-4

Table 4-2. Details of the fitted peaks for O1s XPS spectra of AZO films deposited at different RF power. 4-15

Table 4-3 Details of the fitted peaks for Al2p XPS spectra of AZO films deposited at different RF power. 4-18

Table 4-4. Details of the fitted peaks for O1s XPS spectra of AZO deposited at different sputtering pressure. 4-19

Table 4-5. Details of the fitted peaks for Al2p XPS spectra of AZO films deposited at different sputtering pressure. 4-21

Table 5-1. XRD data analysis using Voigt function for the optimum as-deposited AZO 180 nm thick resolved to two XRD peaks after ELA with different number of pulses at 125 $mJcm^2$. 5-8

Table 5-2.The relative atomic concentration of aluminium, zinc, and oxygen before and after ELA, and RTA treatment. 5-14

Table 5-3.Details of the resolved peaks of O1s XPS spectra for the optimised as-deposited and ELA-treated AZO samples. 5-15

Table 5-4. Details of the resolved peaks of O1s XPS spectra for the optimised as-deposited and RTA-treated AZO samples. 5-17

Table 5-5. Details of the resolved peaks for Al2p XPS spectra obtained from AZO films pre and post ELA and RTA treatments. 5-18

Table 5-6. Details of AZO and ITO samples subjected to the (IEC) test 61646. 5-30

Table 5-7. Details of AZO and ITO samples used for photovoltaics test, and the achieved efficiency. 5-35

Table 6-1. A summary of the investigated deposition parameters for IGZO thin films…..… 6-1

Table 6-2. Investigated sputter-deposition parameters of IGZO TFTs. 6-15

Table 6-3. The extracted electrical parameters for as-deposited IGZO TFTs deposited at different RF power, RT, 2 Torr of 2% O_2 in Ar. 6-16

Table 6-4. The extracted electrical parameters for as-deposited IGZO TFTs at different O_2 in Ar%, RT, 50 W, and 2 mTorr. 6-17

Table 6-5. The extracted electrical parameters for as-deposited IGZO TFTs deposited at different sputtering pressure at RT, 50 W, and 2% O_2 in Ar. 6-19

Table 6-6. The extracted electrical parameters for the optimised as-deposited IGZO TFTs upon ELA with one pulse at different energy densities. 6-20

Table 6-7. The extracted electrical parameters for IGZO TFTs on PEN upon ELA with one pulse at different energy densities. 6-28

1 Introduction

1.1 Overview

Functional oxide materials including aluminium doped zinc oxide (AZO) and indium gallium zinc oxide (IGZO) are of interest for numerous electronics applications because they combine good visible light transparency with controllable electrical characteristics. The research presented in this PhD thesis is focused on investigating the potential for nanosecond excimer laser annealing (ELA) as a low thermal-budget annealing approach to improve the electrical and optical characteristics of AZO and IGZO thin films deposited by radio frequency (RF) magnetron sputtering at room temperature. Thermal-budget is defined as the total thermal energy amount that is transferred to the substrate during an elevated temperature process [1].

1.2 Motivation of the present work

Metal oxide thin films have been extensively explored for various electronics including, but not limited to, photovoltaics (PVs), thin film transistors (TFTs), and flat display panels (FPDs). In general, oxide materials can be classified based on their functionality in electronic applications either as transparent conducting oxides (TCOs), with resistivity < 10^{-3} Ω.cm, or as transparent semiconducting oxides (TSOs), with resistivity in the range of 10^{3} - 10^{4} Ω.cm. Among TCOs, tin doped indium oxide (ITO) has been the most commonly used material for transparent electrode applications. The increasing demand for transparent conducting materials, coupled with the ITO limitations, such as high cost and poor mechanical stability, have stimulated research interest in ITO alternatives. For instance, ZnO-based TCOs such as AZO that offers relatively lower cost and growth temperature compared to ITO. Moreover, the achieved electrical conductivity of ZnO-based TCOs is getting closer to that of ITO transparent electrodes [2-4]. In regard to TSOs, IGZO is the latest thin film material for TFTs used as switching element in FPDs. Unlike most investigated semiconducting materials for TFTs, IGZO offers high visible transparency, good electron mobility, large area uniformity, and low temperature fabrication. Therefore, IGZO is considered as the most promising material applied to TFTs for current and emerging display technologies [5, 6].

Due to the fast growth of PVs and FPDs industries, there will be an increasing demand for oxide-based materials TCOs and TSOs. Also, oxide materials are expected to play important

roles in various emerging electronics' developments, such as the realisation of transparent and flexible electronics fabricated on polymer substrates. Therefore, the science and engineering of the fabrication techniques of these materials are always challenging and demand innovative approaches to satisfy the prospective applications' constraints, as well as developing cost-efficient, reliable, and reproducible materials. For instance, it is challenging to fabricate reliable oxide thin films for application to PVs and TFTs at low thermal-budget. Meanwhile, there has been an increasing desire for oxide thin films fabrication at low thermal-budget in order to maintain the characteristics and the electronic interfaces of any underlying layers or the substrate itself. Consequently, economical, light-weight, large-area and roll-to-roll compatible, and heat-sensitive flexible substrates such as polymer substrates will take over conventional glass substrates [3, 4, 7]. To date, there has been a large body of investigations reported into the fabrication of various oxides for electronics applications. However, there is very limited work combining RF magnetron sputtering at room temperature with laser annealing as a low thermal-budget and large-area applicable fabrication approach for oxide materials.

1.3 Research aim

The primary aim of this research was to investigate the potential of ELA using a pulsed krypton fluoride (KrF) excimer laser (λ=248 nm and pulse duration 25 ns) as an alternative to thermal annealing, in order improve the electro-optical characteristics of room temperature deposited AZO thin films for use as transparent electrodes, and IGZO thin films for use as an active layer in thin film transistors.

1.4 Research objectives

1. Undertake a background study of the microstructural, electrical, and optical characteristics of AZO and IGZO thin films.
2. Undertake a background study of TFTs, and oxide based TFTs in particular.
3. Perform background reading and familiarisation with radio frequency magnetron sputtering, excimer laser annealing, and relevant thin film characterisation techniques.
4. Review radio frequency sputter-deposition and post-deposition annealing research that has been reported on AZO and IGZO thin films for low thermal-budget fabrication.
5. Investigate the effects of radio frequency sputter-deposition parameters (oxygen to argon ratio, radio frequency power, and sputtering pressure) on physical properties of AZO and IGZO thin films with no external substrate heating.

6. Study the influence of excimer laser annealing in air at ambient temperature on the deposited AZO and IGZO thin films aiming at better electrical and optical properties.
7. Compare rapid thermal annealing (RTA) of AZO thin films with excimer laser annealing in terms of the achieved electrical and optical properties enhancements.
8. Examine the use of the optimally fabricated AZO as transparent electrodes for PVs.
9. Investigate the environmental robustness of AZO thin films under the conditions of the international electrotechnical commission (IEC) test 61646 (85°C, 85% RH, and 1000h).
10. Examine the effects of IGZO deposition and ELA conditions on IGZO TFTs performance.
11. Investigate the ELA application to IGZO TFTs on heat-sensitive polymer substrates.
12. Attempt to determine the exact mechanism through which any observed enhancements are obtained upon ELA.

1.5 Overview of research methodology

In this research, a combination of radio frequency magnetron sputtering at room temperature and excimer laser annealing was adopted to fabricate the explored oxide thin films at low thermal-budget. Radio frequency magnetron sputtering is the most widely used deposition technique in industry and research applications due to its attractive strengths including samples deposition at low substrate temperature down to no external substrate heating, applicability to a wide range of materials and to large-area applications, and efficient control over various deposition parameters. In sputter-deposition process, the target material i.e. the material to be deposited is bombarded with energetic gas ions in a vacuum chamber. As a result, the surface atoms and ions of the target are sputtered (removed) and then travel in a low pressure environment. Finally, the sputtered particles are deposited on a substrate. Sputter-deposited thin films with no external substrate heating typically require post-deposition annealing to further enhance their characteristics [8, 9]. Unlike thermal annealing, laser annealing offers very attractive merits such as very short processing times and localised heating both in area and depth i.e. heating selectivity. In laser annealing, the annealed material is irradiated with photons of energy higher than the annealed material's bandgap. Consequently, the laser photons' energy is absorbed leading to very rapid and highly localised heating as well as temperature gradient from the surface layer to the underlying layers or the substrate [10, 11]. For detailed discussions on both magnetron sputtering and laser annealing, see chapter 3.

The physical characteristics of sputter-deposited films are profoundly controlled by the deposition conditions [8, 9]. Hence, to optimise the deposition conditions of AZO and IGZO in this

study and based on their application requirements, one deposition parameter was changed at a time, while the others were held constant. The examined deposition parameter's effect on the deposited film characteristics was studied. Thereafter, the deposited AZO and IGZO films were subjected to excimer laser annealing in air at room temperature with a Krypton Fluoride (KrF) excimer laser using different laser energy densities and number of pulses. For comparison with excimer laser annealing, rapid thermal annealing was examined on AZO. The annealed AZO and IGZO films were studied to determine the exact mechanism through which annealing enhance AZO and IGZO characteristics. The study includes microstructural, compositional, and electrical characterisation.

1.6 Significant contribution to the field of oxide-based electronics

This research study has investigated low thermal-budget fabrication of two functional oxides (AZO and IGZO) for important electronics applications, including PVs and TFTs.

1. It was demonstrated how the microstructural and compositional characteristics of AZO and IGZO are controlled by their sputter-deposition conditions. Consequently, the electrical properties are optimised.
2. Post-deposition annealing with ELA and RTA was demonstrated to noticeably enhance the characteristics of room temperature deposited AZO and IGZO films via local atomic rearrangement and modification of the density and distribution of structural defects.
3. Due to the fast growth of PVs and FPDs industries, there is an increasing demand for tin doped indium oxide (ITO), which is known of a high cost and a limited raw materials availability. Therefore, alternative transparent conducting materials are intensively investigated. Annealed AZO films by means of ELA and RTA demonstrate electrical and optical characteristics very close to those of ITO transparent electrodes, but crucially at lower raw materials cost and lower thermal-budget fabrication.
4. With an increasing interest in electronics on economical flexible polymer substrates, it is important to develop techniques of annealing that can meet the demands relevant to this area. ELA of AZO and IGZO demonstrate KrF ELA as a promising and powerful low thermal-budget processing approach to further enhance the electrical and optical characteristics of room temperature deposited oxide thin films. In addition, for the first time KrF ELA was successfully applied to IGZO TFTs on flexible polymer substrates.

1.7 Structure of the thesis

This thesis is composed of seven chapters organised as follows:

1. Chapter one (Introduction) presents the research motivation, aim, and objectives, as well as an overview of the research methodology and contribution to the field. Finally, the chapter outlines the thesis structure.
2. Chapter two (Background and Literature Review) provides background information on the fundamental properties (structural, electrical, and optical) of the studied oxide materials in this research (AZO and IGZO). It also contains the essential aspects of thin film transistors including structures, operation modes, characterisation, and active layer technologies. This background information is required in order to explain and discuss the results obtained from the performed experimental work. Finally, this chapter summarises previous reports on room temperature sputter-deposition and laser annealing of the studied thin film materials.
3. Chapter three (Thin Film Fabrication and Characterisation Techniques) describes the experimental techniques employed in this research for deposition, post-deposition annealing, and thin film characterisation. Emphasis is given to the physics and experimental set up of RF magnetron sputtering and excimer laser annealing.

Thereafter, chapters four, five, and six are devoted to the experimental work of this research, as follows:

4. Chapter four (Room Temperature Sputter-deposition of AZO Films) presents and discusses the results of room temperature deposition of AZO by RF magnetron sputtering. The influence of various deposition parameters (oxygen to argon ratio, applied RF power, and sputtering pressure) on the structural, compositional, electrical, and optical properties of AZO samples systematically investigated is presented in this chapter.
5. Chapter five (Annealing Studies on AZO Films Sputter-deposited at Room Temperature) presents the investigation of the application of ELA and RTA to AZO thin films deposited at room temperature for further electro-optical characteristics improvements. The structural, compositional, electrical, and optical properties of the annealed AZO samples are examined and analysed as a function of different annealing conditions. The chapter discusses the mechanisms of ELA and RTA in enhancing AZO characteristics. The fabricated AZO samples' potential application to PVs, in terms of performance as well as environmental stability, is presented.
6. Chapter six (Low Thermal Budget Fabrication of IGZO Thin Film Transistors) is devoted to IGZO thin films and TFTs fabrication at minimal substrate heating utilising RF magnetron sputtering at room temperature and ELA at different conditions. The potential of KrF ELA to enhance the performance of IGZO TFTs on silicon or heat-sensitive Polyethylene naphthalate (PEN) flexible substrates is demonstrated in this chapter.
7. Chapter seven (Conclusions and Future Perspectives) presents the conclusions and key outcomes of this body of work. It also suggests some thoughts for future work on oxides materials deposition, laser annealing, and applications.

2 Background and Literature Review

2.1 Introduction

This chapter provides background information on the fundamental aspects of the studied oxide materials and applications in this research. For more exhaustive background information on oxide materials, interested readers are directed to [5, 12-15]. Also, this chapter explores previous literature on sputter-deposition and laser processing of the studied materials. This research is aimed at low thermal budget fabrication of functional transparent conducting oxides (TCOs) and transparent semiconducting oxides (TSOs).

2.2 Introduction to transparent conducting oxides (TCOs)

TCOs are a unique class of materials exhibit high visible transparency > 80% coupled with good electrical conductivity > 10^3 $S.cm^{-1}$ and are ubiquitous in many current and emerging electronics applications including flat panel displays (FPDs) and photovoltaics (PVs). In FPDs, TCOs are used in pixel addressing circuits to supply a driving signal to a desired pixel, while allowing the produced light to pass through. Also, TCOs are used as the contact terminals in thin film transistors (TFTs). In PVs, the incident solar light passes through a TCO layer to the active layer that generates a photocurrent which is then collected via the TCO layer [12]. TCOs were first realised in 1907 when cadmium oxide was prepared by Baedeker [12]. Cadmium oxide, however, has some drawbacks preventing its applications as practical electrodes, such as high toxicity and a narrow bandgap of 2.3 eV [12, 16]. Since then a vast amount of research has been conducted into commercialising different oxides as transparent electrodes, with emphasis on polycrystalline oxides of tin, indium, and zinc as well as their doped and mixed versions [12, 17]. Amongst TCOs, tin-doped indium oxide ITO (90% of indium oxide and 10% of tin oxide by weight), has been the front-runner material as shown in Fig. 2-1. Nevertheless, although ITO demonstrates superior conductivity ~ 10^4 $S.cm^{-1}$ and visible transparency > 85%, there are some identified drawbacks associated with ITO for different applications [3, 17]. For example, flexible electronics that force some additional fabrication and environmental constraints, such as low temperature fabrication, and conductivity stability against mechanical stress to which ITO is not efficiently applicable due to its brittle nature, and the need of temperature ~ 200°C for crystallisation [2, 3]. This need for crystallisation temperature restricts the substrate choice to relatively expensive

heat-resistive substrates, also it increases the cost of ITO electrodes fabrication which is already high owing to the limited availability of indium in continental crust ~ 0.1 ppm compared to ~ 130 ppm for zinc [3, 18]. Indium has been identified as the 10th of twenty critical raw materials in a recent report by the European Union [19]. As a result, the cost of ITO accounts for the largest percentage of the total cost of PVs. For example, ITO cost is in the range of 38-51% of the total cost of organic photovoltaics (OPVs), compared to 21-27% being the active materials cost [20]. Considering the current rapid increase of the PVs industry, there is an increasing demand for alternative materials to ITO.

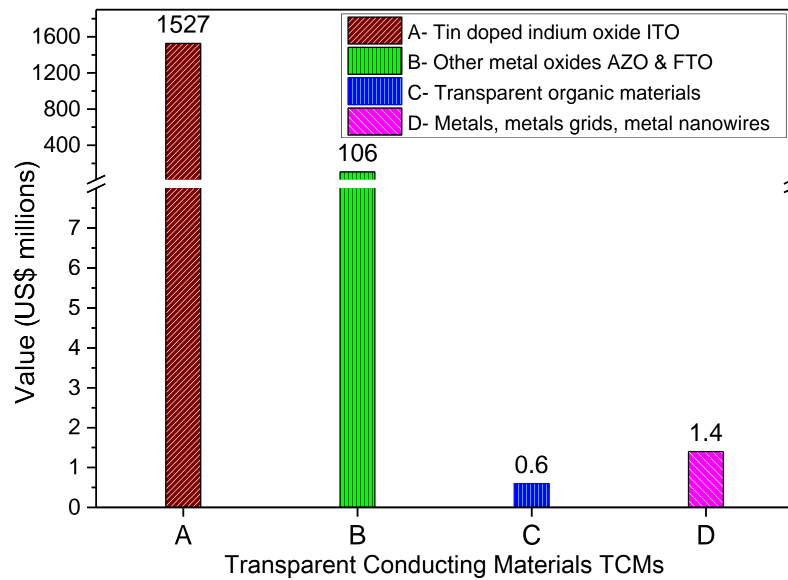

Fig. 2-1 The commonly used transparent conducting materials TCMs in FPDs and PVs industries with their value in 2012 [21].

Therefore, the TCOs' research has been directed to explore less-indium content or non-indium based transparent conducting materials for further electronics developments such as flexible electronics on heat-sensitive polymer substrates, as well as for reducing the fabrication costs for electronic applications. ITO alternatives' value is anticipated to grow to 350-400 US$ million in 2025 compared to ~ 110 US$ million in 2012 [22]. Various potential candidates have been examined to replace ITO including:

1. ZnO-based TCOs such as such as aluminium doped zinc oxide (AZO), and gallium doped zinc oxide (GZO) [3, 18]. Relevant background on ZnO based TCOs studied in this work is presented in following sections.
2. Organic transparent conducting thin films such as PEDOT: PSS, which achieves good conductivity but still suffers from instability issues [23].
3. Metal-based nanotubes, grids, and nanowires [24].

2.3 Zinc oxide-based TCOs

ZnO has an extensive research history dating back to the early beginning of the 19th century due to its attractive features such as deposition as a crystalline material at room temperature, relatively low cost compared to most oxides, and a wide bandgap Eg~3.37 eV [13, 25]. In addition to the pure ZnO merits, doped-ZnO provides attractive characteristics for various applications. For instance, ZnO doping with group III elements such as aluminium, gallium, or indium was proposed for transparent electrodes [3, 18]. Aluminium doped zinc oxide, in particular gained an increasing interest due to its comparable electrical conductivity to that of ITO, high chemical stability against hydrogen plasma commonly used in PVs manufacturing, and easy post-deposition etchability [12, 25, 26].

2.4 Zinc oxide crystal structure:

ZnO crystallises in three crystal structures hexagonal wurtzite, cubic zinc blende, and rocksalt. However, wurtzite is the most thermodynamically stable under ambient conditions, and thus is the commonly observed for doped and undoped zinc oxide samples fabricated by means of different techniques. In this structure, as in Fig. 2-2, the bonds are tetrahedral where each oxygen ion is bonded to four nearest neighbours of zinc ions and vice versa.

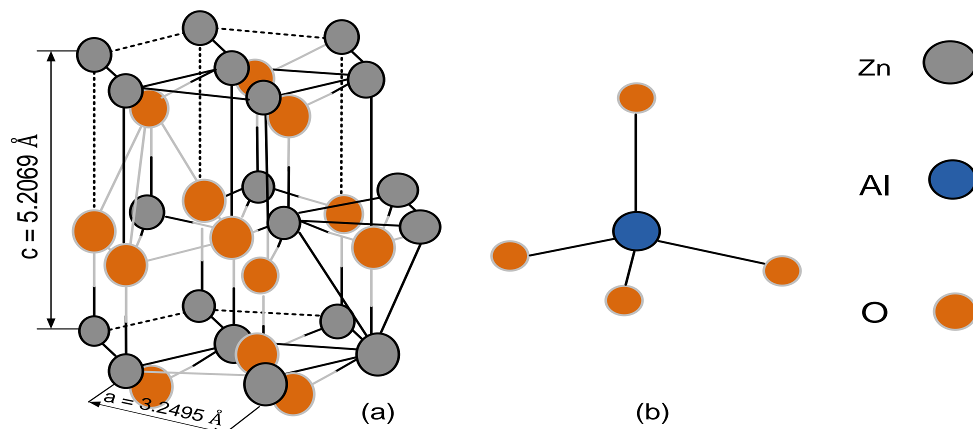

Fig. 2-2 (a) The ZnO wurtzite structure, (b) an Al atom introduced to the ZnO lattice. Adopted from [15].

The zinc blende structure can be stabilised only once deposited on highly mismatched substrates or on a buffer layer of zinc sulphide [13]. While, the rocksalt phase is formed at relatively high pressure of about 10 GPa, but it reverses to wurtzite structure at 2 GPa [13]. For doped ZnO samples, a certain ratio of dopants is introduced to the ZnO lattice [13]. During ZnO thin film deposition, the deposited atoms typically prefer to crystallise along the (002) plane of

wurtzite structure parallel to the substrate surface, while the crystallographic c-axis is perpendicular to the substrate surface. This preferred orientation is commonly observed for ZnO-based thin films and is explained by ‘‘survival of the fastest’’ model proposed by Drift [27]. Following this model, various random orientations along different crystal planes might be exhibited at the beginning of the growth, the orientations compete with each other to grow. But, given that the (002) plane of wurtzite structure has the minimal surface free energy and thus the fastest growth rate, it is the only orientation that can survive during the growth. The orientation becomes stronger whenever the deposited species gain kinetic energy via tuning the deposition parameters, external substrate heating, or post-deposition processing [28].

2.5 Electronic band structure and optical bandgap

Owing to differences in the electron affinity and ionisation energy between metals and oxygen, charge transfer occurs from metal atoms (because of their lower ionisation energy) to oxygen atoms (due to their higher electron affinity energy) during oxide formation, i.e. forming ionic bonding. The oxides conduction band minimum (CBM) is composed of unoccupied ns-orbitals of metal cations; whilst, the valance band maximum (VBM) is composed of occupied 2p orbitals of oxygen anions. Therefore, oxides usually have very low VBM since oxygen 2p orbitals are relatively small compared to the valence orbitals of metallic ions, for example 4s orbitals in the case of zinc. The difference between the VBM and the CBM determines the optical bandgap Eg. Bandgaps are represented by energy (E) versus wave vector (K) curves. When the CBM and the VBM occur at the same wave vector the bandgap is referred to as a direct bandgap in which electrons undergoing energy transitions from the VBM to the CBM exhibit no or negligible change in wave vector. Like most widely investigated oxides, ZnO has a direct bandgap of about 3.37 eV [12, 29]. If a ZnO film is undoped, the Fermi level E_f would be located in the middle of the bandgap, as shown in Fig. 2-3 (a), and therefore the film is insulating since only few electrons can be excited across its wide bandgap. However, as the electron density in ZnO is increased by means of doping, the Fermi level E_f will be moved towards or even in the CBM, thus making ZnO conductive [30]. Heavily-doped semiconductors are referred to as degenerate semiconductors where the carrier population exceeds Mott’s critical density for a metal–semiconductor transition which is in the range of (0.15-1.20) $\times 10^{-19}$ cm^{-3} for AZO films [31].

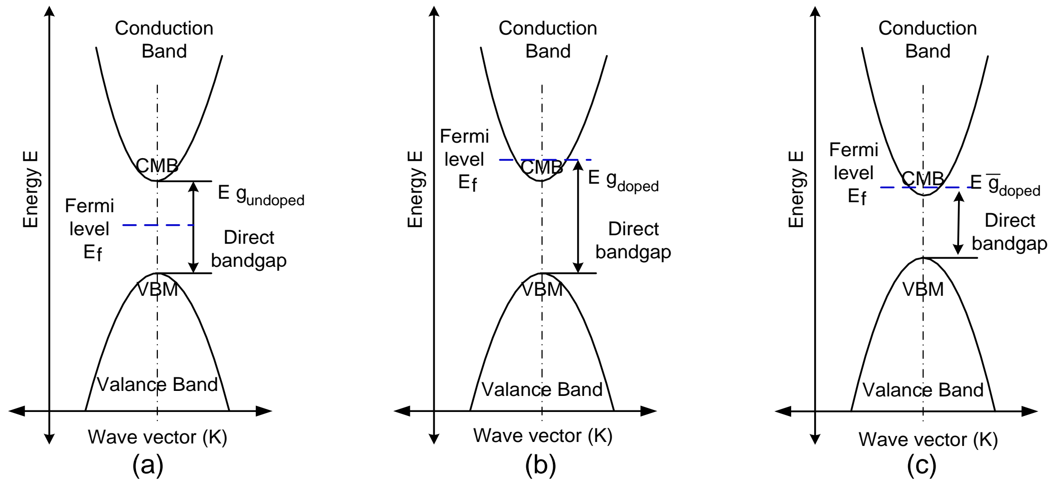

Fig. 2-3. Schematic representation of the electronic band structure (a) undoped ZnO, (b) doped ZnO in the case of Burstein Moss effect, and (c) doped ZnO in the case of bandgap renormalisation effect [31].

In degenerate semiconductors, the optical bandgap is sensitive to the electron density owing to the Burstein-Moss effect [32], and the bandgap renormalisation effect [33]. The former, which is widely observed in most TCOs, comes into play when the electron density is increased to populate the trap states below the CBM. As a consequence of lack of unoccupied states below the CBM, and taking into account the Pauli principle that does not permit states to be doubly occupied and the optical transitions in direct band materials occur vertically, the Fermi level E_f is pushed towards or even into the conduction band, Fig. 2-3 (b). Hence, electrons at the VBM can only be excited above the Fermi level in the conduction band. Thus, the threshold energy required for incident light photons to be absorbed and excite electrons is increased which means the optical bandgap is enlarged to a level which correlates with the carrier density [32]. However, at higher donor concentration and therefore higher electron population, the bandgap will be narrowed according to the bandgap renormalisation effect due to electron-electron and electron-donor interactions during their correlated motions where electrons repel from each other, but attract positively charged dopants which lead to lowering the energy of the electrons in the conduction band. Consequently, the CBM is pushed downward, but the VBM will move up resulting narrowing the bandgap, Fig. 2-3 (c). The overall optical bandgap of a doped-ZnO at different carrier population can be expressed as:

$$Eg_{doped} = Eg_{undoped} + \Delta E_{BM} - \Delta E_{BGR} \quad 2\text{-}1$$

where: ΔE_{BM} and ΔE_{BGR} are changes in bandgap due to Burstein-Moss effect and bandgap renormalisation effect, respectively [33, 34].

2.6 Electrical properties

N-type conductivity is obtained in ZnO-based materials via two doping approaches:

1. Intrinsic doping that results in increasing the electron density from 10^{13} cm^{-3} for pure ZnO to 10^{17} cm^{-3} via deviations from the stoichiometric structure i.e. creating native defects during fabrication. ZnO native defects include zinc interstitials (Zn_i), which ionise introducing electrons, and oxygen vacancies (V_o), which leave behind electrons liberated from the related zinc atoms [35, 36]. Also, in many fabrication techniques hydrogen is reported to present and act as a shallow donor [37]. The origin of n-type conductivity of undoped ZnO has been intensively debated based on electronic structure studies and thermodynamic considerations. However, oxygen vacancies are the most commonly reported source of electrons in ZnO. This is experimentally evidenced through studying the effect of oxygen pressure during deposition, or the effect of post-deposition annealing ambient [12, 13]. Intrinsically doped ZnO is not stable against oxidation that leads to conductivity reduction [12, 38].
2. Intentional doping via addition of higher valence atoms like group III elements at certain concentrations leading to degenerate doping when the donors are effectively incorporated into ZnO and overlap with its conduction band. Consequently, the electrons density increases to 10^{20}-10^{21} cm^{-3}, leading to metal-like conductivity [28]. Meanwhile, the ZnO bandgap is enlarged due to the Burstein-Moss effect.

For sufficient electrical conductivity σ, simultaneous improvements in the free carrier density N and mobility μ are crucial [12], as presented in Eq. 2-2.

$$\sigma = N\mu q \qquad 2\text{-}2$$

where q = is an electron's charge 1.602 x 10^{-19} coulombs. The mobility as a measure of how easily electrons move in a material is expressed as:

$$\mu = q\tau_{relx} / m_{eff} \qquad 2\text{-}3$$

where τ_{relx}, and m_{eff} are the electrons' relaxation time between consecutive scattering events and the effective mass in the conduction band respectively. From Eq. 2-3 it can be seen that the mobility is affected by the relaxation time, as the other parameters are constants for a material. In polycrystalline films such as ZnO, the carrier relaxation time is influenced by two main scattering mechanisms including grain boundaries scattering and ionised impurity scattering. Both these mechanisms depend on the electron density and the material microstructure properties, and the highest conductivity is achieved once these mechanisms are suppressed [39, 40].

2.6.1 Grain boundaries scattering

In polycrystalline thin films, a large density of grain boundaries is exhibited in particular with room temperature deposition [16, 41]. Trap states like oxygen atoms tend to diffuse into grain boundaries and surface defects causing electrons capturing from the grains and hence resulting in negatively charged grain boundaries [42]. This leads to band bending and to creation of carrier-depleted regions on both sides of the grain boundaries as schematically demonstrated in Fig.2-4. Also, potential barriers (Φ_b) between the grains are created which strongly impede the carrier mobility between neighbouring grains in particular when the depletion regions become comparable to the grain lateral dimension [16, 39, 40].

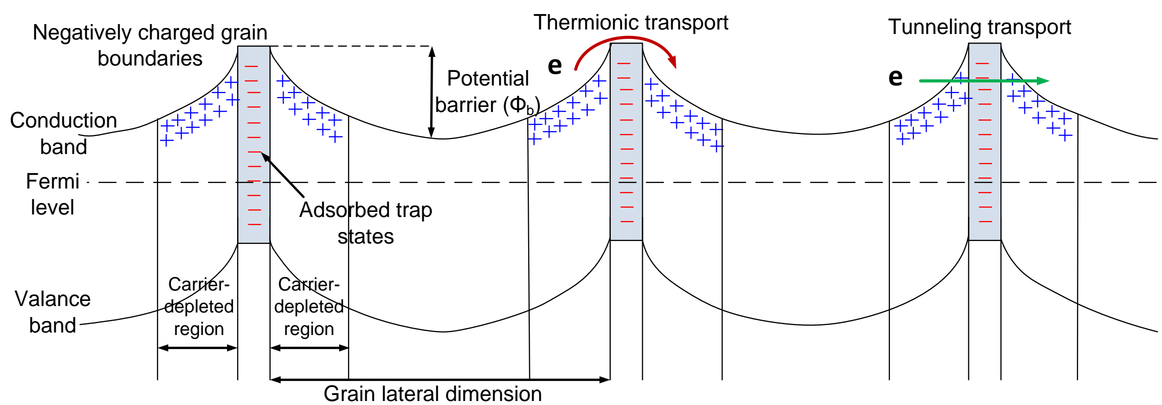

Fig.2-4. Schematic representation illustrates the band bending due to the grain boundaries impact on the carrier transport in an n-type polycrystalline material. Adopted from [15, 43].

The created potential barriers' height depends on both the trap states density at grain boundaries and on the free electrons density. For heavily doped films with carrier density 10^{20}-10^{21} cm^{-3}, the number of free electrons in the grains should be higher than the number of trap states at the boundaries, which leads to the acceptor states to be totally filled and only a small portion of the grain is carrier-depleted. Consequently, the potential barriers are reduced and carriers would transport across the created barrier via thermionic and/or tunnelling transport [39, 40, 43]. The above mentioned effect of grain boundaries scattering on the carrier mobility and thus the material conductivity was first modelled by Seto in 1975 [43].

It is well known that ZnO exhibits piezoelectric properties which could induce charges at grain boundaries under intrinsic stress. Consequently, additional scattering is induced at grain boundaries [13, 43]. Furthermore, non-activated dopants could be segregated at grain boundaries causing carrier scattering known as neutral impurity scattering [12, 43].

2.6.2 Ionised impurity scattering

In practical TCOs, metal-like conductivity is achieved via high electron density originated from high concentration of donor defects i.e. impurities which ionise contributing to free electrons. An electrostatic field is created because of interactions between electrons and the positively charged ionised impurities leading to deflection of electrons limiting their transport. Therefore, the electrons that are close to Fermi level only would participate in conduction. Ionised impurity scattering depends on the free carrier concentration and is the dominating scattering mechanism in most TCOs at electron densities > $5x10^{20}$ cm^{-3}. Enlarging the grain sizes in polycrystalline TCOs is an effective approach to reduce the ionised impurity scattering via increasing the electrons' mean free paths [39, 40, 44].

2.7 Optical properties

An effective TCO exhibits high optical transmission over the visible (VIS) region, and parts of the near infrared (NIR) region. The ZnO bandgap of 3.37 eV allows having an average transmission >80% over this range, as shown in Fig. 2-5. This wide bandgap is attributed to the large electronegativity of oxygen, and to low energy of 2p orbitals in the VBM of ZnO [12, 16].

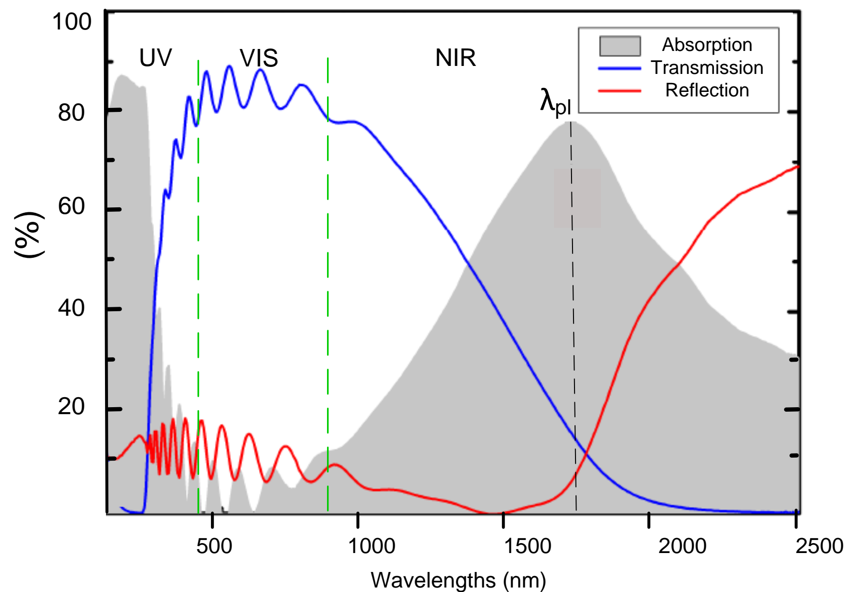

Fig. 2-5. Absorption, Transmission, and Reflection spectra for ZnO thin film [12].

The transmission window of ZnO is defined by the absorption edges in the ultraviolet (UV) region (λ_{gap} < 400 nm), and in the NIR region (λ_{pl} > 1000 nm) corresponding to the material optical bandgap, and to the free electron plasma absorption respectively. In the former, photons absorption results in exciting electrons across the bandgap. While in the latter, according to Drude

free electron model [45], due to electrons interaction with the electrical field component of the incident light the material dielectric permittivity is changed. Consequently, most of the light is absorbed by the electrons at a wavelength known as the plasma wavelength at which electrons oscillate in phase with the electric field component. The material becomes reflecting at wavelengths longer than the plasma wavelength due to faster response of the electrons to the electric field. Increasing the electron density typically pushes the plasma wavelength towards the visible range of the spectrum. Thus, enhancing the electron mobility via eliminating the scattering mechanisms is essential in order to achieve high conductivity and simultaneously maintain good transparency in the NIR [12, 16]. In addition to the electron density, the optical properties are affected by microstructural and morphology properties owing to scattering and absorption of structural defects, and losses at rough surfaces. [12, 16].

2.8 Introduction to transparent semiconducting oxides (TSOs)

Another category of oxide materials is transparent semiconducting oxides (TSOs) which were first reported in 1954 when vanadium oxide-based glass exhibited semiconducting properties [46]. Various oxides of heavy metals have been explored for semiconducting properties. H. Hosono's group obtained high and promising electron mobility values > 10 cm^2/Vs for different amorphous oxides [47]. TSOs have been intensively examined for TFTs [7]. Relevant background information about TSOs and TFTs is provided in the following sections.

2.9 Thin-Film Transistors (TFTs)

TFTs are a class of field effect transistor composed of thin films sequentially deposited on an insulting substrate. The most simplistic structure of TFT includes three contacts source, drain, and gate electrodes, a semiconducting material such as indium gallium zinc oxide (IGZO) as the active layer deposited between the source-drain electrodes, and an insulting material between the semiconducting material and the gate electrode. The separation between the source and drain is referred to as the channel length (L), while, the distance along which the source and drain are parallel to each other is the channel width (W). The working principle for TFTs is to create a flow of electrons between the source-drain electrodes via varying the potential between the gate-source electrodes, resulting in an accumulation layer of electrons at the semiconductor-insulator interface. This layer in turn modulates the semiconducting film conductivity and thus a

current flow is obtained between the drain-source electrodes. TFTs functionally can be simply described as voltage-controlled current sources [7, 48].

2.9.1 TFT structures and classifications

There are four basic configurations for a TFT, shown in Fig. 2-6. These structures are classified based on the order in which the TFTs layers are deposited. Namely, whether the source-drain and gate electrodes are on the same or opposite side with respect to the semiconducting active layer. The former configuration is known as coplanar, while, the latter as staggered [7, 48].

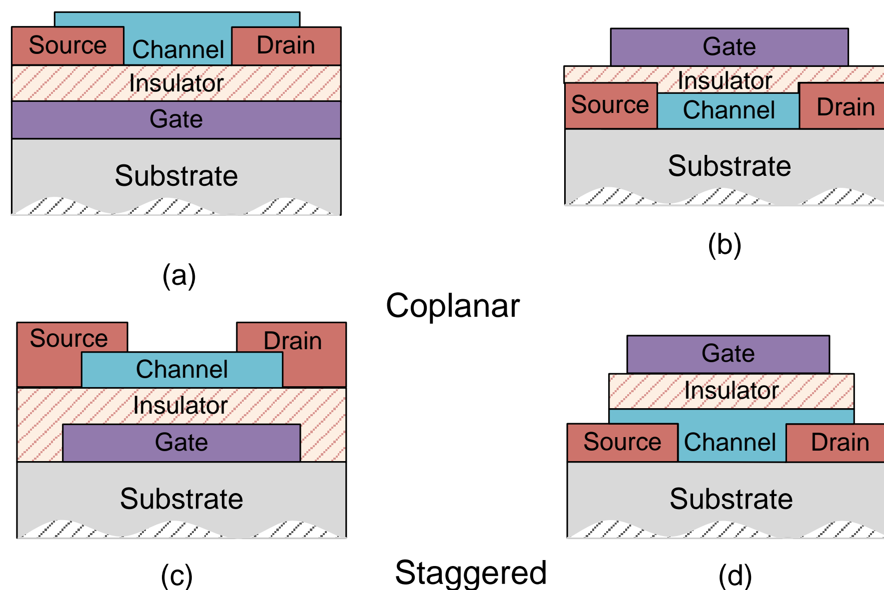

Fig. 2-6. Schematics showing the most common TFT structures, (a) bottom-gated-coplanar structure, (b) top-gated-coplanar structure, (c) bottom-gated-staggered structure, and (d) top-gated-staggered structure. Adopted from [48].

The configurations are further classified based on the gate electrode location in relation to the active layer, TFTs with the gate above the active layer are referred to as top-gated, while, when the gate electrode is underneath the active layer, the TFTs are bottom-gated. Each of these arrangements has certain pros and cons dominated by the active material and the fabrication process applied [7, 48]. In this research, the staggered top-gated structure was used. TFTs can be also classified in terms of operation mode. For an n-type TFT that is normally in off-state and is turned to on-state once a positive gate voltage is applied, the operation mode is enhancement. Whilst, in the depletion mode the TFT is normally in on-state and is turned to off-state when a negative gate voltage is applied. In most of TFT applications as switches, enhancement mode is preferred for simpler circuits and less power consumption [7, 48, 49].

2.9.2 Basic TFT operation

Studying the energy band diagram for a stack of semiconductor-insulator-metal upon different voltages applied to the metal is commonly used for to explain the ideal TFTs operation.

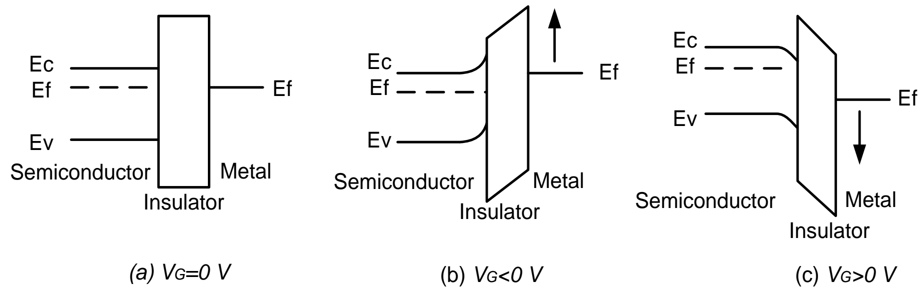

Fig. 2-7. Energy band diagram for a semiconductor-insulator-metal stack representing n-type TFT-enhancement mode, (a) Vg=0 V (equilibrium), (b) Vg<0 V (depletion), and (c) Vg>0 V (accumulation). Adopted from [48].

Considering a TFT with an n-type active layer (semiconductor) in enhancement mode, when zero voltage is applied to the gate (metal) $V_G=0$ V, the stack band is considered to be in equilibrium state and ideally there is no effect on the electrons at the semiconductor-insulator interface Fig. 2-7(a). Applying a negative gate voltage $V_G<0$ V would repel electrons from the semiconductor-insulator interface creating a depletion layer which causes a positive band-bending i.e. moving the metal's Fermi level up compared to that for the semiconductor Fig. 2-7 (b). In equilibrium and depletion sates the TFT is ideally considered in off-state. However, applying a positive voltage $V_G>0$ V, results in attracting electrons forming an accumulation layer at the semiconductor-insulator interface. This causes a negative band-bending as shown in Fig. 2-7 (c). The accumulation layer in a TFT allows for a connection between the source and drain electrodes. To switch the TFT to on-state, a positive drain voltage V_D is applied in order to inject electrons from the source, which is grounded, to the accumulation layer that in turn transports the elections to the drain. Consequently, drain current I_D passes between the drain and source. Since the electron density in the accumulation layer is a function of the gate voltage V_G, the drain current can be modulated by varying the gate voltage [48]. Once the TFT is switched to on-state, different operation regimes can be identified depending on the drain voltage.

1. When $V_D < V_G - V_{TH}$, where V_{TH} is the threshold voltage to induce the accumulation layer, the I_D increases linearly as the V_G is increased. This operation regime is referred to as the linear regime in which the electron accumulation is uniform throughout the accumulation layer Fig. 2-8 (a), and the I_D is described as in Eq. 2-4.

$$I_{D lin} = \frac{W\mu_{lin}C_i}{L}(V_G - V_{TH})V_D \quad 2\text{-}4$$

where W and L are the channel width and length respectively, C_i is the gate dielectric capacitance per unit area, and μ_{lin} is the electron mobility in the linear regime.

2. When $V_D \geq V_G - V_{TH}$, high drain voltage results in an electric field applied parallel to the semiconductor-insulator interface that acts perpendicularly to the V_G electrical field. Therefore, the accumulation layer at the drain contact is electron-depleted Fig. 2-8 (b), and the I_D is saturated independently of the V_G. Under these biasing conditions, the TFT is operated in the saturation regime, and the drain current I_D is described as in Eq. 2-5.

$$I_{D sat} = \frac{W\mu_{sat}C_i}{2L}(V_G - V_{TH})^2 \quad 2\text{-}5$$

where μ_{sat} is the charge carrier mobility in the saturation regime.

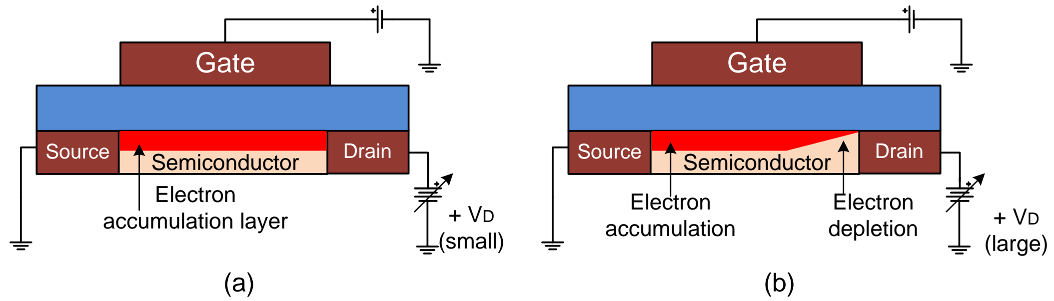

Fig. 2-8. Schematics represent TFT operation regimes, (a) linear regime, and (b) saturation regime. Adopted from [48].

The above equations are based on the gradual approximation model developed by Shockley to describe field effect transistors operation [50]. The model assumes that the lateral field parallel to the semiconductor-insulator interface caused by the drain voltage is much smaller than that induced by the gate voltage. Thus, the semiconductor layer is considered to be under one-dimensional field. This approximation is not physically correct when a TFT operates in the saturation region, due to the carrier depleted region near the drain. However, the model is generally considered as the standard model to describe field effect devices operation [48].

2.9.3 TFT Electrical Characterisation

There are two standard methods to quantitatively assess TFT performance, transfer characteristic curve and output characteristic curve. In the former, a constant voltage is applied across drain-source terminals, while the gate voltage V_G is swept forward and backward. Then, the drain current I_D is recorded as a function of the V_G. In the output characteristic curve, a variable voltage is applied across drain-source terminals V_D, while the V_G is held constant. Then, I_D is

recorded at different drain voltage V_D to clearly distinguish TFT operation regimes. Important TFT figure-of-merits are extracted from the transfer characteristic curve. Thus, it is used to evaluate the examined TFTs in this research. The extracted parameters are:

1. Turn-on voltage V_{ON}, which is the gate voltage at which the drain current increase is observed. In this research, V_{ON} is considered as the gate voltage at which the I_D is 1 nA. Large positive V_{ON} values indicate high density of trap states, thus, a large positive V_G is needed to fill the trap states first to turn the TFT to on-state. Whilst, large negative V_{ON} values imply high electron density in the active layer which requires large negative V_G for complete carrier depletion and turn the TFT to off-state [7, 48]. V_{ON} values close to zero are of importance for low off-state current as well as power consumption.
2. I_D on/off ratio, is the ratio between the maximum I_D when the TFT in on-state, to the minimum I_D when the TFT in off-state. Large on/off ratios > 10^6 are of interest for TFTs as switching elements or current drivers in FPDs [7, 48, 51].
3. Subthreshold swing S, indicates the V_G needed to increase the I_D by one decade in the linear region of operation. It describes how effectively the charge accumulation layer is formed, which is affected by the bulk and interfacial trap states density for the active layer. S is determined as the reciprocal of the maximum slope of the transfer curve.

$$S = \frac{\partial V_G}{\partial(\log_{10} I_D)} \quad \text{2-6}$$

S < 0.3 V/dec is desired for higher operation speeds and lower power consumption [51].

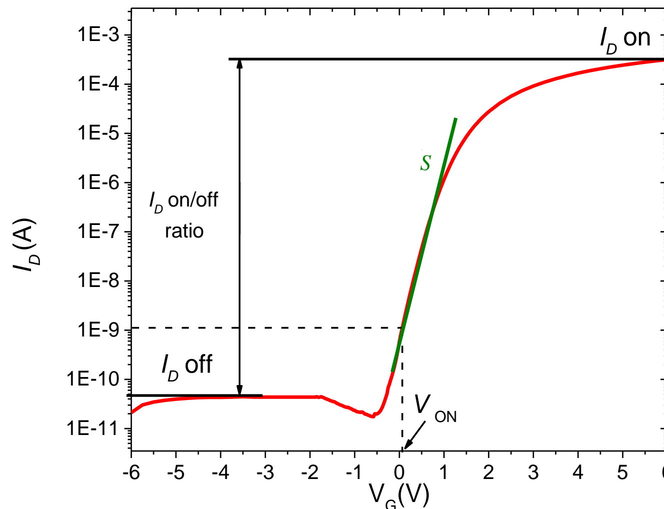

Fig. 2-9 Typical transfer characteristics curve for n-type semiconductor TFT

4. Carrier mobility in a TFT active layer directly affects the maximum I_D and the maximum operating speed between on and off states [7, 48]. TFT mobility can be either extracted in the linear regime and is known as the field effect mobility or linear mobility Eq.2-7, or extracted from the saturation regime, known as saturation mobility Eq.2-8.

$$\mu_{FE} = \frac{L}{C_i W V_D} (\frac{\partial I_{Dlin}}{\partial V_G}) \quad \text{2-7}$$

$(\frac{\partial I_{Dlin}}{\partial V_G})$ in the linear regime of the transfer curve is known as the transconductance (g_m)

$$\mu_{sat} = \frac{2L}{C_i W} (\frac{\partial \sqrt{I_{Dsat}}}{\partial V_G})^2 \quad \text{2-8}$$

Since the gradual approximation is not valid in the saturation regime, the saturation mobility is not physically correct [7, 52]. In this thesis the field effect mobility is used.

2.9.4 Materials used as the active layer in TFTs

The first functional n-type TFTs were reported in 1960s by Weimer using polycrystalline cadmium sulfide [53]. Since then, various materials were explored for TFTs, the largest TFT improvement was the application of amorphous hydrogenated silicon (a-Si:H) by LeComber in 1979 demonstrating a performance that was good enough for addressing liquid crystal displays [54]. Moreover, a-Si:H offers relatively low cost and large area uniformity. However, a-Si:H TFTs have some disadvantages such as limited field effect mobility ~ 1 cm^2/Vs, and opacity [7, 48]. Poly-crystalline silicon TFTs were introduced by Depp et al. in 1980 [55] with a mobility of 50 cm^2/Vs using high fabrication temperature (1000°C). In 1986, low temperature poly silicon LTPS TFTs were reported for the first time via XeCl excimer laser (λ=308 nm) annealing achieving a mobility of 180 cm^2/Vs [56]. Organic materials have been also examined for TFTs since 1986 due to their low fabrication temperature and cost. However, organic materials are known for poor environmental stability and the achieved mobility is less than that of a-Si:H [57]. Oxide TFTs were first reported in 1964 using tin oxide [58]. This work motivated many research groups to explore oxide materials for TFT devices. In 2003, a number of publications from reputable research groups, such as Hoffman et al [49] and Carcia et al [59] reported good performance polycrystalline ZnO TFTs using sputtering at 300°C. These devices exhibited field effect mobility values > 2 cm^2/Vs. Due to crystalline materials issues such as poor uniformity and instability of TFT performance, as well as the high free electron density for zinc oxide and tin oxide, the TSO research was directed to amorphous multicomponent oxides. In 2004, Nomura et al [6]. published for the first time a-IGZO TFTs with relatively high saturation mobility of 8.3 cm^2/Vs. This work opened the door for an increasing interest and research on amorphous TSOs for TFTs. The achieved performance of amorphous oxide TFTs so far is considered to be sufficient for FPDs

and several prototype displays have been demonstrated using amorphous TSOs TFTs [60, 61]. Thus, most of the recent development research of oxide-TFTs has been focused on the fabrication techniques aiming at better long-term stability and lower fabrication cost [62, 63].

Active layer	μ_{FE} cm^2/Vs	Bandgap - VIS transparency	Uniformity	Processing Temp.	Comments
a-Si:H	~ 1	1.75 eV - Poor	Good	~ 250°C	Good uniformity. Low mobility and I_D, and opaque.
Poly-Si	50-200	1.12 eV - Poor	Poor	> 500°C	High mobility. Opaque, and high-cost fabrication.
Organic	0.1-1	2 eV - Moderate	Good	RT - 250°C	Low fabrication cost. Poor mobility and stability.
ZnO IZO	20-50	3.37 eV - Good	Poor	RT - 300°C	Grain boundaries and high electron density issues.
a-IGZO	3-30	3.1 eV - Good	Good	RT - 300°C	Good mobility. Stability improvements needed.

Table 2-1. Summaries the most common TFT technologies [14, 48, 64]

2.9.5 Conduction mechanism of amorphous TSOs

Hosono et al. [6, 47] explained that the origin of a relatively high electron mobility for amorphous semiconducting oxides of heavy metals is their electronic structure in which the bonds are ionic and the CBM is primarily composed of unoccupied valence orbitals of metal cations with an electronic configuration (n–1) $d^{10}ns^0$ (n≥5). These orbitals exhibit relatively large sizes and spread. This would maintain a large overlap between adjacent cations orbitals to a level that is insensitive to the amorphous structure and bonding angles changes, as shown in Fig. 2-10. Consequently, the CBM is greatly dispersed that preserves the carrier transport paths even in amorphous state and thus achieving relatively high electron mobility [6, 62, 65, 66].

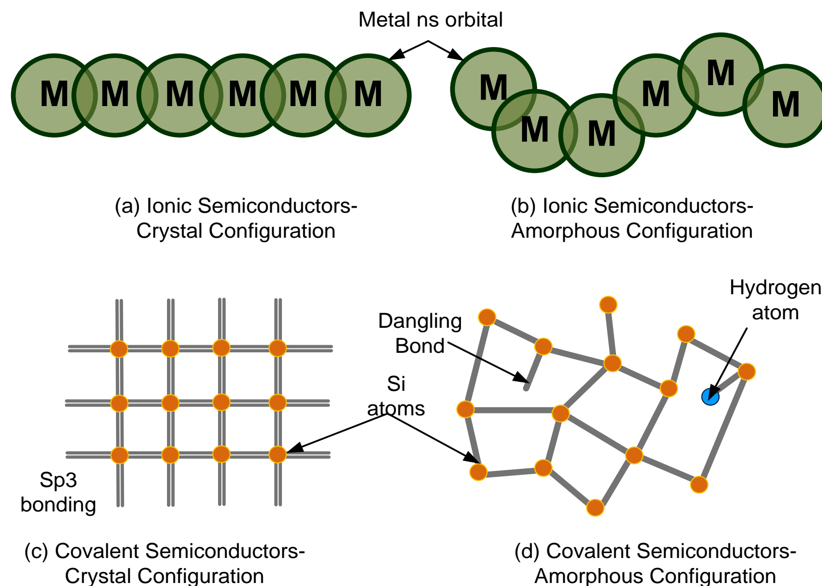

Fig. 2-10. Schematic representation for "the carrier transport paths" in the CBM for ionic semiconductors (a) crystal, (b) amorphous, and in covalent semiconductor (c) crystal, (d) amorphous. Adapted from [6]

Unlike, in covalent semiconductors like silicon where the CBM is made of strongly directional and anisotropic sp^3 orbitals which are sensitive to bonding angles changes. Therefore, when moving from crystalline to amorphous structure, distortions would be caused to the bonding accompanied with high density of localised traps between the CBM and VBM leading to carrier trapping/scattering. Thus, the carrier transport is performed via hopping between the trap states within the bandgap resulting in deteriorated carrier mobility [62, 67].

2.9.6 Amorphous TSOs for TFT active layer

After the Nomura et al publication [6], various amorphous TSOs have been examined for TFTs, including zinc indium oxide [68], indium barium zinc oxide and indium strontium zinc oxide [69], and zinc indium tin oxide [70]. Due to the already stated indium issues, indium-free oxides have been also studied, such as gallium tin zinc oxide [71] and amorphous zinc tin oxide [72]. Although high performance was obtained for indium-free oxides, high temperature 300°C - 600°C was needed. Among amorphous TSOs, a-IGZO has been the most attractive material for replacing silicon based materials in TFTs due to combining higher electron mobility even at room temperature deposition, compared amorphous silicon, with better uniformity, compared to crystalline silicon. Moreover, the high visible transmittance of > 80 % of oxides in general is very attractive for the realisation of transparent electronics [5, 62]. In contrast, silicon based materials demonstrate rather low visible transmittance < 30 %. In regard to other oxides such ZnO and IZO, IGZO TFTs exhibit more stable and better performance originating from:

1. Wide controllability in the electrical properties of IGZO via varying the contained metals ratios. Each of the contained metals plays an essential role in defining the overall electrical performance of IGZO. Indium due to its large ionic radius (n=5) maintains good overlap between the CBM metal cations and thus better carrier mobility [6, 67]. Gallium because of its stronger bonds with oxygen, helps in reducing the oxygen vacancies and thus the free electron density in IGZO, which is an issue for amorphous IZO [66]. Zinc adds structural disorder to the cations distribution in IGZO that prevents crystallisation [73]. It was reported that if the zinc ratio in sputtered films is < 10 at.%, the films would be less amorphous and have better chances for crystallisation [64].
2. Compared to crystalline oxides like ZnO, a-IGZO exhibits excellent large area uniformity and smoothness, surface roughness ~ 0.3 nm, associated with the amorphous nature which is desired for devices stability and ease of manufacturing [5, 6].

2.10 Fabrication of TCOs and TSOs

TCOs and TSOs have been deposited by various solution and vacuum based technologies. Solution based technologies such as spin-spray and sol-gel are very promising for cost-efficient and large-sized applications. However, post deposition processing at high temperature (> 350°C) for long dwell times (>1h) is typically essential to remove hydroxides and stabilising agents, and to promote material densification [63, 74]. Sputtering is a mature vacuum based deposition technique that is commonly used in thin film deposition because of various strengths including large-area applicability and deposition at room temperature [75, 76]. According to E. Fortunato et al. [7], during the 2001-2010 decade, about 200 papers were published on IGZO thin films and TFTs and more than 90 % of which used sputtering. Post-deposition annealing is commonly applied to room temperature sputtered oxides to enhance their electro-optical characteristics. Thermal annealing is the most common approach due to its simplicity. However, high temperature and/or long dwell time as well as expensive rigid substrates, due to non-selective heating, are often required [77, 78]. In contrast, laser annealing offers ultra-rapid processing with heating selectivity [10, 79, 80]. The studied oxides in this research AZO and IGZO are fabricated by room temperature RF magnetron sputtering combined with excimer laser annealing ELA using Krypton fluoride laser (KrF λ=248 nm). It is should be noted that only limited studies have been reported on laser annealing of AZO and IGZO. These reports are presented below in the sections 2.10.2 and 2.10.4.

2.10.1 Previous publications on sputter-deposition of AZO

Deposition of AZO has been widely explored and many studies have reported AZO with resistivity in the range of 2-5×10^{-4} Ω.cm either at elevated temperature 300-500°C [81, 82], or via pulsed laser deposition (PLD) [83]. Elevated temperature is not applicable for low temperature applications, while, PLD is not easily scaled for large-area applications and high volume production. A few publications reported room-temperature deposition of AZO by sputtering, and below a summary of some previous reports in chronological order is presented. Since the essential characteristics of TCOs are high optical transmittance and low resistivity, this summary is focused on these characteristics trends upon different deposition conditions.

W. Yang et al. [84, 85] have examined the effects of AZO deposition conditions (RF power, sputtering pressure, and substrate-to-target distance) on quartz substrates at room

temperature. The content of Al_2O_3 in the sputtering target was 2 wt.%, and the target was water-cooled at 30°C. All the samples showed resistivity values ≤ 10^{-3} Ω.cm. High-quality AZO was achieved at the optimised conditions (300 W, 30 sccm flow of Ar, and substrate-to-target distance of 7 cm) with resistivity of 2.9×10^{-4} Ω.cm for 500 nm thick, and 4.6×10^{-4} Ω.cm for 250 nm thick films, while, the visible transparency was ~ 90 %. However, although the authors did not mention the target size, the optimised RF power is relatively high at which the target could be over-heated even with the reported cooling temperature. In RF-sputtering, most of the applied power becomes heat in the target, which will lead to inevitably increasing the substrate temperature during growths. Also, it is well-known that ceramic targets, including AZO, have a low thermal conductivity and a high thermal expansion coefficient which are likely to cause a brittle target. Hence, sputtering targets are typically cooled with chilled water (10°C) [75, 86].

Z.A. Wang et al [87] reported an optimisation study of AZO sputter-deposition. They observed that the sheet resistance of 800 nm thick AZO decreases from 160 to 10 Ω/sq as the RF power is increased from 100 to 180 W. While, it increases gradually as the pressure is increased. The optimised AZO samples deposited at 180 W and 2.25 mTorr of argon exhibited a sheet resistance of 10 Ω/sq (resistivity of 8×10^{-4} Ω.cm) and a VIS transparency ~ 85%.

For PVs on flexible substrats S. Fernández et al. [88, 89] have examined the effect of RF power 25-125 W, and sputtering pressure 1.5-8.25 mTorr on the structural, electrical, and optical properties of AZO deposited on polyethylene terephthalate (PET) substrates. AZO films were deposited from a ceramic 3-inch in diameter AZO target with 2% wt. Al_2O_3, at a substrate temperature of 100°C, the films thickness was in the range of 500–700 nm. In agreement with other reports, it was shown that the resistivity decreased as the RF power is increased or as the pressure is decreased. The lowest resistivity of about 1.1×10^{-3} Ω.cm was obtained for AZO deposited at 75 W and 1.5 mTorr, for which the visible transmission was 80%. A resistivity increase at higher RF powers was observed and attributed the sputtered particles energy being too high causing the PET deformation and the grown film properties degradation.

D.K. Kim, and H.B. Kim [90] have examined the effect of argon pressure on AZO deposited by RF magnetron sputtering. 250 nm thick AZO films deposited on glass substrates at room-temperature, 25 W applied to 3-inch in diameter target with the standard doping level. They reported that increasing the pressure from 1 to 2 mTorr increased the AZO resistivity from 3.5

$\times 10^{-3}$ to 8.5×10^{-3} Ω.cm, this was assigned to reinforced electron scattering by microstructure defects like grain boundaries. Visible transmittance of 85% was obtained at 25 W and 1 mTorr.

R. Wen et al. [91] have studied the substrate temperature effect on structural, electrical, and optical properties of AZO. 400 nm thick AZO samples were deposited by RF magnetron sputtering on quartz glass wafers at different temperature ranging from room temperature to 400°C, while, other parameters were fixed. It was demonstrated that the substrate temperature strongly affects the crystal quality of AZO samples, the ZnO (002) peak intensity was enhanced and the average grain size increased from 24 nm to 43 nm as the substrate temperature increased to 300°C. Also, the substrate temperature helps to activate aluminium dopants into the ZnO lattice. Therefore, the samples resistivity was decreased from 3×10^{-3} Ω.cm at room-temperature to 5×10^{-4} Ω.cm at 300°C. A bandgap enlargement from 3.35 eV to 3.50 eV, and a visible transmission of 90% were also obtained at 300°C.

2.10.2 Previous publications on laser annealing of AZO

For a summary of previous publications on laser annealing of AZO, see Table 2-2.

The first report on laser annealing of AZO was presented in 2008 by W.M. Tsang et al [92]. 200 nm thick AZO films were deposited by sol-gel technique on glass substrates and baked at 300˚C, then, subjected to KrF ELA (λ=248 nm) with 1, 3, or 5 pulses at different fluences 93, 124, 155 mJ/cm^2. When the baked samples were ELA treated with 5 pulses at 155 mJ/cm^2, the resistivity was reduced from 330 to 4.4×10^{-2} Ω.cm, while the visible transmission was enhanced from 80 to 90%. These achievements were attributed to AZO films crystallinity enhancement, microstructural defects reduction, and Al activation into ZnO.

M. Y. Zhang and G. J. Cheng [93] have demonstrated high quality AZO by pulsed laser deposition and KrF ELA. 250 nm thick AZO films were deposited at room temperature on glass substrates coated with 50 nm intrinsic zinc oxide (i-ZnO). The AZO films were annealed in vacuum at 10 mTorr with different fluences 20-200 mJ/cm^2 and number of pulses 10-150. ELA with 50 pulses at 25 mJ/cm^2 or with 30 pulses at 30 mJ/cm^2 decreased the resistivity from 1.4×10^{-3} to 2.2×10^{-4} Ω.cm, while the visible transmission was enhanced from 80 to 90%. These improvements were assigned to grain size enlargement and grain boundaries density reduction.

Q. Xu et al. [94] combined RF magnetron sputtering with laser annealing using solid-state Nd:YAG laser (λ=1064 nm) to fabricate AZO films. 200 nm thick samples were deposited at room

temperature, 150 W, and 60 sccm flow of argon. The samples were annealed via scanning a beam of 25 mm × 2 mm area at a velocity of 2 mm/s, and different power densities 18.5, 27.8, 36.4 and 41.8 W/mm^2. At 27.8 W/mm^2, the resistivity was reduced from 3.4×10^{-3} to 2.2×10^{-3} Ω.cm, while the visible transmission was increased from 80 to 90%. Average grain size showed a rather small enlargement from 23.8 to 25.5 nm upon annealing.

Annealing by diode pumped Nd:YVO_4 laser (λ=355 nm), was applied to AZO samples for patterning and annealing by W.-T. Hsiao et al. [95]. 200 nm thick AZO samples were deposited on glass substrates by RF sputtering, no deposition conditions were reported. Annealing was performed via scanning a continuous wave (cw) beam with a diameter of 3.5 mm and a power of 14 W across the samples at different speeds (400-800 mm/s) and pulse repetition frequency (40, 55, and 70 kHz). Annealing at 600 mm/s and 70 kHz decreased the resistivity from 2.12×10^{-2} to 2.5×10^{-3} Ω.cm, while the VIS transmission was maintained at 83%.

Near infrared (NIR) laser annealing in cw-mode was applied by V. Schütz et al. to AZO achieving highly conductive films [96]. 600 nm thick AZO films were deposited at room temperature by DC-sputtering, then laser annealed in helium or argon by scanning a focused beam of 80 µm diameter from a fiber laser source (λ= 1070 nm) at different interaction times with the samples (400-1000 µs). At an interaction time of 600 µs, the AZO resistivity was significantly reduced from 1.5 ×10^{-3} to 3.6 ×10^{-4} Ω.cm due to increasing the free electron density and mobility. Also, the bandgap was enlarged due to the Burstein-Moss effect, the VIS transparency was increased from 60 to 80%. These improvements were assigned to grain size increase and surface roughness decrease upon annealing.

Nian et al. [97] have applied KrF ELA in vacuum (10 mTorr) to 200 nm thick AZO samples deposited by PLD at room temperature on sapphire substrates coated with 50 nm thick i-ZnO. Different number of pulses 100-200 was applied at a range of fluences 120-200 mJ/cm^2. ELA with 200 pulses at 160 mJ/cm^2, the resistivity was reduced from 1.68×10^{-3} to 9.90×10^{-4} Ω.cm due to crystal quality enhancements and inter-grain voids reduction as observed by SEM and XRD measurements. Whilst, the VIS transmission was maintained at ~ 80%.

W.-T. Hsiao et al. [98] have explored diode laser annealing of 200 nm thick AZO films deposited by RF sputtering, no deposition conditions were reported. The films were processed via scanning a beam of 3 mm diameter from a fiber-optic diode laser (λ=808 nm) operated in cw-

mode and at maximal power of 30 W. Laser energy densities of 20, 40.1, and 60.1 mJ/cm^2 were applied at scanning speeds of 5, 10, and 20 mm/s. At 60.1 mJ/cm^2 and 5 mm/s, the resistivity decreased from 4.0×10^{-2} to 2.8×10^{-2} Ω.cm, while the VIS transmission maintained at 85%.

R. Boukhicha et al. [99] have examined ELA and chemical etching process on AZO aiming at highly textured samples. 1000 nm thick AZO samples were deposited by RF magnetron sputtering at room temperature and different pressures of different oxygen to argon ratios. It was shown that low pressure down to 1 mTorr of zero or low oxygen ratio results in the lowest sheet resistance ~ 11 Ω/sq (ρ=1.1×10^{-3} Ω.cm). ELA was performed via a pulsed XeCl laser (λ=308 nm and pulse duration 150 ns) with a single pulse at different energy densities up to 1000 mJ/cm^2. ELA at 700 mJ/cm^2 changed the visible transmission from nearly opaque to about 80%, while the sheet resistance was reduced to about 7 Ω/sq (ρ=7×10^{-4} Ω.cm). However, this sheet resistance increased to the as-deposited samples values upon chemical etching.

Picosecond laser annealing of AZO was recently reported by D. Scorticati et al [80]. AZO films of different thickness 130-860 nm were deposited on borosilicate glass by RF-magnetron sputtering and plasma-enhanced chemical vapor deposition (PECVD), no growth conditions were reported. The used laser source is Yb: YAG laser whose central wavelength λ = 1030 nm is converted to 343 nm at a pulse duration of 6.7 ps. A focused laser beam is scanned over the AZO samples surface in an environment of argon. Based on the sample thickness, different annealing parameters including laser fluences, pulse repetition frequency, beam diameter, and scanning speed were applied. All the samples showed a resistivity decrease upon annealing, the lowest resistivity was obtained for 460 nm thick films deposited by PECVD and annealed at 36 mJ/cm^2, repetition frequency 400 kHz, beam diameter 390 µm, and a beam speed of 1950 mm/s. The resistivity for this sample was decreased from 1.3×10^{-3} to 6.5×10^{-4} Ω.cm. While, its VIS transmission and the bandgap were maintained at ~ 86% and 3.6 eV. The resistivity reduction was attributed to increasing both the free carrier density and mobility.

Laser annealing was also applied to AZO on PET substrates by L.-j. Huangetal et al. [100]. 300 nm thick AZO films were deposited by DC magnetron sputtering from AZO target with the standard doping level, then laser annealed via scanning a beam of 100 µm diameter and a frequency of 1 kHz from diode pumped Nd:YVO_4 pulsed laser (λ=532 nm) at 700 mJ/cm^2. Different scanning modes were examined in terms of the overlap between either the laser spots or the

scan lines. At the optimised scanning mode, the resistivity was reduced from ~ 7×10^{-3} to 1.95×10^{-3} Ω.cm and the VIS transparency was increased from 62.0 to 76.2%. Grain size increase from 24.7 to 36.1 nm was reported indicating microstructure characteristics improvements.

Ref.	Deposition details	Annealing details	As-deposited properties	Annealed properties
[92]	200 nm thick, Sol-gel, baked at 300 °C.	Pulsed λ=248 nm, 25 ns, 5 pulses at 155 mJ/cm^2.	330 Ω.cm, 80%.	4.4×10^{-2} Ω.cm, 90%.
[93]	250 nm thick AZO on 50 nm thick i-ZnO, PLD, at RT.	Pulsed λ=248 nm, 25 ns, in vacuum, 50 pulses at 25 mJ/cm^2 or 30 pulses at 30 mJ/cm^2.	1.4×10^{-3} Ω.cm, ~ 80 %.	2.2×10^{-4} Ω.cm, 90 %.
[94]	200 nm thick, RF sputtering, at RT, 150 W, and 60 sccm Ar.	cw, 1064 nm, beam area 25 mm × 2 mm, power density 27.8 W/mm^2.	3.4×10^{-3} Ω.cm, 80%.	2.2×10^{-3} Ω.cm, 90%.
[95]	200 nm thick, RF sputtering.	Pulsed, λ=355 nm, beam diameter 3.5 mm, power 14 W, scanning speed 600 mm/s, pulse frequency 70 kHz.	2.12×10^{-2} Ω.cm, ~ 83%.	2.5×10^{-3} Ω.cm, 83%.
[96]	600 nm thick, DC sputtering, at RT.	cw λ=1070 nm, in helium or argon, interaction time 600 µs.	1.5×10^{-3} Ω.cm, 60 %.	3.6×10^{-4} Ω.cm, 80%.
[97]	200 nm thick AZO on 50 nm thick i-ZnO, PLD, at RT.	Pulsed λ=248 nm, 25 ns, 200 pulses-160 mJ/cm^2 in vacuum.	1.68×10^{-3} Ω.cm, 80%.	9.9×10^{-4} Ω.cm 77%.
[98]	200 nm thick, RF sputtering.	cw, λ=808 nm, 3 mm beam diameter, power of 30 W, at 60.1 mJ/cm^2 and 5 mm/s.	4.0×10^{-2} Ω.cm, 85%.	2.8×10^{-2} Ω.cm 85%.
[99]	1000 nm thick, RF sputtering, at RT, and 1 mTorr.	Pulsed 308 nm, 150 ns, 1 pulse at 700 mJ/cm^2.	1.1×10^{-3} Ω.cm, Almost opaque.	7×10^{-4} Ω.cm, 80%.
[80]	130-860 nm thick, RF Sputtering or PECVD.	Pulsed λ=1030 nm converted to 343 nm, 6.7 ps. When 460 nm samples deposited by PECVD and annealed in Ar, 36 mJ/cm^2, repetition frequency 400 kHz, beam diameter 390 µm, and a beam speed of 1950 mm/s.	1.3×10^{-3} Ω.cm, 86%.	6.5×10^{-4} Ω.cm, 86%.
[100]	300 nm thick, DC sputtering, at RT on PET substrates.	Pulsed λ=532 nm, frequency of 1 kHz, beam diameter 100 µm and affluence of 700 mJ/cm^2.	7×10^{-3} Ω.cm, 62%.	1.95×10^{-3} Ω.cm, 76.2%.
[101]	180 nm thick, RF sputtering at RT, 180 W, and 2 mTorr of 0.2% O_2 in Ar.	Pulsed λ=248 nm, in Air, RT, 25 ns, 5 pulses at 125 mJ/cm^2.	1×10^{-3} Ω.cm, 82% (at 550 nm)	5×10^{-4} Ω.cm, 86% (at 550 nm)
[102]	300 nm thick Pulsed-DC sputtering, at RT.	**RTA**, at 400 °C, for 30 s, at atmospheric pressure, and in nitrogen environment.	1.7×10^{-3} Ω.cm, 73%.	5.1×10^{-4} Ω.cm, 86%.

Table 2-2. A summary of previous reports on laser annealing of AZO thin films. Results of rapid thermal annealing RTA [102] are included for comparison. The ref. [101] is from the results of this PhD study.

The lowest AZO resistivity achieved via laser annealing in the previous reports was for AZO samples deposited by PLD, which is not large area compatible. For AZO samples deposited by RF or DC sputtering, the resistivity achieved after laser annealing, in general, is higher than that of practical transparent electrodes (< 10^{-3} Ω.cm) [12]. Also, the reported resistivity by laser annealing in some reports is achievable by optimised room temperature deposition of AZO as

mentioned in section 2.10.1. Moreover, the effect of AZO growth conditions on the achieved characteristics by laser annealing has not been investigated.

The work presented in this thesis examines the effect of ELA on the characteristics of AZO thin films deposited by RF magnetron sputtering at room temperature and a wide range of growth parameters. In addition, the work includes a comparison study between the application of ELA and RTA to AZO thin films.

2.10.3 Previous publications on sputter-deposition of a-IGZO

As stated earlier, the first high performance IGZO TFTs were reported by Nomura et al. in 2004 [6]. Top-gated coplanar structure was used, the active layer IGZO was 30 nm thick deposited by pulsed laser deposition at room temperature on PET substrates. The IGZO metallic composition was In= 35.48 at.%, Ga =35.48 at.%, and Zn 29.04 at.%. A saturation mobility of 8.3 cm^2/Vs, an on/off ratio of ~ 10^3, and a small hysteresis of < 0.5 V were reported.

A couple years later, the first high performance IGZO TFTs by RF sputtering at room temperature were reported by Yabuta et al [76]. A staggered-top-gated configuration was used with 50 nm IGZO deposited at 4 mTorr of different oxygen to argon ratios. The optimised active layer metallic composition was In=40 at.%, Ga=36 at.%, and Zn=24 at.%. The fabrication process temperature was found to reach 50˚C and 140˚C during the active layer and the gate insulator deposition respectively. A field effect mobility of about 12 cm^2/Vs and an on/off ratio of ~ 10^8 were obtained. Exploring the effect of oxygen to argon ratio showed that TFTs sputtered at low oxygen ratios had poor performance due to too conductive IGZO. While, at oxygen to argon ratios around 3 %, the IGZO conductivity was < 10^{-4} S/cm and thus functional TFTs were obtained.

The active layer metallic composition effect on IGZO thin films and TFTs performance was examined by Iwasaki et al [103]. Bottom-gated-staggered TFTs were fabricated on silicon substrates. The active layer was 50 nm thick IGZO deposited via RF magnetron co-sputtering of three oxide targets In_2O_3, Ga_2O_3, and ZnO at room temperature. It was concluded that varying the active layer metallic composition is very effective to control the IGZO conductivity and thus the TFTs performance. The best TFTs performance was obtained when the active layer metallic composition is In= 37 at.%, Ga =13 at.%, and Zn=50 at.% corresponding to IGZO conductivity ~ 10^{-3} S.cm, TFTs saturation mobility of 12 cm^2/Vs, and an on/off ratio <10^8.

Chiang et al. examined the effects of different fabrications conditions on IGZO TFTs performance [104]. Staggered-bottom-gated TFTs were fabricated on silicon substrates, IGZO was deposited by RF magnetron sputtering from 3-inch IGZO target at different deposition conditions including RF power, oxygen to argon ratio at a total pressure of 5 mTorr, and thickness. After IGZO deposition, the structure was thermally annealed in air for 1h at temperatures 200-800°C. A reference TFT was fabricated with 50 nm IGZO deposited at an RF power of 75 W and at 5 mTorr pressure of pure argon, and annealed in air at 175°C for 1h. This device demonstrated a saturation mobility of ~17 cm^2/Vs, a subthreshold swing S = 0.6 V/decade, and an on/off ratio ~10^7. All non-annealed devices showed poor performance. Annealing at a temperature ≤ 500°C increased the channel mobility for IGZO TFTs of different deposition conditions, due to better interface properties and local atomic rearrangements. At higher temperatures, however, the mobility is reduced, attributed to the onset of IGZO crystallisation. Increasing the applied RF power from 75 to 100 W decreased the turn on voltage from positive 2 to 0 V when the TFTs were annealed ≤ 400°C, due to better electron density and atomic bonding, as well as lower trap states density. Different oxygen to argon ratio 0, 5, and 10 % was used, it was demonstrated that the channel mobility is significantly reduced to < 1 cm^2/Vs as the oxygen to argon ratio is increased due to higher interfacial and/or bulk defect densities. TFTs with IGZO sputtered in pure argon and annealed in air at 400°C demonstrated the best channel mobility for this set of TFTs. The TFTs stability in terms of the turn on voltage V_{ON} was examined as a function of IGZO thickness (10, 25, and 50 nm) over a period of 18 weeks in air. It was demonstrated that TFTs with thicker IGZO had the best stability. 50 nm devices showed less than 0.5 V positive change, while the 25 nm and 10 nm TFTs showed a positive shift of about 1.5 V and 6 V respectively.

Jeong et al. examined the active layer sputtering pressure effect on IGZO TFTs performance [105]. Bottom-gated-staggered TFTs were fabricated on glass substrates with 50 nm IGZO deposited by RF magnetron sputtering at room temperature, a power density of 1.4 W/cm^2, and different sputtering pressure 5, 3, and 1 mTorr of 35% oxygen and 65% argon. Finally, the completed TFTs were annealed at 350°C in nitrogen for 1h. A reference TFT was fabricated at 5 mTorr exhibited a field effect mobility of 11.4 cm^2/Vs, an on/off ratio of 10^7, and a subthreshold swing S of 0.87 V/decade. Reducing the sputtering pressure to 1 mTorr results in noticeable TFT performance enhancement achieving a field effect mobility of 21.8 cm^2/Vs, an on/off ratio of 7×10^7,

and a subthreshold swing S of 0.17 V/decade. To study the origin of these enhancements, IGZO films were deposited at the same conditions. It was shown that the sputtering pressure has no apparent effect on the deposited IGZO films metallic composition which was as follows In=41.67 ± 0.01 at.%, Ga=40.67 ± 0.01 at.%, and Zn=17.67 ± 0.01 at.%. However, the IGZO films density was found to increase noticeably from 5.50 g/cm^3 at 5 mTorr to 6.27 g/cm^3 at 1 mTorr. This was attributed to enhancing the sputtered particles energy at lower pressure leading to higher surface mobility and thus better densification for the resultant IGZO film. The subthreshold swing S reduction at lower pressure is a strong indication of reducing the interface and/or bulk defects for IGZO. To investigate which of these defects is linked to the pressure, the authors have deposited a 50 nm thick bilayer IGZO for TFTs in which IGZO at lower pressure 1 mTorr, which showed the best performance, is deposited first at different thicknesses x nm and then capped with 50-x nm of IGZO deposited at 5 mTorr, i.e. the interfacial defects density is expected to be the same for all the TFTs. It was shown that as the first layer thickness x is increased, the TFTs performance is noticeably improved. This indicated that the improvement is more associated with the bulk traps density reduction, i.e. within x thickness, sputtered at lower pressure.

2.10.4 Previous publications on laser annealing of a-IGZO

For a summary of previous publications on laser annealing of IGZO, see Table 2-3.

The first published work on laser annealing of IGZO TFTs was presented by M. Nakata et al. in 2009 [106]. Bottom-gated-staggered TFTs were fabricated on glass substrates. A 20 nm thick IGZO film was deposited by RF sputtering at room temperature, power density 2 W/cm^2, and 3.75 mTorr of oxygen in argon mixture. The completed TFTs were subjected to XeCl excimer laser annealing (λ=308 nm and pulse duration 25 ns) with two pulses at different fluences of 60 to 160 mJ/cm^2 at room temperature in air. For comparison, furnace annealing in air at different temperatures 150-500°C for 30 min was examined on IGZO TFTs. It was demonstrated that ELA significantly reduced the sheet resistance of IGZO by more than four orders of magnitude as the fluence was increased to 160 mJ/cm^2, the authors attributed this reduction to increasing the electron density upon ELA. Annealing at > 400 mJ/cm^2 or > 500°C results in IGZO crystallisation as observed from XRD measurements. In regard to TFTs, ELA at 130 mJ/cm^2 increased the on-state current by two orders of magnitude and the field effect mobility to 14 cm^2/Vs. When the TFTs processed at 160 mJ/cm^2, the devices were always in on-state because of too conductive IGZO.

Furnace annealing at 300˚C-30 min increased the on-state current by more than two order of magnitude and the filed effect mobility to about 16 cm^2/Vs. TFT performance improvements upon laser and thermal annealing were attributed to reducing the trap states as well as increasing the free electron density in the TFTs active layer.

After successful application of ELA to IGZO TFTs on glass, M. Nakata et al. investigated XeCl-ELA of IGZO TFTs on heat-resistant plastic substrates [79]. First, 400 μm SiO_2 was deposited on the substrates to avoid thermal diffusion from IGZO to the substrates during annealing. Then, IGZO TFTs were fabricated at room temperature with same structure as in the previous publication [106]. Finally, ELA was performed in air at room temperature with two pulses at different fluences. ELA increased the electron density and mobility of IGZO thin films. At 170 mJ/cm^2, the on-state current for IGZO TFTs increased by more than one order of magnitude to 10^8 and the field effect mobility increased from 2.4 to 15.6 cm^2/Vs. These enhancements were attributed to trap states reduction in IGZO upon ELA.

B. D. Ahn et al. have reported selective XeCl-ELA of IGZO TFTs to reduce the contact resistance between IGZO and source-drain electrodes [107]. Bottom-gated-staggered TFTs were fabricated on glass substrates, 200 nm thick molybdenum tungsten was deposited as the gate electrode on SiO_2-coated glass and 200 nm silicon nitride was then deposited as the gate insulator. Next, 50 nm thick IGZO was deposited by RF sputtering at room temperature, RF power density 1.39 W/cm^2, and 1 mTorr sputtering pressure of 35% oxygen and 65% argon. The structure was annealed at 350°C in nitrogen for 1h, and then subjected to ELA at room temperature in air through a mask that allows the XeCl photons to process only the areas of IGZO which are in direct contact with the source and drain, while, the channel length was not processed. The TFTs saturation mobility increased from 11.07 to 21.79 cm^2/Vs and the on/off ratio increased form $7.0x10^7$ to $1.2x10^8$ upon ELA with ten pulses at 130 mJ/cm^2. These enhancements were attributed to reducing the contact resistance between the source-drain electrodes and IGZO originated from decreasing IGZO work function from 5.01 to 4.3 eV due to increasing the electron density in IGZO after ELA. It was also shown that ELA reduced IGZO films resistivity from ~ 10^4 to $3.2x10^{-3}$ Ω.cm because of increasing the electron density and mobility. However, when the ELA-treated films were thermally annealed in air at 400 °C for 30 min, the resistivity recovered to as-deposited samples resistivity because of decreasing the oxygen vacancy and electron density.

Aiming at low temperature annealing H-W Zan et al. have processed IGZO-TFTs with Nd:YAG laser and Xe excimer lamp [108]. Bottom-gated-staggered IGZO TFTs were fabricated on silicon substrates. A 35 nm thick IGZO layer was deposited by RF magnetron sputtering at room temperature, 100 W, and 5 mTorr of argon. Then, the completed TFTs were annealed by a beam form Nd:YAG laser (λ=266 nm) with energy density 10 - 25 mJ/cm^2 and pulse duration 4 ns, or by Xe excimer lamp irradiation (λ=172 nm) at a power density 50 mW/cm^2 and different exposure times 10 to180 min in nitrogen ambient. The Nd:YAG annealed TFTs at 10.7 mJ/cm^2 demonstrated a saturation mobility of 8 cm^2/Vs, an on/off ratio > 10^7, and hysteresis reduction (ΔV_{ON}) from 10 V to ~ 0 V, which implies better stability. Applying higher laser energy densities resulted in too conductive IGZO and thus high off-state current. The lamp treated TFTs for 30 min demonstrated a saturation mobility of 3 cm^2/Vs, an on/off ratio ~ 10^6, and hysteresis reduction to 0 V. These enhancements upon the two annealing approaches were attributed to tuning the IGZO conductivity via adjusting the oxygen content.

Another work by Nakata et al. reported ELA of IGZO TFTs from the back side of glass substrates [109]. First, the effect of XeCl ELA (λ=308 nm - pulse duration 50 ns) on 50 nm thick IGZO films sputter-deposited on glass substrates was examined from the front and back sides of the substrate. It was demonstrated that ELA with ten pulses from the front side at 100 mJ/cm^2 or from the back side at 150 mJ/cm^2 reduced the IGZO samples sheet resistance from 10^7 Ω/sq to < $2x10^3$ Ω/sq (ρ < 10^{-2} Ω.cm). This reduction was assigned to increasing the free electron density. Bottom-gated-staggered IGZO-TFTs were fabricated, gate contact (aluminium), gate insulator (200 nm SiO_2), and active layer (50 nm IGZO) were deposited in turn on glass substrates. Then, the structure was ELA treated with ten pulses at 150 mJ/cm^2 from the back side to utilise the metallic gate electrode as a mask through which the IGZO areas with a direct contact with the source-drain only were annealed. Then, molybdenum is deposited as the source-drain with no overlapping with the gate. IGZO TFTs with the same structure but without backside-ELA were also fabricated. It was demonstrated that the TFTs without the back-side ELA had a relatively poor performance. Whilst, those subjected to backside-ELA exhibited a field effect mobility of 8.2 cm^2/Vs and two orders of magnitude higher on-state current. These enhancements were attributed to reducing the resistivity of IGZO areas in the source-drain regions upon ELA leading to reducing the contact resistance at the source-drain regions.

Chung et al. have reported CO_2 laser annealing of IGZO TFTs leading to better performance compared to furnace annealing [110]. Bottom-gated-staggered TFTs were fabricated on silicon wafers with 50 nm thick IGZO sputter-deposited at 260°C, 120 W, and 5 mTorr of 10% O_2 in Ar. Then, the TFTs were subjected to two annealing techniques including furnace annealing 350°C in dry air for 30 min, and laser annealing via scanning a focused beam at 100 mm/s from CO_2 laser λ=10.6 μm operated in continuous wave mode. Furnace annealing increased the TFTs saturation mobility from 12 to 16 cm^2/Vs, while laser annealing resulted in a saturation mobility of 70 cm^2/Vs. The author attributed the mobility enhancements to tuning the oxygen content as well as to reducing the traps states in IGZO samples.

S. H. Cho et al [111] have applied UV annealing and/or furnace annealing to bottom-gated-staggered TFTs on silicon wafers. The active layer was 50 nm thick IGZO deposited by RF sputtering at room temperature, 75 W and 10 mTorr of argon. The completed TFTs were annealed with UV irradiation for 15 min at a wavelength and a power density of 254 nm and 17.69 mW/cm^2, furnace annealing at 350°C for 1h, and a combination of the UV irradiation and furnace annealing at 150°C for 1h. Appling low temperature annealing to initially UV treated TFTs results in a saturation mobility increase from 5.15 to 10.14 cm^2/Vs and a subthreshold swing S reduction from 0.98 to 0.49 V/decade. These improvements were better than those for furnace annealing at 350°C for 1h. The authors showed via XPS measurements that the combined annealing reduced the oxygen defects, including oxygen vacancies and adsorbed defects, leading to better electronic structure of IGZO and thus better TFTs performance.

P Bermundo et al. have demonstrated the application of XeCl and KrF ELA to Bottom-gated-staggered IGZO TFTs on silicon substrates [112]. The active layer was 70 nm thick deposited by RF sputtering. Next, for better stability the TFTs were coated with a UV transparent passivation layer that required the TFTs heating at 300°C for 1h. ELA is then performed by single pulse from XeCl and KrF lasers at different energy densities. ELA with XeCl at 90-110 mJ/cm^2 and KrF at 80 mJ/cm^2 resulted in a saturation mobility of ~ 12.5 cm^2/Vs and 13 cm^2/Vs respectively compared to very poor performance for the as-deposited devices.

Laser annealing was also examined on IGZO deposited by solution-based technologies. Although high laser energy density > 350 mJ/cm^2 was applied, the achieved improvements were rather small [113, 114]. Also, thermal annealing at low temperatures applicable to plastic

substrates ≤ 150°C has been examined on IGZO TFTs. However, long processing times 2 - 4h were needed to achieve sufficient TFT performance and stability enhancements [115, 116].

Ref.	IGZO deposition details	TFTs annealing details	Deposited TFTs properties	Annealed TFTs properties
[106]	20 nm thick, RF sputtering, at RT, 2 W/cm^2, and 3.75 mTorr.	i) Pulsed λ= 308 nm, 25 ns, 2 pulses at 130 mJ/cm^2. ii) Thermal annealing in air- 300 °C - 30 min.	On/off ratio = 10^5.	i) On/off ratio = 10^7, μ_{FE} =14 cm^2/Vs. ii) On/off ratio >10^7, μ_{FE} =16 cm^2/Vs.
[79]	20 nm thick, RF sputtering, at RT, 2 W/cm^2, 3.75 mTorr, and 10% O_2/ Ar.	Pulsed λ=308 nm, 25 ns, 2 pulses at 170 mJ/cm^2.	On/off ratio = 10^5, μ_{FE} 2.4 cm^2/Vs	On/off ratio = 10^8, μ_{FE} =15.6 cm^2/Vs.
[107]	50 nm thick, RF sputtering, at RT, 1.39 W/cm^2, and 1 mTorr of 35% O_2/Ar, at 350 °C in nitrogen.	Pulsed λ=308 nm, 10 pulses at 130 mJ/cm^2.	On/off ratio = 7x10^7, μ_{sat} =11.07 cm^2/Vs.	On/off ratio > 10^8, μ_{sat} = 21.97 cm^2/Vs.
[108]	35 nm thick, RF sputtering, at RT, 100 W, and 5 mTorr of Ar.	i) Pulsed λ=266 nm, 4 ns, 10.7 mJ/cm^2. ii) cw, λ=172 nm, 50 mW/cm^2, and 30 min.	On/off ratio ~ 10^8.	i) On/off ratio >10^7, μ_{sat} = 8 cm^2/Vs. ii) On/off ratio = 10^6, μ_{sat} =3 cm^2/Vs.
[109]	50 nm thick, RF sputtering.	Pulsed, backside, XeCl λ=308 nm, 50 ns, 10 pulses at 150 mJ/cm^2.	On/off ratio =10^5, μ_{FE} ~ 1 cm^2/Vs.	On/off >10^7, μ_{FE} 8.2 cm^2/Vs.
[110]	50 nm thick, RF sputtering, at 260 °C, 120 W, and 5 mTorr of 10% O_2 Ar.	i) Thermal annealing in air, at 350 °C, for 30 min. ii) cw λ=10.6 µm at 100 mm/s.	μ_{sat} =12 cm^2/Vs.	i) On/off ratio = 10^6, μ_{sat} 16 cm^2/Vs. ii) On/off ratio =7x10^7, μ_{sat} 70 cm^2/Vs.
[111]	50 nm thick, RF sputtering, RT, 75 W, and 10 mTorr of Ar.	cw, λ=254 nm, for 15 min at 17.96 mW/m^2 and annealing at 150°C for 1h.	μ_{sat} = 5.15 cm^2/Vs, S = 0.98 V/dec.	μ_{sat} = 10.14 cm^2/Vs, S = 0.98 V/dec.
[112]	70 nm thick, RF sputtering. Heated at 300°C for 1 h.	i) Pulsed λ=308 nm, 25 ns, 100 mJ/cm^2. ii) Pulsed λ=248 nm, 25 ns, 80 mJ/cm^2.	On/off ratio < 10^5.	i) On/off ratio ~ 10^8, μ_{sat} 12.5 cm^2/Vs. ii) On/off ratio > 10^8 μ_{sat} 13 cm^2/Vs.

Table 2-3. A summary of previous reports on laser annealing of IGZO thin films.

Most of the publications reviewed on laser annealing of IGZO TFTs used a XeCl excimer laser (λ=308 nm) which has a penetration depth of about 70 nm in IGZO [106].This penetration depth is larger than the commonly used IGZO thickness in TFTs (≤ 50 nm). Hence, laser sources with lower wavelengths such as KrF excimer laser (λ=248 nm) is expected to perform more localised annealing and therefore less heating to the underlying layers or the substrate, given that KrF laser has about 45 nm penetration depth in IGZO thin films [114]. Furthermore, laser annealing of IGZO TFTs on flexible polymer substrates is rarely examined. This research consequently explores KrF ELA of IGZO thin films and TFTs aiming at application of KrF ELA to IGZO TFTs on flexible heat-sensitive substrates.

3 Thin Film Fabrication and Characterisation Techniques

3.1 Introduction

This chapter details the deposition and post-deposition processing systems used in this research. Also, it presents an overview of the used thin film characterisation techniques.

3.2 Thin film technology

Thin film materials are used in various applications mainly in the form of thin films deposited on different substrates, including glass and polymers. Deposition techniques and preparative deposition conditions play important roles in defining the physical properties of the resulting thin films [8, 9]. There is a wide variety of well-established thin film deposition techniques. Every deposition technique has its own strengths and weaknesses; the application requirements in terms of the film quality, scalability, cost, and reproducibility determine the most appropriate technique. Deposition technique are classified into three broad groups as shown in Fig. 3-1 [9, 117]. Because of the flexibility, controllability, and thus the excellent reproducibility offered by sputtering, it is the primary deposition technique employed throughout this work.

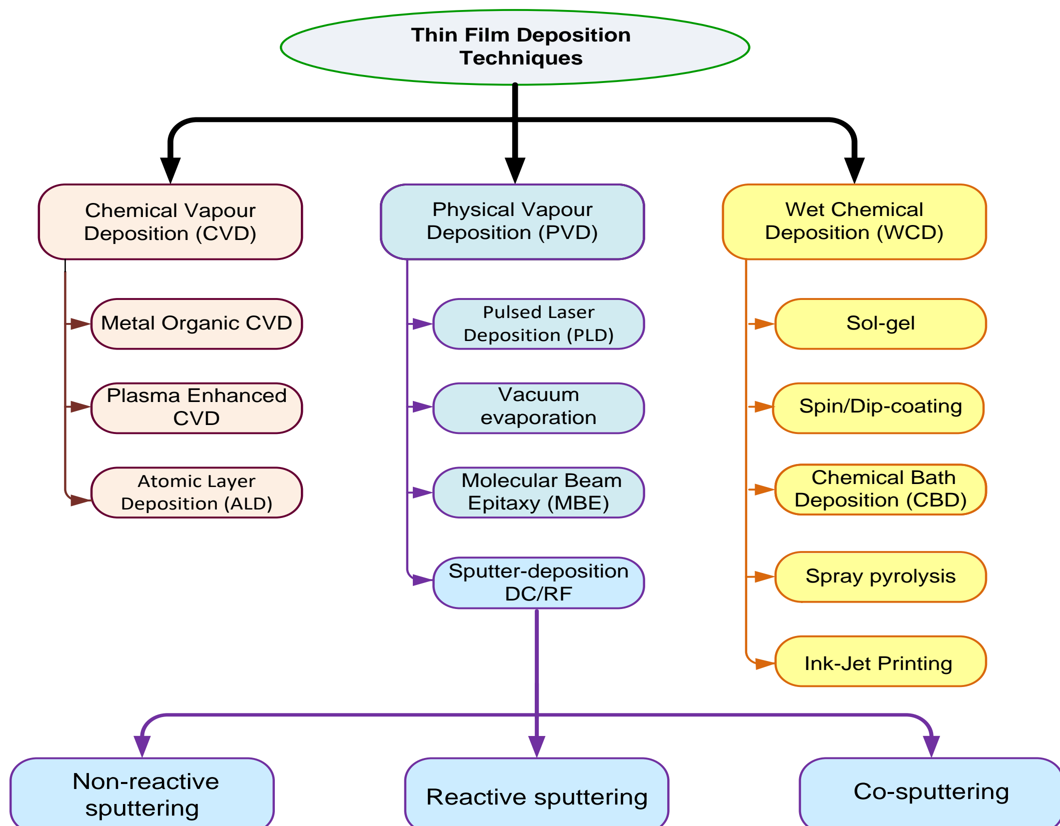

Fig. 3-1. Commonly used thin film deposition methods, adapted from [9, 117].

3.3 Thin film sputter-deposition

Sputtering is a physical vapour deposition (PVD) technique whereby atoms from the surface of a solid target are sputtered (removed) by energetic gas ion bombardments, and subsequently deposited on a substrate [118, 119]. Sputtering has established a long history dating back to 1850's and it is now of overriding significance both in the mass production and research of various thin film materials. This is due to several strengths such as:

1. Simple and safe setup since the interaction between the user and the process is very limited compared to WCD techniques. Also, typically no toxic gases are involved.
2. Applicable to a wide range of materials, and to large area and large volume applications.
3. Deposited films exhibit relatively good uniformity, purity, and adherence to the substrate.
4. Low substrate temperature down to no intentional heating, which permits minimal thermal effects on any underlying materials or the used substrates.
5. Ease of automation and efficient control over various deposition parameters resulting in optimising the properties, thickness, and composition of the deposited films, as well as achieving excellent reproducibility [75, 118].

The main weaknesses of sputtering include:

1. The need for expensive high vacuum systems.
2. Poor utilisation of the target materials in particular for magnetron sputtering set up.
3. Most of the energy of the sputtering gas ions ~75% becomes heat in the target that needs to be effectively cooled [86, 118].

3.3.1 Physics of thin film sputter-deposition

In an evacuated sputtering chamber, an electric field is created between the anode (the substrate holder and the chamber's walls), and the cathode (the target material to be sputtered). Meanwhile, a sputtering gas at a specified pressure is introduced into the sputtering chamber. Typically, non-reactive argon (Ar) is used as the sputtering gas since it is a noble gas i.e. will not react with sputtered particles, it has sufficiently heavy ions that easily sputter particles from source targets, and has a relatively low ionisation potential (15.76 eV) [86, 118]. Under these conditions, a series of collisions occurs between energetic primary electrons travelling between the anode-cathode and the argon atoms resulting in ionisation or excitation of the argon species depending on the transferred energy in the collisions. The former produces positively charged argon ions (Ar^+) and additional electrons (e^-) that might participate in further argon ionisation/excitation, while the latter ends up with photon emission (glow discharge).

Ionisation: $Ar + e^{-} = Ar^{+} + 2e^{-}$ 3-1

Excitation: $Ar + e^{-} = Ar^{*} + e^{-}$ 3-2

The positively charged argon ions are then accelerated towards the cathode resulting in a sequence of intense bombardments on the target material causing one of the following phenomena (see Fig. 3-2): [86, 118, 120].

1. Sputtering (removing) neutrally charged atoms and possibly a few ionised species (1-5%) from the target surface, owing to a gained kinetic energy via a collision cascade and momentum transfer between the argon ions and target surface' atoms during the bombardments. The gained energy should be larger than the target atoms' binding energy in order to perform sputtering. Positive charges are also accumulated on the target surface as a result of sputtering.
2. Electron emission from the target material, which is referred to as a secondary-electron emission.
3. The bombarding argon ions are reflected at the target surface as energetic neutrals.
4. Highly energetic argon ions are implanted in the target material.

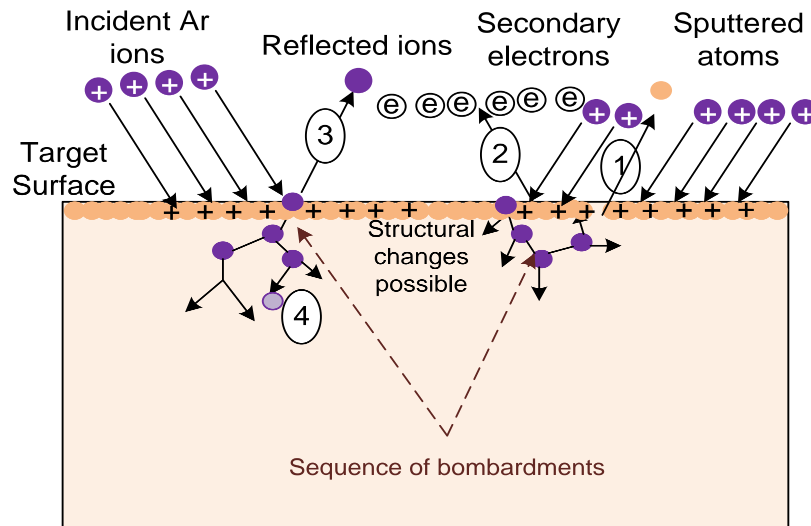

Fig. 3-2. Phenomena arising from interactions of argon ions with the sputtering target [86, 118, 120].

The sputtered species then travel inside the sputtering chamber through a low pressure environment (1 to 10 mTorr) that offers low impedance to the sputtered species' diffusion via increasing the sputtered atoms mean free path[i]. Therefore, the atoms would undergo none or just a few collisions. Hence, they retain most of their kinetic energy upon the substrate arrival and finally gradually get deposited on the substrate producing a thin film. Furthermore, the low

[i] Mean free path is the distance which can be travelled by a sputtered atom between two successive collisions with other atoms in the sputtering chamber.

pressure environment is also needed to maintain the argon ions' energy leading to increasing the sputtering yield[ii], and consequently increases the growth rate [86, 118].

In short, thin film sputter-deposition process involves three steps:

1. Interaction of the sputtering gas ions with the target material that results in sputtering the target species (atoms and ions).
2. Transport the sputtered species via a low pressure environment.
3. Thin film deposition process.

Generally, sputter-deposition systems can be categorised in terms of the way in which they are powered, either by the application of direct current (DC) power, or radio frequency (RF) power. DC-mode is simpler and less costly given that DC power is more straightforward to generate and use than RF power. However, DC-mode is not applicable to sputtering insulating materials due to surface charging during sputtering that cannot be dissipated via the insulating target material and the cathode bias. Therefore, as an insulating target material is bombarded with positive argon ions, positive charges will be built-up on the target surface preventing any further bombardment with argon ions and thus hinder any further sputtering [86, 118, 121]. In RF-powered systems, however, an alternating electric field of high operating frequency (13.56 MHz) is used, capable of sputtering both insulating and conducting target materials. Because of this very high frequency, a quick polarity alternation can be achieved. In this manner, the target material is bombarded with argon ions and then with electrons. When the target acts as an anode (i.e. during the positive half of the RF signal), electrons will accumulate at the target surface, which has a relatively smaller surface area compared to the anode (including the substrate holder and the sputtering chamber walls). Electron accumulation neutralises the positive charges that are accumulated due to argon ions bombardments during the negative half of the RF signal. Moreover, given that electrons have smaller mass and hence higher mobility compared to ions, more electrons would approach the target surface during the positive half of the RF signal than positive argon ions during the negative half of the RF signal. Therefore, the positive charge accumulation on the target surface will be annihilated even when an insulating target material is used. It should be noted that the argon ions with a mass of 6.68×10^{-26} Kg are not affected by the

[ii] The sputtering yield is the average number of sputtered target spices per an incident ion of argon.

quick polarity alternation, since their mass is massively higher than that of electrons 9.11×10^{-31} Kg [86, 118].

In order to enhance the deposition rate, magnetron sputtering systems with a permanent magnetic superimposed just behind the target were introduced. The resultant magnetic field strength should be sufficient to confine electrons, while not affecting the movement of the ions, and it is usually in the range of 20–50 mT. The magnetic field lines are mostly parallel to the target surface and perpendicular to the electric field. The magnetron confines the primary and secondary electrons in particular in helical path orbits close and parallel to the target's surface instead of being lost out of the glow discharge region. Consequently, the plasma density close to the target is increased due to more collisions between electrons and argon atoms leading to higher sputtering rates even at low sputtering pressure. Secondly prevents the secondary electrons from travelling near the substrate resulting in damaging the deposited film and increasing the substrate temperature during the deposition process. Thirdly since the plasma generation is focused in the vicinity of the target's surface and minimised elsewhere, the target only will be sputtered rather than other materials close to the cathode i.e. avoiding undesired contamination on the resulting film [118, 120]. The depositions of the studied thin films during this PhD research were performed using a radio frequency (RF) magnetron sputtering system.

3.3.2 Experimental RF magnetron sputtering system

The RF magnetron sputtering system used in this work, shown in Fig. 3-3, consists of:

1. A sputtering chamber that houses two or four[iii] magnetron-equipped electrodes and a substrate holder. Each of these electrodes can handle a three-inch diameter and 5 mm thick ceramic target, which is water-cooled (~10°C) to avoid being overheated during sputtering. The substrate holder, which is rotated during deposition to improve the coating uniformity, holds a four-inch wafer and is equipped with a heater and a thermocouple for thin film deposition at elevated temperatures. The electrodes are tilted in a sputter-up geometry and maintained at a fixed distance (~10 or ~15 cm) from the substrate during deposition. This geometry enhances the sputtered atoms surface mobility upon the substrate arrival and hence the resulting film uniformity. Also, it reduces the film damage due to energetic species bombardments compared to a substrate-facing-target arrangement [86, 118].

[iii] The system used to deposit AZO samples has two electrodes and the substrate-to-target distance is ~10 cm, while the system used to deposit IGZO samples has four electrodes and the substrate-to-target distance is ~15 cm.

2. An RF power supply system comprising an RF power source that supplies a maximum power of 330 W (13.56 MHz) and has an output impedance of 50 Ω, a tuning unit and a matching unit, which are needed in order to tune the plasma impedance to the RF power source output impedance. As a consequence, a maximum power transfer between the RF power source and the plasma is established.
3. A gas supply and regulation system that provides the needed gas mixture to perform thin film sputter-deposition. Mass flow controllers are used in order to accurately mix and control the flow of the desired gasses.
4. A load lock chamber that is interfaced with the sputtering chamber via a knife valve through which the two can be isolated. This configuration permits the loading and unloading of samples without breaking the sputtering chamber's vacuum. A magnetically coupled arm is used to transfer the samples between the load lock and the sputtering chamber.
5. A pumping system including a diffusion pump, and a rotary pump to evacuate the sputtering chamber and establish a minimum base pressure around 7.5×10^{-5} mTorr (always measured just before introducing the gases to the sputtering chamber), and to maintain a prescribed sputtering pressure in conjunction with the gases supply system. The mechanical pump is also used to rough the load lock chamber to ~ 40 mTorr during sample loading and before the knife valve is opened up.
6. Instrumentation elements to measure and tune the deposition parameters.
7. A water-cooling system to cool down the targets and the diffusion pump.
8. An interferometer to monitor the growing film thickness during deposition (in-situ monitoring).
9. Finally, a set of manual valves to facilitate switching the rotary pump between the main and load lock chambers, and to vent the loading chamber.

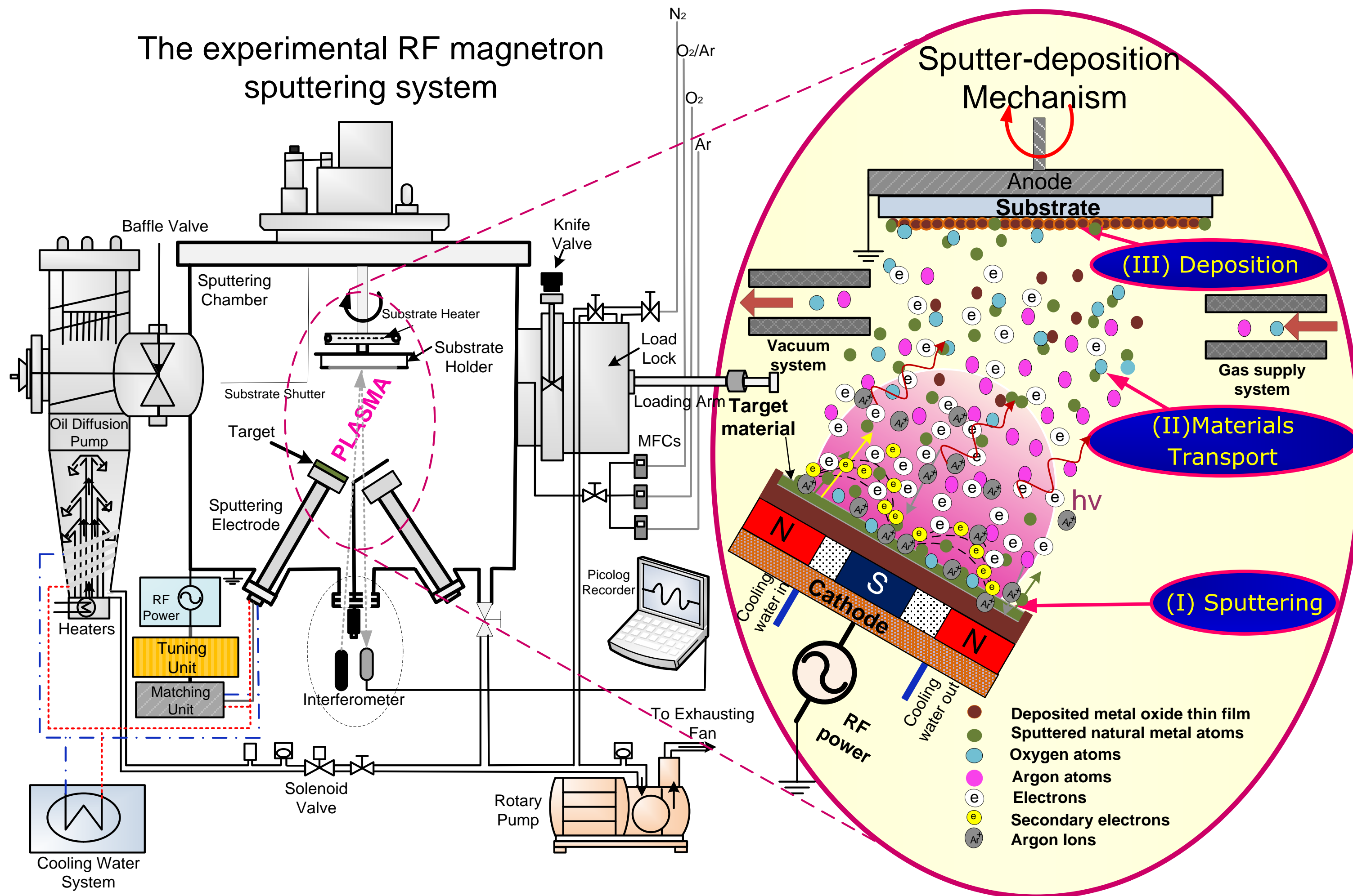

Fig. 3-3. Illustration of the experimental RF magnetron sputtering system, and the sputter-deposition mechanism.

3.4 Post-deposition annealing

Most PVD techniques including sputtering rarely produce thin films with the sought physical properties at room temperature deposition. Hence, post-deposition annealing is performed to further optimise the physical properties of room temperature deposited films. Annealing is performed by increasing the film's temperature to a predetermined temperature (in air or in a controlled ambient), keeping this temperature for a specific time (known as the dwell time), and then allowing the film to cool to room temperature. Consequently, the film's stoichiometry, microstructure, and defect density and/or distribution are altered via atomic rearrangement. For metal oxides, the oxygen content typically has a strong influence on the oxides' physical properties. Hence, annealing can be used to tune the oxygen content in order to enhance the physical properties based on an application requirement. During annealing, oxygen is either incorporated into or removed from the structure of oxide materials, depending on the metal oxide sample's stoichiometry and the annealing environment [9, 118]. Thin film post-deposition annealing approaches can be classified as:

1. Direct annealing such as Excimer Laser Annealing (ELA) where the processing heat is generated in the processed thin film itself via absorbing photons of high enough energy.
2. Indirect annealing such as Rapid Thermal Annealing (RTA) and Conventional Furnace Annealing (CFA) in which the processing heat is generated externally and then transferred by radiation, conduction, or convection to the processed film.

In this work, ELA via Krypton Fluoride (KrF) excimer laser with a wavelength of 248 nm is the main processing approach investigated for low thermal budget fabrication of AZO and IGZO thin films. At the same time, RTA was also tested on AZO thin films for comparison with ELA. CFA has not been in scope of this work since it typically requires long processing times.

3.5 Excimer laser Annealing (ELA)

Excimer lasers of different wavelengths have been used as unique sources of energy in many methods of thin films growth and processing. For instance, excimer laser annealing has been utilised as a processing approach in the area of microelectronics such as processing of amorphous silicon layers to produce poly-silicon for thin film transistors on low-cost glass substrates that thermal annealing techniques would not permit [56, 122]. This approach has been also utilised for processing other functional materials, such as metal oxide thin films and related

devices [80, 123], but limited work has been reported compared to thermal annealing techniques. ELA is an ultra-rapid, large area compatible, and localised (both in surface area and depth) processing technique. Furthermore, ELA offers controllable heating and electronic property enhancement that in many cases cannot be achieved with other means of annealing. Due to these attributes, ELA is very promising for innovative applications of thin film technology, including thin films on inexpensive low-melting-point substrates or processing of multi-layered devices without affecting the underlying layers. Nevertheless, ELA is considered as one of the expensive processing techniques in terms of the equipment initial and maintenance costs.

3.5.1 Basic concept of excimer laser annealing (ELA)

ELA selectively increases the temperature in a specific area of the processed material to high temperatures in very short times (tens of nanoseconds) via intense light photon absorption. The photons must be at an energy higher than the processed material's bandgap in order to ensure that the required laser energy absorption for efficient processing is practically achievable. Hence, the photons transfer a large amount of energy to the processed material, which in turn absorbs within a thin layer near to the surface most of the energy, resulting in inter-band and intra-band transitions i.e. exciting the valance band electrons and the electrons at the trap states within the bandgap to the conduction band producing photo-generated holes. Given that the absorbed energy is very high, the number of these transitions should be large and these excited electrons contribute to a multi-phonon cascade emission upon de-excitation in a very short time in the vicinity of a few tens of picoseconds for ZnO-based materials [11, 65, 80]. The emitted phonons cause lattice vibrations and localised instantaneous heating that causes the top layer annealing at high temperatures. The rest of the processed material will be heated to some extent via the heat diffused from the top-layer. In this manner, a temperature gradient is achieved from the surface layer, where the temperature is high, to the underlying layers or the substrate, where the temperature is relatively low. This is can be ascribed to the high energy deposited to the surface layer of the annealed film in extremely short processing periods [10, 11]. The top-layer heating process is highly dependent on the optical properties of the processed sample and in particular on the absorption coefficient (α) at the utilised laser wavelength, which influences the laser photons penetration depth. Following photon absorption, the resultant effect is governed by the material thermal and physical properties such as the thermal conductivity $K(T)$, density $\rho(T)$,

and specific heat capacity $C\,(T)$, which control the thermal diffusivity of the material (D_h) as shown in Eq. 3-3. The thermal diffusivity is linked to the heat diffusion length L_{th} through the processed material as shown in the Eq. 3-4. The heat diffusion length is defined as the distance along which the generated heat by the laser photons absorption propagates through the annealed sample [10, 11].

$$D_h = \frac{K(T)}{\rho(T) \times C(T)} \tag{3-3}$$

$$L_{th} \approx \sqrt{D_h \tau} \tag{3-4}$$

where τ is the laser pulse duration.

To process ZnO-based materials which have a direct bandgap of about 3.37 eV, the needed wavelength to ensure efficient processing can be calculated by Planck's equation as follows:

$$E_g = \frac{hc}{\lambda} \tag{3-5}$$

where: E_g stands for the bandgap energy (in Joules), h is Planck's constant 6.625×10^{-34} J.s, λ is the required wavelength (in nm), and c is the speed of light 3×10^{8} m/s.

$$\lambda = \frac{hc}{E_g} = \frac{6.625\times10^{-34}\,J.s \times 3\times10^{8}\,m/s}{3.37\times1.6\times10^{-19}\,J} = 368nm \tag{3-6}$$

Hence, the applied laser photons should have a wavelength less than 368 nm. The used ELA system with a KrF excimer laser (λ =248 nm = 5 eV) will serve this purpose of annealing. The table below illustrates the absorption coefficient and penetration depth for the explored thin film materials in this work (AZO and IGZO) at the used laser wavelength of (KrF = 248 nm).

Thin film sample	Absorption coefficient (cm^{-1})	Penetration depth (nm)	Reference
AZO	1.7×10^{5}	55	[124]
	2.26×10^{5}	44	This Work (as-deposited)
IGZO	2.0×10^{5}	50	[79]
	2.2×10^{5}	45	[114]

Table 3-1. The absorption coefficient and penetration depth for AZO and IGZO thin film at the wavelength of KrF laser (248 nm).

3.5.2 Experimental ELA system

The used ELA system in this research is made up of three main parts, as illustrated in Fig. 3-4, including:

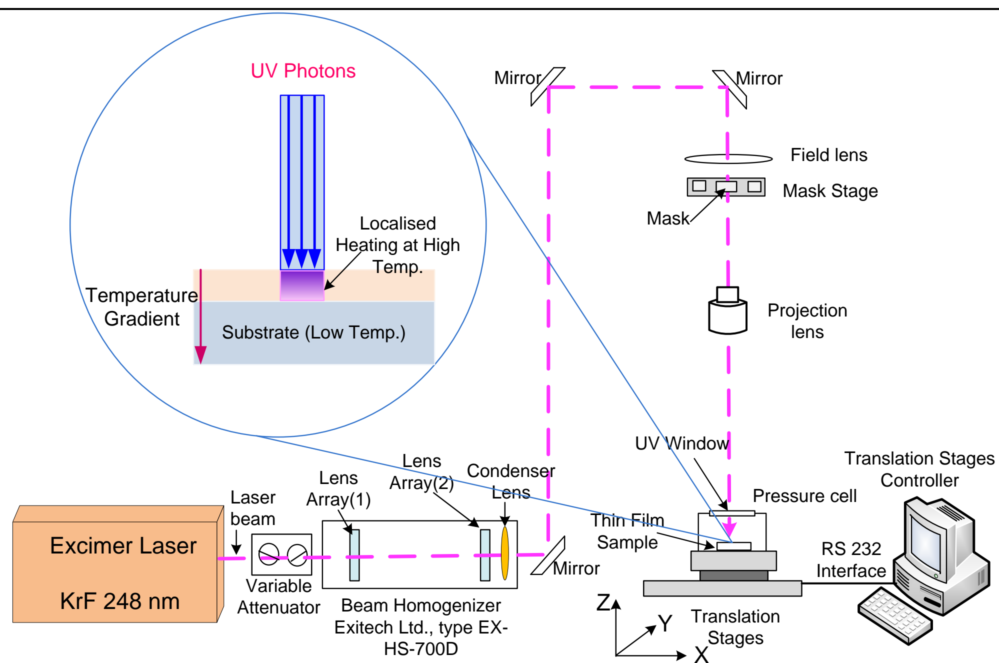

Fig. 3-4. Schematic diagram of NTU Excimer Laser Annealing system.

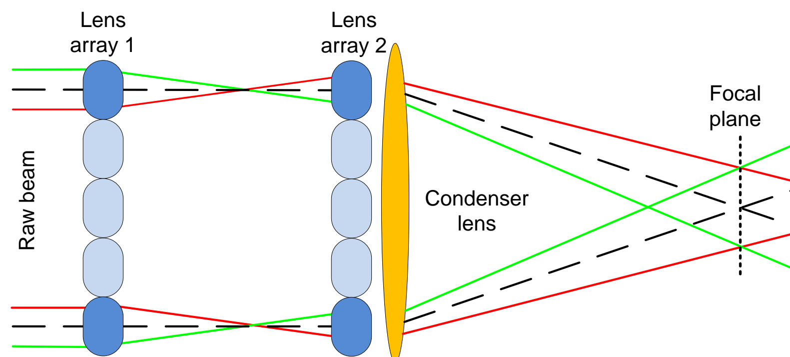

Fig. 3-5. Beam homogenizer (Exitech Ltd., type EX-HS-700D)

1. The laser source, a Krypton Fluoride (KrF) excimer laser (Lambda Physik LPX 305i) which emits pulses of un-polarized light at a wavelength λ of 248 nm, with a pulse duration of ~ 25 ns, and an average energy per pulse up to 1500 mJ.
2. The beam shaping and delivery system that consists of a variable attenuator at the excimer aperture to adjust the laser energy per each pulse, a beam homogenizer (Exitech Ltd., type EX-HS-700D), and optics including mirrors, a field lens, a mask stage for different mask sizes, and a projection lens with a magnification M of 1/1.
3. A computer-controlled XYZ stage with micro precision, where the processed samples are mounted to facilitate large area samples manipulation during processing.

The beam shaping and delivery system converts the raw laser beam, which has an extended area of poor uniformity, to focused laser spots with uniformity better than ± 2%, required to achieve uniform annealing over the entire irradiated area of the sample. The beam

homogenizer is composed of two arrays of lenses and a condenser lens at the homogenizer exist. Corresponding lenses in the arrays spilt the raw beam into many segments, while the condenser lens overlaps these segments on a common (focal) plane that coincides with the position of the mask stage. The produced laser spot at the focal plane has a rectangular profile with a flat-top along both X and Y axis. The beam is transferred via mirrors to the field lens, which projects the beam to the projection lens through a mask of a specific size (to shape the beam into the desired foot print on the sample). Finally, the projection lens images the mask features on the processed sample plane at high resolution [10, 125]. The energy of the laser pulses E is measured via an energy meter after passing the beam delivery system. Then, the energy density E_d expressed in mJ/cm^2 for the treatment area A is calculated:

$$E_d = E / A \quad (3\text{-}7)$$

The deposition and post-deposition ELA of the studied metal oxide thin films in this work were carried out at the innovations in Surfaces Materials and Related Technologies (iSMART) facility in the School of Science & Technology at Nottingham Trent University (NTU). The facility has three RF-magnetron sputtering systems. In order to reduce the chances of cross-contamination among the systems, system number one was employed for TSO growths (IGZO), system number two is typically used by the group to deposit metallic thin films, and the system number three was used to deposited TCO films (AZO and ITO). All the systems' load locks are accessible via a class 1000 clean room to avoid introducing contamination into the systems. Also, iSMART has a photonic processing system with a KrF, and an ArF Excimer laser operating at 248 nm and 193 nm, respectively.

3.6 Rapid Thermal Annealing (RTA)

Rapid Thermal Annealing (RTA) offers important advantages over Conventional Furnace Annealing (CFA) including better control of the annealing temperature and relatively short processing times. Rapid thermal annealing of AZO thin films was examined for comparison with ELA. The utilised equipment is AnnealSys AS–One processor (accessed at the University of Nottingham-School of Physics & Astronomy). The system consists of a processing chamber, a rotary pump, a controller, and a gas supply system. The processing chamber is made of two parts:

1. The sample holder is a silicon carbide coated graphite susceptor at the bottom of the chamber. It accommodates up to 4-inch diameter samples, and is equipped with a

pyrometer and a thermocouple whose measurements are fedback to the process controller.

2. The heating source is on the top side of the chamber and utilises 12 tubular halogen infrared (IR) lamps to heat the sample holder by radiation through a quartz window.

The IR radiation is absorbed with the sample holder which converts the radiation to heat and transfers it to the processed sample. The processing can be performed in a different gaseous environment. The gases are bled into the processing chamber via a mass flow controller at 18 sccm during temperature ramping, and is shut off when the target temperature is reached for better temperature stability and uniformity. Prior to annealing, the processing chamber is evacuated and then purged with nitrogen to clear away any traces of contaminants. The equipment is computer driven and the processing profiles can be edited in terms of the heating rates, target temperatures, and dwell times. The lamps are connected with power convertors to regulate the applied power to the lamps as a function of the processing profile parameters. After processing for the desired dwell time, the power is turned off and the sample is cooled down to about 45°C via heat dissipation before being removed from the processing chamber.

3.7 Thin-film materials characterisation techniques

In this PhD, different characterisation techniques were used to examine the microstructural, chemical composition, surface morphology, electrical, and optical properties changes of the fabricated oxide thin films as a function of the deposition parameters and also to evaluate property changes between as-deposited and annealed thin films. The techniques used are X-ray diffraction (XRD), X-ray Photoelectron Spectroscopy (XPS), Energy Dispersive X-ray microanalysis (EDX), four-point probe (4PP), Van Der Pauw technique (VDP), Hall Effect measurement, Atomic Force Microscopy AFM), and UV-VIS-NIR optical transmittance and reflectance spectrometry. An overview of the used techniques is now presented.

3.7.1 X-Ray Diffraction (XRD)

XRD is one of the most popular non-destructive techniques for revealing microstructural properties of materials including crystalline phase, the interplanar spacing of the structure, grain size, crystallographic orientations, lattice constants, and any introduced strain. In XRD, a monochromatic X-ray beam at a specific wavelength *(λ)* incident at a known angle of incidence *(θ)* penetrates deeply inside the specimen under test, in which atoms or molecules are periodically

arranged forming three dimensional arrays of crystallographic planes spaced with a distance referred to as d-spacing *(d)*. Consequently, the beam will be scattered in all directions owing to oscillation of the atoms' electrons. X-ray diffraction occurs when the scattered rays interfere with each other either with constructive or destructive interference. According to the Bragg's law, Eq. 3-8, once the path difference between diffracted rays from two successive crystallographic planes is an integer number *(n)* of the X-rays wavelength in use, the interference will be constructive at an optical path difference of $2d\sin\theta$. Thus, the diffracted radiation intensity is maximised in a specific direction, indicating a certain crystal structure [126, 127].

$$n\lambda = 2d\sin\theta \tag{3-8}$$

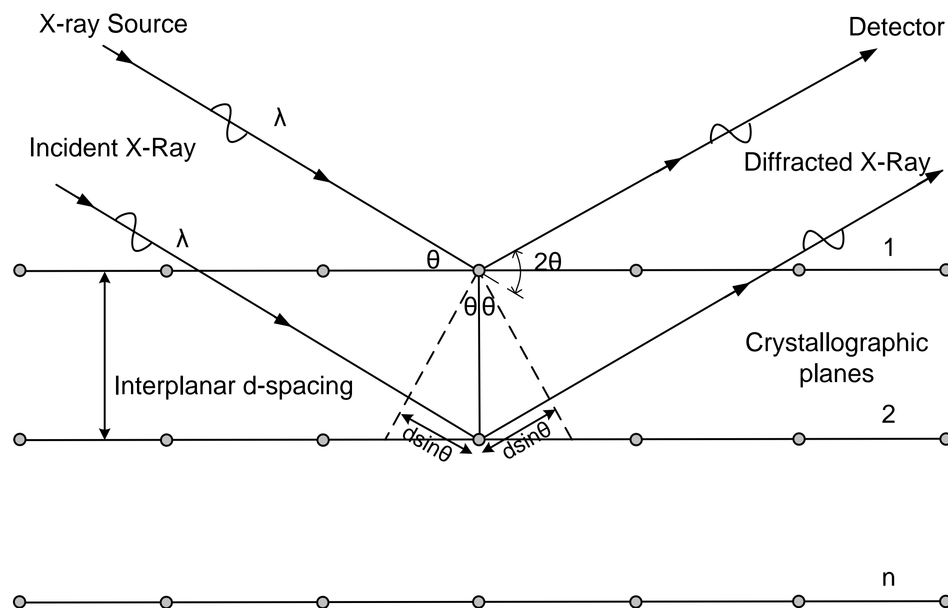

Fig.3-6. The concept of Bragg's law for interaction between X-ray beam and crystallographic planes. Adapted from [126].

The diffracted radiation intensity is collected in either Grazing-Incidence X-ray Diffraction (GIXRD), or Bragg-Brentano X-ray Diffraction (BBXRD), known as $\theta/2\theta$ scan mode. The latter was used in this work, in which the sample is rotated at an angle θ, while the detector is rotated at 2θ collection angles with respect to the incident radiation as illustrated in Fig 3-7. Whenever the Bragg's law is satisfied, the collection angle 2θ is called a Bragg peak. Because the sample and the detector rotation angles are mutually dependent, the geometrical configuration is always maintained fixed. Thus, the extracted data from the XRD $\theta/2\theta$ scan mode always originates from the diffraction crystallographic planes that are parallel to the sample's surface. Hence, the extracted data from BBXRD is more correlated with the thin films' growth process and the ELA

process explored in this research whose effect propagates from the sample surface. Conversely, with GIXRD the extracted data are originated from crystallographic planes of different angles with respect to the examined sample's surface and the growth direction [126, 128].

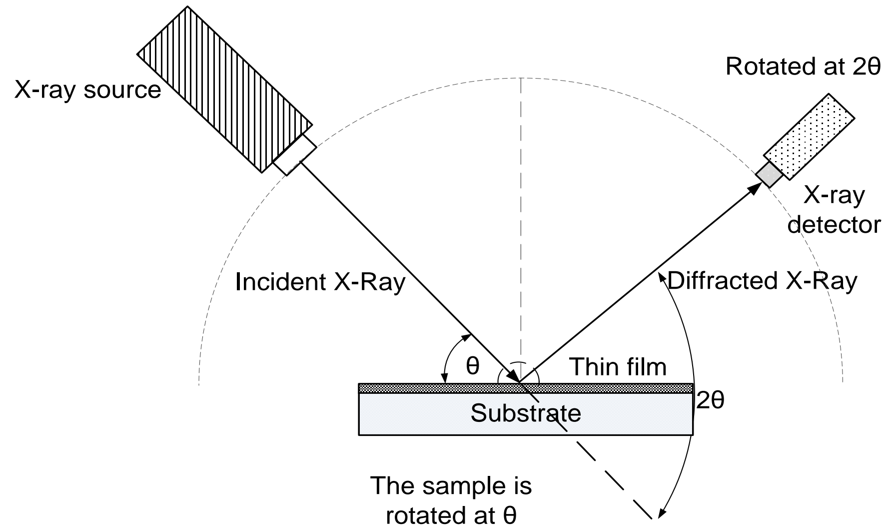

Fig. 3-7. A schematic representation of XRD measurements in θ/2θ scan mode (Bragg-Brentano XRD. Adopted from [126].

The collected diffraction radiation intensity at various angles is known as the diffraction pattern, which is a unique fingerprint of the examined sample and conveys valuable information including:

1. The position of 2θ peak, which is linked to the material interplanar spacing d between the crystallographic planes that are creating the X-rays diffraction.
2. The 2θ peak intensity which indicates the degree of texturing i.e. the degree of preferential orientation of the material [75, 128].
3. The obtained XRD peak broadening from which important data could be extracted. The reasons for the XRD peak broadening are instrumental and physical including grain size and lattice strain effects, as discussed below:

a) Instrumental contribution due to non-ideal optics and focus. This can be determined by using a standard sample in which stress and grain size contributions to the XRD peak broadening are not significant [126, 128].

b) Small grain size contribution. Ideally for X-ray powder diffraction (XRD), the crystallite size should be in the range of (0.5 -10) μm [126]. For thin film materials, however, the grain size is much smaller than this range, which causes additional broadening to the diffraction peaks. This broadening has a Lorentzian line shape and depends on the average grain size. Large grain sizes contain larger number of crystallographic planes that act as X-ray reflecting planes and interference sources, hence they produce sharper diffraction peaks. On the other hand, for small grain sizes, the small number of

crystallographic planes, i.e. X-ray reflecting planes and interference sources, would result in broader diffraction peaks broadening [129]. Scherrer was the first to establish the formula 3-9 to relate the peak broadening to the grain size [128, 130].

$$D = \frac{K\lambda}{\beta_{size}\cos\theta} \qquad 3\text{-}9$$

where D is the average vertical diameter of the grains (in the direction normal to the diffracting crystallographic planes) in angstrom, K is a dimensionless constant which generally has a value of 0.94, λ is the X-ray wavelength, β_{size} is the diffraction peak broadening due to grain size in radians, and 2θ is the is the Bragg angle in radians.

c) Lattice strain contribution. In thin films deposition, residual stress is inevitably created because of many reasons that could contribute to the growth process. These reasons may include variations in coefficients of thermal expansion and lattice parameters between the deposited film and the used substrate, microstructural defects (including vacancies, and dislocations), incorporation of foreign atoms into the deposited film such as substitutional atoms or the sputtering gas ions, and atomic peening i.e. the atoms on the film surface are pushed into the film via energetic particles bombardments including the sputtered atoms and sputtering gas atoms [131, 132]. The lattice parameters of the deposited film will be changed in response to the residual stress causing strain to the film. The strain can be either uniform (macro-strain) or non-uniform (micro-strain). The former results in expanding or contacting the unit cell and thus XRD peak position shift, without XRD peak broadening. The latter is accompanied with systematic displacements of atoms from their ideal locations as well as XRD peak broadening of a Gaussian line shape. Stokes and Wilson [133] were the first to report strain as another source of X-ray line broadening. The average strain can be estimated from Eq. 3-10:

$$\varepsilon_{micro-str} = \frac{\beta_{micro-str}}{4\tan\theta} \qquad 3\text{-}10$$

where $\varepsilon_{micro-str}$ is the average micro strain, $\beta_{micro-str}$ is the diffraction peak broadening due to strain in radians, and 2θ is the Bragg angle in radians.

Based on the biaxial strain model [134], the macro-strain in direction of C axis for hexagonal structure such as ZnO is calculated using Eq. 3-11 below:

$$\varepsilon_{macro-str} = \frac{c_{film} - c_{bulk}}{c_{bulk}} \qquad 3\text{-}11$$

where c_{film} is the lattice constant of c-axis for the thin sample under consideration, which equals 2d-spacing, and c_{bulk} is the lattice constant of c-axis for the unstrained material, which equals 0.5204 nm for ZnO. The sample d-spacing values for the thin sample under consideration is measured from XRD data via Bragg's law. The film residual stress parallel to its surface for

hexagonal lattice structure such as zinc oxide can be calculated from the estimated macro-strain and elastic constants using the following formula:

$$\delta_{stress} = \frac{2c_{13}^{2} - c_{33}(c_{11} + c_{12})}{2c_{13}} \times \varepsilon_{macro-str} \qquad 3\text{-}12$$

For AZO samples studied in this work, the elastic constants data for single crystalline ZnO is used, C_{13} = 104.2 GPa, C_{33} =213.8 GPa, C_{11} = 208.8 GPa, and C_{12} = 119.7 GPa [134]. By applying these values to the Eq. 3-12 we obtain:

$$\delta_{stress} = -233 \times \varepsilon_{macro-str}(GPa) \qquad 3\text{-}13$$

Residual stress in thin films can be either compressive or tensile, negative sign for the calculated stress using the Eq. 3-13 indicates that the examined thin film is subjected to compressive stress.

Most of the reported XRD data analysis of ZnO-based films tends to assume the observed XRD peak broadening is primarily due to the effect of finite grain sizes. However, in XRD, the measured peak profile is a convolution of the profiles resulted from all the aforementioned broadening sources. The instrumental broadening is considered as a characteristic of the utilised instrument and would not affect comparison between different samples as long as they are measured in the same way [135, 136]. In other words, the relative sense among the examined samples will still provide reliable information on grain size and strain trends without the need to consider the instrumental broadening. Thus, the instrumental broadening has not been taken into account in the reported XRD results in this study. However, it is crucial to resolve the peak profile into individual components to separate grain size and micro-strain broadening and thus obtain more accurate determination of the grain size and strain. The Williamson-Hall analysis and Voigt-function analysis are commonly used for XRD peak analysis Voigt-function, used here, is a rapid, simple, and effective approach to analyse XRD peak broadening via fitting the XRD peak into Gaussian and Lorentzian components. The former is related to the average strain, while the latter is due to the average grain size [135, 136]. It was reported that for accurate evaluation grain size and strain from the XRD peak broadening, the integral breadth (τ), defined as the total area under the peak divided by the peak height, should be used instead of FWHM (β), defined as the peak's width at half of its maximum intensity, as a measure of XRD peak profile broadening given that the former takes into account the grain size distribution [135].

$$\tau_{\text{gaussian}} = [\frac{\pi}{4\ln 2}]^{1/2}\beta_{\text{gaussian}} \quad 3\text{-}14$$

$$\tau_{\text{lorentzian}} = [\frac{\pi}{2}]\beta_{\text{lorentzian}} \quad 3\text{-}15$$

For the studied AZO samples, the ZnO (002) XRD peak was fitted with Voigt function using OriginPro 9.0 in order to separate micro-strain and grain size broadening components following the approach of de Keijser et al [135].

The used XRD system in this work is X-Pert Panalytical operated in Bragg–Brentano configuration and uses Cu Kα radiation (λ=1.5418 Å) generated via bombarding a copper anode with energetic electrons at 40 mA and 45 kV. First, wide scans were performed covering the range of angles of (2θ =10°- 80°) to identify any possible diffraction peaks. Then, focused scans were performed in the range of interest for AZO (2θ =33˚ - 38˚). The collected XRD spectra from both the wide and focused scans were analysed. The obtained data and the observed trends on the average grain size, average strain, and stress showed good consistency, with less than 5% deviations. In addition, the XRD patterns for the optimised as-deposited AZO and IGZO samples before and after annealing were collected and analysed for three samples of the same fabrication conditions and provided results with excellent consistency.

3.7.2 X-ray Photoelectron Spectroscopy (XPS)

For each element the binding energy of its core electrons is a characteristic of its atoms. Thus, this energy is used for the identification of atoms in a material via a technique known as X-ray Photoelectron Spectroscopy (XPS). In XPS, a beam of monochromatic X-rays with energy in the range of 200 – 2000 eV is directed to the sample under test. Then, the X-ray photons' energy is transferred to the contained atoms' electrons leading to ejecting the core electrons from different electronic levels of the atoms. The process is known as photoemission, and the ejected electrons are referred to as photoelectrons. To reduce photoelectrons' collisions and to avoid surface contaminations, the sample is kept in an ultrahigh vacuum < 10^{-7} Pa. The kinetic energy of the photoelectrons KE is measured by an energy analyser. KE is related to the atoms binding energy BE, the system work function φ[iv], and the X-rays energy hv according to the Eq. 3-16.

[iv] The minimum energy required to eject an electron from the Fermi level into vacuum, it is in the range 3 to 4 eV.

$$KE = h\nu - BE - \varphi \qquad 3\text{-}16$$

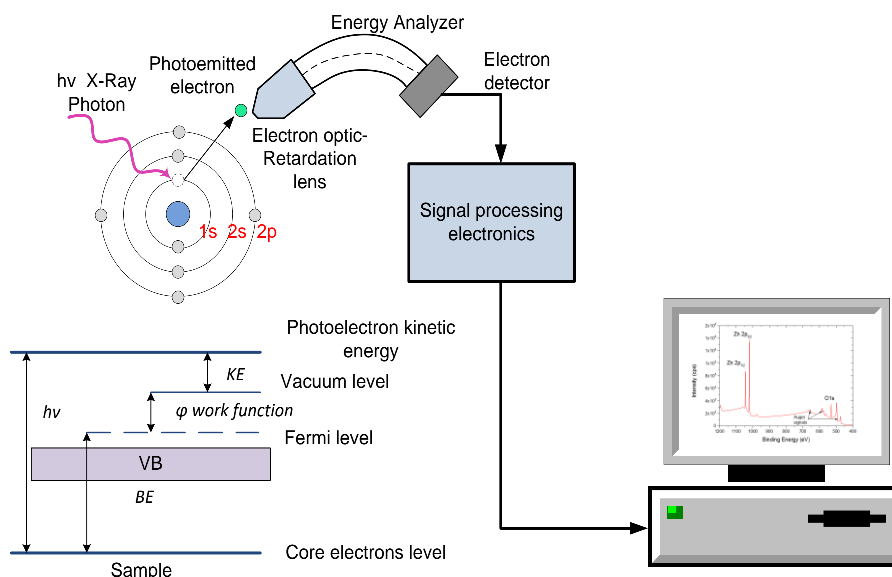

Fig. 3-8. Schematic diagram of photoelectron emission, energy level diagram for photoelectron effect, and XPS measurement. Adopted from [137].

The contained elements are then identified via analysing the peaks distribution in the binding energy spectrum [137, 138]. A peak position in the binding energy spectrum is directly related to a specific element, and the peak intensity is linked to the concentration of that element presented within the irradiated area of the sample's surface. To describe which electrons are involved in the photoelectron effect, spectroscopists' notation is used which labels the peaks with the format nlj:

n: the principal quantum number (1, 2, 3 etc.).

l: orbital angular momentum (s, p, d, f = 0, 1, 2, 3).

j: the interaction between the orbital angular momentum and the electron angular momentum due its spinning $S = \pm \frac{1}{2}$, and $j=l+S$. When the orbital angular momentum $l=0$, a single XPS peak is raised. But, for orbital with momentum $l>0$ (p, d, f), this interaction results in splitting XPS peaks into two energy levels known as a doublet. The separation between the two levels is known as spin orbital splitting. For example, a photoelectron emitted from a p orbital would have j values of 1 – ½ = ½ or 1+ ½ = ³⁄₂. For an element in different compounds, the spin orbital splitting and the peaks' area ratio of the two energy levels are nearly the same [137, 138]. Fig. 3-9 shows an XPS spectrum from an AZO sample with the two peaks for Zn2p labelled according to the above notation, corresponding to the spin orbital splitting for electrons from the p orbital for the zinc atom.

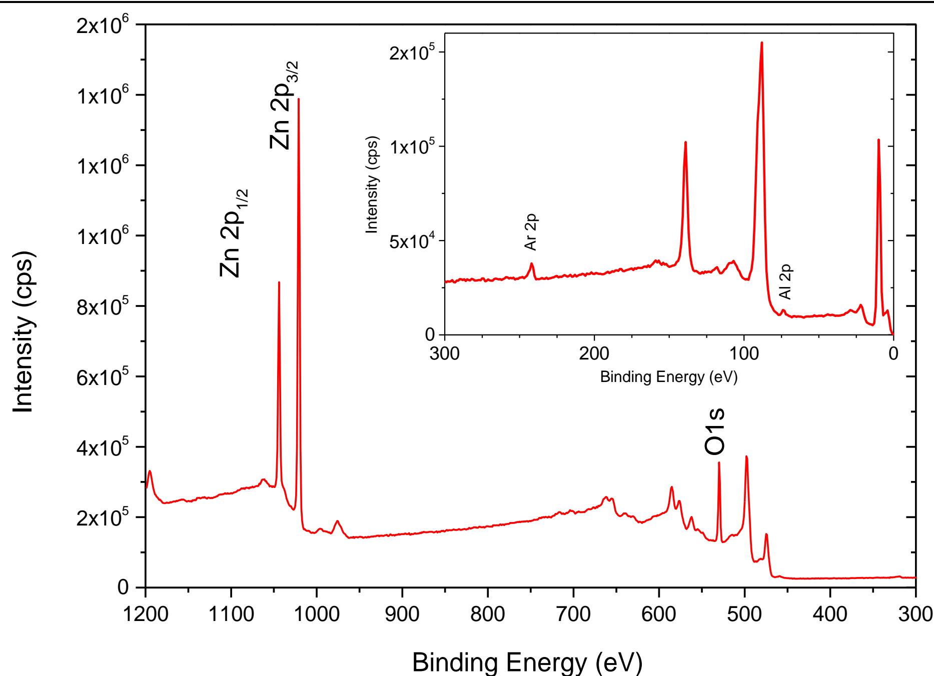

Fig. 3-9. Wide scan of XPS measurement for an AZO thin film.

A change in bonding configurations of an atom due to combining other atoms in its surrounding, results in an observable shift for XPS peak position compared to that of a pure element. This is because of changing the atom's valance electrons density via sharing or exchanging electrons between the atom and the surrounding atoms. Thus, XPS is a powerful tool among other techniques in determining atoms' chemical state [137, 138].

Since electrons in a solid have relatively short mean free paths, the photoelectrons emitted from a certain depth from the sample's surface only are able to liberate themselves from the material under irradiation without losing their energy. Hence, XPS is known as surface composition analysis technique, typically for a depth resolution of 0.5 – 5 nm. Electrons from deeper atoms at different depths in the sample result in a background signal in the XPS spectrum once they manage to escape from the sample. There are different baseline approaches to subtract the background signal form the XPS spectra such as linear, Shirley, and Tougaard background. For depth profiles an in-situ etching apparatus is used typically with argon ion beam, argon is used to avoid interacting with the sample. The etching apparatus is also used to remove any surface contamination due to samples exposure to air [137, 138].

XPS measurements for the studied thin films in this research were carried out at the Aristotle University of Thessaloniki – Greece, Professor Panos Patsalas is acknowledged for the measurements. The used system is an AXIS Ultra system by Kratos Analytical Ltd., with a UHV

chamber (~10^{-9} mbar), a monochromated Al-Kα1 X-ray beam (1486.6 eV) as the excitation source, a hemispherical energy analyser, and a 128-channel detector. To remove any surface contamination, the samples' surface was etched with argon ions. Low resolution (wide-scan) spectra were collected over a range of binding energies (0 to 1200 eV). Then, high resolution (narrow-scan) spectra were obtained for the regions of interest in the XPS spectrum. The examined area has an elliptical shape with the two axes being ~ 400 and 700 µm. Data interpretation was performed with the Kratos-Vision software using a linear background type. A doublet of two Gaussian-Lorentzian GL (30), 70% Gaussian 30% Lorenzian, line shape peaks was used for fitting the Al2p spectra into Al2p$_{3/2}$ and Al2p$_{1/2}$ peaks. The peaks are linked to each other with an offset of 0.4 eV, have very similar FWHM, and the area ratio between the peaks was fixed at a value of 2. For O1s data, the spectra were fitted into two peaks, O1s(I) and O1s(II), using the commonly reported data for O1s peaks' position, similar FWHM for each of the fitted peaks, and a GL(30) line shape.

3.7.3 Energy Dispersive X-ray Spectroscopy (EDX)

Energy Dispersive X-ray spectroscopy (EDX) is a rapid characterisation technique for qualitative and quantitative information of chemical composition obtainable from the bulk of the examined samples. EDX is based on collection and analysis of X-rays generated from the sample under test due to bombardments with a focused beam of highly energetic electrons in a low vacuum chamber. The beam interacts with the contained atoms resulting in ejecting electrons from their inner shells and creating core-holes. Then, electrons from outer shells tend to fill the core-holes, X-rays are consequently emitted to balance the energy difference between the shells. The X-rays are characteristic of the atoms from which they are emitted since the X-rays' energy is dependent on the atomic number of the element [137, 139].

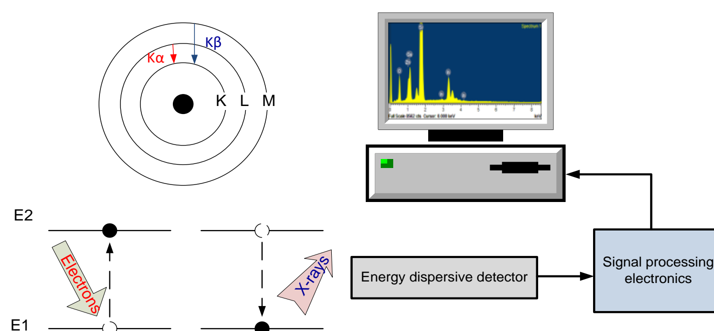

Fig. 3-10. Schematic of an EDX system and the types of X-ray lines observed in generated x-ray spectra. Adopted from [137].

An energy dispersive detector is used to collect and convert the generated X-rays into an electric signal, which is proportional to the X-rays' energy. The electrical signal is fed to a software to analyse the X-rays' energy spectra which typically consists of Gaussian-shaped peaks referred to as X-ray lines [137, 139]. X-ray lines are named after the shell in which the core-hole is created under the energetic electrons bombardments. If the core-hole is created on the K shell and electrons transfer from L to K, the X-rays are referred to as Kα, and for M to K transitions Kβ X-rays are emitted. Each line in the X-rays spectra is assigned to a specific element in the sample, while, the intensity of each line is related to the concentration of each element [137, 139]. For high enough excitation efficiency and thus to obtain enough X-ray photons, the exciting electron beam should be at least twice the critical excitation potential for a given line in the X-rays spectra [137, 140]. For instance, the X-ray line for indium L is about 3.3 KeV, thus the accelerating voltage for the incident beam of electrons should be > 7 KV [137]. In this research, EDX examinations for the studied IGZO thin films (200 nm thick) and the utilised IGZO sputtering targets were performed on a JEOL JSM-A840A scanning electron microscope (SEM). The system was operated at an accelerating voltage of 10 KV and a filament current of 100 µA, for a magnification of 5000 and an examined area of 25 µm x 25 µm. The generated X-ray spectra were collected using a Silicon Drift Detector (SDD), and fed to INCA software for background subtraction and X-ray spectra analysis. X-ray lines of indium L, gallium L, and zinc L were found at 3.3, 1.1, and 1.05 KeV respectively and used for quantification. Spectra from three parts of IGZO wafer were collected, the samples found to demonstrate a good chemical homogeneity and the averaged concentrations are reported. The system was tested with a ZnO sample (from Bayville chemical supply inc.) and it was found that the obtained EDX data in agreement with the composition provided by the supplier.

3.7.4 Resistivity measurements by four-point probe (4PP) technique

In the field of material fabrication for electronic applications, resistivity is one of the essential characteristics examined to study its evaluations upon different fabrication steps and in order to ensure that the potential application requirements are satisfied [141]. For a regular 3-D sample, the resistance of its bulk R is related to the resistivity ρ as below:

$$R = \rho \frac{l}{A} = \rho \frac{l}{wt} \qquad \text{3-17}$$

where A is the cross-sectional area l is the length, w is the width, and t is the thickness of the sample. If l=w (quadratic sample), the Eq. 3-17 can be simplified to:

$$R = \frac{\rho}{t} = R_{sh} \tag{3-18}$$

where R_{sh} is the sheet resistance measured in ohms per square (Ω/sq or Ω/□) which expresses the resistance (number of ohms) presented by one nominal square sheet of a material independently of its lateral dimensions. Thin films of uniform thickness (t) are often evaluated by their sheet resistance [141]. The four-point probe (4PP) technique is commonly used to measure sheet resistance due to its simplicity, no sample preparation is needed, and superior accuracy. The technique dates back to 1916, detailed discussions and explanations of the technique were published on its100th anniversary [142]. Four-point probe technique is based on the concept that the electrical potential distribution created in a material in contact with a current-injecting electrode is dependent on the material resistivity and of course the applied current density. In this technique, four equally spaced needle-like metal electrodes are brought in contact with a thin film material under test. The outer two electrodes are used for sourcing a measured direct current (I) into the film, while the resulting electrical potential (V) across the film is measured through the inner two electrodes as shown in Fig.3-11.

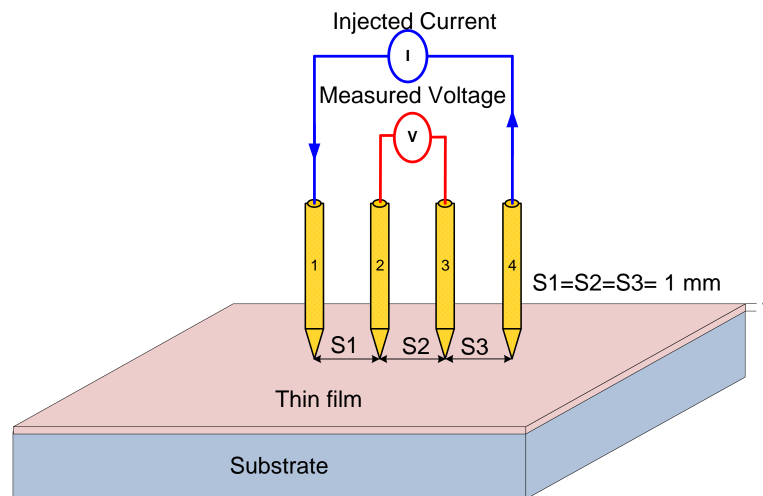

Fig.3-11. Schematic drawing of the linear four-point probe sheet resistance and resistivity measurement system. Adopted from [141].

Because of the high input impedance of a voltmeter, a negligible current flows through the inner probes. Therefore, the impact of the contact resistance between the inner metal probes and the sample, as well as of the inner probes' resistance on the measured voltage, are eliminated

with the use of such a configuration. The probes are spring-loaded to reduce the sample damage, whilst ensuring good contact with the sample. The known current (I) and the measured voltage (V) are used to calculate the sheet resistance (R_{sh}) by using the well-known four-point probe Eq. 3-19. And, the resistivity (ρ) of a bulk material of thickness (t) is calculated with Eq. 3-20 below [141, 143, 144]. A mathematical derivation of this formula can be found in [141, 142].

$$R_{sh} = 4.532 \times \frac{V_{measured}}{I_{injected}} \quad 3\text{-}19$$

$$\rho = 4.532 \times t \times \frac{V_{measured}}{I_{injected}} \quad 3\text{-}20$$

A collinear four-point probe station by Signatone was used during this research with probes made of tungsten carbide and have a probe spacing of 1 mm. The four-point probe station is equipped with a dual-channel Keithley SourceMeter unit (Model 2636A), which has a very high output and measurement accuracy. The used set up was cross checked against a commercial ITO sample obtained from KINTEC Company with sheet resistance measured by the supplier at nine points across the sample. Sheet resistance and resistivity measurements are performed on 1 cm x 1 cm or 1.3 cm x 1.3 cm samples (i.e. finite sized areas) and therefore correction factors should be applied. There are some publications and technical reports that have calculated and tabulated the needed correction factors based on the sample thickness and the probes placement on the sample (i.e. the sample size). According to [141, 144], a correction factor for the probes placement should be applied if the lateral dimension of the sample is less than 20 times the probe spacing, but there is no need for any thickness correction factor if the sample thickness is much less than the probe spacing ($t \ll s$, t=180 nm for the AZO samples and 40 or 200 nm for the IGZO samples studied in this research). Therefore, 0.93 was used as the probes placement correction factor [144].

3.7.5 Resistivity measurements by Van der Pauw (VDP) technique

The technique is based on conformal mapping mathematics done by Van der Pauw in 1958 [141, 145]. In this technique, four contacts on the sample's periphery are used, a direct current (I) is forced on two adjacent contacts and the induced voltage (V) is measured between the remaining contacts as illustrated in Fig. 3-12.

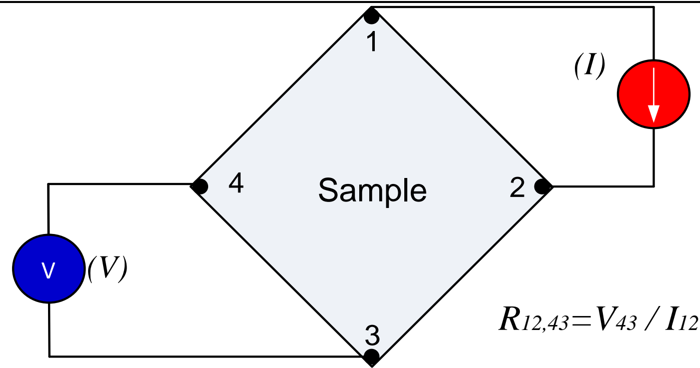

Fig. 3-12. A schematic drawing of van der Pauw method for resistivity measurement. Adopted from [141].

For minimising the impact of the sample geometry and the contacts imperfection, this process is performed on all four sides of the sample with reversing the current direction, yielding a total of eight measurements. Moreover, the contacts' diameter and the sample thickness must be much smaller than the contacts spacing to minimise the measurement error [141, 145]. These conditions were all met for the performed VDP measurements in this work.

Characteristic resistances related to the Van der Pauw method, commonly referred to as R_A and R_B, are then calculated and averaged for each two sides of the samples.

$$R_A = (R_{12,43} + R_{21,34} + R_{34,21} + R_{43,12})/4 \qquad 3\text{-}21$$

$$R_B = (R_{23,14} + R_{32,41} + R_{41,32} + R_{14,23})/4 \qquad 3\text{-}22$$

$R_{ij,kl}$ is the measured resistance when current (I) is applied from terminal i to j, while the resulting voltage (V) is measured across terminals k and l; i.e. Eq. 3-23 applies:

$$R_{ij,kl} = \frac{V_{kl}}{I_{ij}} \qquad 3\text{-}23$$

Sheet resistance R_{sh} is calculated via the Van der Pauw Eq. 3-24, and finally the resistivity is calculated with knowing the film thickness (t).

$$1 = e^{(-\pi R_A / R_{sh})} + e^{(-\pi R_B / R_{sh})} \qquad 3\text{-}24$$

3.7.6 Hall Effect measurement

Hall Effect measurement is the most commonly used approach to obtain carrier concentration, type (electrons or holes), and mobility in a material and is based on the effect discovered by Edwin Hall. When an electric current (I) is injected into a material in X-direction,

while a perpendicular magnetic field (B) is applied in Z-direction, the moving charge carriers will be deflected by the Lorentz force (F_L) in Y-direction to one side of the sample creating an excessive extra negative charge (for n-type material) on one side of the sample. As a result, an electric field between the sample sides (E) and an electrostatic force (F_e) are created [141].

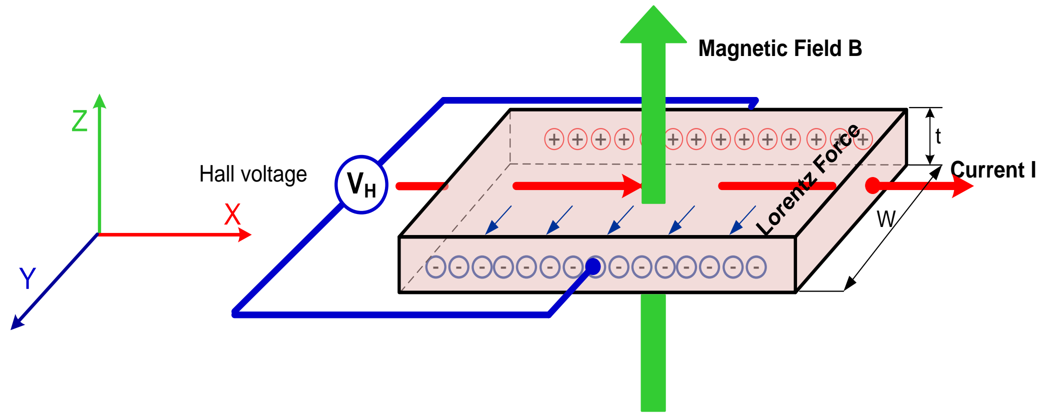

Fig. 3-13. A schematic diagram of the Hall Effect concept and standard geometry. Adopted from [141].

Once the system is in equilibrium (i.e. the electrostatic force between the sample sides balances the Lorentz force), the electric field creates a measurable potential difference between the sample sides that is referred to as `Hall voltage V_H' which is mutually perpendicular to both the injected current and the applied magnetic field, as shown in Fig. 3-13 [141]. The Lorentz force and electrostatic force are given by the equations:

$$F_L = qvB \tag{3-25}$$

$$F_e = qE \tag{3-26}$$

where q is the charge of the majority carriers, and v is the carrier drift velocity.

When the system is balanced $F_L = F_e$:

$$\boldsymbol{vB = E} \tag{3-27}$$

since an electric current (I) can be expressed as the total amount of charge passing a given point in a material of a cross-sectional area (A) at a drift velocity (v), we have,

$$I = NqAv \tag{3-28}$$

where N is the free carrier concentration.

$$v = \frac{I}{NqWt} \tag{3-29}$$

where W is the distance between the sample sides i.e. the sample width, and t is the sample thickness.

The created electrical potential (V_H) is related to the electric field (E) as below,

$$E = \frac{V_H}{W} \tag{3-30}$$

By substituting Eq. 3-29 and 3-30 into Eq. 3-27 we obtain,

$$V_H = \frac{IB}{Nqt} \tag{3-31}$$

From V_H, the Hall coefficient (R_H), and carrier density (N) are extracted,

$$R_H = \frac{V_H t}{IB} \tag{3-32}$$

The Hall coefficient sign indicates the carrier type; a negative Hall coefficient means that the majority carriers are electrons (n-type material) such as in AZO and IGZO samples.
From Eq. 3-31 and 3-32 the carrier density is,

$$N = \frac{IB}{qtV_H} = \frac{1}{qR_H} \tag{3-33}$$

The Hall mobility is calculated from:

$$\mu_H = \frac{1}{\rho N q} = \frac{R_H}{\rho} \tag{3-34}$$

where ρ is the resistivity that is measured by the VPD technique (section 3.7.5).

The above Eq. 3-34 was initially established for single crystal materials in which minor scattering is expected. However, for polycrystalline and amorphous materials, Hall mobility is related to carrier mobility $(\mu_{carrier})$ as below:

$$\mu_H = r\mu_{carrier} \tag{3-35}$$

where r is the scattering factor that depends on the dominating scattering mechanism. Typically, r is 1.18 for lattice scattering and 1.93 for impurity scattering. Impurity scattering dominates in polycrystalline AZO, whilst lattice scattering dominates in amorphous IGZO [141]. Hall mobility values are reported throughout the thesis.

Most of Hall Effect measurement systems perform Hall effect measurement in Van der Pauw configuration i.e. four contacts at the sample periphery as demonstrated in Fig. 3-14. A

current is injected via two opposite contacts while a magnetic field is applied perpendicular to the sample, and the resulting Hall voltage is measured across the remaining two contacts. For Hall voltage measurement with better accuracy, the injected current polarity and the applied magnetic field direction are changed resulting in eight Hall voltage measurements whose average is used to calculate the other parameters as explained above.

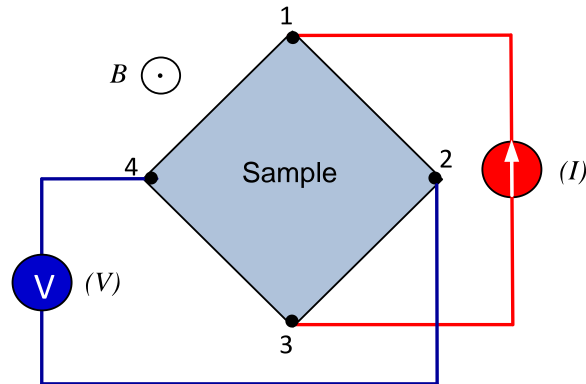

Fig. 3-14. A schematic representation of Hall Effect measurement in van der Pauw geometry.

The electrical characteristics for AZO samples of 1 cm × 1 cm in size deposited on glass substrates are evaluated with a Phystech RH2035 Hall measurement system at room temperature, in Van der Pauw geometry with a magnetic field of 0.55 T. For the IGZO study, an Ecopia HMS-3000 Hall effect measurement system was used in van der Pauw geometry at room temperature and with a magnetic field of 0.55 T. The IGZO thin films on glass substrates of 1.3 cm × 1.3 cm had titanium/gold electrodes deposited through a shadow mask at the corners of the samples in order to make good ohmic contacts. I–V curves test was performed before the Hall Effect measurements in order to determine the appropriate current range for Ohmic contacts between the gold dots and the examined IGZO samples. The gold contacts were tested and found not needed for AZO samples due to the low resistivity of AZO resulting in always linear IV characteristics i.e. Ohmic contacts. The measurements were repeated three times for every sample and the average is reported throughout the thesis. Furthermore, the resistivity measurement with VPD was cross checked with 4PP measurement and was always found in very good agreement.

3.7.7 Atomic Force Microscopy (AFM)

Atomic Force Microscopy (AFM) is a powerful scanning probe microscopy technique for materials topography characteristics. AFM provides 3-D surface profiling at a very high-resolution

down to nanometre-scale, from which surface related data, such as surface roughness and average surface-particle size, can be obtained. Unlike, scanning electron microscopy (SEM) and transmission electron microscopy (TEM), AFM is typically performed in air or even in liquid environments for both insulator and conductive materials. The AFM scan area can be in the range of 100 nm square up to 1000 µs square [137, 146]. Given these merits, AFM is employed in many research fields including material science and chemistry.

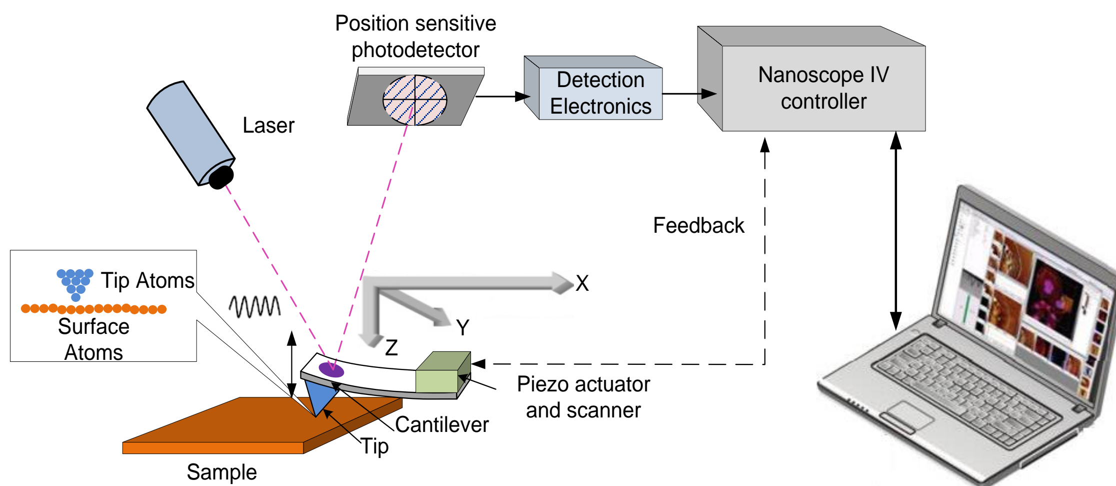

Fig. 3-15. Schematic representation of the AFM concept. Adopted from [137].

In AFM imaging, the surface information is gathered via scanning a sharp micro-fabricated tip (of a radius with curvature typically about 10 nm) in a raster pattern across the surface of the sample under consideration. The tip is typically made of silicon or silicon nitride, and is attached to the end of a flexible and reflective cantilever. There are three imaging modes for AFM including contact, non-contact, and tapping mode. The modes have different scanning approaches in terms of the interaction between the AFM tip and the sample surface. Contact mode and tapping mode are commonly used. Tapping mode, which is an intermediate between the other two modes, is used in this work due its simplicity, higher lateral resolution, less damage to the examined sample and less time consuming in terms of setting up the measurement. In this mode any lateral dragging forces can be reduced and therefore sample damage is avoided. In this mode, the tip/cantilever assembly is driven to oscillate vertically back and forth at or close to its resonant frequency (in the range of 200-300 kHz) and with an amplitude of oscillation in the range of 20-100 nm, via means of a piezo actuator. The tip lightly taps on the sample surface at the bottom of its swing for a minimal time during which a repulsive force is developed between atoms on the

tip and those on the sample surface resulting in a deflection of the cantilever in Z-axis as the surface morphology changes in X and Y axes. The oscillation is controlled with a feedback loop in order to maintain the oscillation amplitude and thus the tip-sample interaction fixed during the scan. The cantilever deflection is monitored typically with a laser beam which is incident on the cantilever's back and reflected to a position sensitive photodiode. Then, the changes for the Z-position of the tip/cantilever assembly indicate the local sample height variations for each X and Y data points on the sample surface, and are used to create an image whose colour contrast represents the surface topography [137, 146].

Generally, surface roughness within a given area is measured in nm and quantified using the following parameters:

1. The Root Mean Square (R_{RMS} or R_q) roughness, which is the standard deviation of the surface height values Z from their arithmetic mean height.

$$R_{RMS} = \left[1/n \sum_{i=1}^{n} (Z_i - \overline{Z})^2 \right]^{1/2} \quad \text{3-36}$$

2. The Arithmetic Roughness (Ra), the arithmetic mean of the absolute values of the surface data points deviations from the arithmetic mean height.

$$R_{\mathrm{a}} = 1/n \sum_{i=1}^{n} (| \mathrm{Z_i} - \overline{Z} |) \quad \text{3-37}$$

3. The Z range, defined as the difference in the vertical distance between the highest and lowest points in the scanned area.

$$Z_{\mathrm{range}} = Z_{\mathrm{max}} - Z_{\mathrm{min}} \quad \text{3-38}$$

where n is the total number of data points in a given image, Zi is the surface height at a given point, $\overline{Z}$ is the arithmetic mean of the surface height in the image, Z_{max} and Z_{min} are the highest and lowest points of the scanned area respectively [137].

AFM in tapping mode was used to examine the surface morphology and roughness of AZO films with a Digital Instruments Nanoscope IV Dimension 3100 scanning probe microscope operated in air. Nanoscope 6.12r1 software (Veeco Instruments Inc.) was used for real time operation and post-capture image analysis. The AFM system was rested on a vibration isolation table to eliminate the ambient noise contribution to the measurements. The used tip was made of

antimony doped silicon with nominal radius of 8 nm. Three areas (1 μm x 1 μm) for each sample were examined at a frequency of 0.3 Hz making 256 × 256 array of pixels. In other words, the scanned lines are 256 and each of which has 256 data points. The obtained roughness details from the three areas of each sample demonstrated a good consistency with very minor deviations. Before the AFM scans, the samples were cleaned with ethanol and blown with the high purity dry nitrogen to remove any dust from the surfaces.

3.7.8 Optical transmittance and reflectance spectra

In this work, optical transmittance and reflectance spectra for AZO films on UV grade fused silica substrates were recorded on the Ocean Optics SpectraSuite Software with a UV/VIS (Ocean Optics USB4000) spectrometer, a NIR (Ocean Optics NIR 256-2.5) spectrometer, a deuterium-halogen light source (Ocean Optics DH 2000), and optical fibers to transfer the light between the sources, the specimen, and the spectrometer. The set-up is illustrated in Fig. 3-16.

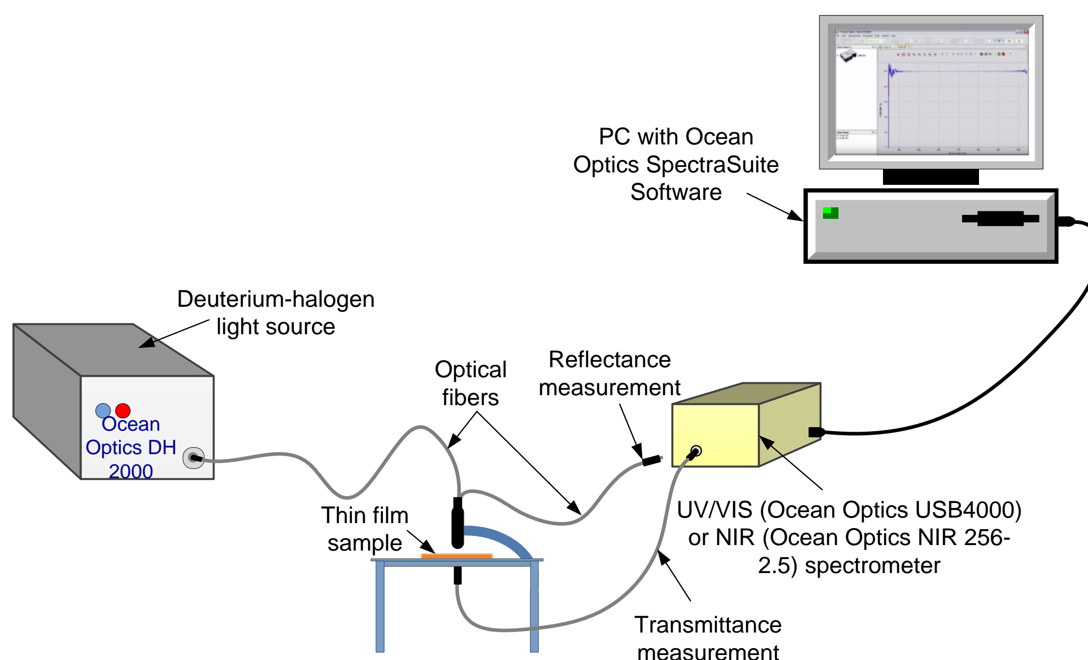

Fig. 3-16 Schematic illustration of optical transmittance and reflectance measurements set-up.

First, the spectra of the lamp and the dark measurements were recorded. Next, the examined sample was illuminated with light photons at the wavelengths of interest, and the transmitted or reflected light was collected by the relevant spectrometer. Then, the relative light intensity transmitted or reflected is calculated. The measurements were performed in a dark room to avoid additional light affecting the measurements. The reported transmittance and reflectance spectra are for the system of the films on the substrate. Essential optical characteristics of metal

oxide thin films can be extracted from the transmittance T and reflectance R spectra measurements, such as the material absorbance A, the absorption coefficient α, the optical bandgap Eg defined as the threshold energy of the light photons at which the material starts absorbing light [137, 141].

$$A = 1 - T - R \quad (3\text{-}39)$$

$$\alpha = -\tfrac{1}{t}\ln\left(\frac{\sqrt{(1-R)^4 4T^2R^2-(1-R)^2}}{2TR^2}\right) \text{ [141]} \quad (3\text{-}40)$$

where t, R and T are the sample thickness, reflectance, and transmittance at the wavelength of interest respectively. From the absorption coefficient, the light photons' penetration depth can be estimated, which is the average distance travelled by photons before their energy being completely absorbed by the material. The penetration depth is defined as the inverse of the absorption coefficient (α^{-1}) [137, 141]. The penetration depth is an essential parameter to study the effect of laser annealing on metal oxide thin films explored in this work.

According to Tauc et al model [147], the relation between the absorption coefficient and the incident light photons energy is expressed as:

$$\alpha(hv) = C(hv - Eg)^n \quad (3\text{-}41)$$

where α, h, v, and Eg are the absorption coefficient, the Plank constant, the frequency of the incident light, and the optical bandgap respectively, C is a proportionality constant, and the exponent n has discrete values depending the nature of carrier transitions across the bandgap. For direct bandgap materials such ZnO-based materials studied here $n=1/2$ [13], so the Eq. (3.41) becomes,

$$\alpha(hv) = B(hv - Eg)^{1/2} \quad (3\text{-}42)$$

The optical bandgap for thin films can be estimated via a linear extrapolation of $(\alpha hv)^2$ versus hv plot to intercept the energy (hv) axis, given that the optical bandgap Eg equals photon energy (hv) when $(\alpha hv)^2$ is zero i.e. at $\alpha \approx 0$, (known as Tauc plot).

4 Room Temperature Sputter-deposition of AZO Films

4.1 Introduction

This chapter presents an investigation of room temperature sputter-deposition of AZO thin films by radio frequency RF magnetron sputtering. Detailed studies are presented concerning the fabricated AZO thin films' properties as a function of various sputter-deposition parameters, including oxygen to argon ratio, applied RF power, and sputtering pressure. The results demonstrate that the AZO microstructural, compositional, morphological, electrical, and optical characteristics are strongly dependent on the deposition parameters applied. Optimisation of the deposition parameters facilitated the reproducible fabrication of good quality AZO electrodes during this study without intentional substrate heating.

4.2 Experimental investigation of AZO deposition parameters

This task commenced by selecting the Al_2O_3 wt.% used as a dopant source in the AZO target, which is one of the influential parameters that strongly affect the resultant AZO thin films' electro-optical properties. In Al-doped ZnO (AZO), a certain ratio of Al atoms is introduced to the ZnO lattice to substitute the zinc atoms in the ZnO crystal structure forming a substitutional solid solution. Several factors dictate the limits of substitutional solubility in a solid solution. The Hume-Rothery rules provide guidelines to achieve maximum substitutional solubility [148, 149]. The rules are as follows:

1. The relative difference between the atomic radii of the solute atoms (the dopant atoms) and the solvent atoms (the host atoms) should be less than 15%. Aluminium atom has an atomic radius of 0.143 nm, compared to 0.133 nm for zinc [150]. This results in 7% mismatch of atomic radii.
2. The crystal structures of the solute atoms and the solvent atoms should be the same. Aluminium has a cubic crystal structure, while zinc has a hexagonal crystal structure.
3. The valances of the solute atoms and the solvent atoms should be the same. Aluminium has +3 valence, compared to +2 for zinc.
4. The electronegativity of the solute atoms and the solvent atoms should be very similar. Aluminium has an electronegativity of 1.61 on the Pauling scale which is very comparable to that for zinc 1.65.

This shows that aluminium could substitutionally replace zinc in the ZnO lattice forming Al-doped ZnO (AZO). The dopant's solubility is also dependent on the doping level and the fabrication conditions of AZO thin films [18, 151]. In the literature, different AZO target doping levels have been studied and there is general agreement that the optimum doping level for AZO sputtering targets should be in the range of 1-2 wt.% Al_2O_3, in order to obtain AZO films with the highest achievable conductivity and maintain good visible transparency. At higher doping levels, some Al atoms could occupy interstitial sites within the ZnO lattice or become localised at grain boundaries forming clusters and/or Al sub-oxides in the film, leading to ZnO excessive lattice distortion and thus electrical conductivity deterioration [28, 152]. Therefore, a three-inch ceramic AZO target with this level of doping and 99.99% purity was ordered from Testbourne Ltd. and used throughout this work.

Following the AZO target loading into the sputtering chamber, the chamber was baked at 400°C for about two hours to remove any contaminations due to the chamber opening to the atmosphere for the AZO target loading, and to degas the chamber walls which helps to establish a good base pressure in the sputtering chamber. Target conditioning was performed three times for an hour each prior to AZO samples growth, in order to remove any surface contaminants. Low RF power (80-100 W) was used for this conditioning to avoid cracking the new AZO target.

Apart from the sputtering target material selection, the deposited film characteristics are also affected by the system design and the deposition parameters including, but not limited to, the oxygen to argon ratio, the applied RF power, and the sputtering pressure. Generally, the deposition parameters control the kinetic energy input of the sputtered particles and atoms that make up the deposited film. This in turn strongly modulates the surface mobility of the sputtered particles across the substrate's surface, the deposition rate, the chemical composition, and consequently the physical characteristics (microstructural, electrical, and optical) of the growing film. Altering one of the deposition parameters may result in enhancing a specific characteristic and simultaneously degrade another one [153, 154]. Therefore, the sputter-deposition parameters of AZO were investigated and optimised at room temperature based on the transparent electrodes requirements; namely high optical transmittance and electrical conductance. One deposition parameter was changed at a time, while the others were kept constant. Before investigating the deposition parameters, the substrate holder rotation was

optimised at 8 rpm in order to produce AZO coatings of an acceptable thickness uniformity. A thickness deviation as small as 5% was obtained across the 4-inch substrates used. The used UV grade fused silica substrates or microscope slides were cleaned to ensure effective adhesion of the deposited films to the substrates. The following cleaning approach was used:

1. The substrates were first immersed in Decon 90 surfactant solution in water (4% concentration by volume) for 2 hours to remove any dust attached to the substrate.
2. Then, the substrates were washed with deionised water, followed by sequential ultrasonic cleaning in acetone and methanol for 10 minutes each.
3. Finally, the substrates were individually dried with high-purity nitrogen gas.

Prior to the growths, a pumping period (12 hours) of the sputtering chamber was applied to ensure efficient substrate outgassing and a base pressure < $7.5\text{x}10^{-5}$ mTorr. The substrate-to-target distance was kept at 10 cm. The desired gas mixture was adjusted by partial pressure and introduced into the sputtering chamber via mass flow controllers to produce various oxygen to argon ratios. Then, to ignite the plasma the substrate is covered with a shutter, the chamber pressure is increased to 25 mTorr via closing the baffle valve, and an RF power of 40 W is applied. Once the plasma is established, the pressure is slowly reduced to the desired sputtering pressure. Concurrently, the RF power is increased in steps of 20 W to the desired RF power. A pre-sputtering on the substrate shutter for 10 min at the desired growth parameters was performed to remove any contamination from the target surface and stabilise the deposition parameters, which is necessary for reproducibility between consecutive growths. The substrate temperature during the deposition was monitored by using a thermo-label attached to the substrate and was cross checked with the sputtering chamber thermocouple measurements. The film thickness was monitored during the deposition using an in-situ interferometric monitor and was cross checked via Veeco Dektak Stylus profilometer measurements.

4.2.1 Oxygen to argon ratio optimisation

In oxide thin films sputter-deposition for TCOs and TSOs potential electronics applications, oxygen to argon ratio is a crucial parameter that has great influence on the electrical/optical characteristics trade-off, whereby higher oxygen to argon ratio typically improves the deposited thin film transmission, but dramatically degrades its conductivity. When oxide sputtering targets are used, the introduction of oxygen into the sputter-deposition process is typically applied at very low and precise concentrations to tune the deposited oxide thin film

stoichiometry [75, 155]. The introduction of oxygen is also crucial to enhance the resultant films' environmental stability as well as its stability against cracking and peeling off [156, 157].

To investigate the influence of oxygen to argon ratio in AZO films' electrical and optical properties, a series of growths was performed at a constant pressure and RF power, but various oxygen to argon ratios (0%, 0.2%, and 0.5 %). At this stage, the RF power and sputtering pressure are not yet optimised; thus, an RF power of 120 W, and a sputtering pressure of 2 mTorr were adopted based on literature review data [158-160].

4.2.2 The applied RF power and sputtering pressure optimisation

In sputter-deposition without applying external substrate heating, the main source of crystallisation and/or dopant activation energy for the deposited particles is the kinetic energy attained during sputtering. This energy is greatly influenced by the applied RF power in combination with the sputtering pressure [75, 153]. Hence, these two parameters were investigated via varying the RF power first, and then by varying the sputtering pressure, while all other parameters are fixed. Table 4-1 summaries the investigated AZO deposition parameters.

Investigated parameters	**Investigated range of parameters**		
	Sputtering Gases O_2 in Ar (%).	Applied RF Power (W)	Sputtering Pressure (mTorr)
Sputtering Gases	0, 0.2 and 0.5	120	2
Applied RF Power	0.2	(40-240) in steps of 20 W	2
Sputtering Pressure	0.2	180	1.5, 2.0, 3.0, and 5.0

Table 4-1. A summary of the investigated deposition parameters for AZO samples.

4.3 Sputter-deposition results and discussion

4.3.1 Growth rate[v]

Efficient sputtering of a specific material occurs at a certain threshold of energy for the incident sputtering gas ions that depends on the material's atomic number, binding energy, sublimation energy, and crystal structure [86, 154]. Since the sputtering ions energy is controlled by the deposition parameters applied, the growth rate is also influenced by the deposition parameters. For the investigated range of oxygen in argon concentrations no significant impact on the growth rate was noticed. However, the growth rate increased linearly as the RF power

[v] The growth rate is defined as the deposited thin film thickness per a unit time. The reported growth rate in this work is the averaged film thickness for three locations on the substrate, the central spot and the two sides, divided by the deposition time (nm/min).

increased, but almost saturated at RF power higher than 180 W, as illustrated in Fig. 4-1. The increase is due to increasing the electric field density between the electrodes, the argon ionisation, the argon ion energy, the target bombardments, and thus the sputtering yield [153, 161]. The noticed growth rate levelling off at higher RF powers (>180 W) could be attributed to increasing the argon ions' energy to excessive levels. Consequently, some of the argon ions become buried in the target material and thus most of their kinetic energy is transferred to target atoms far below the target surface causing the sputtering yield reduction. [86, 119]. In addition, it has previously been reported that negative oxygen ions from the sputtering target or potentially from the glow discharge, as well as reflected argon ions and/or argon atoms formed in sputter-deposition of oxide thin films can cause energetic bombardments and radiation damage to the resulting film in particular at low sputtering pressures [75, 162, 163]. Hence, since the sputtering pressure is rather low at 2 mTorr, it is expected that when the applied RF exceeds 180 W the growing film bombardments and radiation damage are becoming more pronounced leading to re-sputtering (etching) the film and thus resulting in the growth rate saturation [163, 164].

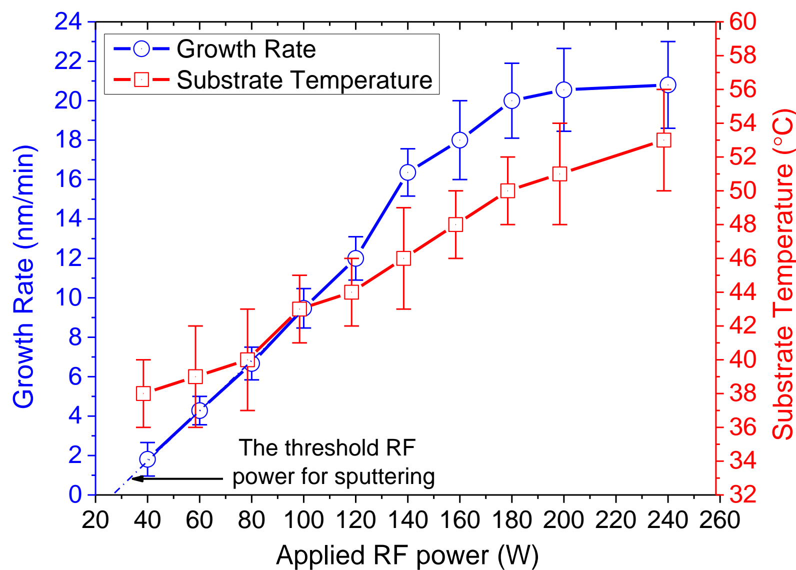

Fig. 4-1. Growth rate and substrate temperature versus RF power.

The growth rate saturation was also accompanied with a substrate temperature increase as shown in Fig. 4-1, which could be due to increasing the growing film bombardments by the energetic species. The substrate temperature increased as the applied RF power increased reaching a maximum of ~ 53°C at 240 W. A linear extrapolation of the growth rate plot to intercept

the RF power axis showed that the threshold RF power for the onset of sputtering from the employed AZO target is about 27 W.

Contrarily, the growth rate decreased with increasing the sputtering pressure; the reduction was rather small at the examined range of sputtering pressure, from about 20.30 nm/min at 1.5 mTorr to 18.50 nm/min at 5 mTorr. This behaviour is due to decreasing the mean free path of the sputtered species and increasing their frequent collisions with the background sputtering gas ions. Consequently, less sputtered particles and atoms could approach the substrate and contribute to the thin film growth. Also, the argon ion energy is reduced at higher sputtering pressure due to the intensified collisions resulting in decreasing the target bombardments and therefore reducing the sputtering yield and the growth rate [153, 161]. It is important to note that the optimised deposition parameters concluded in this research demonstrate a relatively high growth rate of 20 nm/min.

4.3.2 Influence of oxygen to argon ratio on the AZO microstructure characteristics

The wide XRD spectra collected in θ–2θ mode and for a range of 2θ angles of 10° to 80° for AZO samples of different deposition parameters showed two clear crystalline peaks at 2θ values of (34.39°± 0.02°), and (72.50°± 0.02°) corresponding to the (002) and (004) planes of hexagonal wurtzite structure of ZnO respectively. The doping with aluminium caused no extra detectable peaks for aluminium or its oxides such as Al_2O_3 and Al_2O_4. This is because the level of doping for AZO films was too small (~ 2 at% obtained by XPS.) [165, 166]. High-resolution XRD spectra for the examined samples in the diffraction angle window 33° to 38° demonstrated a strong peak at (34.39°± 0.02°) corresponding to the (002) plane of hexagonal wurtzite crystal structure of ZnO, revealing that the AZO grains exhibit a preferred orientation growth along the (002) plane of ZnO parallel to the substrate surface, with their crystallographic c-axis normal to the substrate plane. The observed (002) peak position is close to that for strain-free ZnO samples (34.42°) indicating high-quality AZO thin films [13].The high-resolution XRD data for the AZO samples was studied via performing Voigt-function analysis to separate the grain size and lattice strain contributions to the XRD peak broadening, following the approach of De Keijser et al. [135].

In regard to AZO samples deposited at different oxygen to argon ratio, small changes in the average grain size and lattice strain were observed as illustrated in Fig. 4-2. The films residual

stress estimated by the biaxial strain mode showed a change from compressive to tensile stress and the diffraction angle approached a value close to that of unstrained ZnO when the oxygen ratio increased to 0.5%. At the other end, sputtering in pure argon results in higher stress which could be due to lack of oxygen atoms and thus higher density of native point defects (oxygen vacancies) in the resulting film. Similar observations are reported in the literature [156, 158].

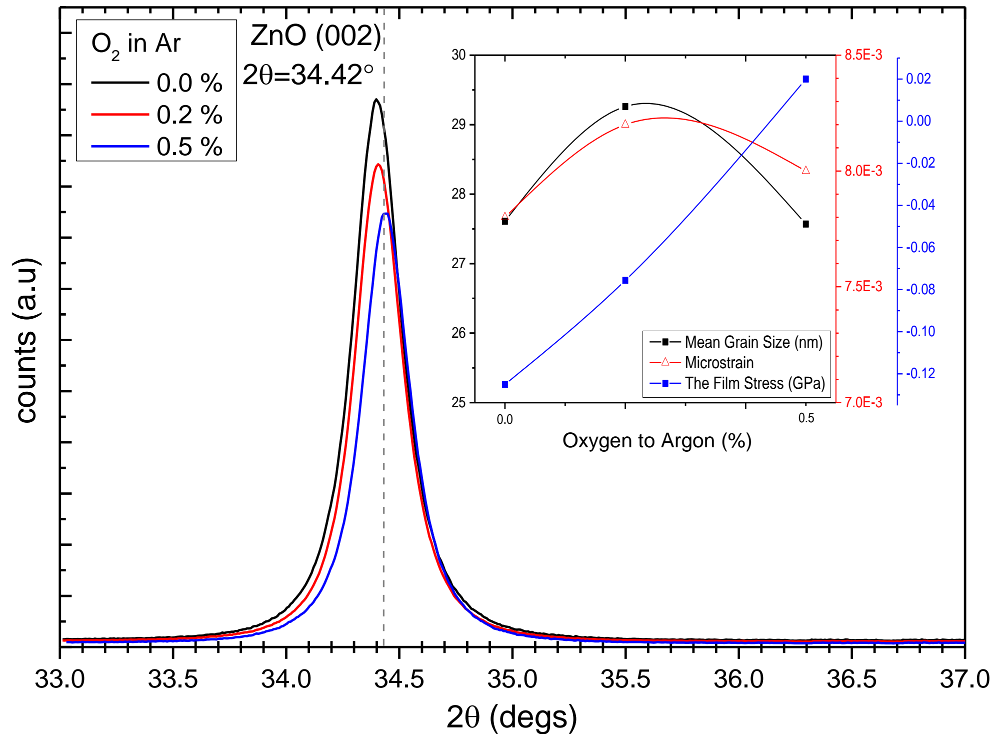

Fig. 4-2. High-resolution XRD spectra for AZO samples as a function of the oxygen to argon ratio, deposited at RT, 120 W, and 2 mTorr. The inset graph shows the results of Voigt-function analysis.

4.3.3 Influence of oxygen to argon ratio on the AZO conductivity and transparency

Electrical characterisation of the deposited AZO at various conditions showed that their electrical properties are profoundly governed by the applied deposition parameters. Resistivity measurements via both 4PP and VDP techniques employed here showed good agreement with the variations between the two techniques being very minor for highly conductive samples.

As the oxygen to argon concentration was increased from 0% to 0.5%, the resistivity noticeably increased form 1.25×10^{-3} to 4.15×10^{-3} Ω.cm due to degradation of both the free carrier density and Hall mobility as depicted in Fig. 4-3. This is attributed to increasing the adsorbed oxygen atoms to the resultant film grain boundaries as the oxygen concentration was increased, causing trapping of the free electrons and a simultaneous degradation of the free carrier mobility via increasing the potential barriers between the grains [158]. Oxygen vacancies are widely

discussed to act as intrinsic donors in metal oxides; thus, higher oxygen concentrations reduce the free carrier density via oxygen vacancies compensation [75, 158]. It is widely reported that for most TCOs at free carrier densities below 2×10^{20} cm^{-3}, the grain boundaries scattering is the dominant scattering mechanism that limits the carrier mobility [39, 40]. Looking at the reported free carrier density and mobility for the above set of AZO samples, it could be concluded that the mobility is limited by grain boundaries scattering for AZO samples deposited at 0.5% oxygen to argon ratio, which is directly linked to the adsorbed oxygen atoms at grain boundaries during the growth process. Furthermore, the negligible changes in the average grain size for the AZO samples of different oxygen ratio implies that the observed Hall mobility reduction is due to adsorbed oxygen defects at grain boundaries. Regarding the films optical transmission, sputtering in pure argon resulted in clear optical transparency degradation. The optical transmission for the AZO samples sputtered in pure argon is 83% at 550 nm compared to 88% for those deposited at 0.5% oxygen to argon ratio. This could be due to better oxidisation chances for the sputtered atoms when oxygen is introduced to the sputter-deposition process [75, 158]. Based on these observed trends, the series of AZO films for the applied RF power and the sputtering pressure investigations were deposited at 0.2% oxygen to argon ratio.

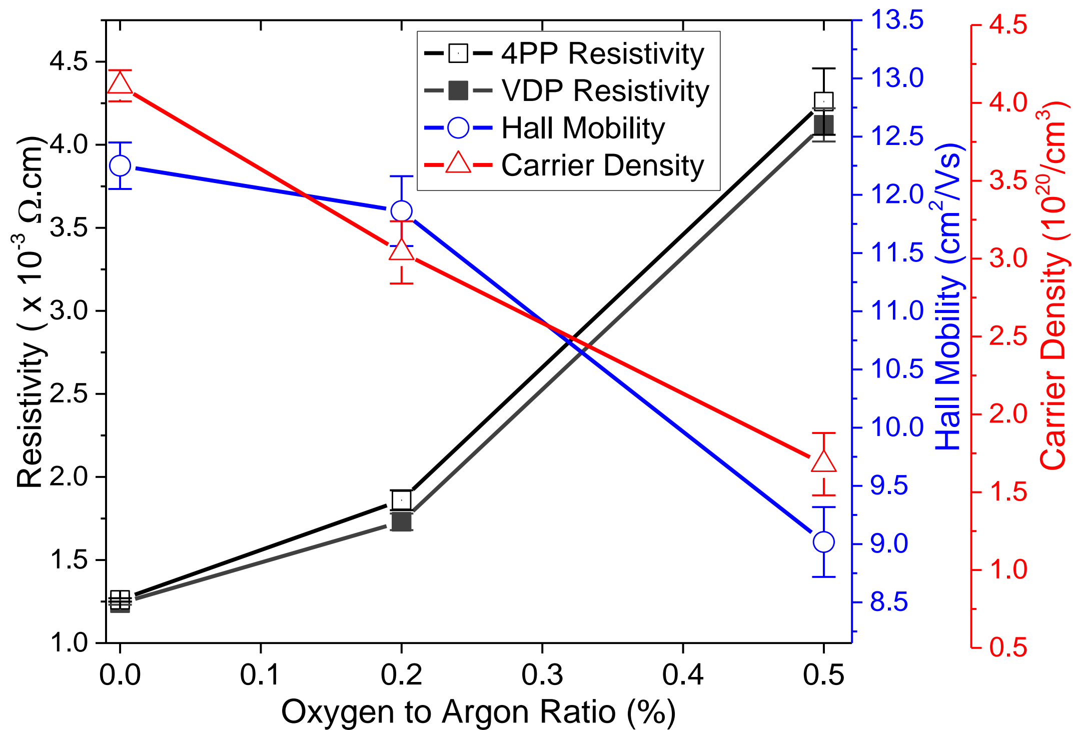

Fig. 4-3. The electrical characteristics (ρ, μ, and N) for AZO as a function of the oxygen to argon ratio, deposited at RT, 120 W, and 2 mTorr.

4.3.4 Influence of the RF power on the AZO microstructure characteristics

Fig. 4-4 illustrates the high-resolution XRD data for AZO films deposited at an RF power of 120, 160, 180, and 200 W, and a pressure of 2 mTorr. The ZnO (002) peak intensity increased as the RF power was increased, which indicates an enhancement of the preferred orientation and reduced microstructural defects [160, 167].

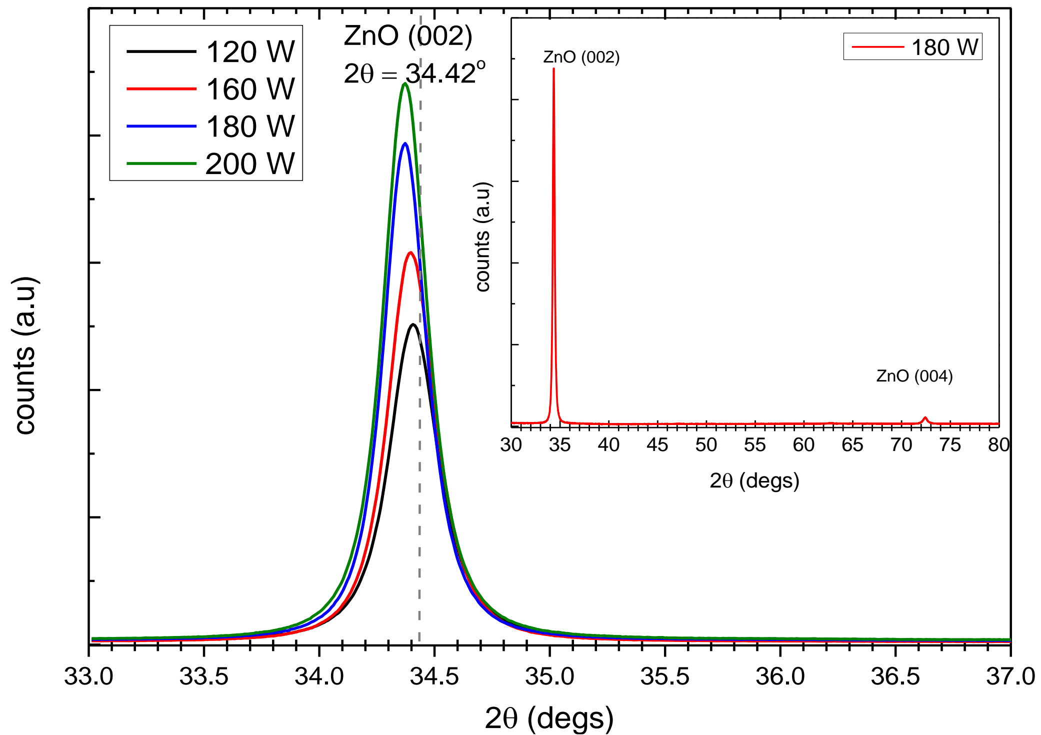

Fig. 4-4. High-resolution XRD spectra for AZO as a function of the applied RF power, deposited at RT, 2 mTorr, and 0.2% O_2 in Ar %. The inset graph is the wide scan for the optimised AZO.

XRD data analysis via Voigt-function were performed on these samples. The mean grain size increased from 29.20 nm to 35.00 nm with increasing the applied RF power, as shown in Fig. 4-5. This is attributed to increasing the sputtered atoms' kinetic energy and their surface mobility across the substrate as the applied RF power increased. Therefore, the atoms will align themselves in a better crystal structure forming bigger grains with reduced grain boundaries density and defects within the grains. At RF power higher than 180 W, however, a marginal reduction in the grain size was observed, which is accompanied with the growth rate levelling off as seen in Fig. 4-1. These trends could indicate that the energy of the sputtered atoms becomes redundant and hinders the grains growth at higher RF powers than 180 W. Regarding the lattice strain, all the examined AZO samples of different RF power as well as sputtering pressure demonstrated compressive stress, which results in creating a strain (macro and micro) in the

lattice. The compressive stress (stress values <0), calculated by the biaxial strain model, is typically observed for sputter-deposited thin films whenever highly energetic species are involved. This is attributed to bombardments of the deposited film by the energetic sputtered species leading to closely packed surface atoms implanting each other into the film, which is known as the atomic peening effect [75, 131]. Fig. 4-5 and Fig. 4-7 show that all the AZO samples exhibit longer inter-planar spacing distances and thus smaller diffraction angles compared to unstrained zinc oxide. These variations became more pronounced as the applied RF power is increased or the sputtering pressure is reduced due to the induced compressive stress by more energetic species bombardments on the deposited film at these conditions [28, 159].

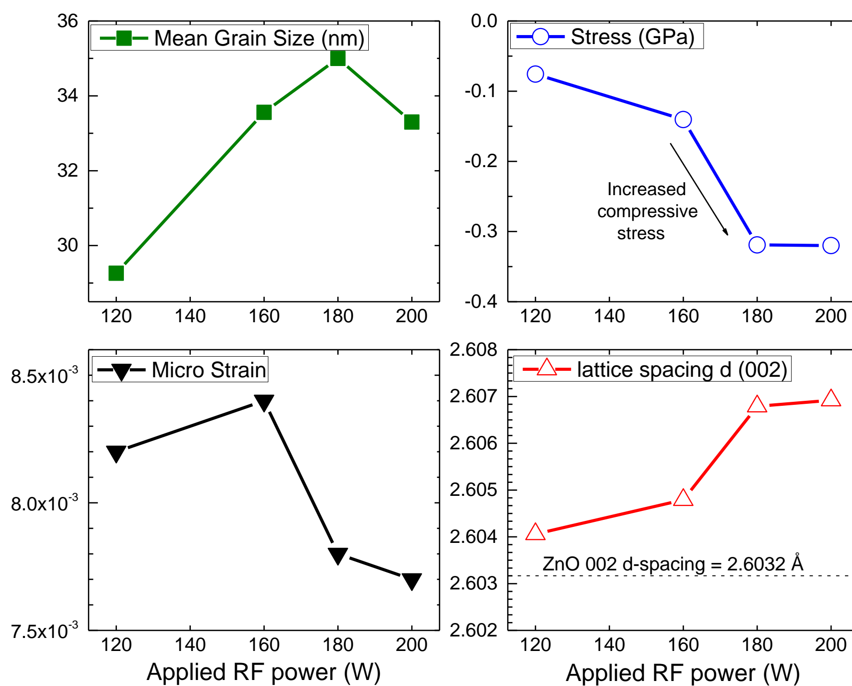

Fig. 4-5. XRD data analysis for AZO as a function of the applied RF power, deposited at RT, 2 mTorr, and 0.2% O_2 to Ar %.

4.3.5 Influence of the sputtering pressure on the AZO microstructure characteristics

The evolution of AZO microstructure characteristics with the sputtering pressure demonstrate opposite trends to those observed with the applied RF power. Fig. 4-6 compares the high-resolution XRD patterns for AZO samples deposited at various sputtering pressure values (1.5, 2.0, 3.0, and 5.0 mTorr), and an applied RF power of 180 W. As the sputtering pressure was increased, the ZnO (002) peak intensity was decreased. XRD data analysis using Voigt-function revealed that the average grain size decreased from 33.85 to 29.00 nm, and the micro strain increased as shown in Fig 4-7. These trends are linked to intensified collisions between the

sputtered species and the sputtering gas particles at higher pressure resulting in lower kinetic energy and insufficient surface mobility for the sputtered species on the substrate. Consequently, the deposited films are highly defective with smaller grains, higher grain boundary density, and larger micro strain [158, 168].

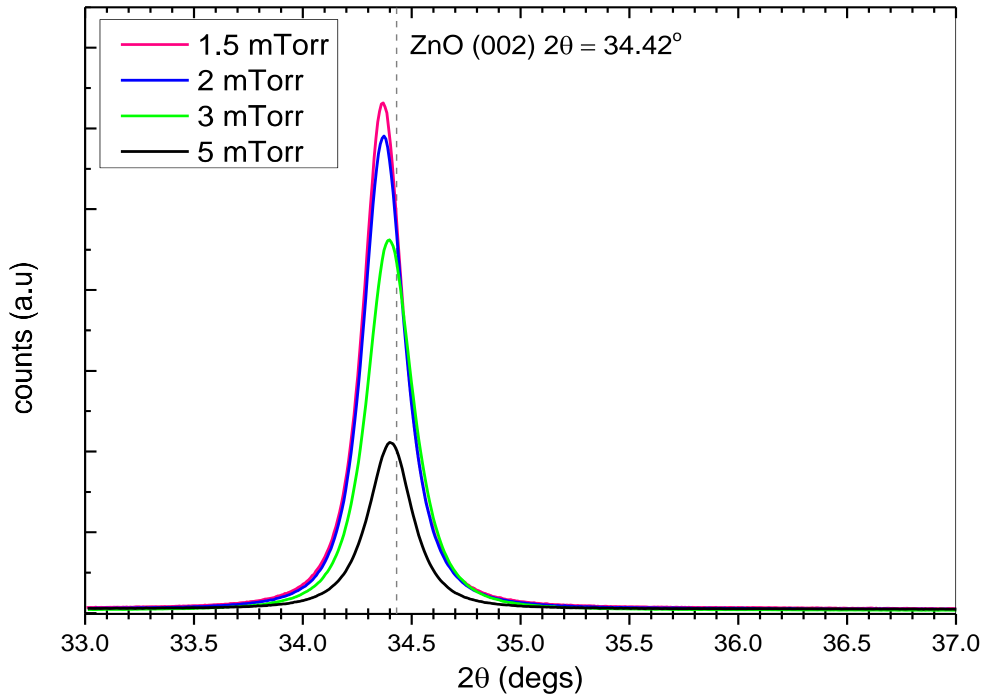

Fig. 4-6. High-resolution XRD spectra for AZO samples as a function of the deposition pressure, deposited at RT, 180 W, and 0.2% O_2 to Ar %.

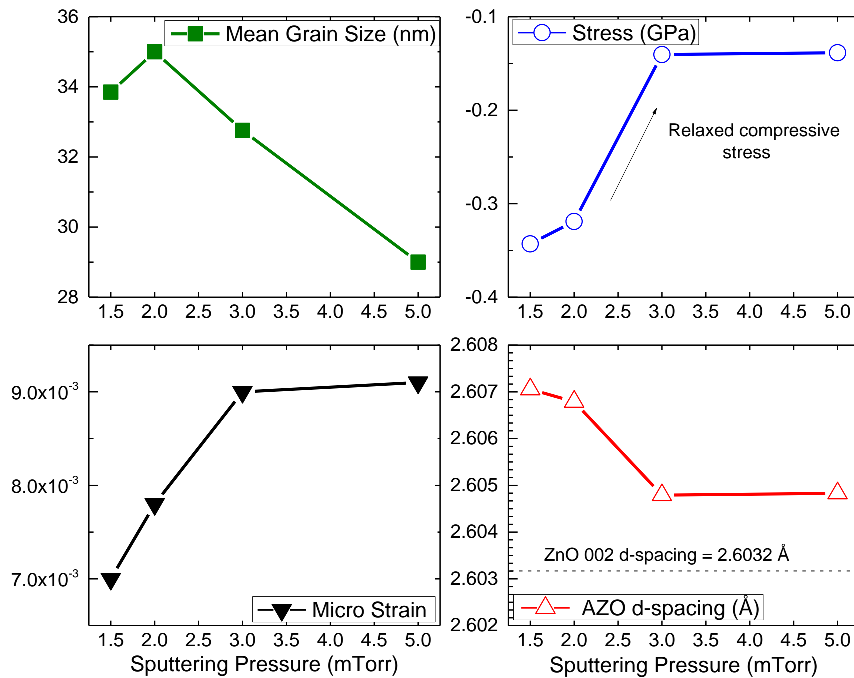

Fig. 4-7. XRD data analysis for AZO samples as a function of the deposition pressure, deposited at RT, 180 W, and 0.2% O_2 to Ar %.

4.3.6 Influence of the RF power on the AZO stoichiometry

In spite of the abundance of many investigations aimed at optimising the fabrication conditions of AZO, there is limited work reported on the correlation between AZO stoichiometry and electrical characteristics. This section presents detailed XPS analysis aimed at studying the deposition parameters effect on AZO stoichiometry ratio and the chemical states of the constituent elements. The observed trends are linked to the AZO electrical properties discussed in the next sections. XPS measurement details are presented chapter 3, section 3.7.2.

Fig. 4-8 demonstrates the wide XPS spectra for an AZO thin film deposited at the optimised conditions (180 nm thick, 180 W, and 2 mTorr of 0.2% O_2 in Ar) before and after 1-min etching by Ar^+ ion sputtering (estimated to have removed about 10 nm of surface layer).

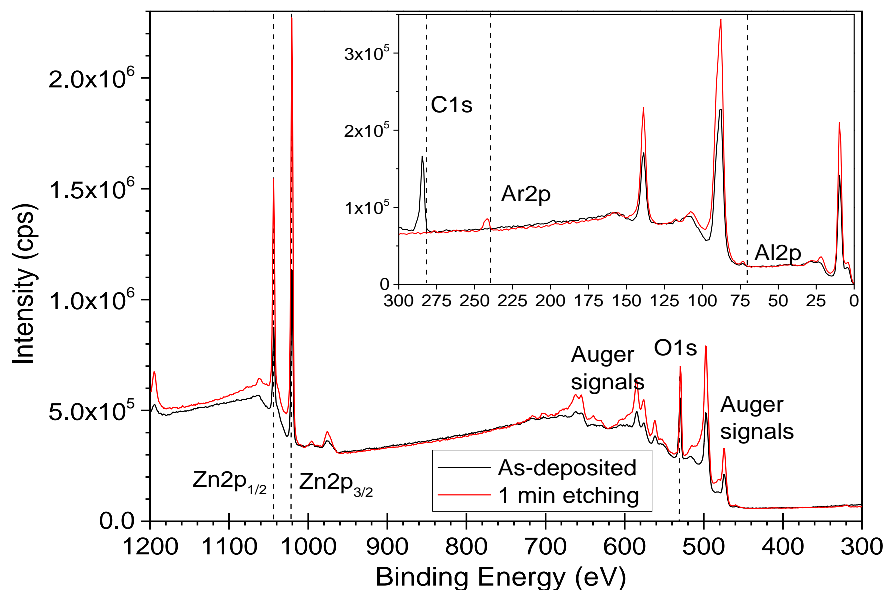

Fig. 4-8 . Wide XPS spectra of the optimised as-deposited AZO thin film before and after Ar etching.

The XPS peaks for Zn2p, O1s, C1s, Ar2p, and Al2p are observed. It can be seen that after argon etching, the C1s peak at ~ 285 eV disappeared, indicating carbon contaminations removal. These contaminations are inevitably created at the sample surface due to air exposure before the XPS measurements [165, 169]. Aluminium was detected in the wide-scans, but the detected signal is very small due to the rather low concentration of aluminium in the film and due to the low ionisation probability of aluminium [165, 169]. For detailed XPS investigations, high-resolution XPS spectra were collected before and after Ar etching. The Zn2p and Al2p spectra (not shown here) demonstrate negligible changes after etching. While, the O1s spectrum showed noticeable changes after etching as depicted in Fig.4-9.

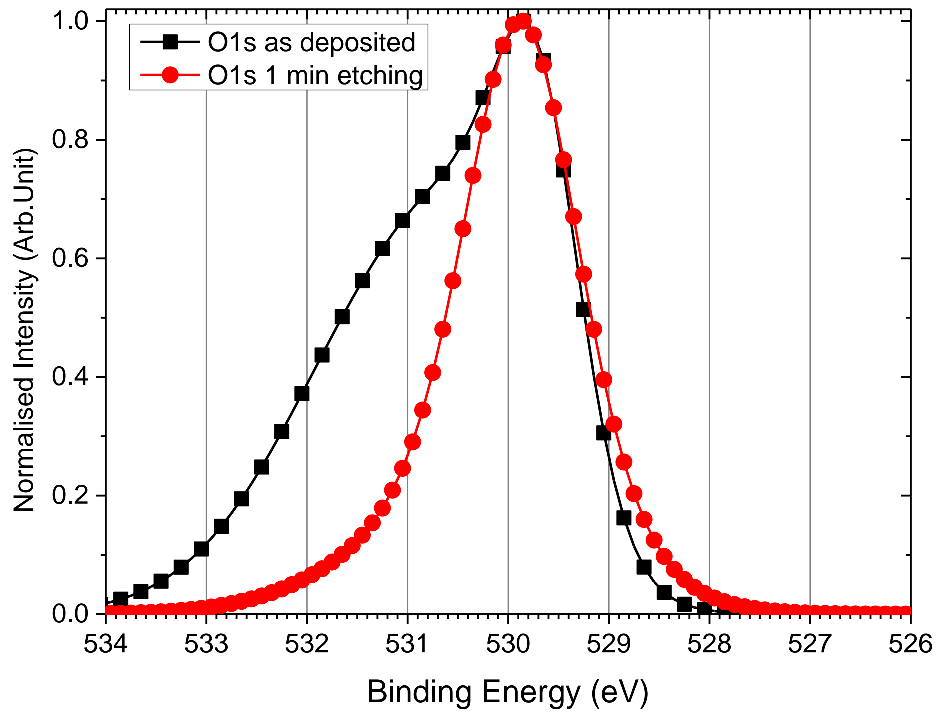

Fig. 4-9. High resolution O1s XPS spectra for the optimised as-deposited AZO before and after Ar etching.

The O1s XPS spectra for the examined AZO samples were fitted into two sub-spectral components of Gaussian-Lorentzian (GL-30) line shape and are positioned at binding energies as follows:

1. O1s(I) at 530.0 ± 0.1 eV: is attributed to the oxygen ions O^{-2} in the hexagonal wurtzite structure of ZnO, fully surrounded by Zn^{+2} cations or the substitutional Al^{+3} cations, i.e. the lattice oxygen.
2. O1s(II) at 531.3 ± 0.1 eV: is linked to the presence of loosely bound oxygen ions belonging to chemisorbed oxygen atoms, hydroxides, or possibly carbonates at the samples' surface and/or grain boundaries [165, 169, 170].

With regard to the second component, higher binding energy in the O1s spectra for ZnO films has been also reported to originate from oxygen ions O^{-2} in the oxygen deficient regions within the ZnO matrix [165, 166, 169]. In this work, however, due to the employed etching procedure for the samples' cleaning, oxygen preferential sputtering will be induced leading to altering the intrinsic oxygen deficiency for the AZO samples. Also, core holes created in the photoelectron emission from oxygen atoms will be screened by electrons from the surrounding zinc atoms leading to higher binding energy relative to the main line (530 eV) in the O1s spectra [171].

It can be seen that the O1s spectrum after Ar-etching exhibited a relatively higher symmetry compared to that for the as-deposited sample due to a reduction of the spectrum at higher binding energy. This indicates reduced adsorbates (oxygen atoms, hydroxides, and carbonates), as well as enhanced ZnO stoichiometry upon Ar-etching. Similar observations have been reported elsewhere [165, 169].

It is well-known that the stoichiometry of oxide films is controlled with their growth process, which in turn is directly linked to the deposition conditions. High-resolution XPS spectra for AZO films of different deposition conditions were collected before and after Ar etching. It was revealed that all the examined AZO films are non-stoichiometric with Zn-rich compositions. No changes were observed among the Zn2p XPS spectra for AZO films of different growth conditions. The O1s and Al2p XPS spectra, which are directly correlated to the films' electrical characteristics [28, 30], were studied in detail. The relative atomic concentrations of (Zinc, Oxygen, and Aluminium) as a function of the RF power are demonstrated in Fig.4-10. It was observed that the atomic concentration of aluminium in the AZO films increases as the applied RF power is increased. This could be attributed to the Al atoms/ions being more reactive and hence more effectively incorporated into the deposited AZO film, due to gaining higher kinetic energy at higher RF power.

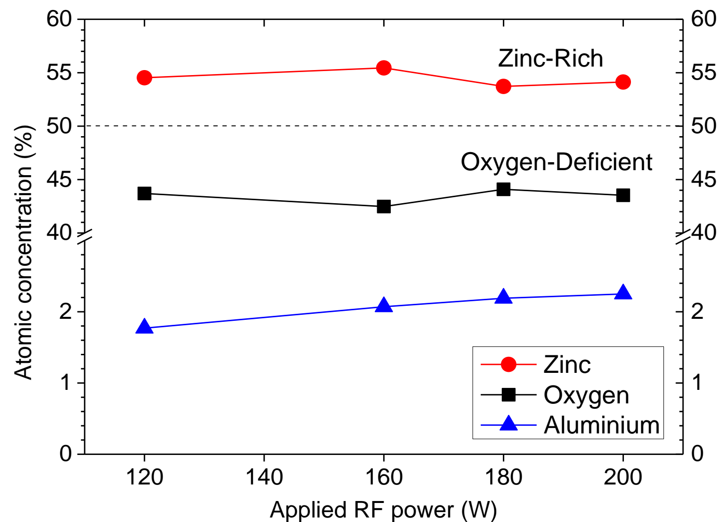

Fig. 4-10. The relative atomic concentration values for Zinc, Oxygen, and Aluminium obtained from the XPS measurements as a function of the applied RF power.

Fig. 4-11 compares high resolution XPS O1s spectra for AZO samples deposited at different RF power values, and a sputtering pressure of 2.0 mTorr of 0.2% oxygen to argon ratio. The obtained spectra were fitted into two distinct peaks each based on the discussion presented above; the details of the fitted peaks are presented in Table 4-2.

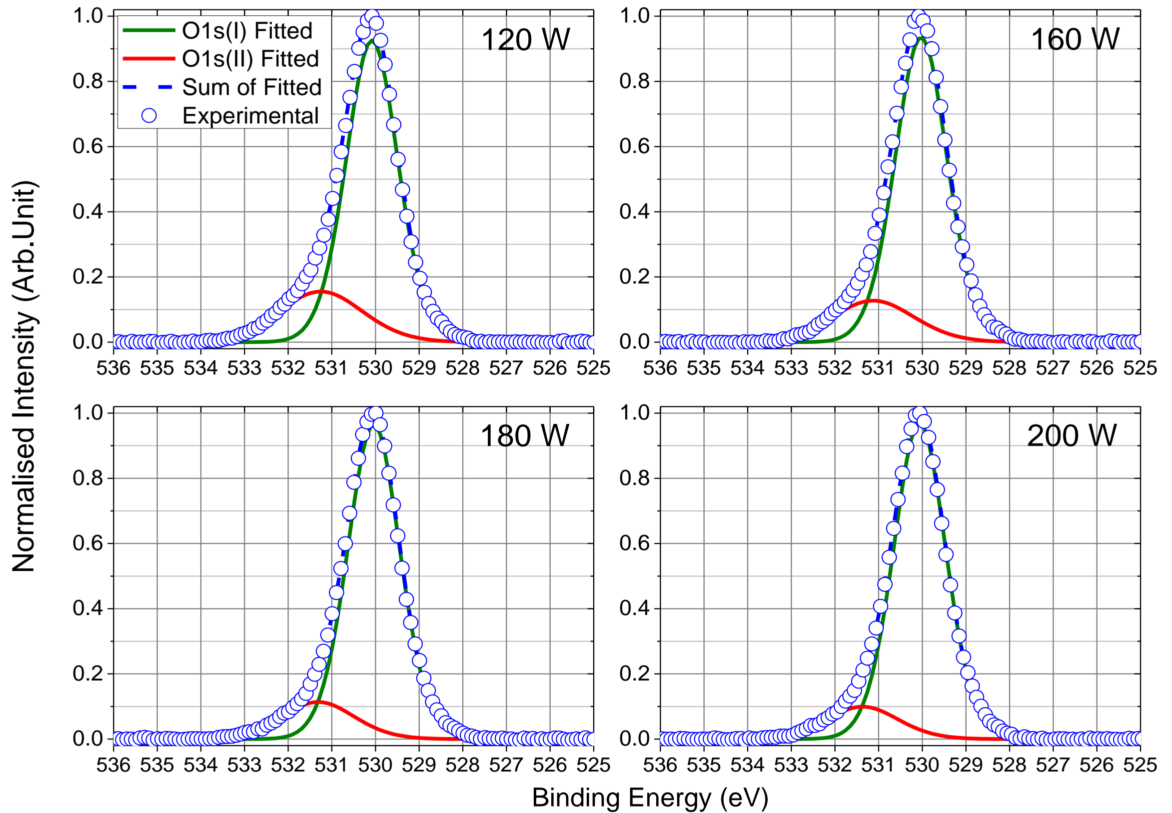

Fig. 4-11. High resolution O1s XPS spectra of AZO films deposited at different RF power fitted into two peaks.

RF power (W)	O1s(I)			O1s(II)		
	Peak at (eV)	FWHM (eV)	Area Ratio (%)	Peak at (eV)	FWHM (eV)	Area Ratio (%)
120	530.1	1.38	78.7	531.3	2.21	21.3
160	530.0	1.38	82.3	531.2	2.20	17.7
180	530.0	1.38	86.0	531.3	1.95	14.0
200	530.0	1.38	87.6	531.3	1.95	12.4

Table 4-2. Details of the fitted peaks for O1s XPS spectra of AZO films deposited at different RF power.

As the RF power was increased, the component for oxygen ions in the ZnO lattice O1s(I) is increased revealing less intrinsic point defects such as oxygen vacancies, i.e. better ZnO stoichiometry and crystal structure properties. This was also confirmed with the XRD results in section 4.3.4. At the same time, the component at the higher binding energy O1s(II) is reduced, indicating less adsorbates including oxygen atoms, hydroxides, and carbonates. This can be explained as a consequence of enhancing the sputtered atoms' kinetic energy and thus their surface mobility across the substrate surface due to the higher RF power. Therefore, the atoms will align themselves in a better crystal structure and form more compact films with reduced spatial gaps (voids) and grain boundary density, as discussed in the XRD data and confirmed by the AFM images in Fig. 4-12. As a result, less oxygen atoms, hydroxides, and carbonates are

adsorbed into the film, since the voids and grain boundaries are the preferred paths for the adsorbates to diffuse into a thin film [169, 172].

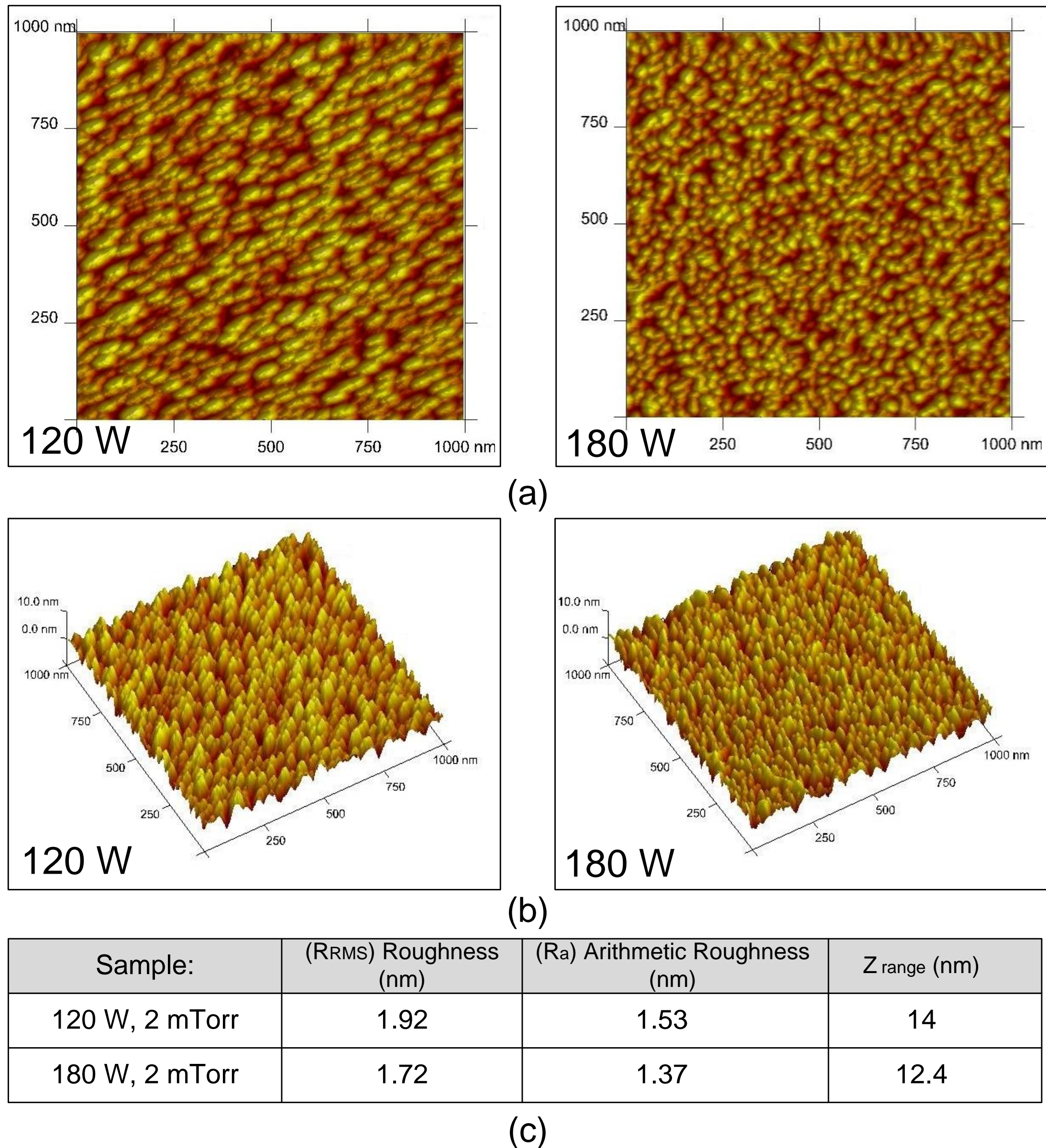

Sample:	(R_{RMS}) Roughness (nm)	(R_a) Arithmetic Roughness (nm)	Z_{range} (nm)
120 W, 2 mTorr	1.92	1.53	14
180 W, 2 mTorr	1.72	1.37	12.4

Fig. 4-12. (a) AFM plan view images, (b) 3-D images, and (c) roughness details, for AZO samples deposited at different RF power

Fig. 4-13 shows the high-resolution XPS data of Al2p for the AZO samples of different RF power. The collected Al2p spectra are centred at intermediate binding energy values (73.90 ± 0.05 eV) with respect to that for Al metal (72.60± 0.05 eV) and for Al in Al_2O_3 (74.60 ± 0.05 eV), this may indicate an oxygen-deficient ZnO lattice. The Al2P XPS spectra for all the as-deposited AZO samples could not be fitted to a single doublet indicating that the Al atoms present in the samples have more than one chemical states. This is because all the AZO samples were deposited without intentional substrate heating, whereby not all the Al atoms are effectively

incorporated into the zinc oxide lattice due to limited energy for the Al atoms to replace the zinc atoms at room temperature deposition [165, 173]. The non-activated Al atoms could be as interstitials within the ZnO lattice or probably segregated at non crystalline regions, such as grain boundaries [85, 165]. Based on this, the Al2p spectra for the as-deposited AZO films were fitted into two doublets i.e. two chemical states (Al(I) and Al(II)), each of which have two peaks of GL(30) line shape corresponding to $2p_{3/2}$ and $2p_{1/2}$ doublet. The chemical states assigned to the aluminium atoms those are activated into ZnO matrix (Al(I) at higher binding energy), and for non-activated Al atoms (Al(II) at lower binding energy). The details of the fitted peaks are presented in Table 4-3. The ratio of the areas under the fitted peaks for the two chemical states to the overall peak for Al2p spectrum is used to estimate the ratio of Al atoms in each chemical state. All the examined AZO samples have ~ 60% of the contained aluminium atomic ratio is activated, while ~40% is non-activated.

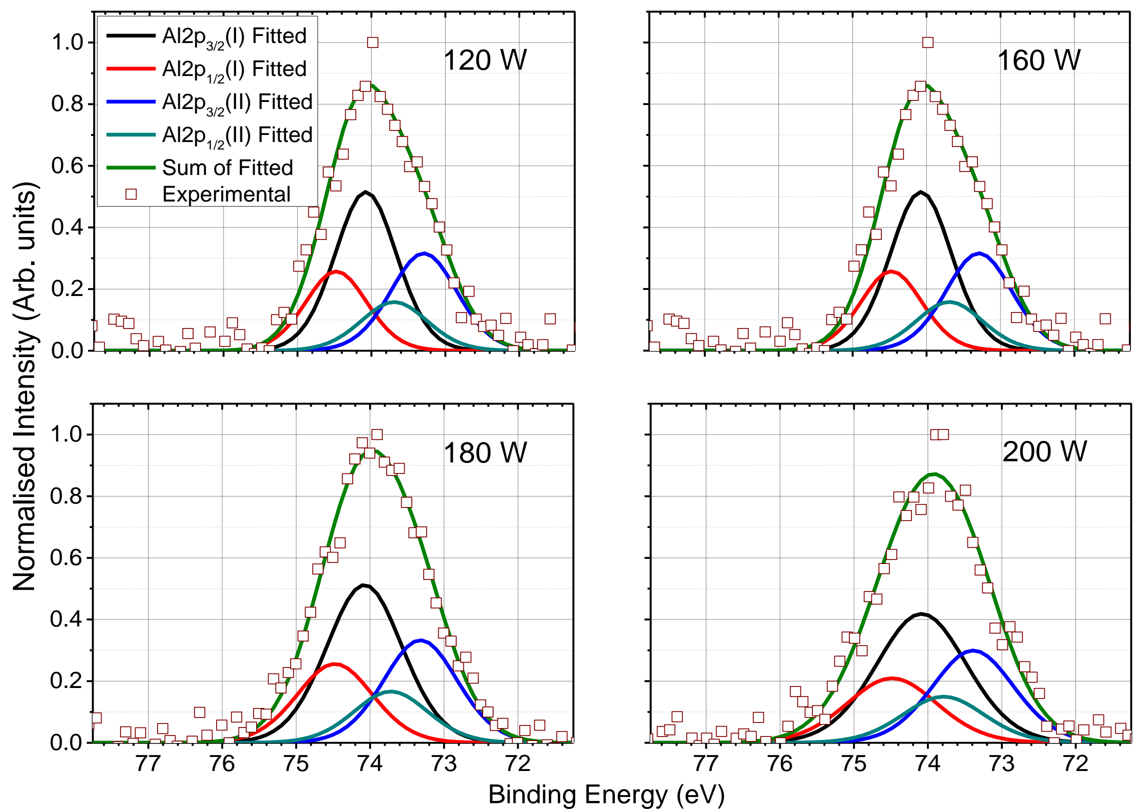

Fig. 4-13. High resolution XPS spectra of Al2p in AZO films deposited at different RF power and fitted into two chemical states.

RF power (W)	XPS peak	Total		Activated Al(I)			Non- Activated Al(II)		
		Peak at (eV)	FWHM (eV)	Peak at (eV)	FWHM (eV)	Area Ratio (%)	Peak at (eV)	FWHM (eV)	Area Ratio (%)
120	$2p_{3/2}$	73.9	1.54	74.1	0.98	40.00	73.3	1.06	26.60
	$2p_{1/2}$			74.5	0.98	20.00	73.7	1.06	13.35
160	$2p_{3/2}$	73.9	1.54	74.1	0.98	40.10	73.3	1.06	26.50
	$2p_{1/2}$			74.5	0.98	20.00	73.7	1.06	13.30
180	$2p_{3/2}$	73.9	1.68	74.1	1.20	40.40	73.4	1.18	26.10
	$2p_{1/2}$			74.5	1.20	20.20	73.8	1.18	13.00
200	$2p_{3/2}$	73.9	1.75	74.1	1.44	40.40	73.4	1.31	26.20
	$2p_{1/2}$			74.5	1.44	20.20	73.8	1.31	13.10

Table 4-3 Details of the fitted peaks for Al2p XPS spectra of AZO films deposited at different RF power.

4.3.7 Influence of the sputtering pressure on the AZO stoichiometry

XPS measurements for AZO samples deposited at 180 W and at varying sputtering pressure revealed that sputtering pressure has minor influences on the relative atomic concentration values for the constituent elements. Similar to the observed trends in the XRD data explained earlier, the sputtering pressure was found to have an opposite effect on the obtained O1s XPS data compared to that observed at different RF powers. For instance, the O1s(II) component that belongs to adsorbates (oxygen atoms, hydroxides, and carbonates) was found to increase as the sputtering pressure was increased, as shown in Fig. 4-14 and Table 4-4.

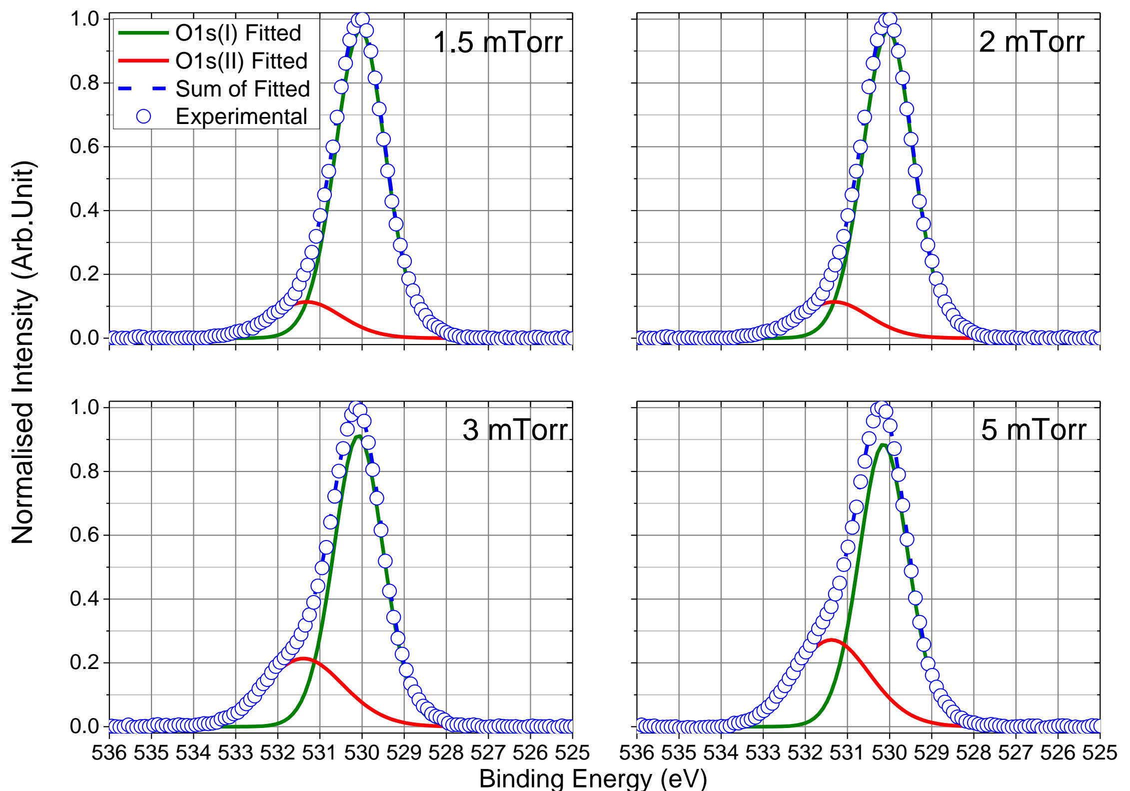

Fig. 4-14. High resolution O1s XPS spectra of AZO films deposited at different sputtering pressure fitted into two peaks.

Sputtering pressure (mTorr)	O1s(I)			O1s(II)		
	Peak at (eV)	FWHM (eV)	Area Ratio (%)	Peak at (eV)	FWHM (eV)	Area Ratio (%)
1.5	530.0	1.38	86.0	531.3	1.95	14.0
2	530.0	1.38	86.0	531.3	1.95	14.0
3	530.1	1.36	72.5	531.3	2.21	27.5
5	530.1	1.36	67.6	531.3	2.15	32.4

Table 4-4. Details of the fitted peaks for O1s XPS spectra of AZO deposited at different sputtering pressure.

This above observation is attributed to the deteriorated surface mobility of the sputtered atoms across the substrate surface at higher sputtering pressure, resulting in creating microstructure defects, as confirmed with the XRD data, and voids, reducing the resulting film compactness. AFM images presented in Fig. 4-15 showed that increasing the sputtering pressure from 2 to 5 mTorr results in less packed surface particles with more voids in between. The AFM images showed also an increase in the surface roughness at higher pressure, the Root Mean Square (R_{RMS}) roughness increased from 1.72 nm to 2.52 nm. After Igasaki and Kanma [168], increasing the surface roughness would indicate larger effective surface area for the film, which can be seen by the noticed Z_{range} roughness increased from 12.4 to 20.3 nm. Hence, the chemisorbed oxygen related defects to the film would be increased through the observed voids and the larger surface area of the film.

The observed microstructure and morphological characteristics evolution with increasing the pressure is in agreement with the structure zone model developed by Thornton to correlate the microstructure and morphology properties of sputtered films with both the substrate temperature and the sputtering pressure [174]. As shown in Fig. 4-16 increasing the sputtering pressure changes the microstructure and morphological characteristics of the resulting film from densely packed fibrous grains to tapered grains with separation voids which was confirmed by the AFM images in Fig. 4-15.

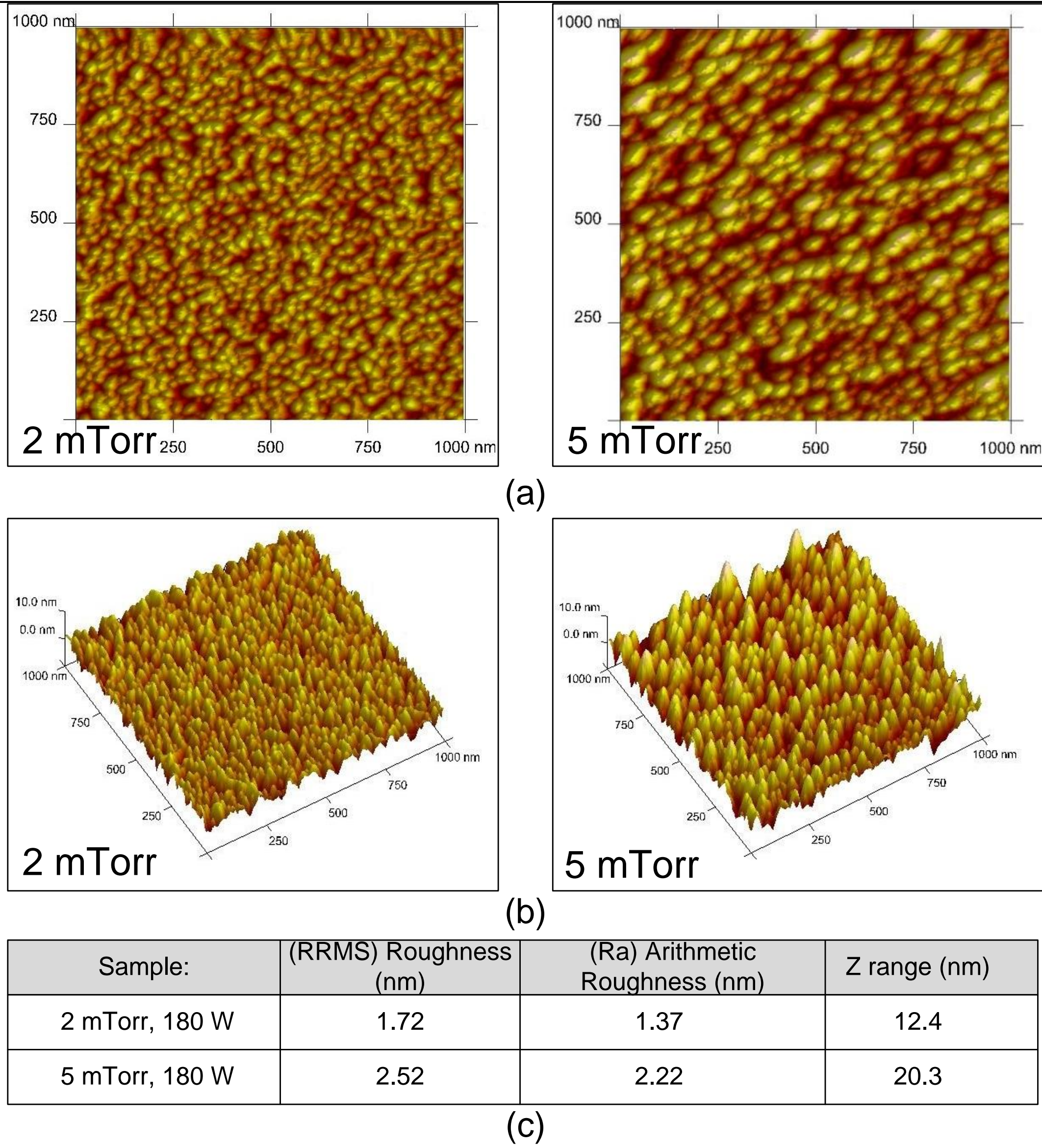

Sample:	(RRMS) Roughness (nm)	(Ra) Arithmetic Roughness (nm)	Z range (nm)
2 mTorr, 180 W	1.72	1.37	12.4
5 mTorr, 180 W	2.52	2.22	20.3

Fig. 4-15. (a) AFM plan view images, (b) 3-D images, and roughness details, and (c) for AZO samples deposited at different sputtering pressure.

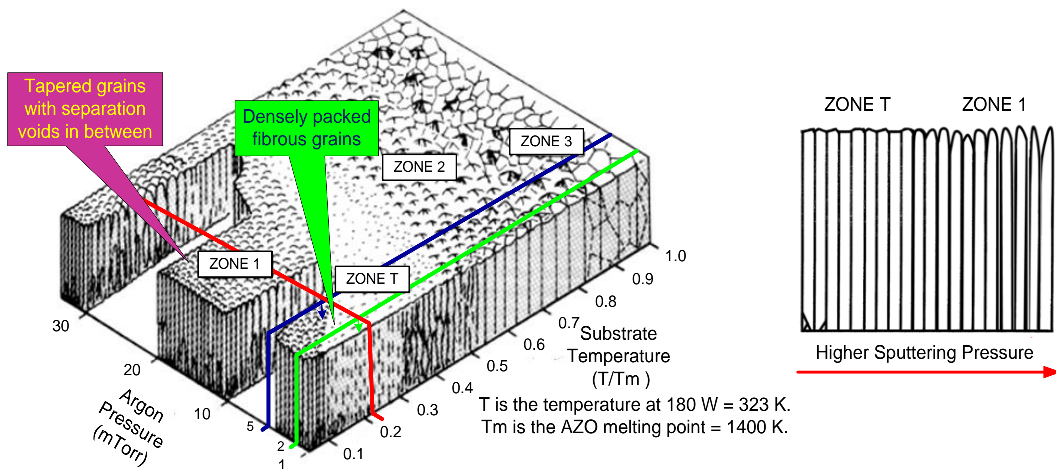

Fig. 4-16. Schematic representation of Thornton structure zone model [174] to linking the deposited film microstructural properties to the substrate temperature and sputtering pressure.

High-resolution XPS spectra for Al2p collected from AZO films of different pressure were fitted to two chemical states of two GL(30) peaks each corresponding to aluminium $2p_{3/2}$ and $2p_{1/2}$ doublets for the activated and non-activated Al similar to the RF power samples.

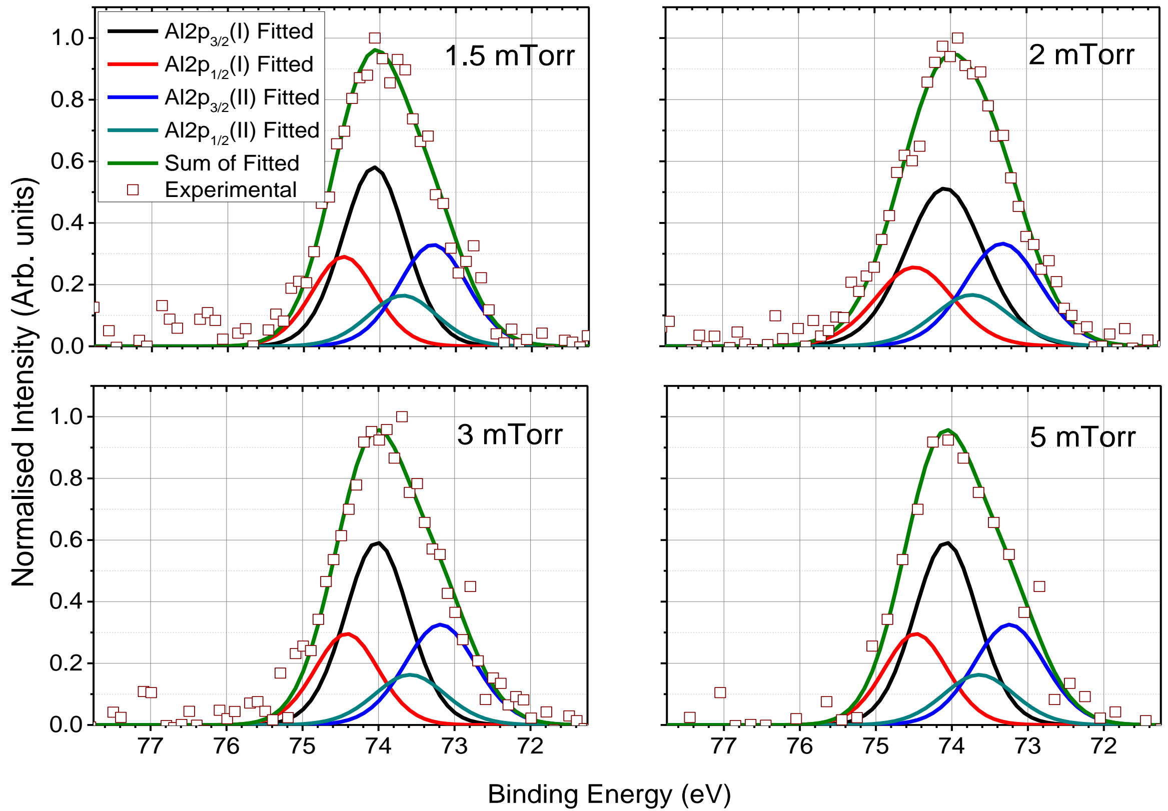

Fig. 4-17. High resolution XPS spectra of Al2p in AZO films deposited at different sputtering pressure and fitted into two chemical states.

Pressure mTorr	XPS peak	Total		Activated Al (I)			Non- Activated Al (II)		
		Peak at (eV)	FWHM (eV)	Peak at (eV)	FWHM (eV)	Area Ratio (%)	Peak at (eV)	FWHM (eV)	Area Ratio (%)
1.5	$2p_{3/2}$	73.9	1.50	74.1	0.98	41.20	73.3	1.07	25.50
	$2p_{1/2}$			74.5	0.98	20.60	73.7	1.07	12.60
2	$2p_{3/2}$	73.9	1.68	74.1	1.20	40.40	73.4	1.18	26.10
	$2p_{1/2}$			74.5	1.20	20.20	73.8	1.18	13.00
3	$2p_{3/2}$	73.9	1.55	74.1	1.00	41.30	73.3	1.11	25.40
	$2p_{1/2}$			74.5	1.11	20.60	73.7	1.11	12.70
5	$2p_{3/2}$	73.9	1.55	74.0	1.00	40.80	73.2	1.11	25.30
	$2p_{1/2}$			74.4	1.00	20.40	73.6	1.11	12.80

Table 4-5. Details of the fitted peaks for Al2p XPS spectra of AZO films deposited at different sputtering pressure.

4.3.8 Influence of the RF power on the AZO electrical properties

Fig. 4-18 demonstrated that as the RF power is increased, the free carrier density (N) and Hall mobility (μ) are increased and hence the electrical resistivity (ρ) is reduced from a maximum value of 1.10x10^{-2} Ω.cm at 40 W to a minimum value of 1.00x10^{-3} Ω.cm at 240 W.

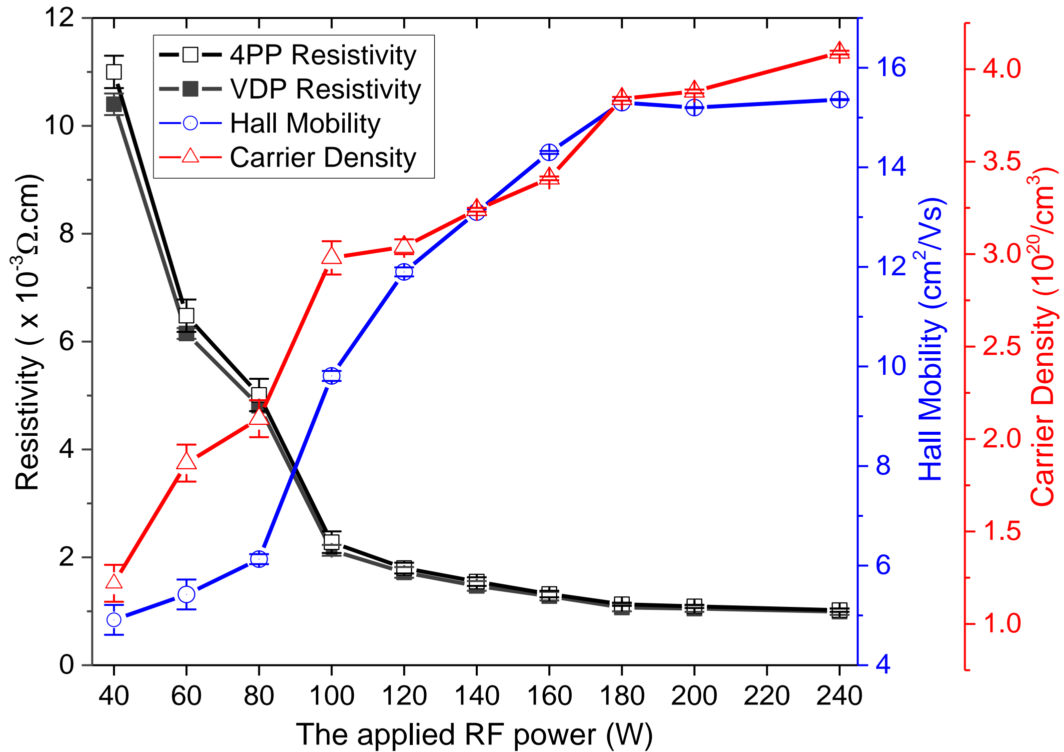

Fig. 4-18. The electrical characteristics (ρ, μ, and N) for AZO samples as a function of the applied RF power, deposited at room temperature, 2 mTorr, and 0.2% oxygen to argon.

These trends are in line with other publications [159, 160, 175]. As discussed in chapter 2, the carrier mobility in polycrystalline TCOs is limited by either ionised impurity scattering, or grain boundaries scattering depending on the microstructure characteristics and the free carrier density. The free carrier density for the AZO samples deposited low RF power revealed that the mobility is limited by the grain boundaries scattering due to lower free carrier density and higher grain boundaries density as seen from the XRD data [39, 176]. The increase in both the free carrier density and Hall mobility at higher RF power correlates with the XRD and XPS data discussed in the previous sections as shown in Fig. 4-19. Larger grain size confirmed with XRD analysis reflects less microstructure defects and grain boundaries density. Considering the XPS results, the reported reduction of the chemisorbed oxygen related defects O1s(II) at higher RF power would result in less carrier trapping and scattering at the grain boundaries. AFM images Fig. 4-12 revealed that increasing the RF power from 120 W to 180 W results in closely packed

surface particles of hillock-like profile with less voids in between. These observed microstructure changes from XRD, XPS, and AFM jointly reduced the impact of the grain boundaries scattering and thus improve the free carrier density and mobility [80, 177]. Also, the increased relative ratio of Al content at higher RF power, as shown in Fig. 4-10, would potentially enhance the ZnO doping efficiency and generate more free carriers in agreement with previous reports [175, 178].

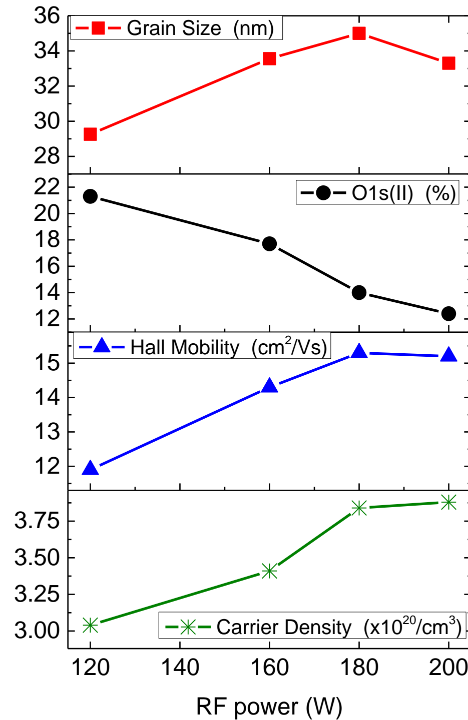

Fig. 4-19. The correlation between the electrical characteristics and the XRD /XPS data for AZO samples deposited at different RF power.

Seto's model [43] developed for polycrystalline thin films explains the simultaneous enhancement of free carrier density and mobility as follows; higher free carrier density leads to reduction of the carrier depleted regions on both sides of a grain boundaries, as well as to deactivating the trap states at the grain boundaries leading to reducing the barriers height between grains. Consequently, the free carrier mobility is enhanced. This model is proven to be applicable to ZnO-based films with carrier density up to $5x10^{20}/cm^3$ [44] which covers the range of the carrier densities for the fabricated AZO samples in this PhD research work.

Nevertheless, the discussed mechanisms for the resistivity reduction with increasing the RF power start to flatten out above 180 W, with marginal electrical properties improvements. The resistivity saturated trend at RF power >180 W could be attributed to the radiation damage originating from energetic oxygen ions at higher power [162]. Also, when high RF power and low pressure are used the sputtered species are reaching the substrate with very high energy that

could cause bombardments to the resulting film, re-sputtering other particles, a more pronounced atoms peening effect, and thus creating higher stress as shown by the XRD data [75, 162, 179]. For these reasons, 180 W is considered as the optimum RF power in this work.

4.3.9 Influence of the sputtering pressure on the AZO electrical properties

Although the investigated window of sputtering pressure is rather narrow, it was found that the sputtering pressure has a significant impact on the electrical properties of AZO samples. The resistivity significantly increased as the sputtering pressure was increased because of deteriorating both the free carrier density and mobility, as depicted in Fig. 4-20. Similar results were reported by Y. Igasaki, H. Kanma and Prabhakar et al. [160, 168].

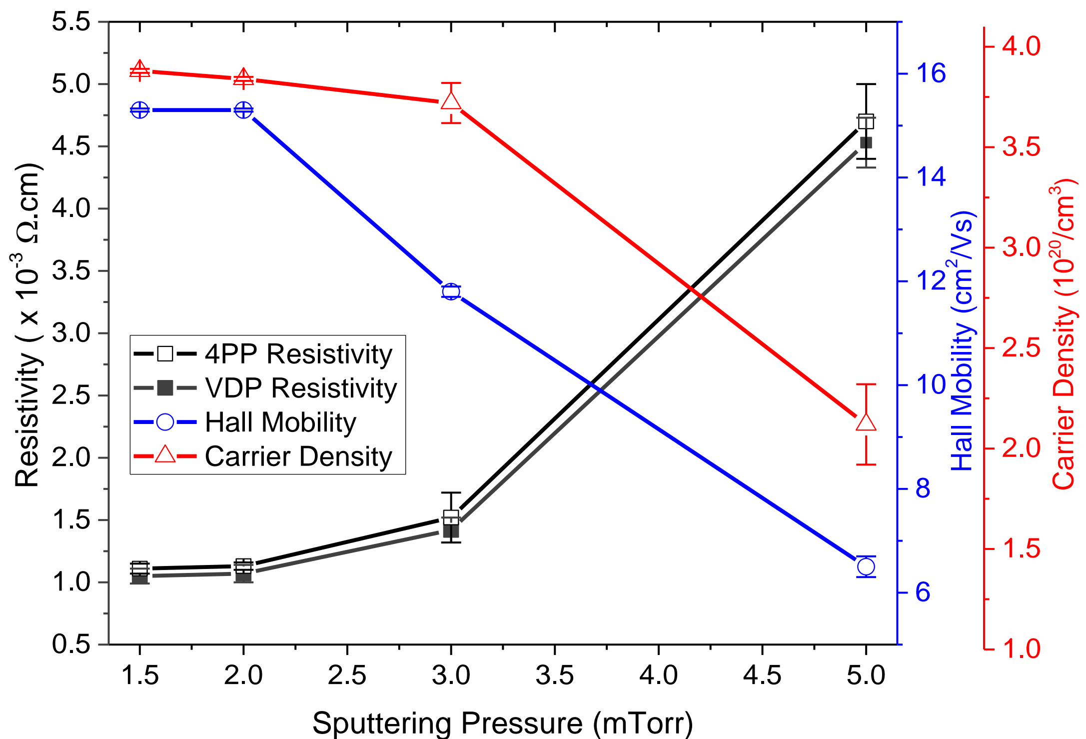

Fig. 4-20 The electrical characteristics (ρ, μ, and N) for AZO samples as a function of the sputtering pressure, deposited at room temperature, 180 W, and 0.2% oxygen to argon ratio.

These impacts of pressure on the AZO electrical characteristics are well-justified by the observed XRD and XPS results as shown in Fig. 4-21, where increasing the sputtering pressure leads to reducing the average grain sizes and increasing the grain boundaries density. Hence, the free carrier density and mobility are reduced. Moreover, the noticeable increase in the chemisorbed defects component O1s(II) when the sputtering pressure increased indicates more trap states are created leading to electron trapping from grains, enlarging the electron-depleted areas in the grains and the potential barriers between the grains. Thus, the electron density and

mobility are reduced. Considering the free carrier density for the 5 mTorr sample, which is $2.1x10^{20}/cm^3$, it is implied that the mobility is dominated by the grain boundaries scattering which in turn is linked to the chemisorbed defects and the average grain size reduction [39, 159, 168].

It should be mentioned that sputter-deposition at 1.5 mTorr results in only a slight resistivity reduction compared to 2 mTorr. However, at lower pressures than 1.5 mTorr the system was not stable enough to perform continuous sputtering, due to an inadequate amount of sputtering gas in the chamber, fewer argon ionisation events, and thus lower target bombardments [75, 86]. Therefore, 2 mTorr is considered as the optimal sputtering pressure in this work.

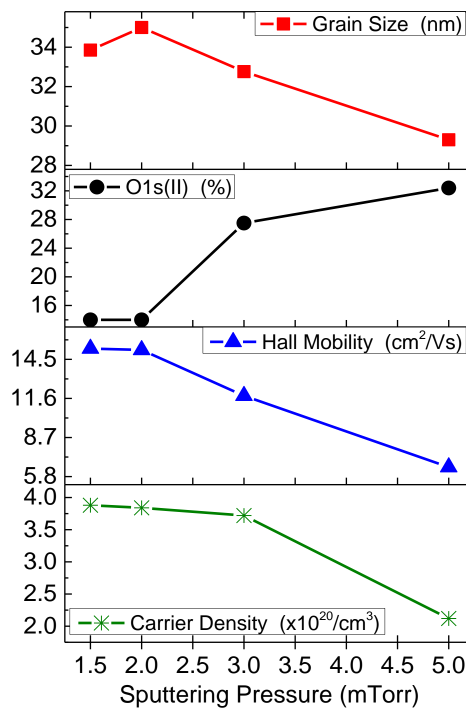

Fig. 4-21. The correlation between the electrical characteristics and the XRD /XPS data for AZO samples deposited at different sputtering pressure.

The insignificant resistivity reduction upon pressure decrease from 2 to 1.5 mTorr indicates that the sputtered atoms' energy at an applied RF power of 180 W is already high enough and it is marginally improved by such a reduction of pressure. To confirm this argument, the effect of this pressure reduction was tested at a lower RF power of 120 W, at which the sputtered atoms have lower energy compared to growths at 180 W. It was observed that the AZO resistivity was reduced by 20% from 1.72×10^{-3} to 1.40×10^{-3} Ω.cm, as shown in Fig. 4-22, due to enhancing the atoms kinetic energy as the pressure is reduced from 2 to 1.5 mTorr. Therefore, the lower pressure facilitates the arrival of more energetic species to the substrate when lower

RF power is used. At 180 W, however, the species are energetic enough to migrate to the best possible sites on the substrate without the need for lowering the sputtering pressure to 1.5 mTorr, which is close to the glow discharge instability region. This discussion reinforces the concept that the energy of the sputtered species can be tuned by both the sputtering pressure and the applied RF power when no intentional substrate heating is involved. In addition, it highlights the fact that the physical characteristics of the resulting film are controlled via the kinetic energy of the sputtered atoms upon the substrate arrival.

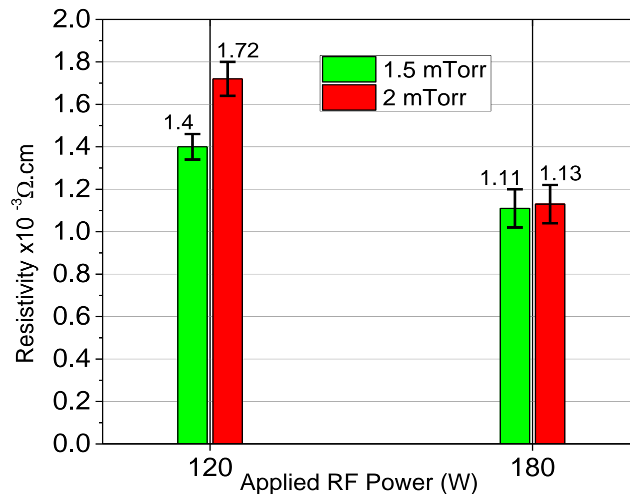

Fig. 4-22. The effect of the sputtering pressure on AZO resistivity at different RF power.

4.3.10 Resistivity lateral distribution across the substrate

Laterally homogeneous thin film characteristics is an essential requirement for TCO applications such as PVs. However, in magnetron sputtering of AZO, a spatial distribution of resistivity across the sample has been widely reported [134, 162, 180-182]. The resistivity lateral variation in magnetron sputtering is mainly due to electrons trapping in front of the target's surface by a permanent magnetic field. Consequently, the glow discharge and target bombardments are maximised in a ring-like area compared to anywhere else on the target surface. This area is well-known in magnetron sputtering and is referred to as the erosion ring or the race track. Hence, there will be a kinetic energy variation among the species sputtered from the race track and those sputtered from anywhere else from the target surface. Tominaga et al. have observed via using time-of-flight apparatus that the sputtered species from the race track are more energetic than those originated from the target centre [162]. The impact of the race track on the resistivity homogeneity typically becomes worse at room temperature deposition due to a limited energy and surface mobility of the sputtered particles compared to growth with elevated substrate

temperature. The impact of the erosion ring on the resistivity lateral uniformity is directly related to the sputtering system geometry and the growth parameters. Therefore, this could explain the contradicting observations that have been reported on resistivity uniformity of sputter deposited AZO transparent electrodes. For instance, Minami et al. reported that the resistivity of AZO was maximised at the positions that correspond to the target erosion ring-like area. They attributed this to non-uniformity of oxygen ions distribution during deposition that influences the uniformity of the free carrier density and mobility [180]. On the contrary, Cebulla et al. found that the resistivity is minimised at the positions in the film corresponding to the erosion ring on the target due to higher plasma density in front of the deposited sample opposite to the erosion ring leading to better microstructural characteristics and doping efficiency [134].

Different sputtering systems have been proposed to enhance the AZO films' resistivity homogeneity, such as using a rotated substrate and a target at a tilted angle with respect to the substrate. This geometry avoids the deposited sample directly facing the race track region on the target, reduces the sample damage, and increases the sputtered atoms surface mobility on the substrate compared to a substrate-facing-target arrangement [86, 173]. Also, using a combination of RF and DC excitation in magnetron sputtering has been found to improve AZO films' resistivity uniformity. The RF excitation is added to the DC-discharge in order to increase the plasma density via electrons oscillation between the electrodes. Thus, the density of ionised species sputtered from the target material is reduced due to higher probability of neutralization in dense plasma. Consequently, the ion damage to the growing film uniformity is reduced [134, 182]. In this work, the tilted-target geometry in which the cathode is at a tilted angle with respect to the anode, as in Fig. 3-3, is used in an RF magnetron sputtering system. The optimised deposition parameters (an RF power 180 W and a sputtering pressure 2 mTorr of 0.2% O_2 in Ar) achieve an excellently uniform resistivity distribution across 4-inch diameter substrates as shown in Fig. 4-23 below, achieving a resistivity deviation as small as 3.75%. However, samples deposited at unoptimised conditions showed larger resistivity variations between the substrate central location and the peripheral locations with a deviation of 12.00% for a deposition at (80 W and 2 mTorr of 0.2% O_2 in Ar), and 4.85% for a deposition at (180 W and 5 mTorr of 0.2% O_2 in Ar). It should be noted that the thickness of the AZO samples showed small variations across the substrate. For instance, at (80 W and 2 mTorr 0.2% O_2 in Ar), the AZO sample was thinner at the centre with a deviation

of about 5%. This thickness difference could not be the main reason for the observed resistivity variation. Hence, the microstructural characteristics for the AZO coating are expected to vary across the substrate because of the electrons confinement.

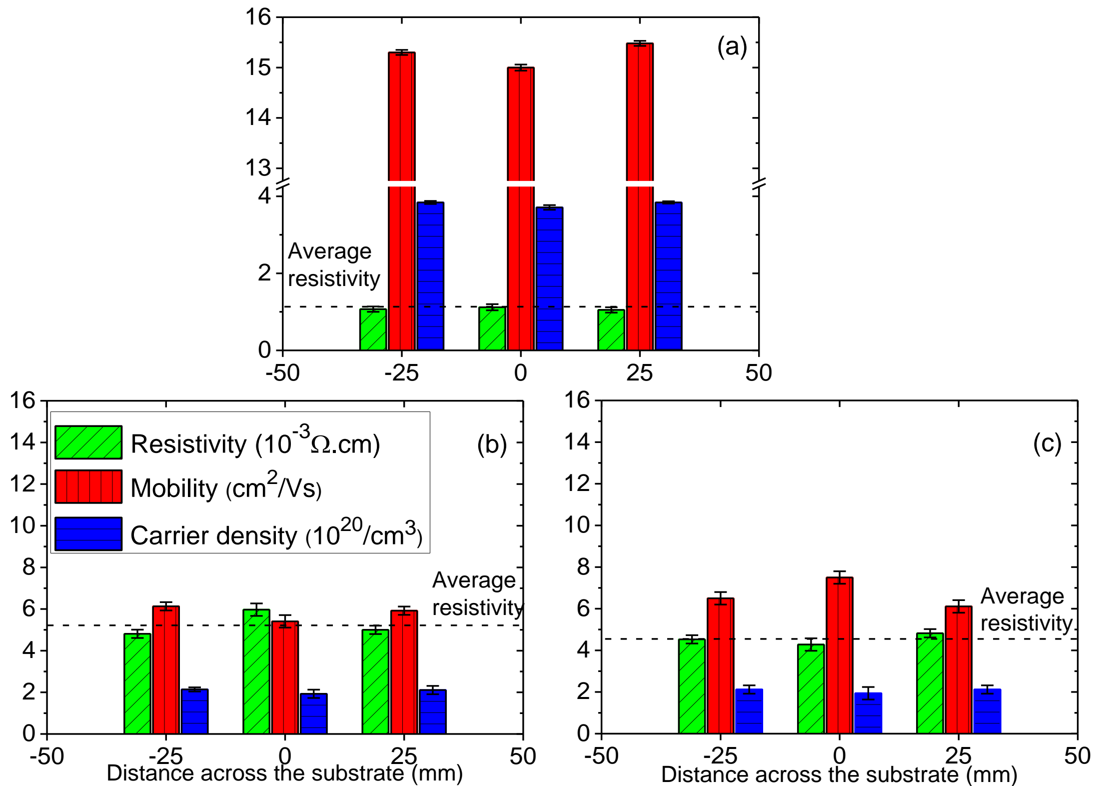

Fig. 4-23. Lateral electrical properties (ρ, μ, and N) distribution of AZO samples of different deposition parameters and as a function of the location on the substrate, (a) the optimised deposition condition 180 W and 2 mTorr, (b) 80 W and 2 mTorr, and (c)180 W and 5 mTorr.

4.3.11 Influence of the RF power and sputtering pressure on the AZO optical properties

All the as-deposited AZO films exhibited a visible transmission around 80% (at λ = 550 nm) that showed a reduction as the RF power is increased or the sputtering pressure is reduced compared to the optimised deposition conditions (180 W and 2 mTorr of 0.2% O_2 in Ar), as seen in Fig. 4-24. This reduction could be attributed to increasing the resultant film surface roughness at high power or low pressure, given that the film bombardments by the energetic sputtered species increase at these conditions [75, 159]. The increase in the film bombardments is confirmed by obtained XRD data discussed in the previous sections, whereby higher compressive stress is observed at higher RF power and lower pressure. In the NIR region (λ>1000 nm), however，the transmission spectra demonstrated a decrease that corresponds well with the observed increase in the carrier density at higher RF power or lower pressure leading to increased free carrier absorption and reflection according to the Drude model [45].This is because of the

interaction between the electrons and the electric field component of light, leading to altering the material relative permittivity and shifting the plasma wavelength towards the visible range [32, 80, 183]. The bandgap Eg for the as-deposited AZO samples at different growth conditions was estimated by Tauc et al. model [147], and found in the range 3.68 - 3.69 eV, as depicted in the inset graphs of Fig. 4-24.

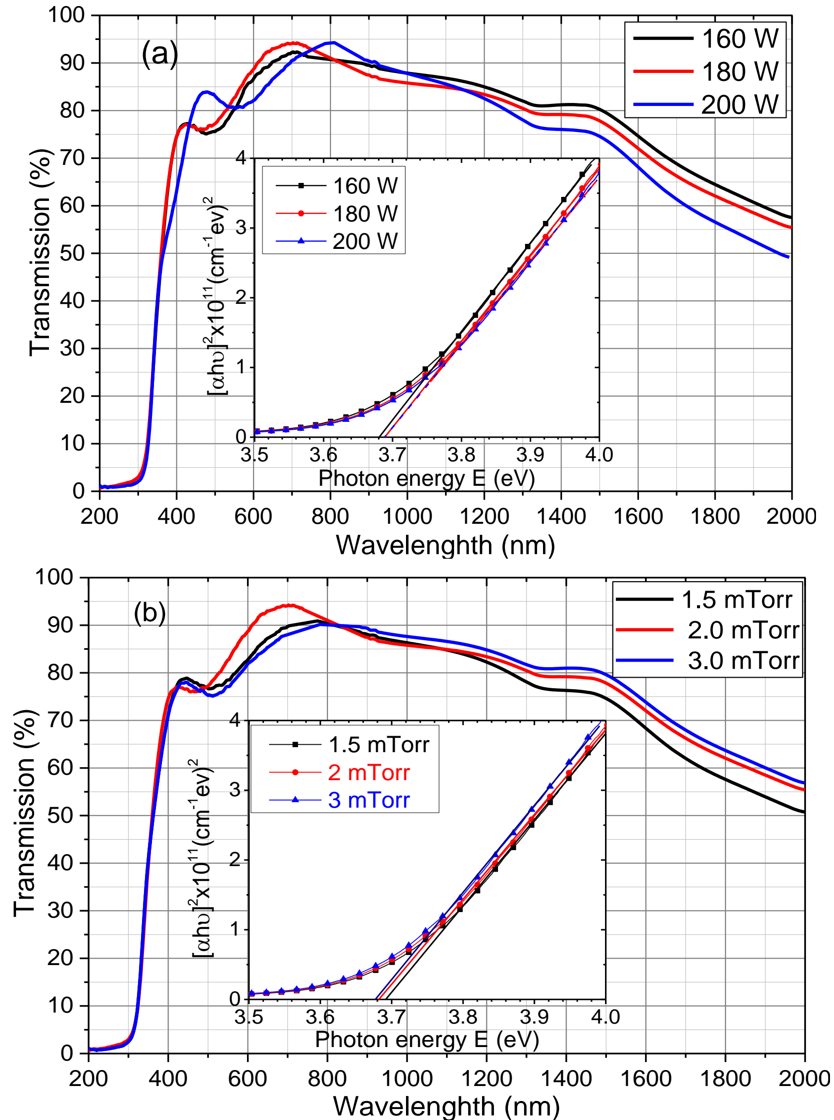

Fig. 4-24. AZO films optical transmittance spectra (a) as a function of the applied RF power at 2 mTorr, and (b) as a function of the sputtering pressure at 180 W. The inset graphs show linear extrapolations of Tauc's plot for these films.

Based on the presented discussions on AZO characteristics changes at different deposition conditions, the optimised deposition conditions at room temperature are an applied RF power of 180 W, and a sputtering pressure 2 mTorr of 0.2% oxygen to argon ratio. For the experimental work conducted in this research, this set of growth parameters was applied many

times, and the fabricated AZO samples demonstrated a good reproducibility with ~ 3 % variations. A list for some of AZO samples deposited at the optimised deposition conditions is shown in Appendix A.

In the next chapter, ELA of AZO using KrF excimer laser is explored aiming at further electrical and optical properties enhancements. Hence, the absorption coefficient (α) for AZO samples at the used laser wavelength (248 nm) was calculated from the transmission and reflection measurements and found to be 2.26×10^5 cm^{-1}. This large absorption coefficient implies that most of the laser energy is selectively absorbed by the AZO samples rather than the underlying substrate.

4.4 Concluding remarks

An empirical approach was followed to fabricate AZO transparent electrodes at room temperature by RF magnetron sputtering. Three series of AZO samples were sputter-deposited, where one parameter (oxygen to argon ratio, applied RF power, or sputtering pressure) was changed only in each series. Different experimental techniques for thin-film material characterisation were used. The dependence of AZO electrical properties on the deposition conditions was investigated and found to be well explained by the observed trends for the microstructural and compositional characteristics studied via XRD and XPS. Structurally, bigger average grain size and thus lower grain boundary density are obtained at higher RF power and lower sputtering pressure because of enhancing the sputtered particles kinetic energy at these conditions. Consequently, the free carrier density and mobility are enhanced leading to better conductivity. In regard to compositional analysis, the adsorbed defects density is associated with AZO compactness and is reduced when the sputtered atoms are energetic enough, resulting in less carrier trapping and scattering and therefor better conductivity. Unlike most of the literature on AZO deposition optimisation at room temperature, the work presented in this chapter demonstrates a clear basis for the carrier conduction mechanism of AZO and how the achieved conductivity is determined by the microstructural and compositional characteristics.

The optimised deposition conditions at room temperature are an RF power of 180 W, and a sputtering pressure 2 mTorr of 0.2 % oxygen to argon ratio. It is worth highlighting that the concluded sputter-deposition demonstrated a relatively high growth rate along with an excellent uniformity and reproducibility.

5 Annealing Studies on AZO Films Sputter-deposited at Room Temperature

5.1 Introduction

This chapter presents two post-deposition annealing techniques applied to AZO thin films deposited at room temperature aiming at further electro-optical characteristics improvements. The techniques are excimer laser annealing (ELA) at 248 nm (KrF) and rapid thermal annealing (RTA) at different processing conditions. Both techniques result in about 50% resistivity reduction and with a concurrent visible transmission enhancement. The optimised ELA or RTA treated AZO transparent conducting electrodes, with a resistivity of ~ 5×10^{-4} Ω.cm and a visible transmission >85% at 550 nm, demonstrated comparable performance to commercial high-quality tin doped indium oxide (ITO) electrodes when applied to organic photovoltaic devices (OPVs). Power conversion efficiency (PCE) of 2.07% and 2.10% were achieved for devices with ELA and RTA treated AZO films respectively compared to favourably 2.17% for those with ITO. Moreover, the IEC test 61646 damp heat (DH) was performed on a set of AZO and ITO electrodes to investigate environmental robustness of the films. The stability of AZO samples found to be directly dependent on the fabrication parameters applied.

5.2 Post-deposition ELA optimisation

All deposited AZO films in the previous chapter (180 nm thick on glass substrates) were subjected to ELA in air at ambient temperature using a KrF excimer laser (λ=248 nm and pulse duration 25 ns). Initially, single pulse investigations were conducted to identify the threshold values of laser energy density needed to cause effects on the processed film characteristics and to cause material ablation. The investigated energy density window was ranged over 25-500 mJ/cm^2 ± 2% in steps of 25 mJ/cm^2 and the laser footprint on the sample was set to be 2.5 mm × 2.5 mm. This approach allows to easily achieve high energy density and does not consume large areas of the as-deposited films. Given that the spot size is relatively small, the two-inner probes of a four-point probe station with 1 mm probe spacing were used to measure the processed film resistance and compare the measurements with the as-grown ones. It was observed that the resistance of the AZO was reduced when processed at laser density ≥ 50 mJ/cm^2; however, the films peeled off at energy density ≥ 150 mJ/cm^2. Thereafter, further investigations were conducted using a different number of pulses up to 100 within the identified energy density window of 50-

125 mJ/cm^2. The AZO-coated glass substrates were first divided into squares each of which was 1 cm $\times$ 1 cm area and with 2 mm separation from the neighbouring squares, so that each square could accommodate a laser beam of 1 cm $\times$ 1 cm without overlapping of the laser spots. The optimised ELA parameters were also tested on the optimised as-deposited AZO samples[vi] in different processing environments including nitrogen and argon at a pressure of 150 psi.

Nian et al. [97] used the COMSOL simulation software to study the temperature changes for 200 nm thick AZO samples during a single pulse ELA with a KrF excimer laser and 25 ns pulse duration. They reported that the AZO temperature would increase to 850 K (577°C) for a period of 60ns when annealed at 120 mJ/cm^2. On the basis of Nian et al findings, it can be anticipated that our AZO samples temperature during KrF ELA with five pulses at 125 mJ/cm^2, as the optimised ELA conditions discussed later, to be elevated to ~ 850 K but several times due to heat generation with multiple pulses [93, 184, 185]. According to the structure zone model by Thornton [174], the desired temperature range for crystallisation of a coating is typically within 50%-80% of the material melting point. The widely reported melting point for AZO is 1400 K, thus the generated temperature via ELA at 125 mJ/cm^2 used here and expected to be > 850 K is within this range (>60% of AZO melting point).

5.3 Post-deposition RTA optimisation

For comparison with ELA, rapid thermal annealing (RTA) was investigated on the optimised as-deposited AZO films on fused silica substrates in an ambient of nitrogen and with various processing profiles covering a range of target temperatures (250, 300, 350, and 400°C), and various dwell times (20, 40, 60, and 120s). The used RTA equipment was AnnealSys AS–One processor. For better temperature stability and minimal temperature overshoot during temperature ramping, the system first reaches 150°C (4°C/s i.e. in 30s) then achieves the annealing target temperature e.g. 300°C at a heating rate of 3-4°C/sec. Once the target temperature is reached, the desired dwell time is observed. Then, the samples are naturally cooled down to 45°C, at rate of 2-3° C/sec via heat dissipation. The heating cycle for the optimised RTA profile is shown in Fig. 5-1.

[vi] The optimised samples are 180 nm thick on glass substrates deposited at room temperature, an RF power of 180 W, and a sputtering pressure 2 mTorr of 0.2% oxygen to argon ratio as presented in the previous chapter.

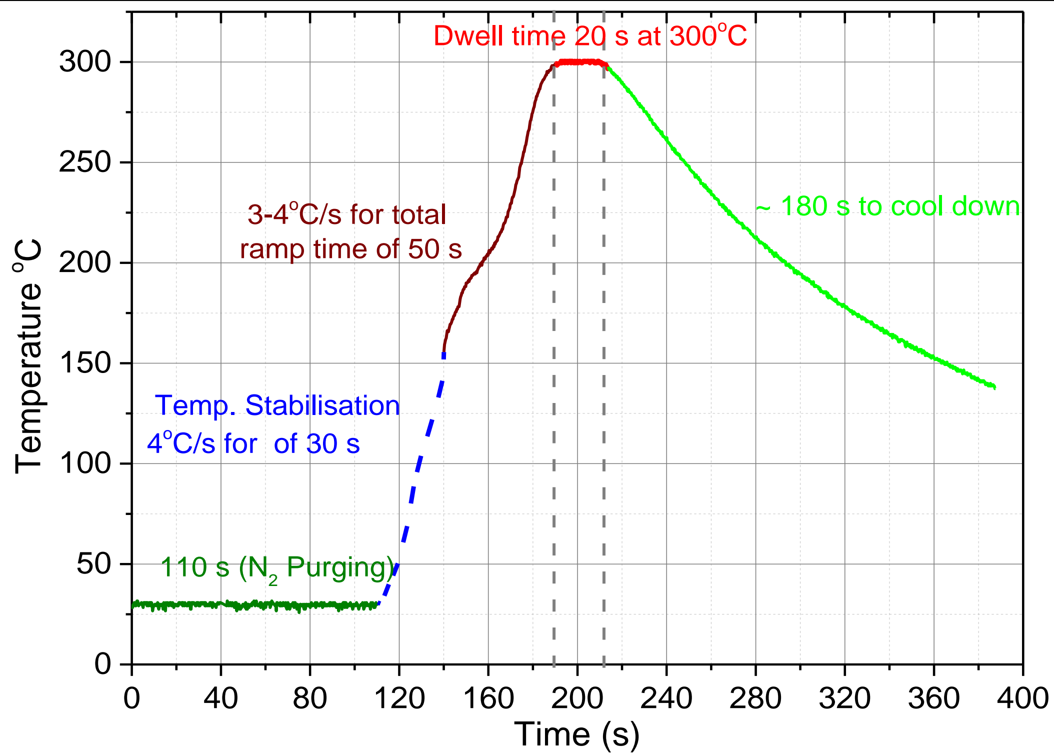

Fig. 5-1. The optimised RTA cycle for AZO samples.

5.4 Combined post-deposition annealing with ELA and RTA

A dual step annealing process via a combination of ELA-RTA or RTA-ELA was examined on the optimised as-deposited AZO samples. The motivation for this investigation was that each of these processing techniques was found to double the conductivity of AZO thin films via different processing mechanisms. Thus, it is worth examining combing the two processing approaches.

5.5 Post-deposition annealing results and discussion

5.5.1 Influence of ELA and RTA on the AZO microstructure characteristics

Fig. 5-2 compares the wide XRD spectra in the range of 2θ = 10°- 80° for AZO samples upon ELA and RTA at the optimised parameters, in terms of the achieved resistivity reduction as discussed in section 5.5.3. It showed only the same clear ZnO (002) and (004) peaks observed in the as-deposited samples i.e. no additional secondary phases were created after both annealing methods. Analogous to the as-deposited AZO samples of different growth conditions, the Voigt-function model was applied to high resolution XRD data for the ELA and RTA treated AZO samples, to discriminate the grain size and lattice strain contributions to the observed XRD peak broadening.

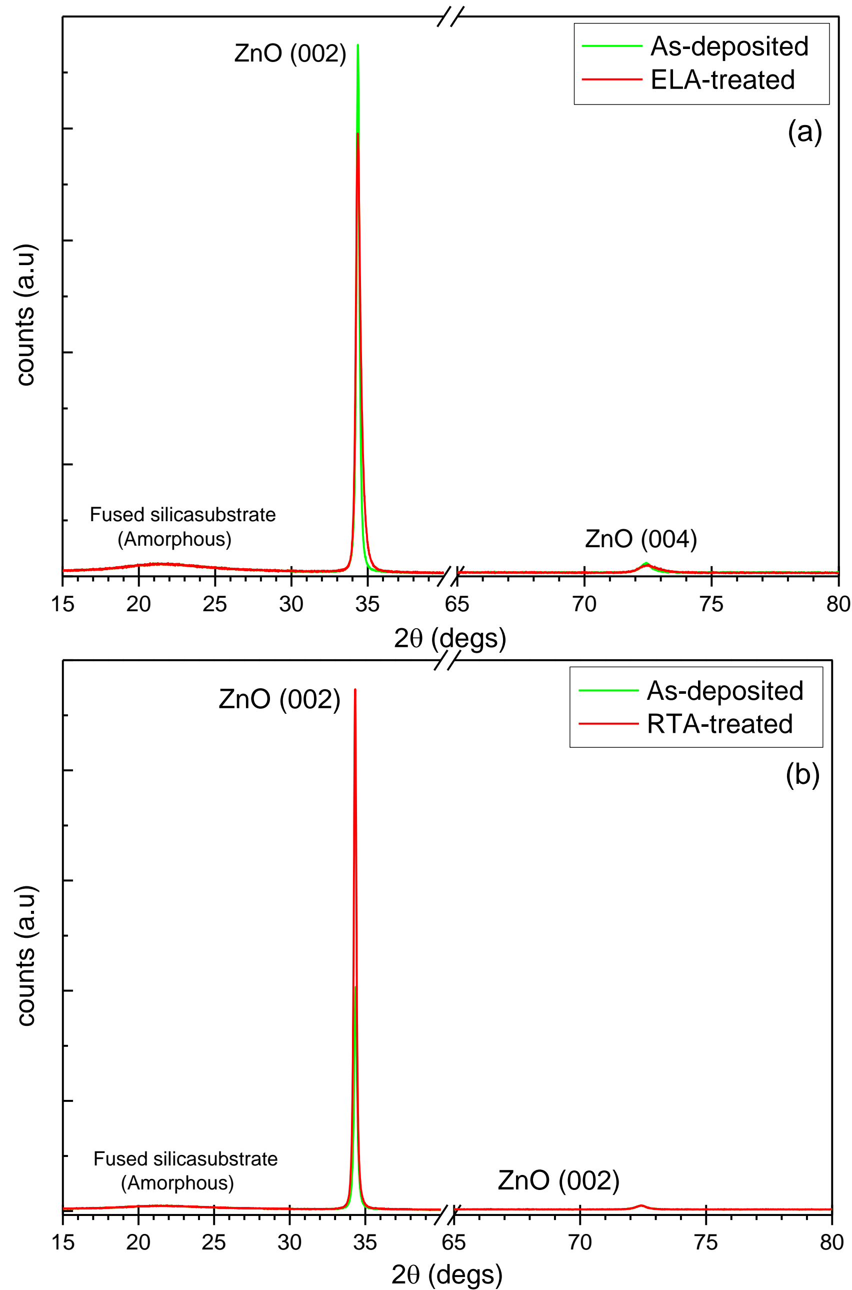

Fig. 5-2. Wide XRD spectra for the optimised AZO samples (a) after ELA with 5 pulses at 125 mJ/cm^2 in air, and (b) after RTA at 300°C for 20s in nitrogen.

Straightforward application of Voigt-function model to the XRD data for the ELA-treated samples at the optimised laser energy density 125 mJ/cm^2 implied that ELA results in grain size reduction which is contradicting the significant electrical conductance enhancement upon ELA, as discussed in the forthcoming section 5.5.3 . This finding is attributed to the significant XRD profile asymmetry observed after ELA treatment as illustrated in Fig. 5-3. Similar results were recently reported for AZO samples processed with laser photon at a wavelength of 343 nm and a pulse duration of 6.7 ps from an Yb:YAG laser source [80].

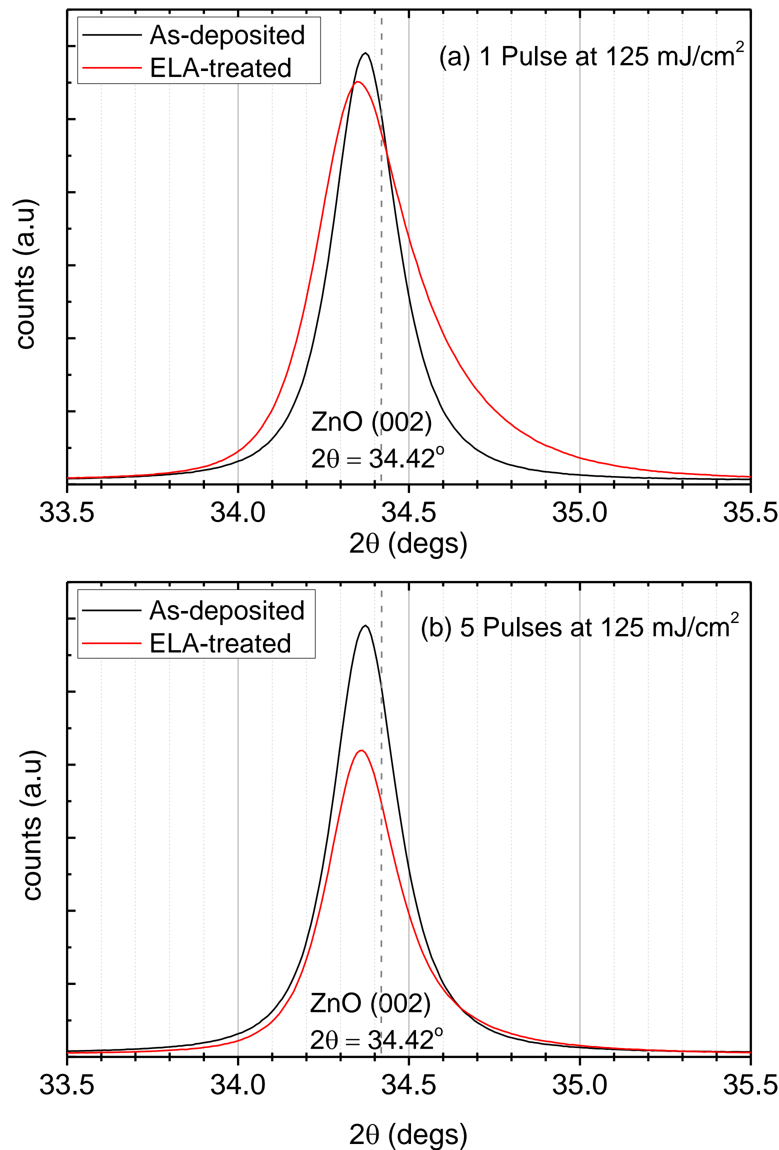

Fig. 5-3. High-resolution XRD spectra for the optimised as-deposited AZO samples ELA-treated at 125 mJ/cm² (a) with one pulse, and (b) with five pulses.

The observed asymmetry upon ELA is ascribed to the heating mechanism of ELA, which can be summarised as below:

1. As stated in chapter 4, the KrF photons (λ = 248 nm) have an absorption coefficient (α) of 2.26×10^{5} cm^{-1} and a penetration depth in AZO of around 44 nm from the surface. Thus, the KrF photons absorption generates heat predominantly in the penetration depth [10, 80], which is labelled with A in Fig. 5-4.
2. The rest of the film, to some extent, is heated via heat diffusion from the top 44 nm. This heat gradually propagates through the AZO film over a length referred to as the thermal diffusion length. This portion of the sample is labelled with B in Fig. 5-4. The layers A and B are considered to be the thermally affected volume of the sample i.e. within the heat-affected zone of the sample upon the KrF photons absorption.

3. The AZO material that is beyond the heat-affected zone is considered as not thermally affected, which is the layer (C) in Fig. 5-4.

The above heating mechanism results in lattice strain, grain size, Al activation state, d-spacing, defect density and distribution being spatially varied throughout the AZO thickness.

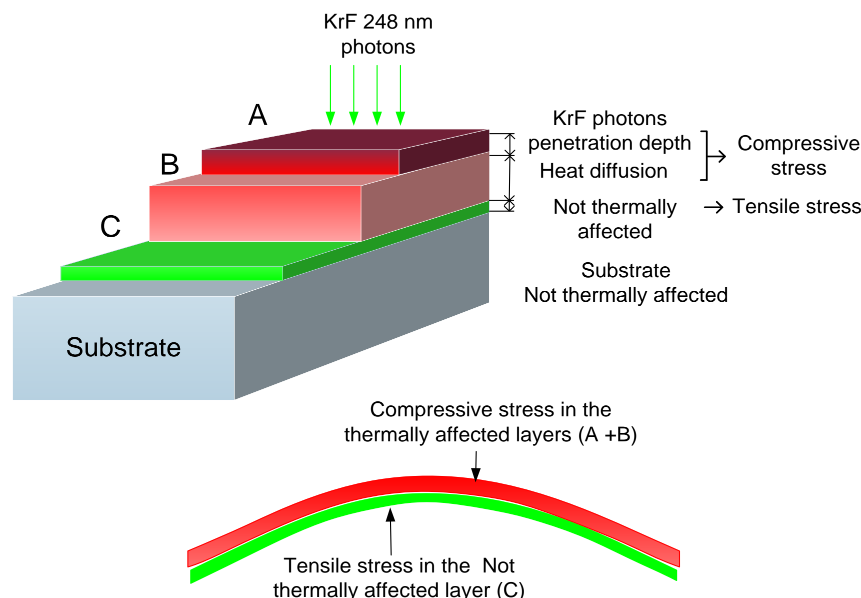

Fig. 5-4. Mechanism for stress state changes throughout the AZO sample thickness upon ELA.

As depicted in Fig. 5-3 the XRD pattern for the ELA-treated samples demonstrates lower diffraction angles compared to the as-deposited state indicating larger compressive stress values. This is due to the heating gradient and therefore thermal expansion mismatch over the sample thickness after ELA causing a thermal stress. The observed overall compressive stress can be explained as follows: the thermally affected layers (A and B) tend to expand parallel to the surface due to the ELA-induced heating. However, both the thermally affected and the not affected layers are required to have the same length at the interface in between. Thus, a compressive stress is generated in the thermally affected layers. This in turn leads to an elongated d-spacing and thus a lower diffraction angle 2θ compared to the as-deposited state and to the standard ZnO diffraction angle (34.42°). Whilst, a tensile stress is induced in the not thermally affected layer to balance the compressive stress developed in the thermally affected layer [186]. Consequently, the not thermally affected layer exhibits a smaller d-spacing and a higher diffraction angle 2θ compared to the thermally affected layers and to the standard ZnO angle (34.42°). The stress state variations over the samples thickness caused by ELA lead to a broadened and asymmetry XRD peak.

Therefore, the XRD patterns for the ELA-treated samples were resolved into two peaks, with a Voigt profile each, as in Fig. 5-5. The first peak corresponds to the thermally affected part of the film including the layers A and B. While, the second peak is assigned to the underneath layer C that is considered as not thermally affected. Thereafter, the Voigt-function model for XRD data analysis was applied to each of the resolved peaks for grain size and lattice strain estimation. The ELA treatment effect over the ELA-treated AZO sample thickness could be estimated from the relevant peak area ratio to the overall XRD peak. The obtained data for the optimised as-deposited AZO samples ELA-treated with different pulses (1 or 5) at 125 mJ/cm^2 is presented in Table 5-1.

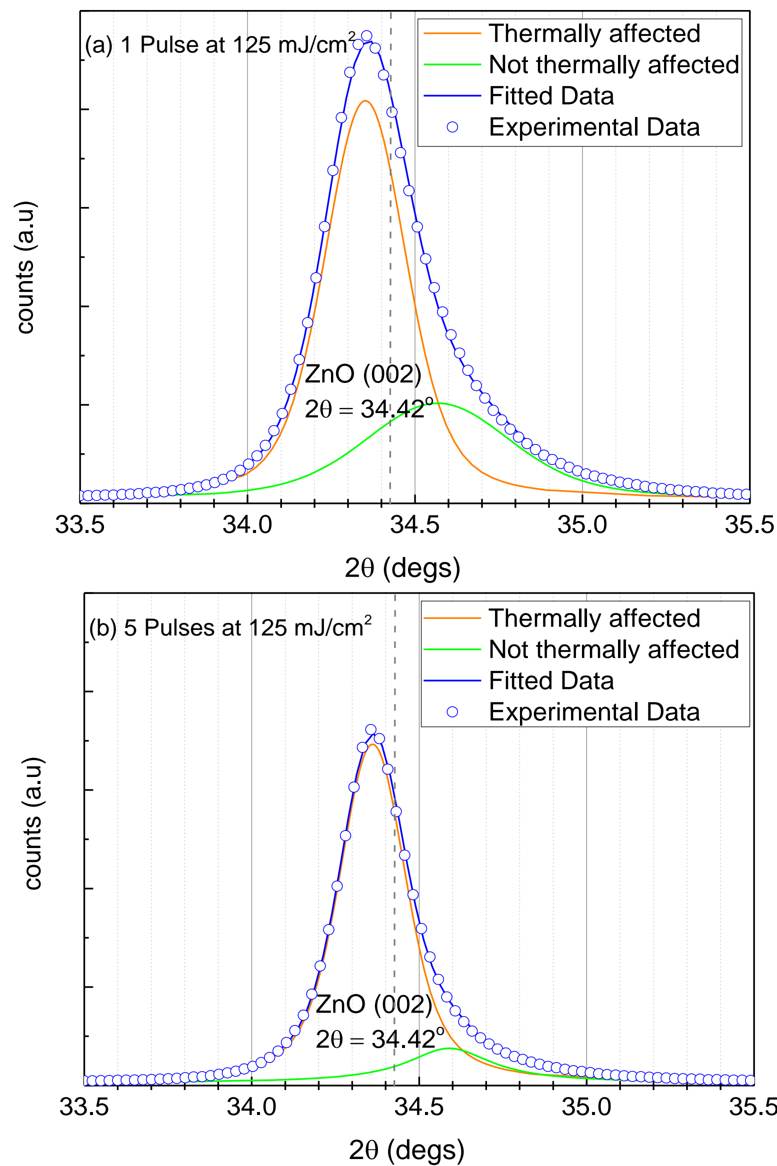

Fig. 5-5. High resolution XRD data for the optimum as-deposited AZO180 nm thick resolved to two XRD peaks after ELA at 125 mJcm^2 (a) with one pulse, and (b) with five pulses.

The physical properties	As-deposited (Voigt)	Processed with 1 pulse at 125 mJ/cm^2		Processed with 5 pulses at 125 mJ/cm^2	
		Thermally affected (Voigt)	Not thermally affected (Voigt)	Thermally affected (Voigt)	Not thermally affected (Voigt)
2θ (deg)	34.37	34.35	34.57	34.36	34.59
d-spacing (nm)	2.606	2.608	2.593	2.608	2.591
$^{*}\beta_{size}$ (deg)	0.148	0.122	0.203	0.115	0.311
Average grain size (nm)	35.70	42.40	26.10	45.80	17.00
$^{*}\beta_{micro\text{-}str}$ (deg)	0.128	0.222	0.404	0.167	4.3×10^{-6}
Weighted average strain	0.007	0.013	0.024	0.01	2.6×10^{-7}
Stress (GPa)	-0.325 compressive	-0.466 compressive	+ 0.942 tensile	-0.410 compressive	+ 1.086 tensile
The layer ratio and thickness		65% 117 nm	35% 63 nm	86% 155 nm	14% 25 nm

Table 5-1. XRD data analysis using Voigt function for the optimum as-deposited AZO 180 nm thick resolved to two XRD peaks after ELA with different number of pulses at 125 mJcm^2.

$^{*}\beta_{size}$ and $\beta_{micro\text{-}str}$ are the diffraction peak broadening due to grain size (i.e. the Lorentzian component), and due to lattice strain (i.e. the Gaussian component), respectively. As illustrated in Table 5-1, the thermally affected volume fraction was found to become larger associated with increasing the number of pulses from one to five. This could be assigned to heat accumulation during ELA with multiple pulses [184].

To validate this approach for XRD data analysis after ELA treatment, AZO samples of different thickness including 50, 100, and 200 nm were deposited on glass substrates at the optimised deposition conditions (room temperature, 180 W, and 2 mTorr of 2% O_2 in Ar). Then, the samples were subjected to ELA with five pulses at a laser energy density of 75, 100 and 125 mJ/cm^2 respectively. These energy density values are the optimised laser energy density to achieve the highest conductivity for each sample. High-resolution XRD data for these samples were resolved into two peaks based on the discussion on ELA mechanism presented above and the results are shown in Fig. 5-6.

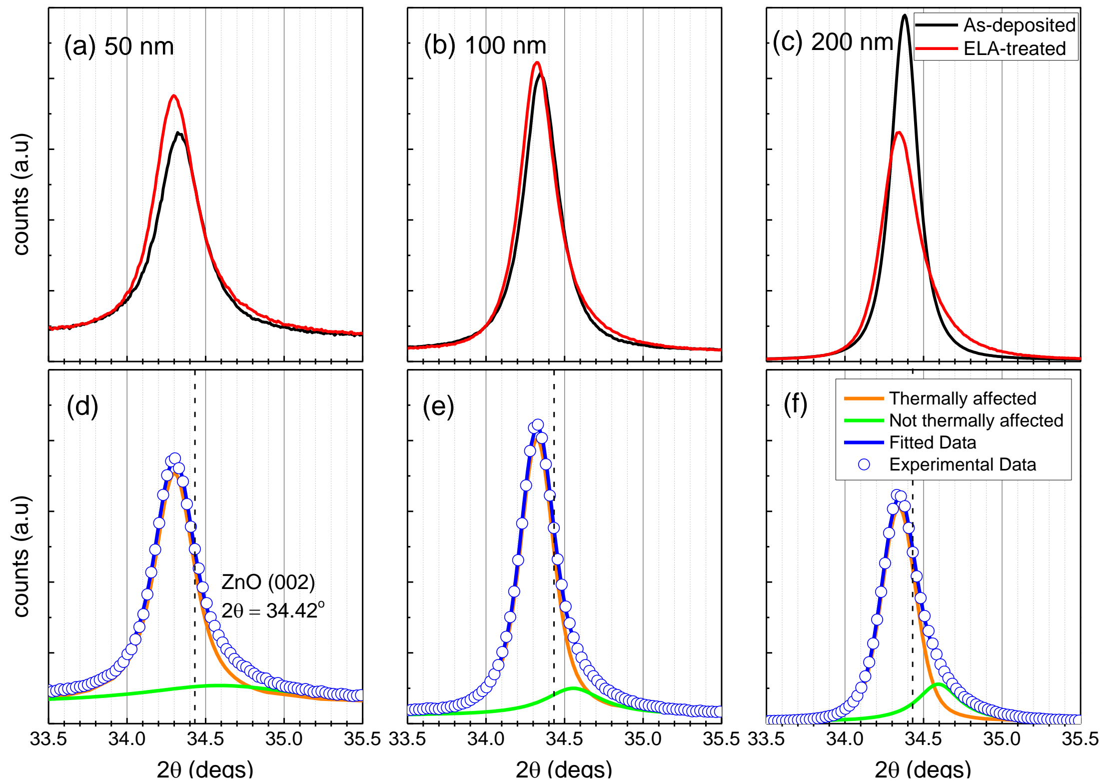

Fig. 5-6. (a-c) XRD patterns for AZO samples of different thicknesses pre and post ELA, and (e-f) the XRD data upon ELA resolved to two peaks.

Looking at the sample of 50 nm thickness Fig. 5-6 (a) and (d), the ZnO (002) peak intensity showed a clear increase upon ELA compared to the as-deposited film indicting improved microstructural properties. The not thermally affected volume fraction of this sample is very small because the thickness is very close to the penetration depth of KrF photons in AZO (44 nm). Given that the optimum laser energy density for this thickness (75 mJ/cm^2) is relatively low, the generated heat due to KrF photons penetration is anticipated to be relatively low leading to more localised heating. However, for thicker samples, e.g. 180 nm thick, which could be annealed at higher energy density, higher heat is generated that propagates beyond the KrF photons penetration depth leading to microstructural properties variations over the thickness as discussed before. When the 180 nm thick sample is ELA-treated at 75 mJ/cm^2, the created microstructural properties variations over the sample thickness are less pronounced and almost undistinguishable from the obtained XRD patterns as shown in Fig. 5-7. D. Scorticati et al. have shown that the observed changes in XRD peak symmetry upon ELA depends on both the AZO thickness and used set of ELA parameters [80].

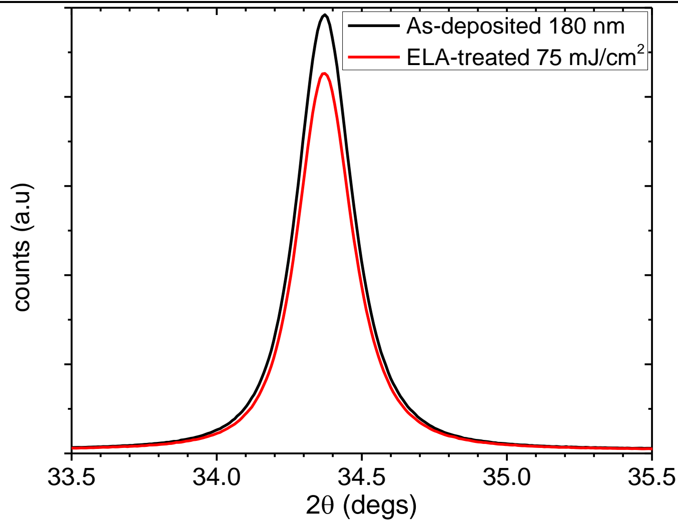

Fig. 5-7. The optimised AZO 180 nm-thick ELA treated with five pulses at 75 mJ/cm^2.

Fig. 5-8 demonstrates the achieved average grain size enlargement by ELA along with the evaluation of the ELA effect over the sample thickness estimated from the relevant peak's area ratio to the overall XRD peak.

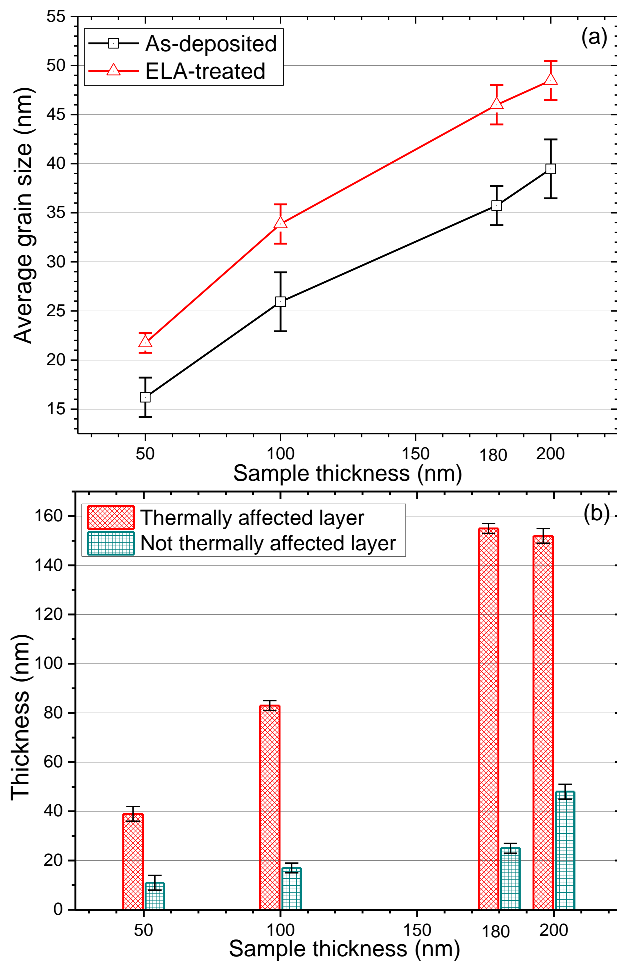

Fig. 5-8. The obtained results from resolving the XRD data for AZO of different thickness upon ELA, (a) the effect of ELA on the average grain size, and (b) the extent of the ELA effect over the sample thickness.

Considering the sample of 200 nm thick upon ELA at the optimum conditions 5 pulses at 125 mJ/cm^2 Fig. 5-6 (c) and (f), the thermally affected segment of the sample is almost the same as that achieved in 180 nm thick AZO sample processed at the same conditions. This observation indicates consistency of the results. In addition, previous work by our NTU research group has investigated the effect of KrF ELA on intrinsic zinc oxide thin films deposited on silicon substrates with no external substrate heating [187]. It was demonstrated via high-resolution TEM that the application of one pulse at 295 mJ/cm^2 to 200 nm-thick ZnO samples results in localised modification to the upper 135 nm layer of the samples, as shown in Fig. 5-9. The modified thickness for ZnO samples observed by TEM is very close to the affected layer thickness 150 nm obtained from the XRD data, presented in this research, when 180 nm or 200 nm thick AZO samples are ELA-treated with 5 pluses at 125 mJ/cm^2.

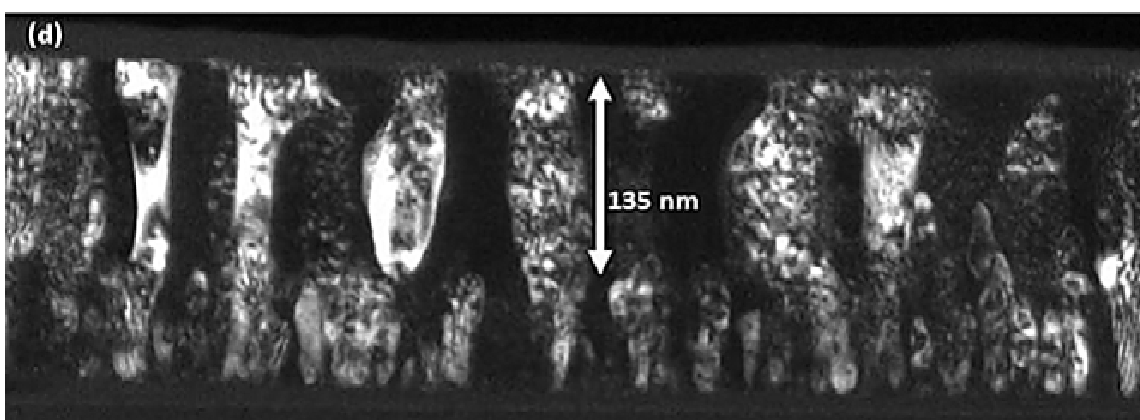

Fig. 5-9. TEM image showing the effect of KrF ELA on a 200 nm thick ZnO film. The upper layer of 135 nm was modified. Adapted from [187] .

Rapid thermal annealing (RTA), which is the second annealing technique applied to AZO samples in this research, does not affect the XRD profile symmetry. This is because of more homogeneous processing over the AZO thickness and much longer heating time in RTA relative to ELA. Fig. 5-10 demonstrates that the intensity of the main ZnO peak (002) is increased as the annealing temperature is increased to 300°C due to local atomic rearrangement resulting in enhancement of the ZnO (002) preferred orientation i.e. better crystallinity [188].

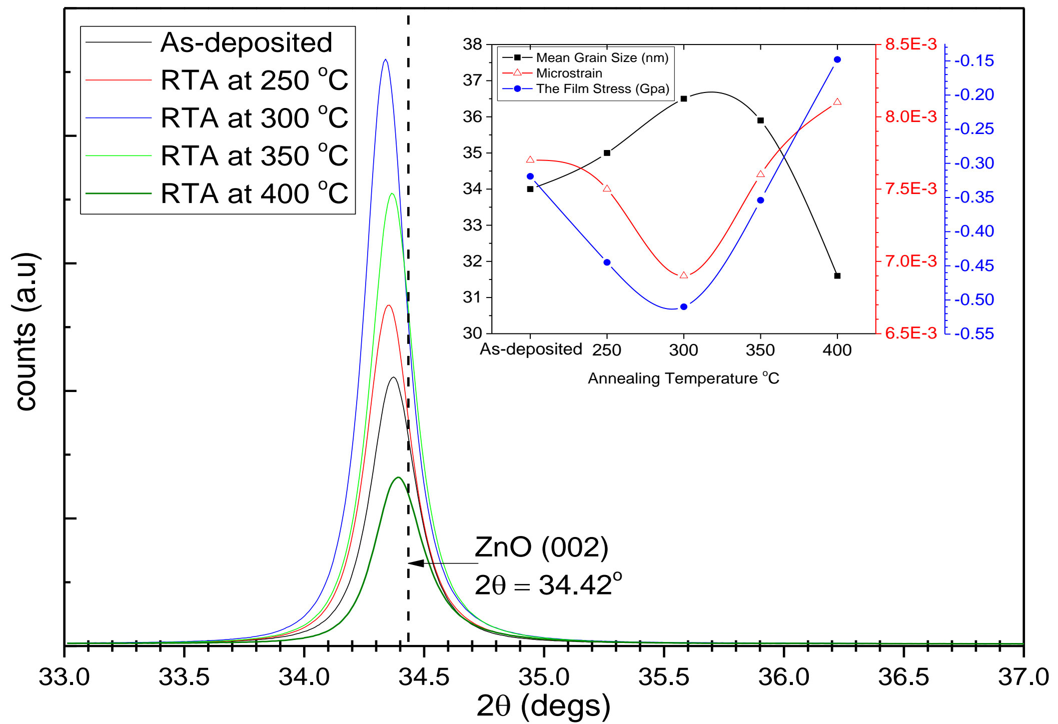

Fig. 5-10. High-resolution XRD data for AZO samples underwent RTA at different annealing temperatures and for a dwell time of 20s, the inset graph illustrates Voigt-function model results.

XRD line-broadening analysis for the RTA-treated samples via the Voigt-function model showed a grain size enlargement from 34.0 nm for the as-deposited sample to 36.60 nm after RTA at 300°C for 20s. The enlargement is less than that achieved with ELA in the thermally affected layer. This could be due to the higher temperature generated in ELA (expected to reach ~ 600°C for 60 ns [97]) compared to RTA. The film stress becomes more compressive as the RTA temperature is increased to 300°C. This is originated from a thermal stress due to variation in thermal expansion coefficients between the processed AZO (7×10^{-6}/°C) and that for the underlying fused silica substrate (5.5×10^{-7}/°C) leading to a thermal expansion mismatch. [134, 167]. As the RTA temperature increases the AZO film tries to expand, whilst, the substrate is less affected due its considerably lower expansion coefficient. Consequently, a compressive stress is created in the film since the film and the substrate are interfaced together and they must have the same length at the interface. At higher annealing temperatures, however, the compressive stress is relaxed reaching a minimum value at 400°C. At this temperature a visible colour change of the AZO coating and a significant resistivity increase were observed indicating the onset of the AZO coating delamination from the substrate which in turn breaks the grain refinement and causes the observed stress reduction [189]. Increasing RTA dwell time from 20s to 40s, results in almost no

changes in XRD data. However, at longer dwell times the AZO crystal quality is degraded as shown in Fig. 5-11. Compressive stress reduction, AZO delamination, and resistivity increase were observed upon RTA at 300°C for 120s.

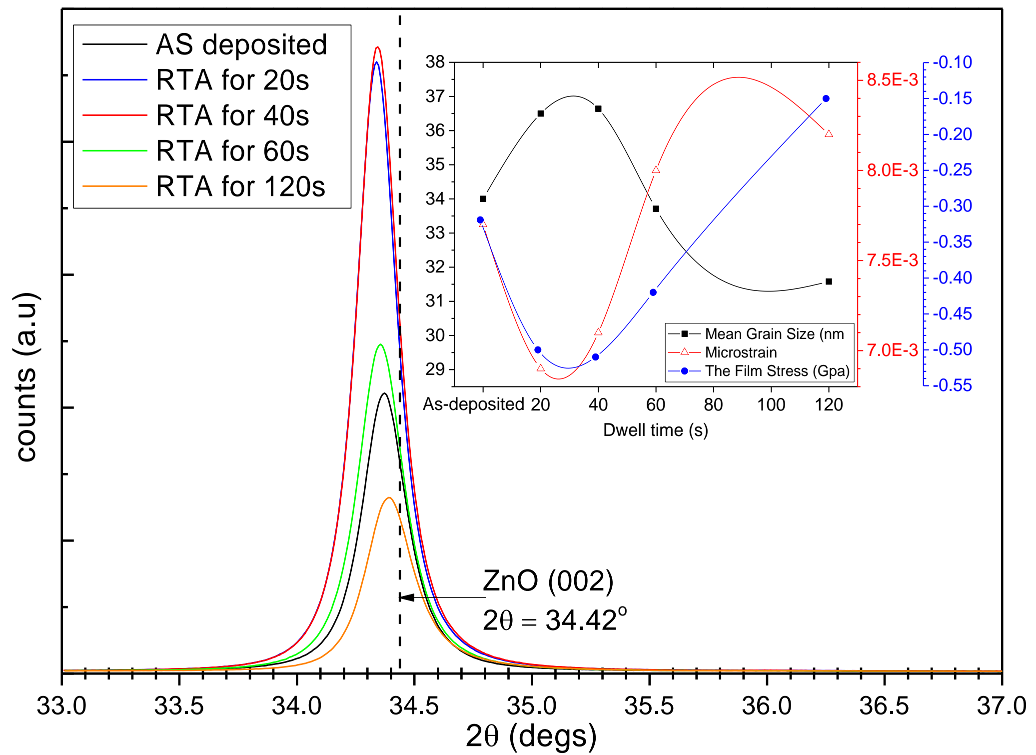

Fig. 5-11 High-resolution XRD data for AZO samples underwent RTA at the optimum annealing temperature (300°C) and for different dwell time, the inset graph illustrates Voigt-function model results.

When the optimised ELA-treated AZO (5 pulses at 125 mJ/cm^2) is RTA-treated at the optimised RTA conditions (300°C for 20s in nitrogen), the XRD profile symmetry is improved as shown in Fig. 5-12. This is due to uniform processing during RTA throughout the sample thickness including both the thermally affected and not thermally affected layers. Consequently, the non-uniformity of lattice strain, grain size, Al activation state, d-spacing, defect density and distribution caused by the ELA gradient heating is smoothened over the sample thickness. This observation supports the explanations presented earlier on ELA heating mechanism partially through the AZO sample thickness that causes the observed XRD profile asymmetry.

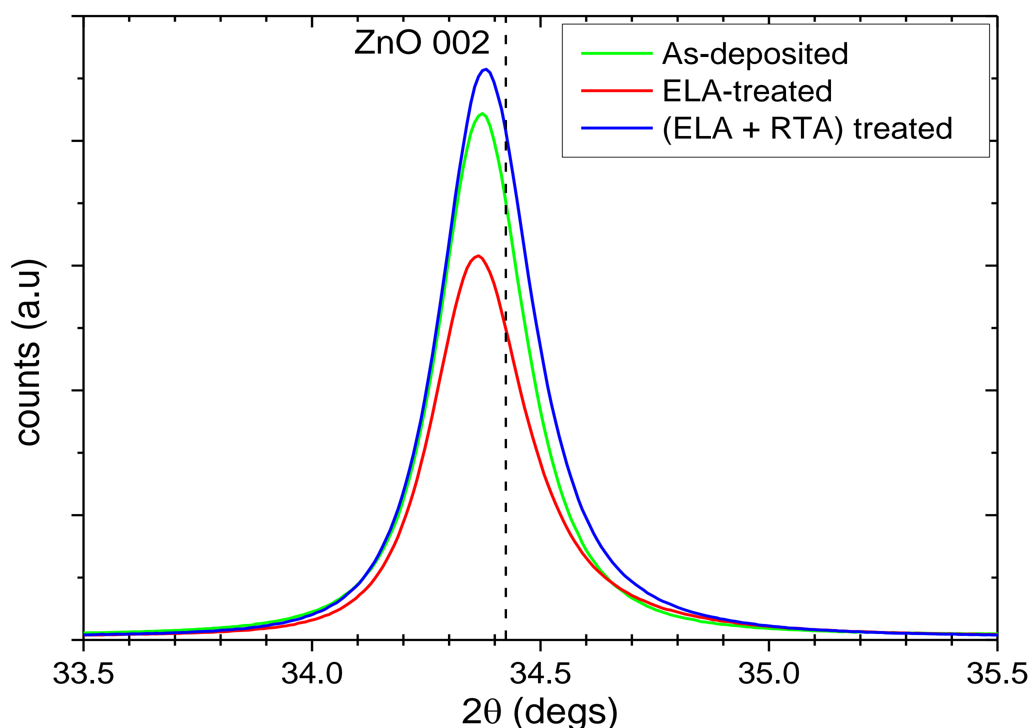

Fig. 5-12 High-resolution XRD data for the optimised as-deposited AZO sample was that initially ELA-treated, followed by RTA-treatment.

5.5.2 Influence of ELA and RTA on the AZO stoichiometry

XPS measurements were carried out on the optimised as-deposited and treated (ELA and RTA) AZO samples; the atomic concentrations of aluminium, zinc, and oxygen are presented in Table 5-2. No clear changes were observed on the wide-scan XPS spectra before and after annealing. To differentiate the chemical state changes for the contained elements upon annealing, high-resolution XPS spectra were collected.

Sample	Aluminium (at.%)	Zinc (at.%)	Oxygen (at.%)
Optimised As-deposited	2.20	53.70	44.10
Optimised ELA-treated	2.15	55.50	42.35
Optimised RTA-treated	2.00	56.14	41.76

Table 5-2.The relative atomic concentration of aluminium, zinc, and oxygen before and after ELA, and RTA treatment.

No changes were observed in the Zn2p photoelectron spectra after annealing using ELA or RTA, as opposed to the O1s and Al2p photoelectron spectra. The high-resolution O1s spectra were fitted into the two components, as discussed in section 4.3.6 in the previous chapter. The details of the fitted O1s components are presented in Fig. 5-13 and Table 5-3.

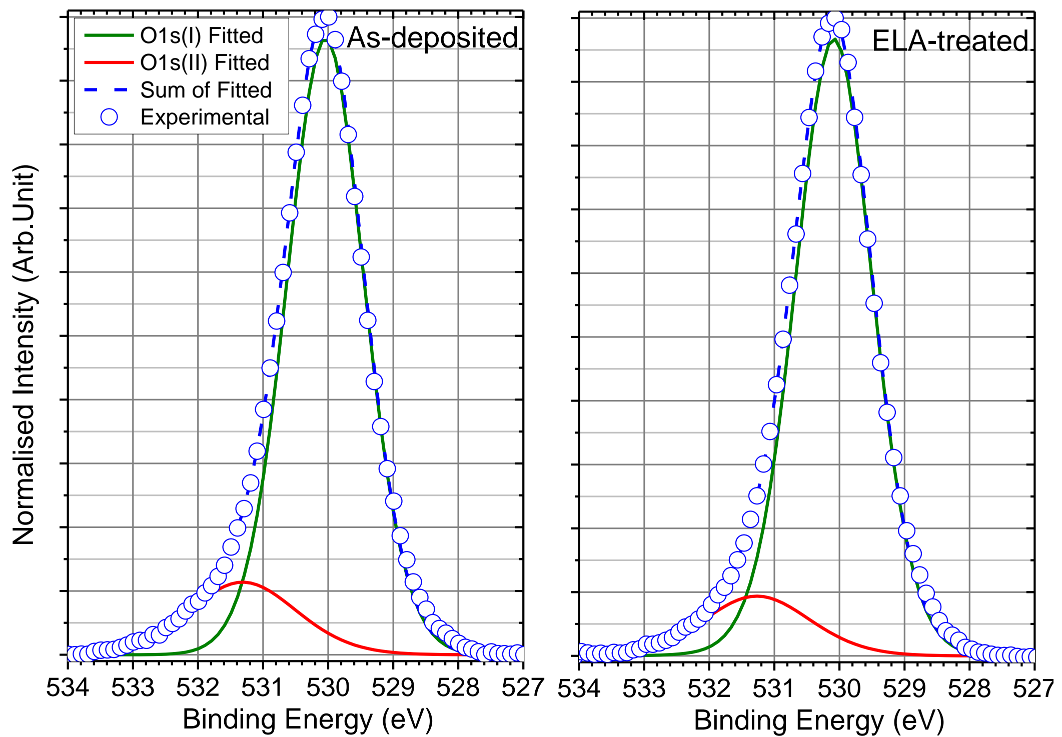

Fig. 5-13. O1s XPS spectra for the optimised as-deposited and ELA-treated AZO samples resolved into two components.

O1s component	Details	As-deposited	ELA-treated
O1s(I)	Peak at (eV)	530.0	530.0
	FWHM (eV)	1.38	1.38
	Area (%)	86.0	88.2
O1s(II)	Peak at (eV)	531.3	531.3
	FWHM (eV)	1.95	1.94
	Area (%)	14.0	11.8

Table 5-3.Details of the resolved peaks of O1s XPS spectra for the optimised as-deposited and ELA-treated AZO samples.

It was revealed that upon ELA, the O1s(I) component is increased, while the O1s(II) component is reduced. As stated in the previous chapter the O1s(I) component can be related to the native microstructure defects density, while, the O1s(II) component is linked to the chemisorbed oxygen-related defects such as chemisorbed oxygen atoms, hydroxides, and carbonates [165, 170]. These results imply that the AZO microstructural characteristics are enhanced upon ELA which was also confirmed via the XRD data analysis presented in the previous section 5.5.1. The O1s(II) component of O1s XPS spectra has a strong impact on the AZO samples' free carrier density, mobility, and thus the achieved conductivity as demonstrated before by the XPS data for the as-deposited AZO samples of various growth conditions in the previous chapter. It has been reported that UV treatment reduces the chemisorbed oxygen-related defects, i.e. the O1s(II) component, from ZnO-based TCOs. Hagendorfer et al have shown

via XPS study that UV treatment is very efficient in reducing the chemisorbed oxygen-related defects from AZO thin films prepared by aqueous solution processing [190]. L. Ding et al studied the electrical properties of ZnO films subjected to three different annealing techniques including thermal annealing at 200°C for 40 min, UV-annealing, and a combination of thermal annealing at 200°C for 20 min and hydrogen plasma annealing. They reported that the UV annealed sample achieves relatively higher Hall mobility as a result of reducing the chemisorbed oxygen-related defects [191]. Similar tendencies were also recently published by J. Hong et al [170]. The chemisorbed oxygen-related defects reduction upon UV-treatment is attributed to the photoconductivity effect during UV-treatment, which can be explained as follows: Typically, the chemisorbed defects are localised at grain boundaries and capture electrons from the conduction band causing negatively charged grain boundaries that act as inter grains barriers and electrons scattering centres. Oppositely charged particles recombination occurs between photo-generated holes during UV treatment and the negatively charged oxygen-related defects at grain boundaries causes the latter neutralisation. Then, the neutralised oxygen-related defects are desorbed, this process is referred to as photodesorption [42, 80, 170]. More detailed discussion on adsorption and photodesorption of oxygen atoms could be found in [42].

The photoconductivity effect is one of the photonic annealing advantages over thermal annealing techniques. Nevertheless, it has been reported that thermal treatment at high temperature (>500°C) and/or long processing times (>30 min) in hydrogen environment could also reduce and/or passivate chemisorbed oxygen-related defects at grain boundaries [78, 170]. In this research, RTA was performed in a nitrogen atmosphere at relatively low temperature 300°C and for a short dwell time 20s. Therefore, our RTA treatment caused smaller reduction to the O1s(II) component compared to ELA as shown in Fig. 5-14. The details of the resolved peaks of O1s XPS spectrum for the RTA-treated AZO sample are shown in Table 5-4.

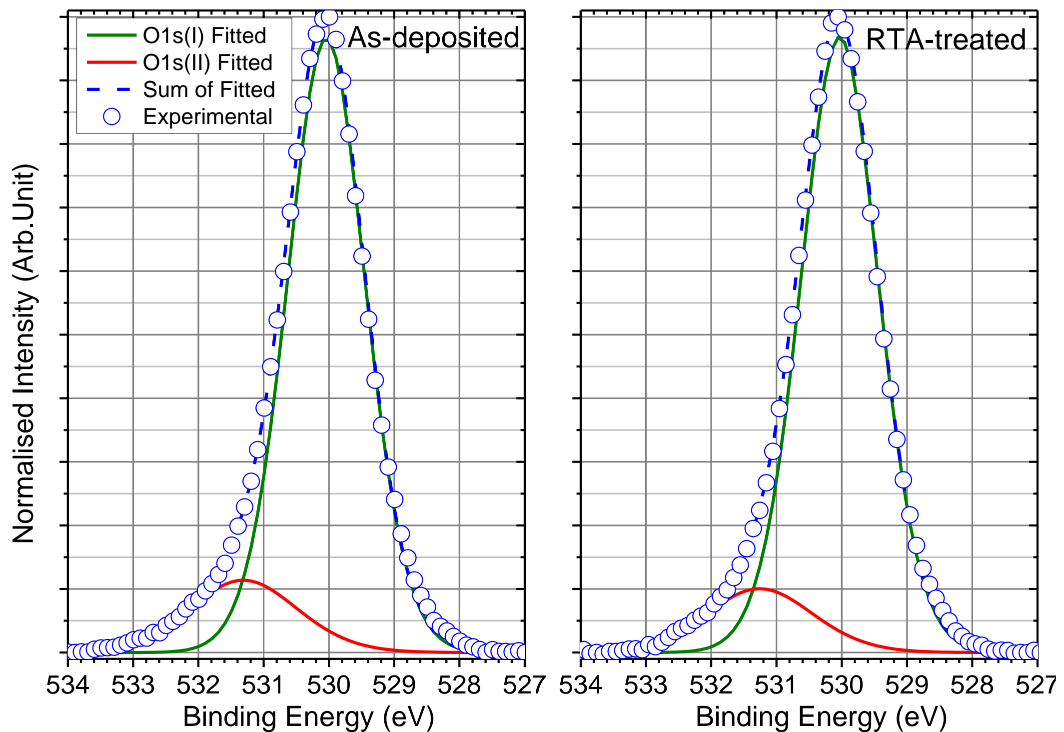

Fig. 5-14 O1s XPS spectra for the optimised as-deposited and RTA-treated AZO samples resolved into two peaks.

O1s component	Details	As-deposited	RTA-treated
O1s(I)	Peak at (eV)	530.0	530.0
	FWHM (eV)	1.38	1.38
	Area (%)	86.0	87.0
O1s(II)	Peak at (eV)	531.3	531.3
	FWHM (eV)	1.95	1.90
	Area (%)	14.0	13.0

Table 5-4. Details of the resolved peaks of O1s XPS spectra for the optimised as-deposited and RTA-treated AZO samples.

Unlike all the as-deposited AZO samples discussed in chapter 4, the Al2p photoelectron spectra for AZO samples after ELA and RTA treatments could be resolved to one chemical state only of one doublet as shown in Fig. 5-15, the details of the resolved peaks are presented in Table 5-5. This implies that both ELA and RTA activated the Al atoms that were presented as interstitials or positioned at grain boundaries in the as-deposited samples. It has been reported that room temperature sputter-deposition does not provide the needed kinetic energy for the sputtered particles to efficiently immigrate to the best energy sites on the substrate. Also, room temperature deposition of doped oxide materials suffers from difficulties in introducing dopants, e.g. Al, into the host lattice, e.g. ZnO [173]. Upon ELA or RTA, the supplied energy by the laser photons absorption or RTA heating provides the Al^{+3} ions with the needed activation energy to replace Zn^{+2} in the ZnO matrix [80, 192].

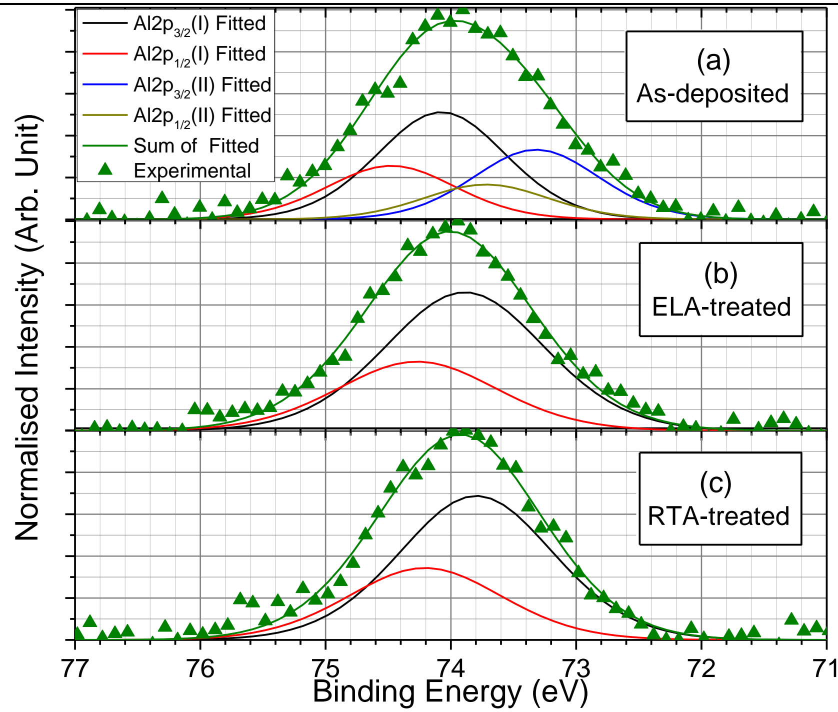

Fig. 5-15. Al2p photoelectron spectra for AZO samples, (a) as-deposited resolved into two chemical states Al2p(I) and Al2p(II), (b) and (c) post ELA and RTA respectively resolved into one chemical state Al2p(I).

Sample	XPS peak	Total		Activated Al (I)			Non- Activated Al (II)		
		Peak at (eV)	FWHM (eV)	Peak at (eV)	FWHM (eV)	Area (%)	Peak at (eV)	FWHM (eV)	Area (%)
As-deposited	2p3/2	73.9	1.67	74.1	1.20	40.40	73.4	1.18	26.10
	2p1/2			74.5	1.20	20.20	73.8	1.18	13.00
ELA-treated	2p3/2	74.1	1.55	73.8	1.50	66.60			
	2p1/2			74.2	1.50	33.30			
RTA-treated	2p3/2	73.9	1.53	73.8	1.45	66.60			
	2p1/2			74.2	1.45	33.30			

Table 5-5. Details of the resolved peaks for Al2p XPS spectra obtained from AZO films pre and post ELA and RTA treatments.

5.5.3 Influence of ELA and RTA on the AZO electrical properties

Fig. 5-16 shows the effect of ELA parameters (energy density and number of pulses) on the resistivity of AZO films of different deposition conditions. Annealing with one pulse reduced the AZO resistivity as the energy density was increased from 50 to 125 mJ/cm^2. Furthermore, with 5 pulses at 125 mJ/cm^2, the AZO electrical resistivity is reduced by about 50% for the optimised as-deposited AZO samples deposited at no external substrate heating, 180 W, and 2 mTorr of 02% oxygen to argon ratio. When the number of pulses was increased above five at 125 mJ/cm^2, either no further resistivity reduction or material ablation and hence resistivity increase were observed. The material ablation is attributed to heat accumulation during ELA with multiple pulses. Likewise, when the laser energy density exceeded 125 mJ/cm^2 (not shown here), the

samples resistivity increased significantly. This is attributed to high energy density delivered to the samples causing visible material ablation [97, 193]. Resistivity changes upon ELA for all the deposited AZO samples of different deposition conditions are presented in Appendix B.

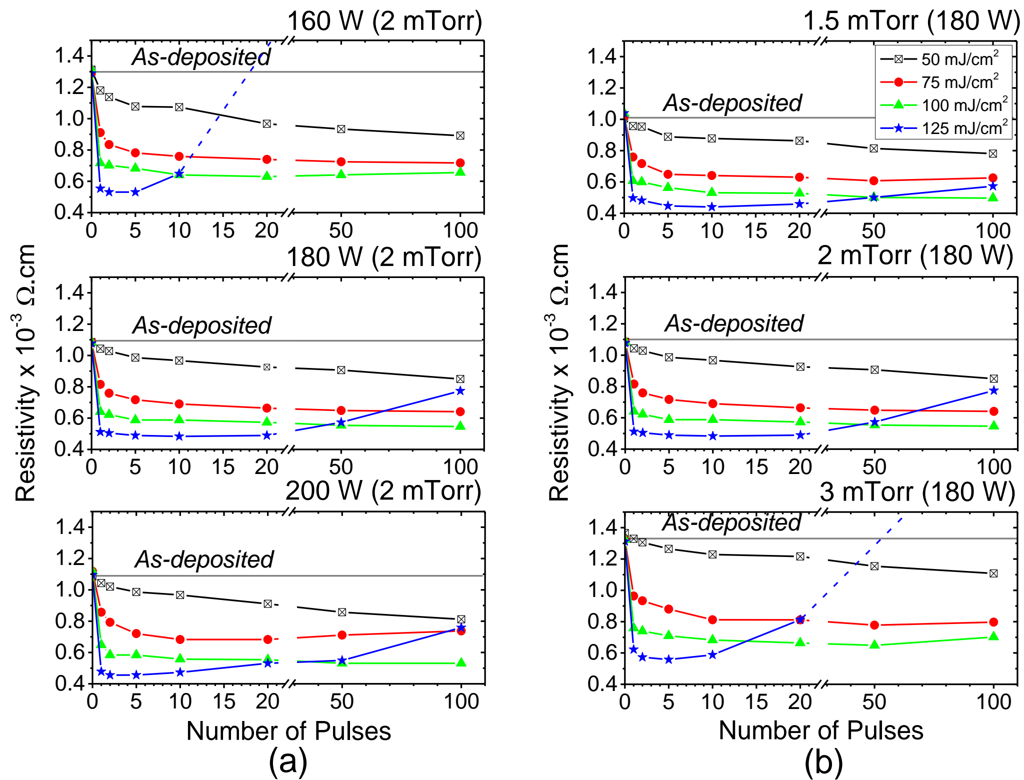

Fig. 5-16. The effect of ELA at different energy densities and number of pulses on AZO resistivity as a function of (a) the applied RF power at 2 mTorr, and (b) the sputtering pressure at 180 W.

As mentioned in the second chapter, both the free carrier density (*N*) and mobility (μ) contribute to the material conductivity. Therefore, Van der Pauw and Hall Effect measurements were performed in order to determine the free carrier density and mobility changes which are causing the remarkable conductivity improvement upon ELA. Fig. 5-17 compares the electrical properties (ρ, N, and μ) for the optimised as-deposited AZO samples processed with 5 pulses at different laser energy densities. It was demonstrated that the reported resistivity reduction of AZO sample upon laser annealing is a result of the simultaneous enhancement of both the electron density and Hall mobility. Likewise, all the as-deposited samples in this work exhibited enhanced free carrier density and mobility upon ELA at the optimised conditions (5 pulses at 125 mJ/cm^2 in air) leading to enhanced conductivity, as depicted in Fig. 5-18. The enhancements are relatively larger for as-deposited AZO samples of higher resistivity values. It should be noted that the 4PP and Hall Effect measurements' errors for the optimised as-deposited AZO samples upon ELA or RTA reduced to insignificant values.

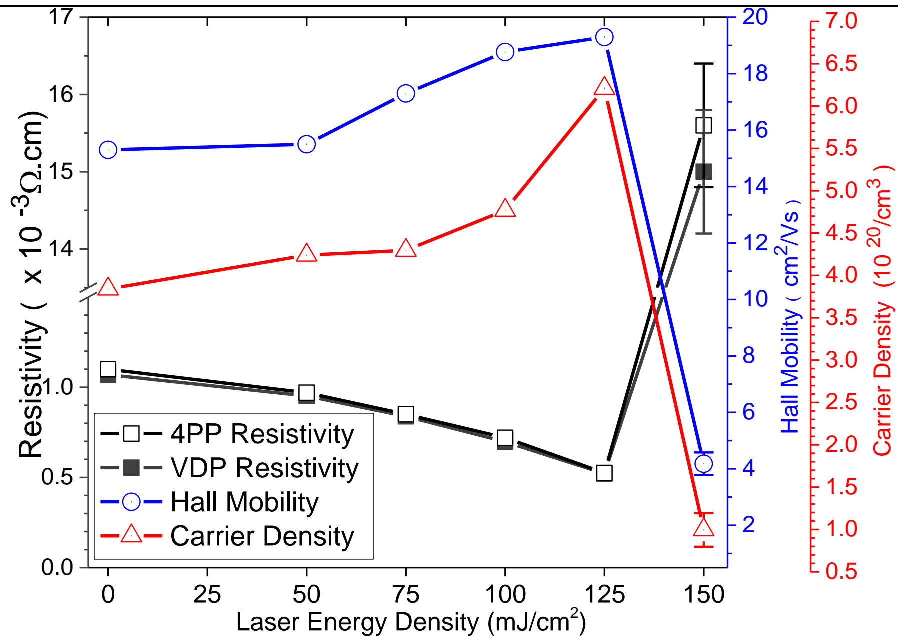

Fig. 5-17. The effect of ELA at five pulses and different energy densities on the electrical characteristics for the optimised as-deposited AZO samples, the values at 0 mJ/cm² are for the as-deposited AZO sample.

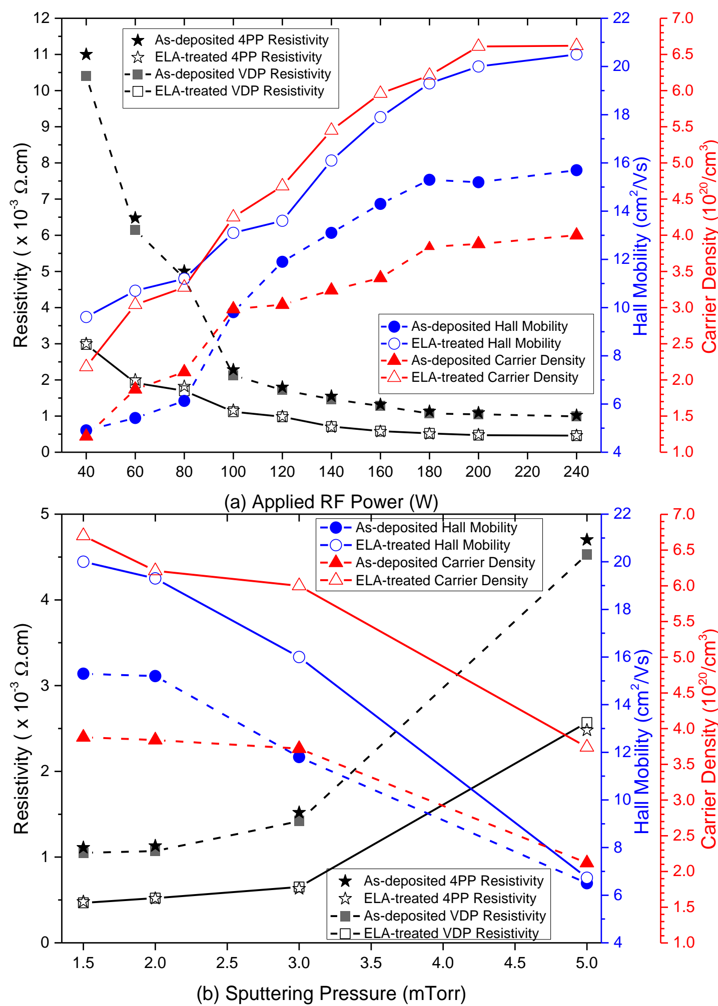

Fig. 5-18. The effect of optimum ELA (5 pulses at 125 mJ/cm² in air) on the electrical properties of all the as-deposited AZO samples, (a) as a function of RF power, and (b) as a function of sputtering pressure.

Fig. 5-19 presents AFM images for a 1 µm ×1 µm areas of the optimised as-deposited AZO samples pre and post ELA with 5 pulses at 125 mJ/cm^2 in air. AFM images showed that the Root Mean Square (R_{RMS}) roughness is reduced after ELA from to 1.72 nm 1.46 nm. This indicates more compact structure with less voids compared to the as-deposited samples. Also, the images demonstrated that ELA resulted in a limited surface particle enlargement. Consequently, the internal trap states density and electron scattering centres at grain boundaries and inter-grain voids are reduced leading to better conductivity [93, 97].

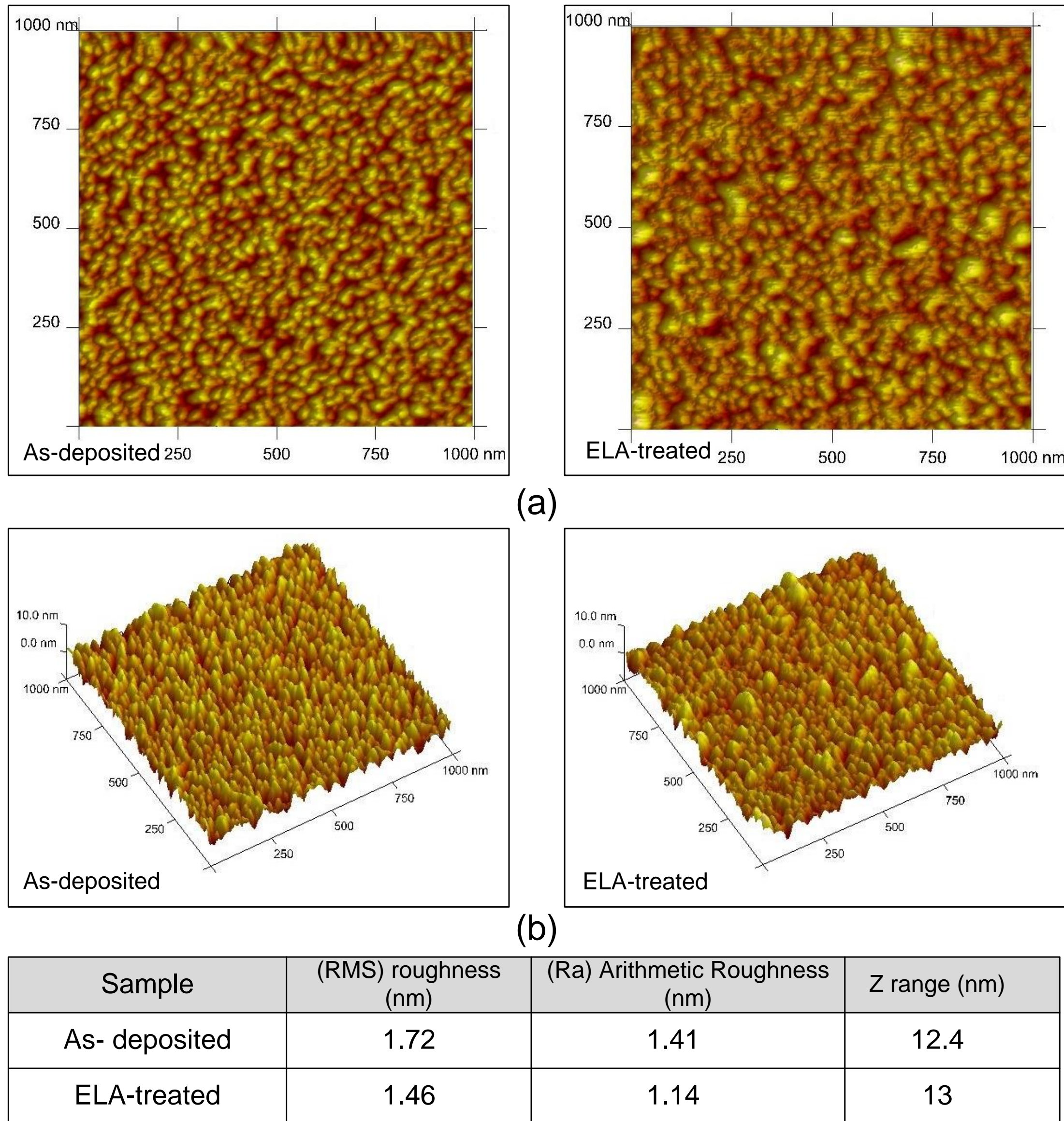

Sample	(RMS) roughness (nm)	(Ra) Arithmetic Roughness (nm)	Z range (nm)
As- deposited	1.72	1.41	12.4
ELA-treated	1.46	1.14	13

(c)

Fig. 5-19. (a) AFM plan view images, (b) 3-D images, and (c) roughness details for AZO pre and post ELA.

The observed enhancements in the electron density (from 3.84×10^{20} to 6.21×10^{20}/cm^3) and Hall mobility (from 15.3 to 19.3 cm^2/Vs) for the optimum as-deposited samples upon ELA are

well justified with the XRD and XPS data discussed in the above sections. The average grain size enlargement from 35.70 nm to 45.80 nm upon ELA observed from the XRD data study indicates that the microstructural defects, inter-grain discontinuities, and grain boundaries are reduced leading to enhancing electron density and mobility [28, 39, 97]. Considering the XPS results, the reduction of O1s(II) component of O1s XPS data reveals reduced electron trapping and scattering at grain boundaries. [80, 92]. Moreover, The ELA-induced heating activated the Al atoms into the ZnO lattice leading to free carrier generation [92, 93, 97].

Fig. 5-20 compares the electrical properties for AZO samples of different thickness before and after ELA. All the films showed resistivity reduction due to increasing both the free carrier density and Hall mobility. These improvements are well explained with the observed changes in XRD data as discussed earlier Fig. 5-6 and Fig. 5-8. The 50 nm-thick AZO sample demonstrates the potential for high quality transparent electrodes at relatively small thickness upon ELA. The achieved resistivity for this sample is $9.25\times10^{-4}\Omega$.cm and the visible transmission is 92% (at λ=550 nm). The deposition time for a 50 nm thick AZO coating at the optimised conditions is about 3 min, and the required laser energy for ELA processing is rather low 75 mJ/cm^2. These conditions are encouraging for cost-efficient and large-area fabrication of AZO transparent electrodes.

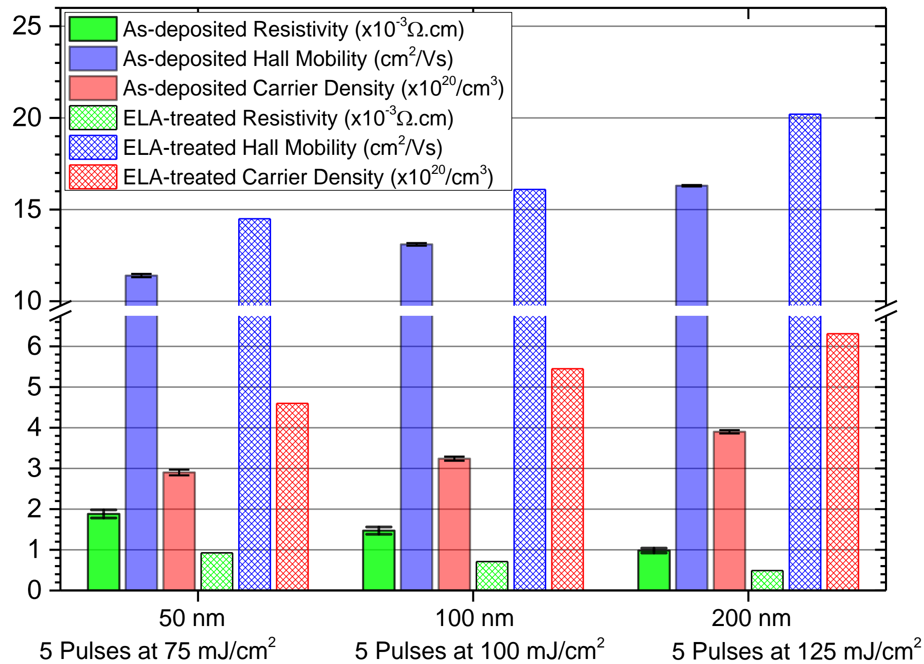

Fig. 5-20. ELA effect on the electrical characteristics (ρ, N, and μ) of AZO samples of different thickness.

The effect of ELA environment on the achieved electrical characteristics of AZO was also examined. The optimised AZO films were ELA-treated at (5 pulses at 125 mJ/cm^2) in different

environments of nitrogen or argon to eliminate any chances for oxygen chemisorption into the samples during processing, which is likely to degrade the samples' conductivity [42, 194]. The annealed samples were placed in a stainless steel pressure cell that was purged with the desired annealing environment gas three times to clear away any traces of air. Then, it was filled with the annealing gas at a pressure of 150 psi. The cell has a UV transparent window through which the laser pulses can reach the sample. Hall Effect measurements showed that the achieved resistivity reduction via annealing in nitrogen or argon is very close to that obtained when AZO is annealed in air, with argon being slightly better than others as depicted in Fig. 5-21. Looking at the free carrier density, annealing in nitrogen or argon ambient results in carrier density of 7.37×10^{20} cm^{-3}, and 7.43×10^{20} cm^{-3} respectively, which are higher than that for films annealed in air that provided 6.21×10^{20} cm^{-3}. This could be attributed to oxygen vacancies generation in the former samples compared to annealing in air, which contains an oxygen ratio by volume of 21 %. However, the Hall mobility was reduced by 6% upon annealing in nitrogen or argon. This is due to the electron density increase leading to increasing the contribution of ionised impurity scattering into the carrier mobility [39, 176]. Hence, the resistivity of AZO annealed in nitrogen and argon was marginally reduced (by 10%) compared to those annealed in air. Also, the carrier density increases when AZO is annealed in nitrogen or argon degrades the AZO transmission in the NIR region. Thus, air is the optimum annealing environment for the ELA of AZO reported in this work.

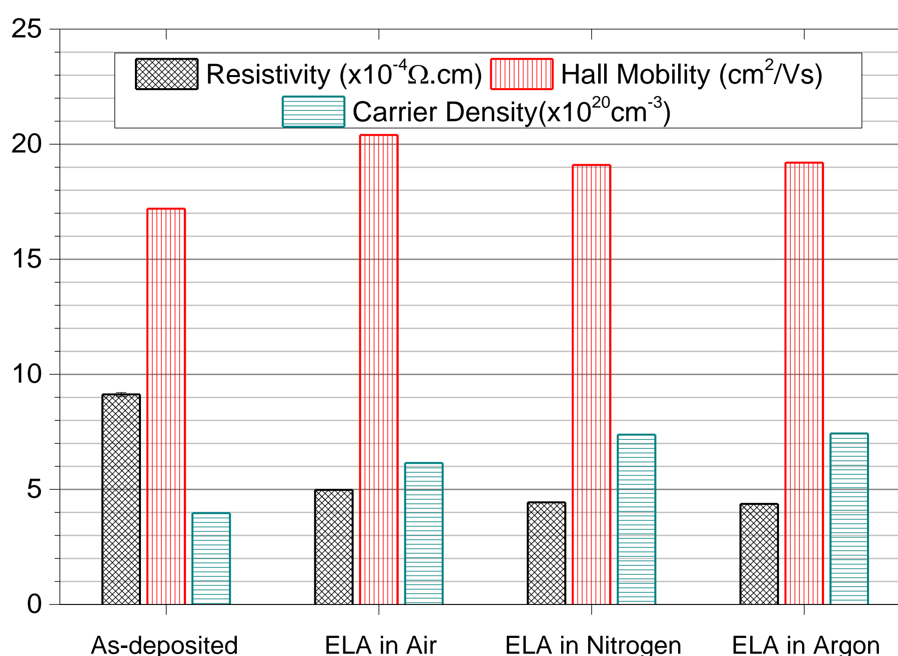

Fig. 5-21. The effect of ELA environment on the achieved electrical characteristics of AZO samples.

In regard to the RTA effect on the AZO electrical properties, Hall Effect measurements showed that increasing the annealing target temperature to 300°C at a dwell time of 20s resulted in increasing both the free electron density and Hall mobility leading to reducing the AZO samples resistivity as shown in Fig. 5-22. These electrical properties enhancements are explained by the observed XRD and XPS data presented earlier. RTA at 300°C and 20s results in grain size increase indicating enhanced crystal structure and defects reduction such as grain boundaries. XPS data also showed that RTA enhanced the samples microstructure and activated Al atoms into the ZnO lattice providing free electrons to the conduction band, in agreement with previous reports [78, 192]. According to the Seto model for polycrystalline materials electrical characteristics [43], the free electron density increase upon ELA or RTA treatments deactivates the trap states at the grain boundaries and reduces the carrier-depleted regions on the grain boundary sides. Therefore, the impact of the potential barriers between adjacent grains on the free electron mobility is reduced leading to better conductivity [39, 43].

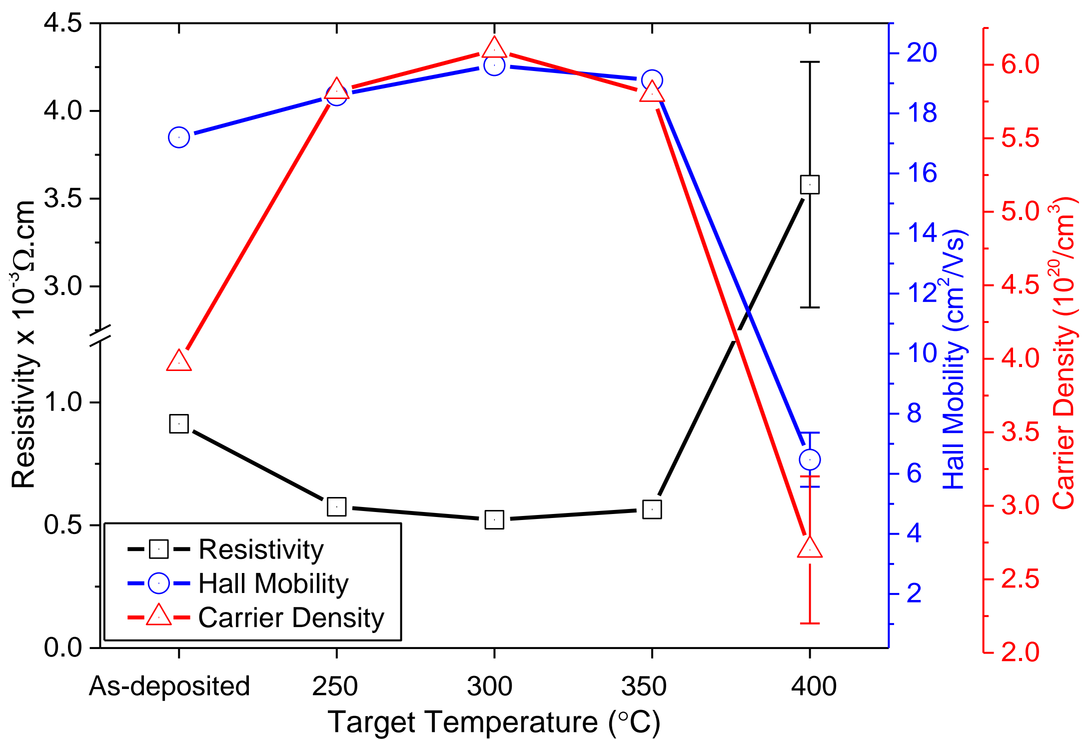

Fig. 5-22. Changes in the electrical characteristics of the optimised as-deposited AZO films upon RTA at different target annealing temperatures for 20 second.

Processing at higher temperature than 300°C or longer dwell time than 20s results in either no further resistivity reduction or in resistivity increase, as in Fig. 5-22 and Fig. 5-23, which is attributed to material loss at these conditions as discussed in the XRD results at the end of

section 5.5.1. Hence, the optimum RTA profile is a target temperature of 300˚C and a dwell time of 20s. This processing profile is very promising for process scaling up.

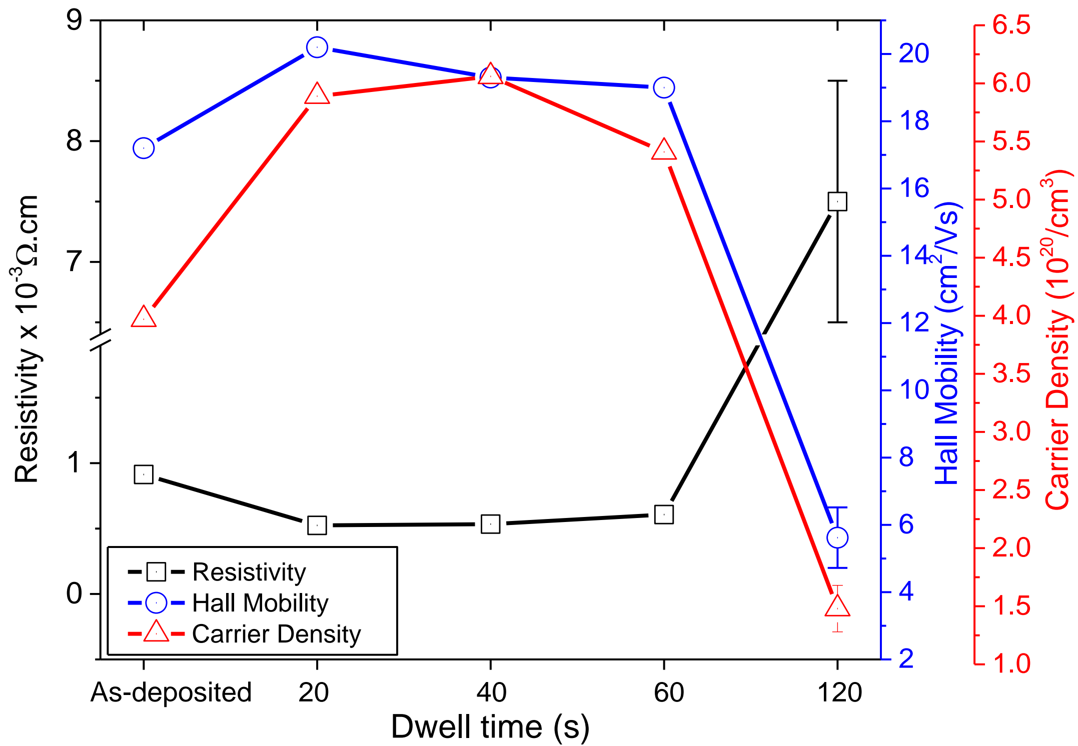

Fig. 5-23. Changes in the electrical characteristics of the optimised as-deposited AZO films upon RTA at 300°C and for different dwell times.

Fig. 5-24 shows AFM images for the optimised AZO pre and post RTA (300˚C-20s- in nitrogen). The images illustrated that RTA treatment results in smoother thin film surface and more closely packed surface particles with less inter-grain discontinuities compared to as-deposited and ELA-treated AZO samples. The Root Mean Square (R_{RMS}) roughness for the RTA-traded sample is 1.14 nm compared to 1.72 nm for the as deposited sample. Similar to the ELA-treated samples, the AZO samples' roughness reduction observed via AFM upon RTA reveals more compact columnar structure with less inter-grain voids [174]. This would result in enhanced electrical conductivity compared to as-deposited samples [97].

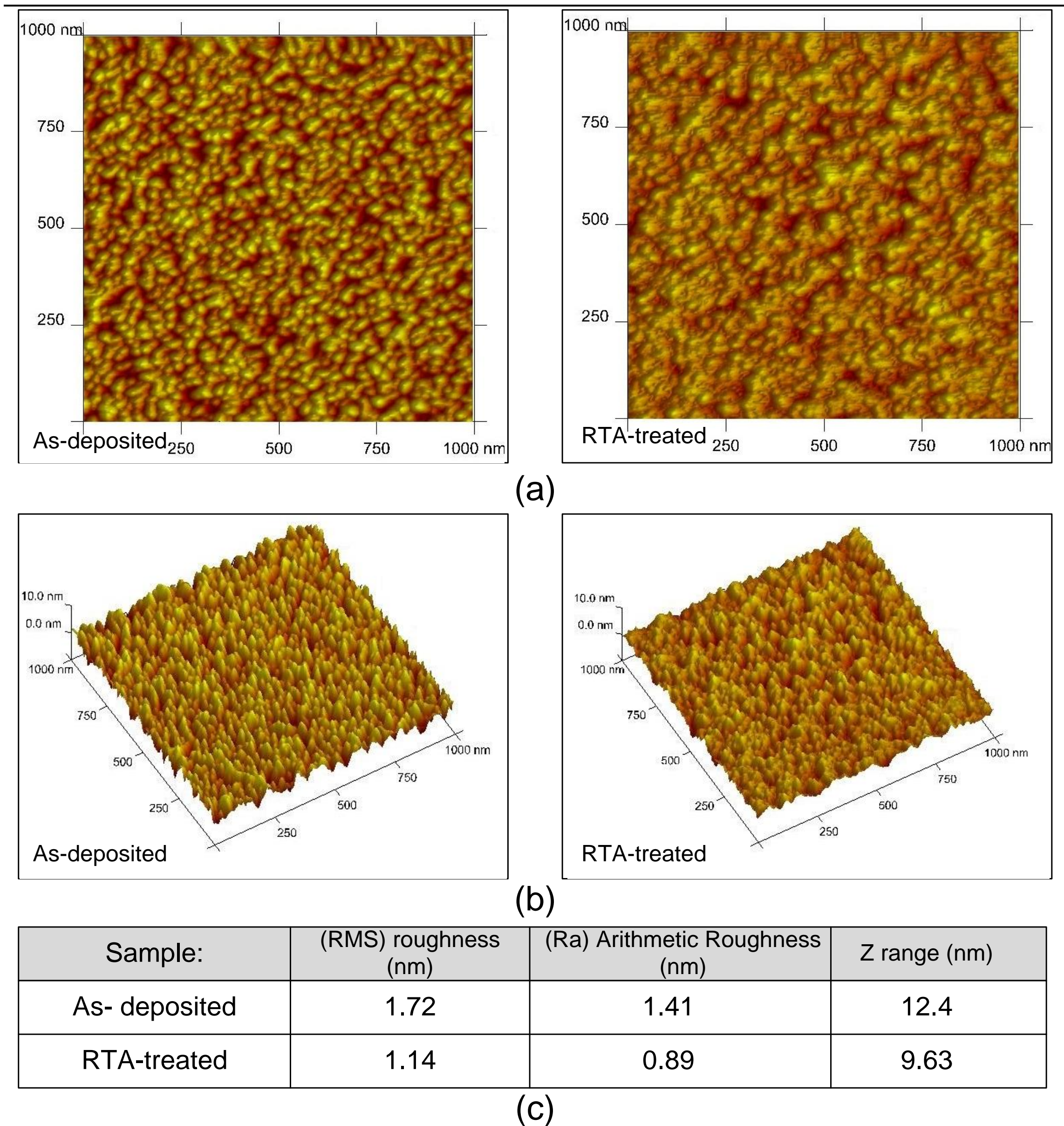

Sample:	(RMS) roughness (nm)	(Ra) Arithmetic Roughness (nm)	Z range (nm)
As- deposited	1.72	1.41	12.4
RTA-treated	1.14	0.89	9.63

(c)

Fig. 5-24. AFM plan view images, (b) 3-D images, and (c) roughness details for AZO pre and post RTA

The optimised ELA and RTA treatments resulted in similar resistivity values. However, different annealing mechanisms are involved, in ELA gradient heating/annealing is performed over the sample thickness, with the top layer of the annealed sample being predominantly affected by the ELA-induced heating relative to the bottom layer. This leads to spatial variations in the microstructural and electrical characteristics created along the samples thickness. As a result, the obtained resistivity upon ELA could be more assigned to the top layer of the samples. However, the obtained resistivity upon RTA is for the entire samples thickness due to uniformly distributed heating/annealing in RTA over the sample thickness and longer annealing time. Both the optimised ELA and RTA annealing conditions demonstrated very small deviations when applied

throughout this research to fabricate the needed AZO samples for the conducted experimental work as shown in Appendix A.

Applying the combination of ELA-RTA or RTA-ELA results in a limited further reduction in resistivity as demonstrated in Fig. 5-25. The resistivity reduction upon RTA of the initially ELA-treated samples could be due to annealing of the layer that was not thermally affected by the ELA-induced heating. Relatively higher resistivity reduction was observed if the samples were initially RTA-treated and then followed with ELA with 4 pulses at 125 mJ/cm^2. This could be attributed to the observed reduction of the chemisorbed oxygen-related defects at grain boundaries (O1s(II) component) upon ELA-treatment, as shown by the XPS results Fig. 5-13, leading to further enhancements in the electrical properties to the previously RTA-treated samples. It was demonstrated that the resistivity of the RTA-treated samples increased when the number is increased to 5, this was observed for three samples and could be due to material ablation.

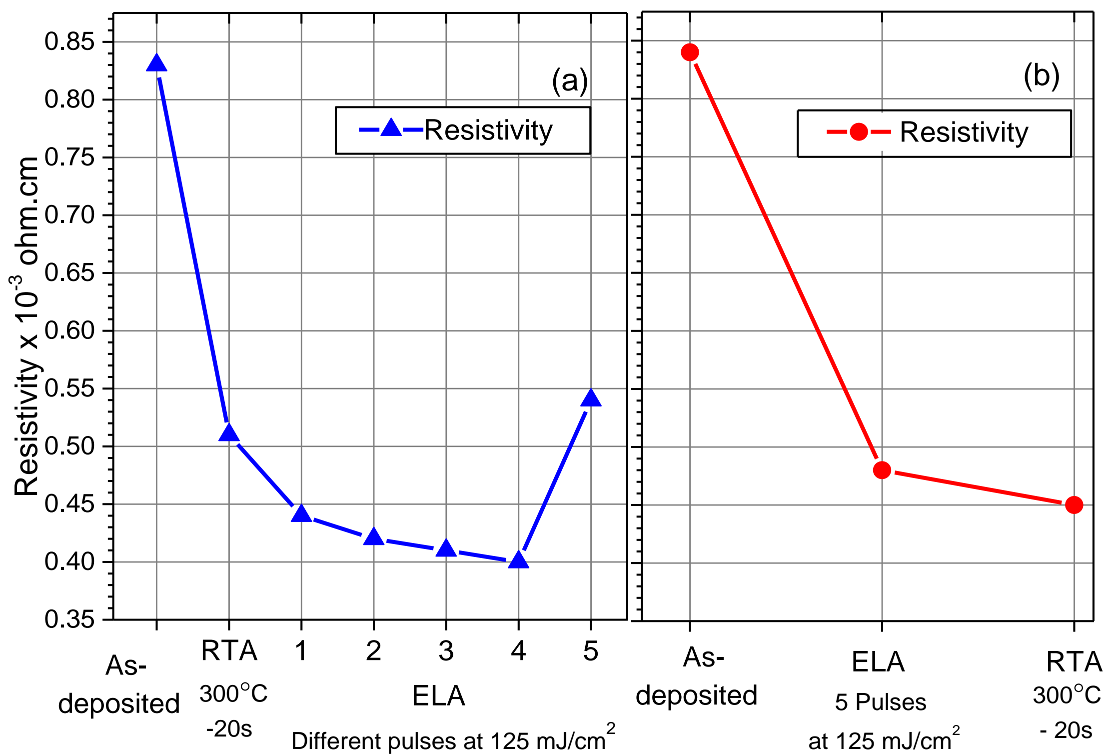

Fig. 5-25. The resistivity changes upon ELA and RTA combination, (a) AZO samples were initially RTA-treated followed by ELA at 125 mJ/cm^2 at different number of pulses, (b) AZO samples ELA-treated then RTA-treated at the optimised conditions.

5.5.4 Influence of ELA and RTA on the AZO optical properties

The visible transmittance for both ELA and RTA treated AZO samples at the optimised conditions is enhanced to 86% and 88% (at λ=550 nm) respectively compared to 82% for the optimum as-deposited samples as shown in Fig. 5-26.

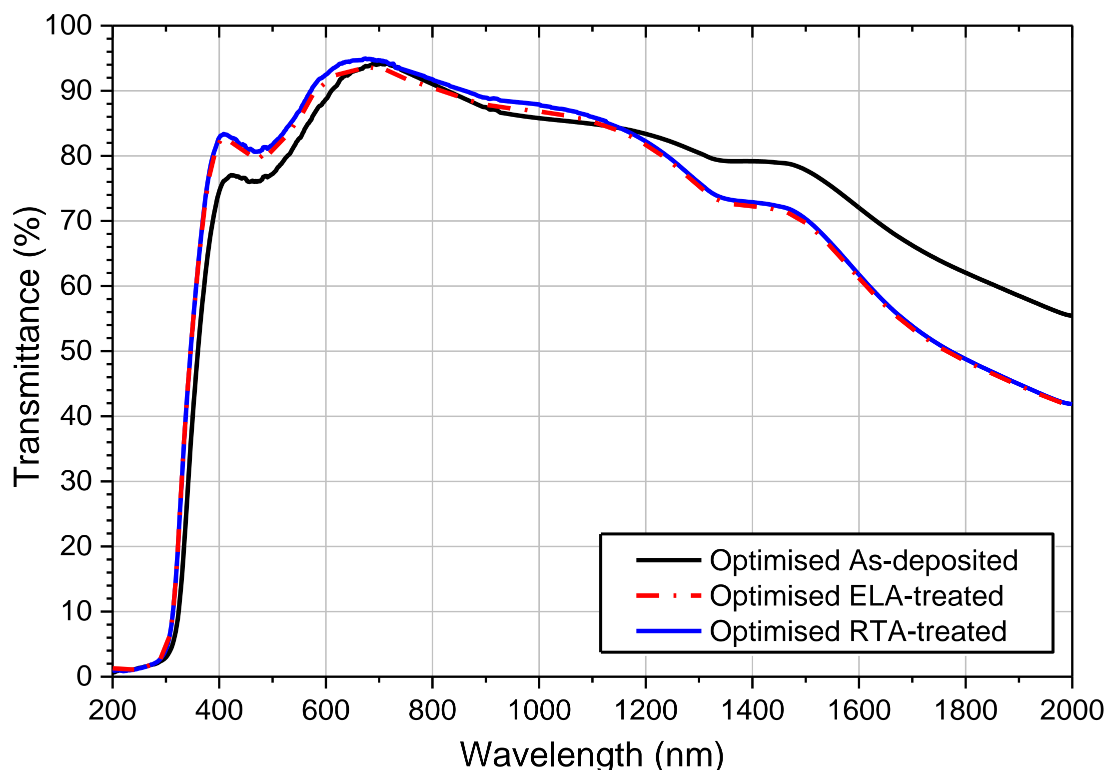

Fig. 5-26. The optical transmittance of the optimised as-deposited AZO after ELA and RTA treatments.

This enhancement is attributed to reduced optical scattering and absorption due to reduction of microstructure defects including surface roughness, inter-grain discontinuities, grain boundaries, and the chemisorbed oxygen-related defects, as demonstrated by the presented AFM, XRD, and XPS results discussed above [80, 188]. The slightly better visible transmittance of the RTA treated AZO sample compared to the ELA-treated one would be attributed to the relatively smoother and compact surface of the former sample as shown in the presented AFM images, leading to less light scattering at the sample surface.

Moreover, the AZO bandgap was widened (the absorption edge was blue shifted) after ELA and RTA, as shown in Fig. 5-27.

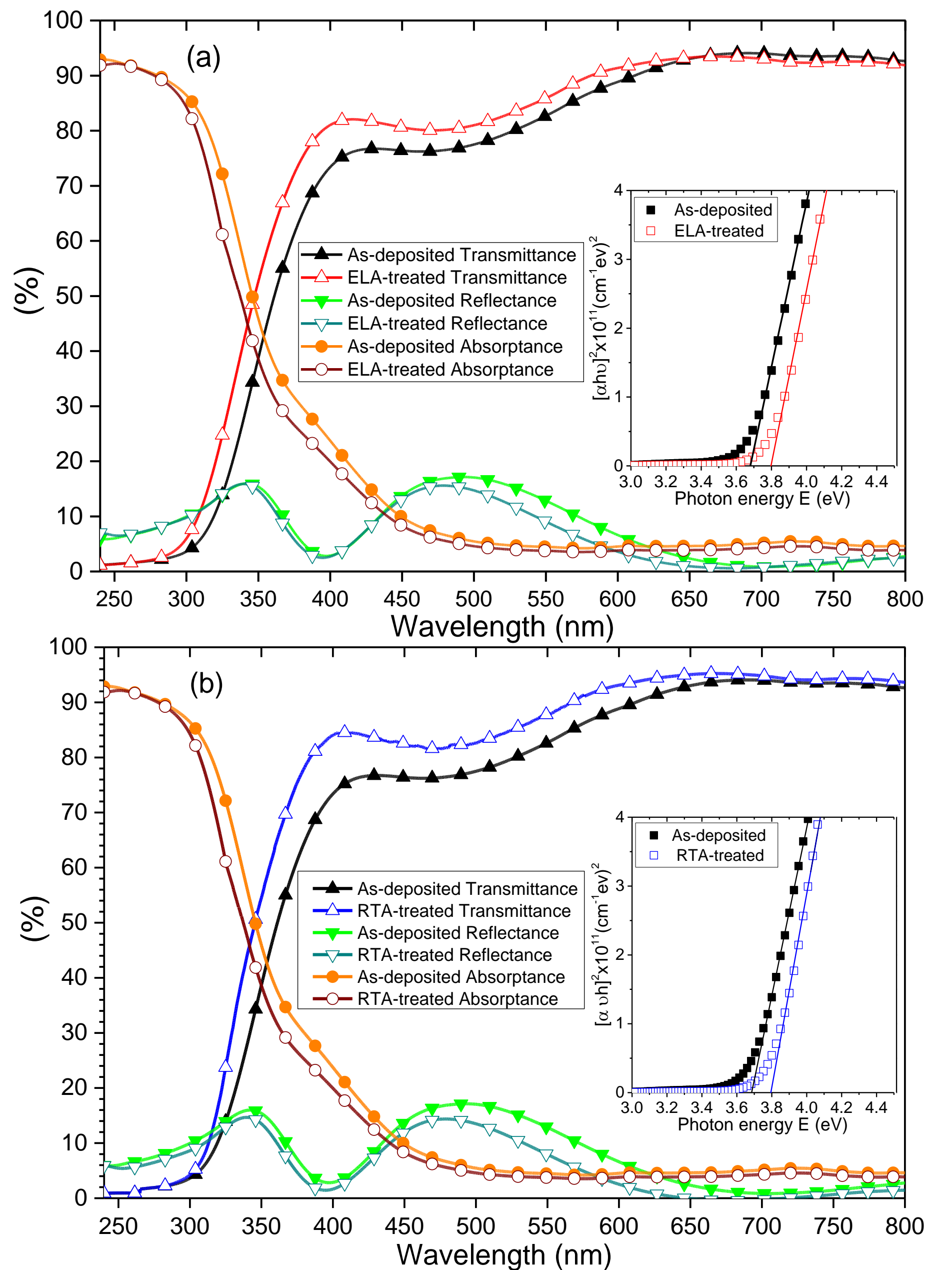

Fig. 5-27. UV/VIS transmittance, reflectance, and absorptance spectra for the optimised AZO, (a) after ELA, (b) after RTA. The inset graphs show linear extrapolations of Tauc's plot for bandgap estimation.

According to the Burstein-Moss model [32], the bandgap enlargement is originated from the electron density increase upon annealing resulting in populating the electron trap states at the conduction band minimum and therefore pushing the Fermi level further in the conduction band. Consequently, higher energy photons are needed for exciting an electron from the valence band maximum to unoccupied states higher than the Fermi level. Fig. 5-27 also shows the high absorptance of AZO samples at the used laser wavelength (KrF 248 nm). The bandgap Eg for the optimum as-deposited AZO (deposited at RT, 180 W, and 2 mTorr of 0.2% oxygen to argon

ratio) was estimated by Tauc et al. model [147], and found to increase from 3.69 to 3.80 eV after ELA (with 5 pulses at 125 mJ/cm^2 in air), and also to 3.80 eV after RTA (at 300°C for 20s in nitrogen) as illustrated in the inset graphs of Fig. 5-27. However, upon annealing ELA or RTA, the transmittance spectra at longer wavelengths (NIR region λ > 1000 nm) showed a decrease that corresponds well to the observed free electron density increase upon annealing resulting in shifting the plasma wavelength towards shorter wavelengths. Consequently, the free electron absorption or reflection increased [32, 80].

5.6 International Electrotechnical Commission (IEC) test 61646 on AZO

The Electrotechnical Commission (IEC) 61646 test is the commonly applied procedure to examine long-term stability and degradation rates of materials for potential applications in harsh environments, such as PVs. The test also helps to understand the mechanisms involved in materials degradation and to find solutions for stability improvement. In this test, the essential characteristics for a material under consideration are monitored in a controlled environment at a temperature of 85°C and 85% relative humidity (RH) for 1000h (~ 41 days) [195, 196]. AZO is one of the commonly used TCOs in PVs like CIGS (Cu(in,Ga)Se_2) as a charge transport layer. The long term stability of AZO is directly linked to the PVs' efficiency stability [195, 197].

Sample	Deposition details	Annealing details	Thickness (nm)
As-deposited AZO	RT, 180 W, and 2 mTorr of 0.2% O_2 in Ar	No	180
As-deposited AZO	RT, 180 W, and 2 mTorr of 0.2% O_2 in Ar	No	360
As-deposited AZO	RT, 120 W, and 2 mTorr of 0.2% O_2 in Ar	No	180
As-deposited AZO	RT, 180 W, and 5 mTorr of 0.2% O_2 in Ar	No	180
ELA-treated AZO	RT, 180 W, and 2 mTorr of 0.2% O_2 in Ar	5 pulses at 125 mJ/cm^2 in Air	180
RTA-treated AZO	RT, 180 W, and 2 mTorr of 0.2% O_2 in Ar	300°C for 20s in Nitrogen.	180
ITO on glass	Purchased from Kintec Company for comparison		150

Table 5-6. Details of AZO and ITO samples subjected to the (IEC) test 61646.

The list of AZO and ITO samples on glass substrates detailed in Table 5-6 above was subjected to the (IEC) 61646 test. The test was carried out examining the electrical resistivity stability for the AZO and ITO as a function of the test time. 150 nm-thick high-quality ITO on glass substrates (ρ=1.2x10^{-4} Ω.cm) from Kintec Company were also examined as a reference for comparison with AZO. The resistivity of the samples was also monitored after the test duration at

room temperature in air to elucidate any possible changes that could be caused upon the damp heat exposure. A THERMOTRON Test Chamber was used for the test. A short run of the test was performed for ten days to examine the used chamber stability at the test conditions, and it was found that the chamber maintains well the test conditions over long operating times demonstrating ~2% humidity changes. For the (IEC) 61646 test, a set of four AZO and ITO samples of the same fabrication conditions was used, and one sample of each group was taken out of the chamber every ten days of the test period for resistivity characterisation by 4-point probe. Also, all the samples had Hall Effect measurements performed before and after the 41 days test. Prior to the IEC 61646 test, the samples resistivity was monitored at room temperature in air and all the samples demonstrated an excellent stability as shown in Fig. 5-28 and Fig. 5-29.

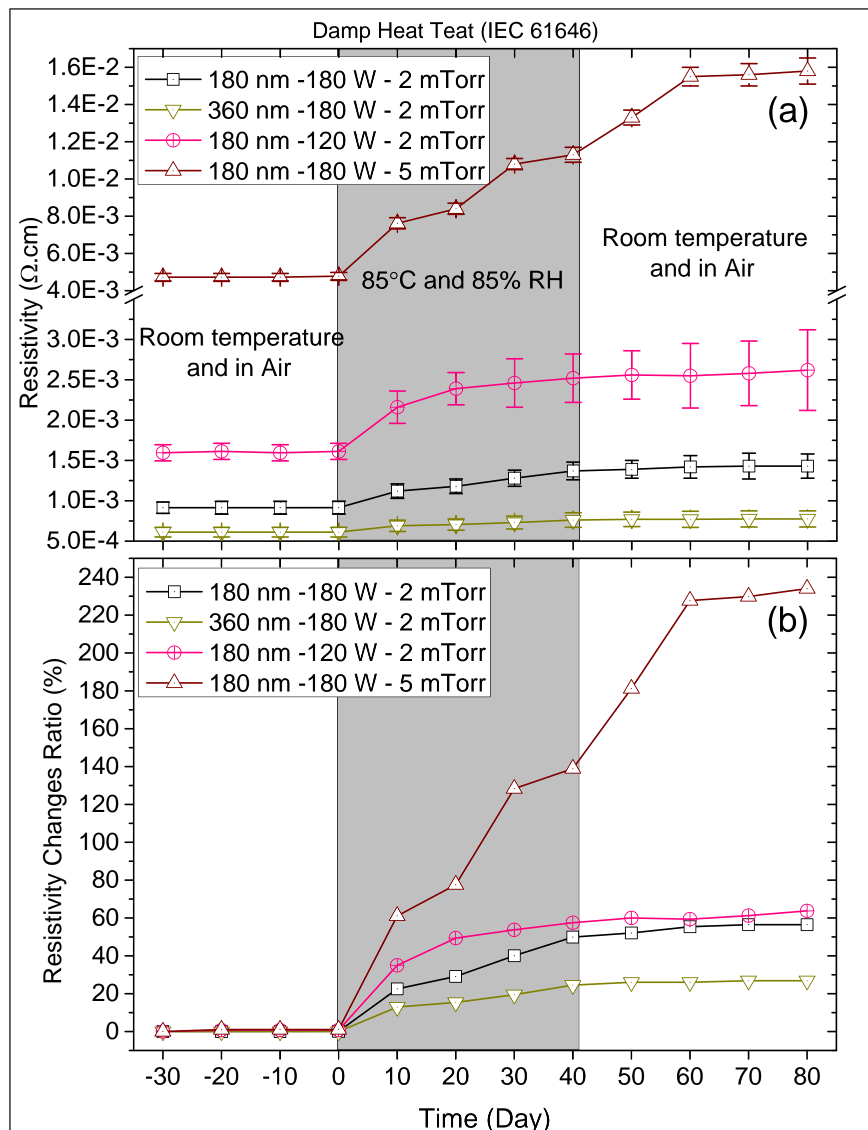

Fig. 5-28. (a) The electrical resistivity changes for AZO samples of different growth conditions as a function of the (IEC) 61646 test time, and (b) the resistivity changes ratio.

However, during the test the resistivity was increased with the test time at various rates depending on the fabrication conditions. Considering the AZO samples of different growth conditions, a substantial resistivity increase of 140% during the test period was observed for the AZO samples deposited at high sputtering pressure (5 mTorr). Moreover, the resistivity of these samples kept increasing even after the test period demonstrating 230% resistivity increase within 40 days after the test. This is attributed to the relatively smaller grain size, i.e. higher density of grain boundaries, rougher surface, larger effective surface, and more surface discontinuity defects compared to growths at 2 mTorr as discussed in chapter 4. Consequently, the 5 mTorr samples adsorb more defects (O_2 and H_2O) from the test environment leading to increasing the electrons trapping and scattering, this will end up with higher resistivity samples [195, 196]. Increasing the samples thickness from 180 nm to 360 nm was found to lead to a noticeably enhanced stability against the test. The 360 nm-thick sample showed just over 20% resistivity increase maintaining a low resistivity of 7.7×10^{-4} Ω.cm even after the test exposure, compared to a nearly 40% resistivity increase that the 180 nm samples showed. This is assigned to relatively large grain size of 48 nm compared to 34 nm grain size for the180 nm samples. This indicates a lower density of grain boundaries and more compact structure for thicker samples. Thus, the 360 nm sample was affected less by the test ambient and the chemisorbed defects [198]. Fig. 5-29 compares the resistivity changes for the optimised AZO films (as-deposited, ELA-treated, and RTA-treated) with the reference ITO. The ITO samples were very stable showing <10% resistivity increase. The annealed (ELA or RTA) AZO samples demonstrated lower resistivity compared to the as-deposited samples after the test. However, the RTA-treated samples showed noticeably better stability compared to the ELA-treated ones, this could be attributed to smother surface and more compact structure for the former, as shown earlier via the AFM images in Fig. 5-19 and Fig. 5-24, leading to less adsorbed defects. The ELA-treated samples resistivity recovered to values very close to that of the optimised as grown samples and exhibited an increasing trend even after the test period. It was observed by XPS data (in section 5.5.2) that ELA reduces the chemisorbed oxygen-related defects such as oxygen atoms, hydroxides, and carbonates at grain boundaries; this could lead to more chances to adsorb O_2 and H_2O species via grain boundaries when the ELA-treated AZO samples are exposed to the test conditions leading to increasing the samples resistivity. The behaviour of the ELA-treated AZO samples upon the test could be related to the

stratified nature of these samples caused by the gradient heating/annealing over the thickness. This results in the annealing being more localised to the top layer achieving better microstructural and electrical characteristics compared to the bottom layer. Hence, upon the test the top layer is in direct contact with the test environment and therefore is more affected by the adsorbed defects. Further investigations are needed to explain the behaviour of the ELA-treated AZO samples.

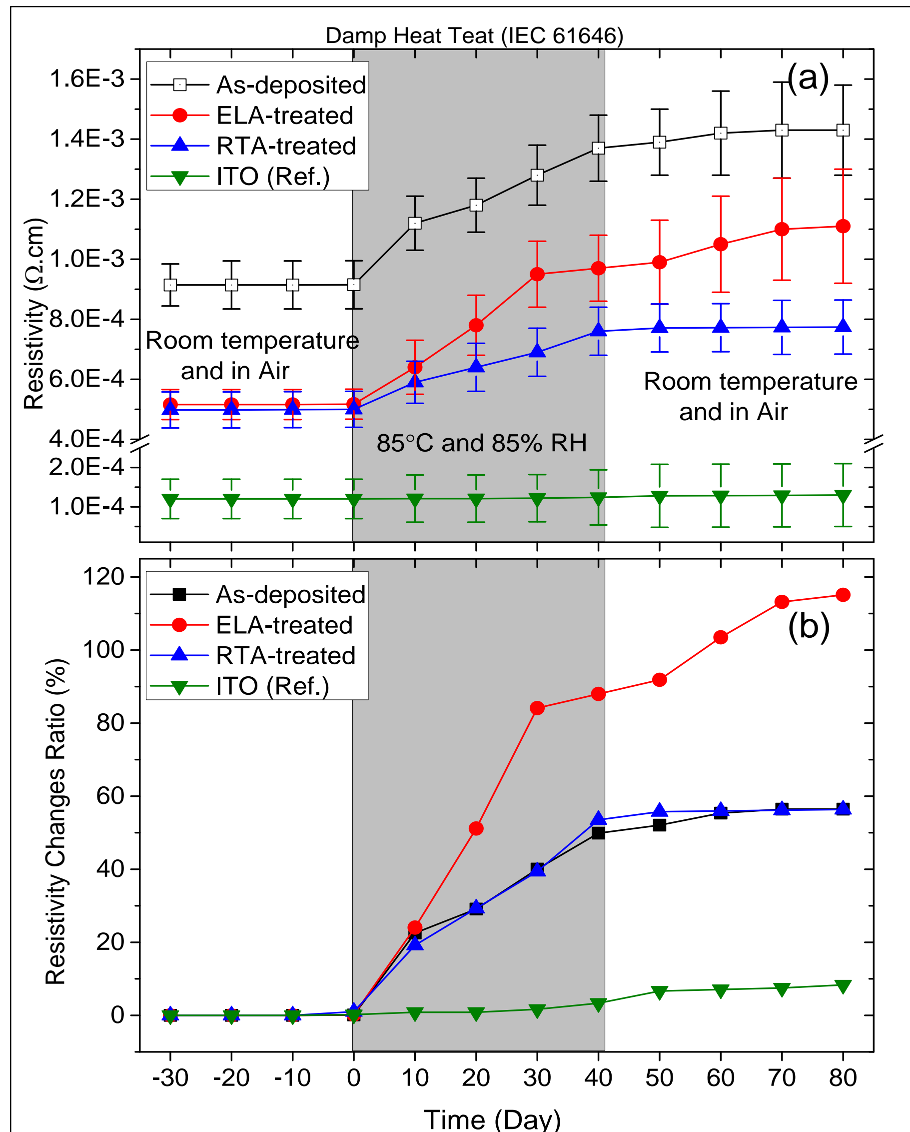

Fig. 5-29. (a) The electrical resistivity changes for the optimised AZO samples and the ITO reference samples as a function of the (IEC) 61646 test time, and (b) the resistivity changes ratio.

To understand the cause of the observed resistivity increase upon the test, Hall Effect measurements were performed on all the AZO and ITO films before and after the test. It was revealed that both the free electron density and mobility are degraded upon the test as shown in Fig. 5-30, leading to higher resistivity values.

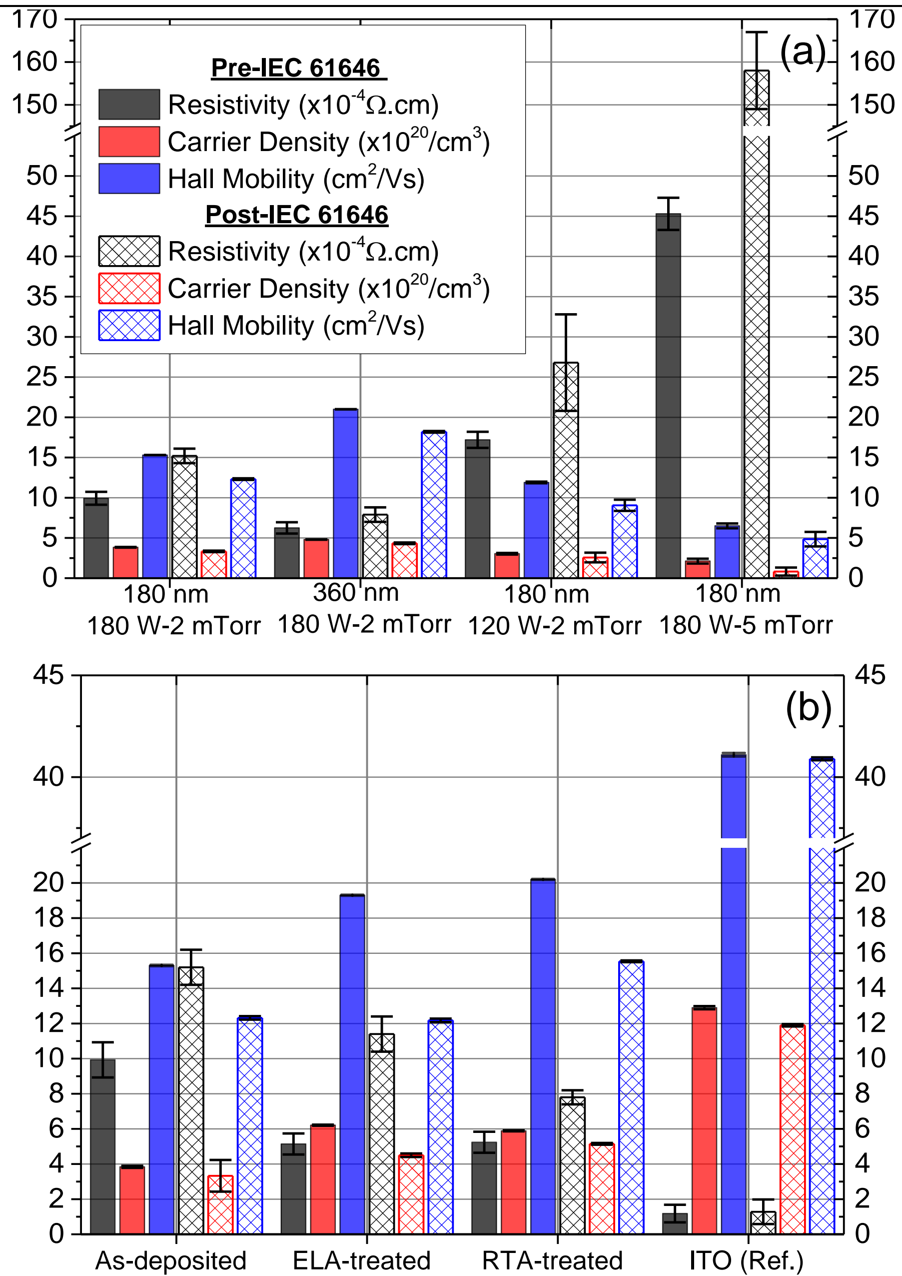

Fig. 5-30. The electrical properties for the examined AZO and ITO samples pre and post the IEC 61646 test, (a) different AZO growth conditions, and (b) the optimised AZO samples and the ITO reference

Y.-S. Liu et al. [196] and D.-w. Lee et al. [197] have shown via XPS measurements that the damp heat test decreases the oxygen vacancies and increases the oxygen-related defects for the examined AZO samples. These observations were attributed to O_2 and H_2O diffusion through grain boundaries and surface voids. This would explain the electron density and mobility degradation, and the degradation mechanisms could be explained as follows:

1. During the test, O_2 and H_2O defects from the humid ambient diffuse into the examined samples via grain boundaries and inter-grain voids. These defects trap electrons from grains, i.e. *N* reduction, causing electrons-depleted areas on both sides of grain

boundaries. Consequently, the potential barriers between grains are increased leading to electron scattering at the grains' boundaries, i.e. μ reduction, [195, 196].

2. The diffused O_2 and H_2O species into the AZO films would result also in reducing the oxygen-vacancies concentration and thus the free electron density. The electron density reduction would strengthen the impact of the grain boundaries on the mobility due to increasing the electron-depleted areas within the grains [195, 196].

5.7 AZO films for potential application in photovoltaics

TCOs	Deposition details	Processing details	Transparency at λ= 550 nm (%)	ρ (Ω.cm)	OPVs Efficiency (%)
As-deposited AZO	180 nm, at room temperature, 180 W, and 2 mTorr of 0.2% O_2 in Ar	No	82%	$1.0x10^{-3}$	1.40
ELA-treated AZO		5 Pulses at 125 mJ/cm^2 in Air	86%	$5.2x10^{-4}$	2.06
RTA-treated AZO		300°C for 20s in Nitrogen	88%	$5.2x10^{-4}$	2.10
ITO on glass	150 nm, purchased from Kintec Company		88%	$1.2x10^{-4}$	2.17

Table 5-7. Details of AZO and ITO samples used for photovoltaics test, and the achieved efficiency.

AZO films were deposited on microscope slides at the optimised conditions followed by the optimum ELA and RTA treatments, and commercial high-quality ITO coated glass substrates, from Kintec Company, were used to fabricate P3HT:PCBM organic photovoltaic devices at Sheffield Hallam University. Dr. Vikas Kumar is acknowledged for his help in performing this test. The OPVs fabrication and characterisation procedure is reported elsewhere in Dr. Vikas Kumar publications [199]. The OPVs structure is depicted in Fig. 5-31.

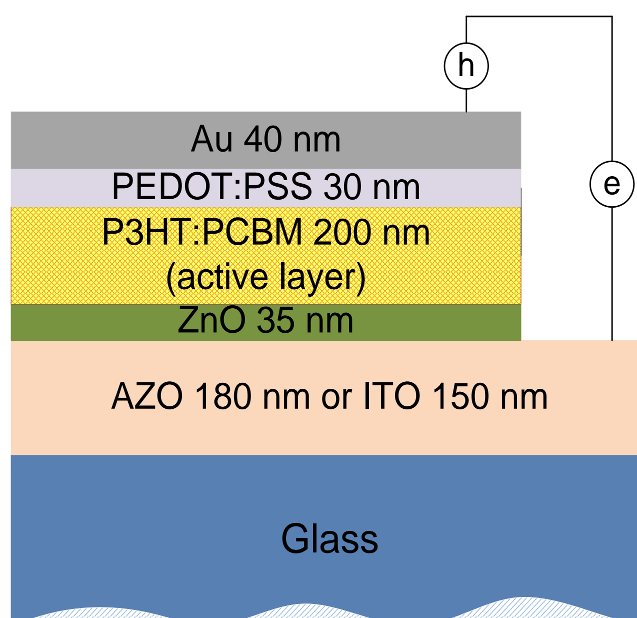

Fig. 5-31 Schematic illustration of cross section for the examined OPV devices

As shown in Table 5-7 above, OPVs fabricated on the optimum ELA and RTA treated AZO samples shown comparable power conversion efficiency (PCE) to the reference OPVs on ITO. The PCE enhancement for the treated AZO (ELA or RTA) compared to the as-deposited AZO is attributed to the observed microstructure, electrical, and optical properties upon ELA and RTA. It is worth noting that, the active layer for the examined OPVs (P3HT:PCBM) exhibits a high absorption coefficient in the visible range (350-650 nm) [199]. Hence, the optical transmittance enhancement for AZO electrodes after ELA or RTA should result in better PCE. The whole test was repeated three times and the performance of OPVs with the ELA and RTA treated AZO was always found to be very close to the reference OPVs with the high-quality commercial ITO. These findings present that AZO as a good candidate for ITO alternatives in photovoltaics.

5.8 Concluding remarks

Post-deposition annealing studies were carried out on room temperature sputter-deposited AZO films via two different techniques, namely excimer laser annealing (ELA) and rapid thermal annealing (RTA). Various experimental techniques for material characterisation were used to elucidate the effect of different annealing parameters on AZO. Both ELA and RTA results demonstrate enhanced electrical and optical properties of AZO. These enhancements were studied in detail and are attributed to microstructural defects reduction and effective Al dopant incorporation into the ZnO upon annealing. The findings of this chapter present two large-area compatible annealing techniques that could be used to further enhance the electro-optical characteristics of room temperature deposited AZO for various electronics. The annealed AZO films at the optimised parameters for both ELA and RTA are ranked among the highest quality ZnO-based TCOs with electro-optical characteristics very close to those of high-quality ITO. Compared to the reported literature on laser annealing of AZO, this chapter examines ELA on AZO samples deposited at a wide ranges of conditions. Also, this chapter compares between ELA and RTA. It should be mentioned that the concluded annealing parameters (ELA and RTA) demonstrated a good reproducibility. In addition, when the optimally fabricated AZO electrodes were integrated into OPVs, comparable efficiency to that achieved with using commercial high-quality ITO was observed. In regard to the environmental robustness of AZO, it was demonstrated that the samples stability under 85°C and 85% RH for 1000h depends on the fabrication conditions applied. The best stability was obtained for thicker AZO (360 nm).

6 Low Thermal Budget Fabrication of IGZO Thin Film Transistors

6.1 Introduction

This chapter presents the work undertaken to investigate low thermal budget fabrication of indium gallium zinc oxide (IGZO) thin film transistors (TFTs) via room temperature sputter-deposition by RF magnetron sputtering followed by KrF-ELA. Oxide TFT electrical performance is generally affected by a wide range of fabrication conditions which are materials and geometry based such as the semiconducting active layer intrinsic characteristics, nature of the source, drain, and gate electrodes, gate dielectric, and the TFT geometry [7, 48]. In this research, the overall target is to examine the potential of ELA as a low thermal budget processing technique to enhance the performance of IGZO TFTs. The first phase of this task was to fabricate suitable IGZO films for TFTs via an investigation of the effect of sputter-deposition and ELA parameters on IGZO films. The electrical resistivity of IGZO thin films was found to be strongly dependent on the deposition parameters including the applied RF power, oxygen to argon ratio, sputtering pressure, and the sputtering target composition. ELA was very effective to tune the electrical properties of IGZO over a wide range. The second phase was to adopt a set of deposition and ELA conditions for TFTs fabrication on silicon substrates. TFT performance was found to be highly dependent on the growth parameters of IGZO active layer. Subsequent ELA with single pulse and very low energy density noticeably enhanced the performance of IGZO TFT. The identified optimum ELA treatment was successfully applied to commercial IGZO-TFTs on heat-sensitive polyethylene naphthalate (PEN) resulting in enhancement of the devices performance.

6.2 IGZO thin films sputter-deposition investigation

Investigated deposition parameters		**Investigated range of parameters**		
		RF Power (W)	O_2 to Ar ratio (%)	Sputtering Pressure (mTorr)
***IGZO (1:1:1) in mole %**	RF power	50, 75, and 100	2	2
	Oxygen ratio	50	2, 5, and 8	2
	Sputtering pressure	50	2	2, 5, and 8
Target composition in mole %	IGZO (2:1:1)	50	2	2
	IGZO (2:1:2)	50	2	2
	IGZO (2:3:3)	50	2	2

Table 6-1. A summary of the investigated deposition parameters for IGZO thin films.

*IGZO (1:1:1) in mole % = In_2O_3 (1 mole):Ga_2O_3 (1 mole):ZnO (1 mole).

In order to define guidelines for the dependence of IGZO thin film electrical properties on the deposition conditions, various conditions were examined without external substrate heating as illustrated in Table 6-1, with the overall aim being reliable and reproducible IGZO thin films with moderate-to-high resistivity, hence suitable for TFTs. One parameter was changed at a time, while the others were fixed. All the depositions were performed at a base pressure and a substrate rotation of 3.75 x10^{-4} mTorr and 12 rpm respectively. A mixture of different oxygen to argon ratios was supplied from high-purity gas cylinders via mass flow controllers. 15 minutes pre-sputtering was performed to ensure better plasma stability and IGZO samples properties reproducibility, since the target surface was found to be affected by the last used set of deposition parameters and in particular the oxygen to argon ratio. A similar tendency was reported by [76, 200]. The film thickness was chosen to be 200 nm in order to achieve reliable measurements from the utilised thin-film characterisation techniques; thinner films (40 nm) were used for TFT fabrication. The IGZO films' thickness was monitored via an in-situ interferometric monitor and was cross-checked via Veeco Dektak 6M Stylus Profilometer measurements. In the used sputter-deposition system, the target is tilted in a sputter-up configuration with a target-to-substrate distance maintained at 15 cm. This configuration demonstrated an excellent thickness uniformity across the sample (4-inch diameter) with rather small thickness deviations of ± 5% as measured by the profilometer. The substrate temperature was monitored with an internal thermocouple and was found to be around 30˚C. All the samples were deposited on 4-inch silicon wafers coated with 50 nm of alumina (Al_2O_3) as an insulator, which was also used for TFT fabrication. Before the IGZO deposition, the substrates were ultrasonically cleaned in methanol for 10 minutes and dried with high purity nitrogen. Several 3-inch IGZO (In_2O_3:Ga_2O_3:ZnO) ceramic targets of different compositions and 99.9% purity were used to study the influence of the target composition on the resulting IGZO film electrical resistivity.

6.3 IGZO thin films ELA investigation

As mentioned in chapter 3, ELA offers materials processing at high temperature, while the substrate heating is minimised due to selective laser energy absorption. In this work, post-deposition ELA is applied to IGZO thin films to facilitate low thermal budget integration of IGZO into TFTs. ELA was conducted in air at ambient temperature using a KrF excimer laser (λ=248 nm - pulse duration 25 ns). One pulse was always applied at energy density of 50 -125 mJ/cm^2 in

steps of 25 mJ/cm^2, and with a treatment area of 13 mm x 13 mm. At high laser energy densities 100-125 mJ/cm^2, the IGZO samples become very conductive demonstrating a conductivity close to that of TCOs i.e. not suitable for TFT devices which require semiconducting materials. Therefore, higher laser energy densities than 125 mJ/cm^2 were not investigated.

6.4 TFT devices fabrication and ELA treatment investigation

Top-gate-staggered TFT devices with 40 nm-thick a-IGZO active layer were fabricated in collaboration with PragmatIC Printing Ltd (PPL). In this structure, the TFT active layer IGZO is not exposed to air which could affect the active layer properties such as in bottom-gate design, leading to better TFT stability for the former design [7, 48]. The diagram in Fig. 6-1 illustrates a process flow for the examined TFT fabrication, as per the next steps:

1. A 50 nm-thick alumina (Al_2O_3) thin film is deposited on silicon substrates at PPL.
2. A bilayer 55 nm-thick of titanium 5 nm and gold 50 nm is deposited by evaporation and patterned as the source and drain electrodes at PPL. The titanium is used as an adhesion layer. The bilayer Ti/Au typically achieves good Ohmic contacts with ZnO-based thin films [201, 202], but, it is not desired for fully transparent TFTs. (Note - The optimised AZO transparent electrodes in the previous chapters are worth investigating as source, drain, and gate electrodes for fully transparent IGZO TFTs).
3. A 40 nm-thick IGZO layer is deposited by RF-magnetron sputtering using different deposition parameters at NTU. Generally, IGZO TFTs demonstrate better stability when the active layer thickness 40-50 nm [104, 200]. Also, the used thickness for the examined TFT devices is comparable with the KrF photons' penetration depth in IGZO ~ 45 nm [79] which facilities uniform processing throughout IGZO layer.
4. Then, the IGZO-TFT substrates were subjected to ELA at rather low energy densities (15, 30, 45, and 60 mJ/cm^2). Each of the 4 inch IGZO-TFT substrates was divided to five groups of different laser energy density. Each laser pulse has an area of 13 mm x 13 mm that could easily cover the whole structure of 30 TFTs. The used ELA system is detailed in chapter 3, the system is equipped with a computerised sample stage which offers very accurate and easy sample manipulation in XYZ directions during ELA treatment according to the planned processing map.
5. The IGZO thin film is patterned by photolithography and wet etching at PPL defining the channel dimensions as 5 µm length (L), and 1000 µm width (W).
6. Alumina layer deposited by atomic layer deposition (ALD) and vias etched by photolithography and lift off at PPL as the gate dielectric.
7. A 55 nm-thick bilayer of titanium/gold is deposited by evaporation and patterned as the gate electrodes at PPL. Finally, an automated probe station testing was used for characterising all fabricated TFTs at PPL, and data analysis was undertaken at NTU.

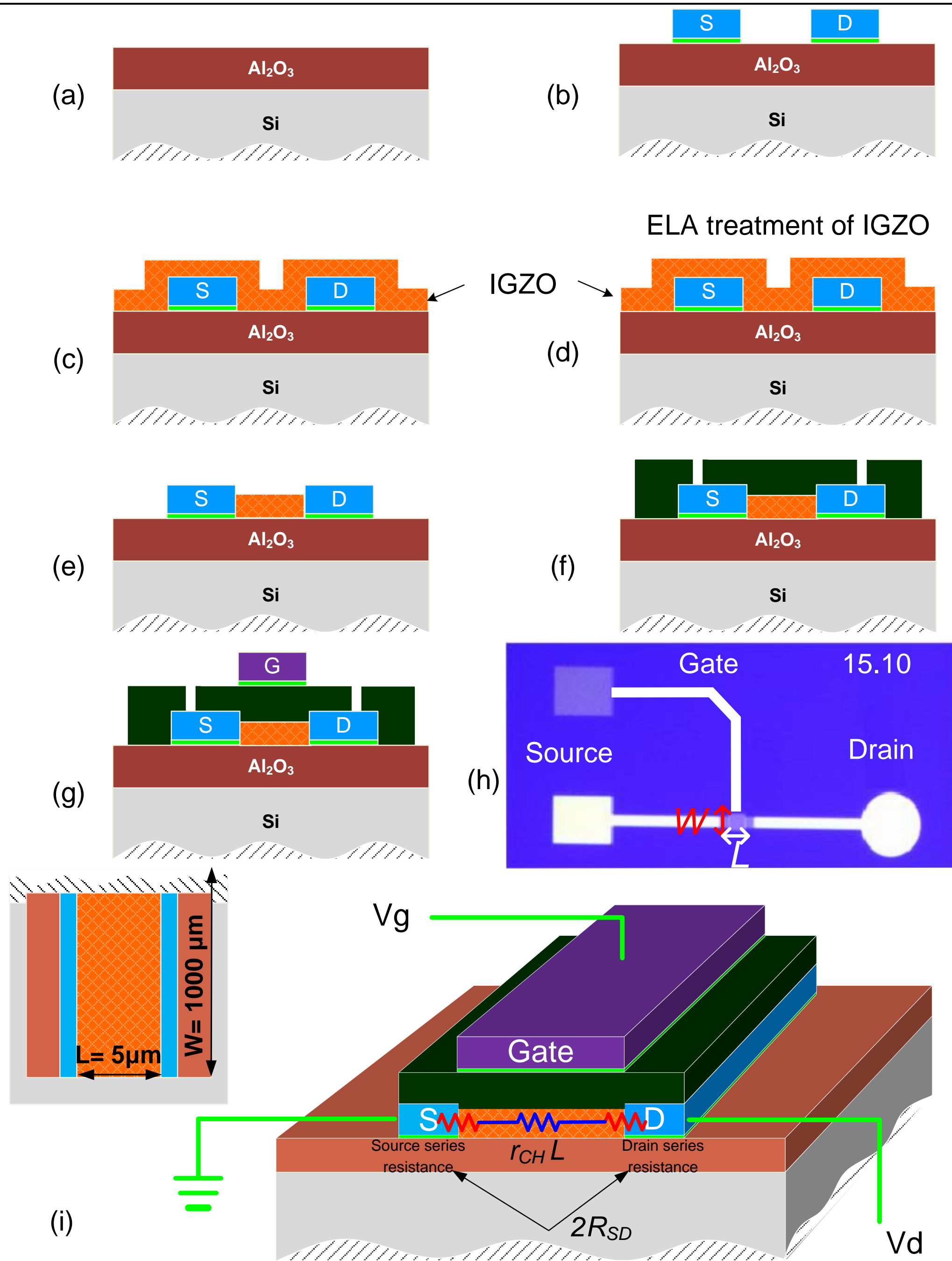

Fig. 6-1. (a-g) a process flow for IGZO TFTs fabrication, (h) top-view optical micrograph image, and (i) 3D schematic illustration and top view of the fabricated TFTs structure.

6.5 IGZO thin films sputter deposition and ELA results and discussion

6.5.1 Dependence of the growth rate on the deposition parameters

It was found that the growth rate of sputtered IGZO exhibits consistent trends with those observed for AZO growths. The growth rate increases linearly with the applied RF power, Fig. 6-2 (a), due to increasing the argon ions energy and thus the target bombardment i.e. more material coming off the target as the RF power is increased. On the other hand, the growth rate is

decreased as the oxygen % is increased as shown in Fig. 6-2 (b). As stated in chapter 3, oxygen and argon ions generally are not affected by quick polarity alternation in RF sputtering since their masses are many times larger than that of electrons. Therefore, at higher oxygen ratio in argon more energetic negative oxygen ions would be created in the plasma which are directed towards the substrate (anode) leading to bombarding and re-sputtering the growing film and thus reducing the growth rate. In addition, at higher oxygen ratio the target surface oxidation state is increased which results in increasing the threshold energy required for the argon ions to onset sputtering [66, 200]. The growth rate also decreases as the sputtering pressure increased as demonstrated in Fig. 6-2 (c) because of reducing the mean free path of sputtered species and increase scattering events during their path to the substrate. Thus, less material reaches the substrate and contributes to the thin film growth.

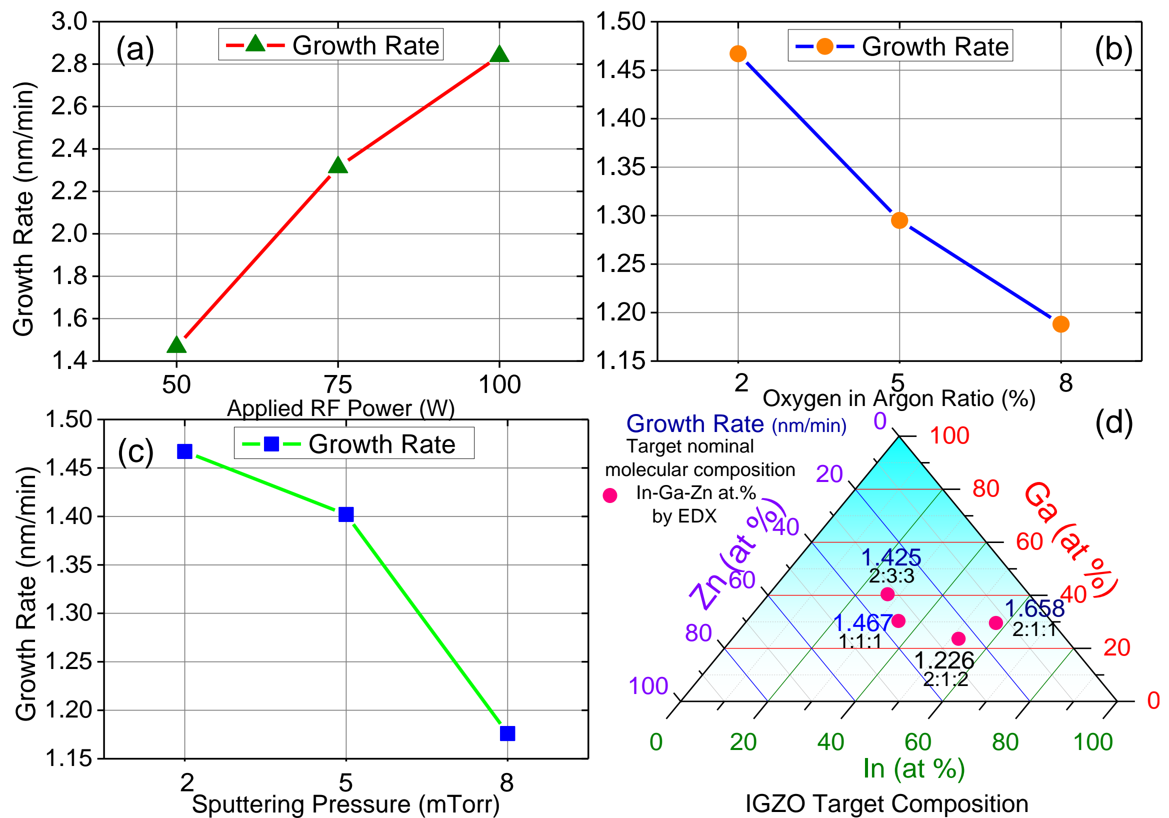

Fig. 6-2. The effect of the deposition parameters on IGZO films growth rate, (a) the RF power, (b) the O_2 to Ar %, (c) the sputtering pressure, and (d) the used target In-Ga-Zn at. % determined via EDX.

Given that isolated oxides of In_2O_3, Ga_2O_3, and ZnO have different sputtering rates, the sputtering rate of the multicomponent oxides depends on the contained ratio of these oxides within the target. IGZO thin films were deposited from IGZO targets of different compositions, but at the same sputter-deposition conditions RT, 50 W, and 2 mTorr of 2% oxygen to argon ratio. It

was determined that increasing the indium content in the target from IGZO (1:1:1) to IGZO (2:1:1) results in higher sputtering rate by ~15 %, while increasing the zinc ratio from IGZO (2:1:1) to IGZO (2:1:2) reduces the sputtering rate by ~25 % as shown Fig. 6-2 (d). These observed trends are due to different sputtering rates of the contained oxides, which are in turn attributed to variations in elements atomic numbers and binding energies. Similar trends were reported by P. Barquinha [200].

6.5.2 Dependence of the IGZO films metallic composition on the deposition parameters

The electrical characteristics of IGZO films are very sensitive to their metallic composition because of different physical properties of the contained metals (In-Ga-Zn) [66, 200]. The metallic composition of the deposited IGZO thin films was evaluated with energy-dispersive X-ray spectroscopy (EDX) and the results were compared with the used IGZO targets composition. Oxygen concentration in IGZO samples also has a strong impact on the achieved electrical properties. However, it was excluded from the EDX results due to the detection of aluminium from the Al_2O_3 used as a dielectric layer before IGZO depositions, which reveals that the detected oxygen must have some contribution from the Al_2O_3. Hence, oxygen was not taken into account and the ratio of the metals only is reported. Fig. 6-3 shows that increasing the RF power results in varying the stoichiometry of the deposited film. Namely, indium is increased and zinc is reduced as the RF power is increased. These effects are attributed to the higher and lower sputtering rates of In_2O_3 and ZnO respectively [200, 203]. Therefore, as the RF power is increased the target surface bombardment is increased leading to sputtering more indium and thus incorporating higher ratio of indium into the deposited film and at the same time decreasing the zinc ratio.

By way of contrast, the EDX measurements for IGZO films' metallic composition in Fig. 6-4 revealed that increasing the oxygen to argon ratio from 2 to 8 % results in reducing the indium ratio to other metals in the deposited film. This is attributed to increased density of energetic oxygen ions in the plasma which are directed to the substrate causing re-sputtering indium atoms from the growing film, because of its relatively high sputtering rate. This indicates that the IGZO samples surface roughness would be increased at higher oxygen %. Similar tendency was reported by P. Barquinha et al [200, 204].

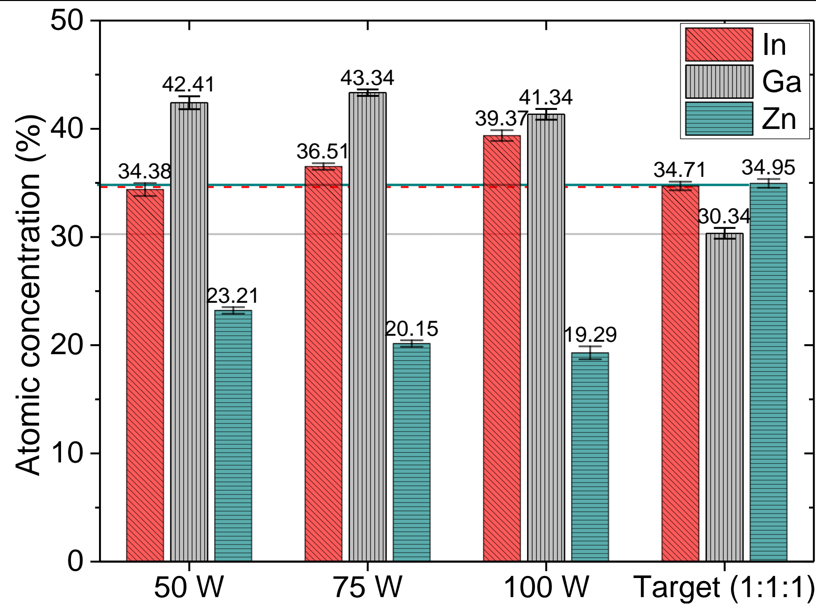

Fig. 6-3. In-Ga-Zn atomic concentrations for IGZO samples vs. applied RF power at 2 mTorr of 2% O_2 in Ar, determined via EDX.

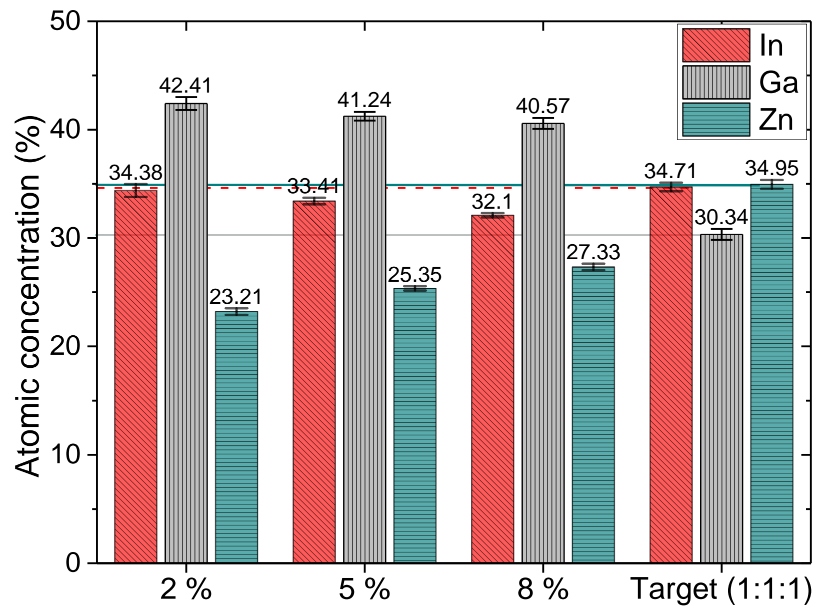

Fig. 6-4. In-Ga-Zn atomic concentrations for IGZO samples vs. oxygen to argon ratios, at 50 W, and 2 mTorr, determined via EDX.

The metallic composition of the deposited films was found to be less affected upon increasing the sputtering pressure from 2 to 8 mTorr as demonstrated in Fig. 6-5. This revealed that the target sputtering process was not significantly affected for the examined pressure range.

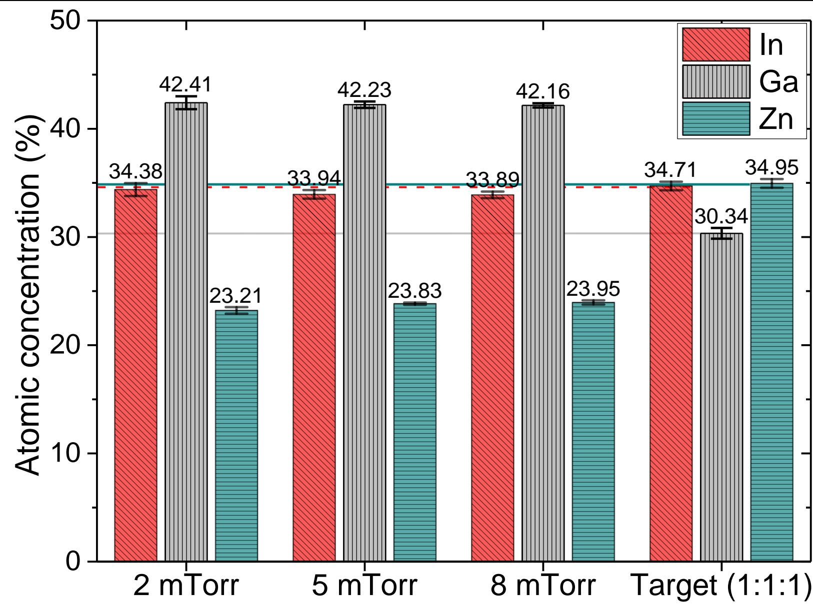

Fig. 6-5. In-Ga-Zn atomic concentrations for IGZO samples vs. sputtering pressure, at 50 W, and 2% O_2 in Ar, determined via EDX.

The IGZO films metallic composition dependence on the used IGZO target composition was also analysed with EDX for IGZO films deposited from IGZO targets of different composition and at the same sputter-deposition conditions RT, 50 W, and 2 mTorr of 2% O_2 to Ar ratio.

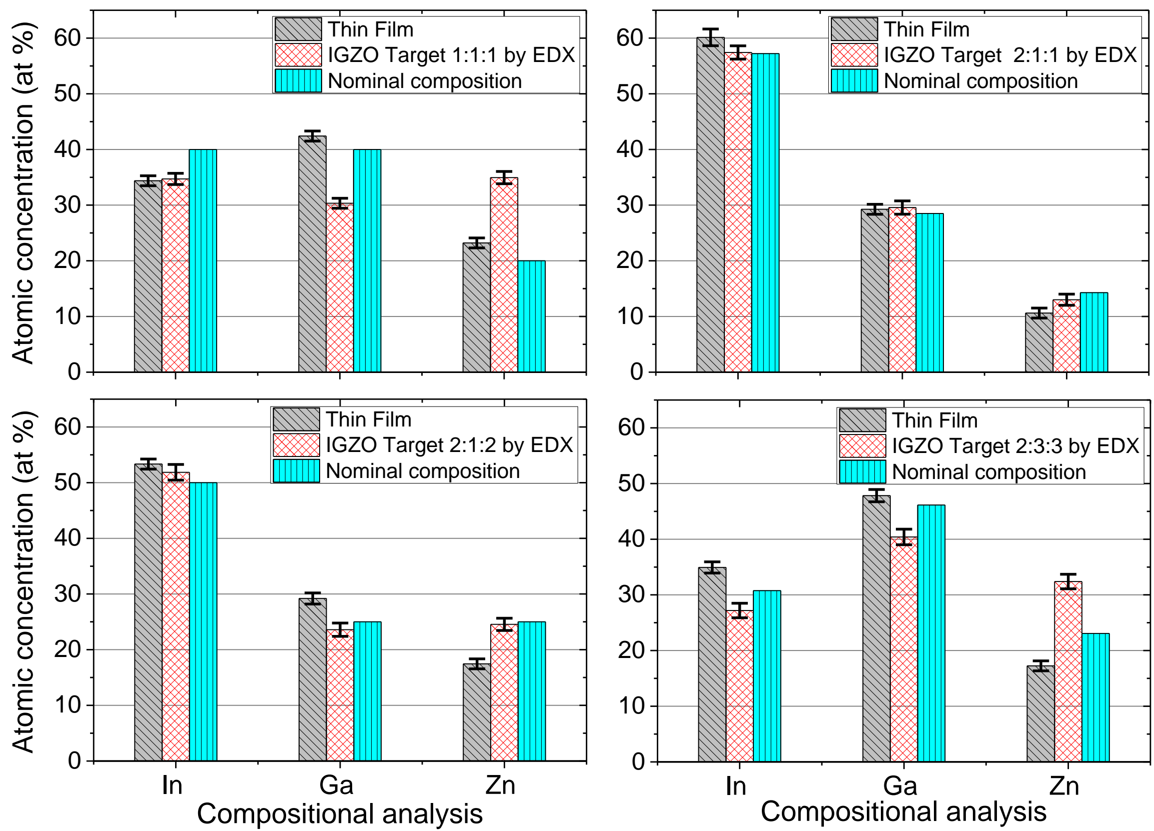

Fig. 6-6. In-Ga-Zn atomic concentrations for IGZO samples vs. the used IGZO target composition, IGZO films deposited at RT, 50 W, and 2mTorr of 2% O_2 in Ar, determined via EDX.

Fig. 6-6 shows that regardless of the used target composition, a zinc deficiency is observed on the deposited IGZO films compared to the employed targets' composition, due to the fact the ZnO has the lowest sputtering rate among the three oxides. This is in agreement to previous reports found in literature [200, 203, 204]. It should be noted that the observed variations between the nominal metallic composition and the obtained metallic composition by EDX for IGZO (1:1:1) and IGZO (2:3:3) targets are due to the fact that these targets were previously used in other study by the NTU research group and PhD research. Hence, the metallic composition of these two targets was changed via sputtering compared to their nominal metallic composition. It can be seen that the zinc ratio for these targets increased due to zinc relatively lower sputtering rate from the targets. However, the obtained metallic composition by EDX for IGZO (2:1:1) and IGZO (2:1:2) targets is very close to their nominal metallic composition.

6.5.3 Dependence of the IGZO films resistivity on the deposition parameters

All the as-deposited IGZO films were highly resistive and were not measurable by 4PP. However, upon ELA the resistivity was considerably reduced as the laser energy density is increased to 125 mJ/cm^2. The measurements via 4PP station showed that the resistivity of IGZO films is profoundly governed by the set of conditions at which the films are deposited or annealed.

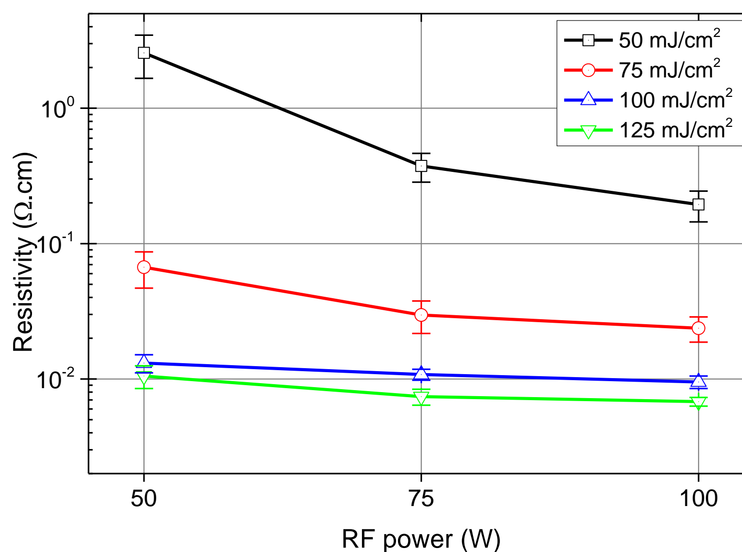

Fig. 6-7. IGZO thin films resistivity vs. applied RF power at RT, and 2 mTorr of 2% O_2 in Ar upon ELA with one pulse at different laser energy densities.

Fig. 6-7 shows that as the RF power is increased, the electrical resistivity demonstrates a declining trend. This can be attributed to increasing the sputtered atoms' kinetic energy and thus their surface mobility on the substrate at higher RF power, resulting in enhanced local atomic

bonding forming more compact films with lower defect density. Moreover, at higher RF power the impact of oxygen ions on the resulting film is anticipated to increase and probably cause oxygen atoms removal from the growing film surface since oxygen has relatively higher sputtering rate than metals. Consequently, higher oxygen vacancies concentration and thus higher free carrier density are created [104, 204, 205]. Since ELA caused almost no metallic composition changes to IGZO films as shown later in Fig. 6-19, the observed composition changes for different deposition conditions are still applicable to the ELA-treated films whose resistivity trends are discussed in this section as a function of the growth conditions. Increasing the applied RF power to the IGZO (1:1:1) target resulted in altering the deposited IGZO films' metallic composition. The indium ratio, relative to the other metals, was increased, while the zinc ratio, relative to the other metals, was decreased. As a result, the film resistivity was reduced given that the conduction band minimum CBM of IGZO is mainly made of ns orbitals of the contained metals and indium has largest orbitals compared to gallium and zinc. This enhances the overlap between neighbouring atoms and thus improves the carrier mobility [66, 203].

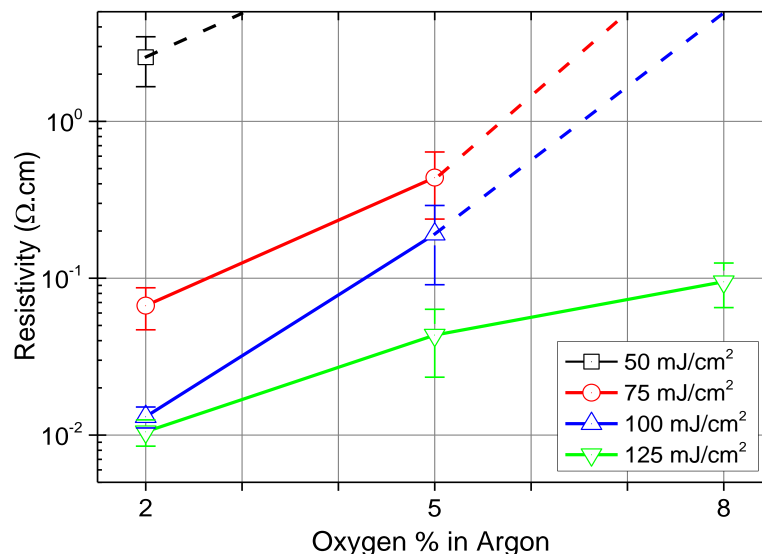

Fig. 6-8. IGZO thin films resistivity vs. O_2 to Ar % at RT, 50 W, and 2 mTorr upon ELA with one pulse at different laser energy densities. Dashed lines correspond to unmeasurable values by 4PP.

On the contrary, the resistivity increased considerably by more than an order of magnitude when the oxygen to argon ratio was increased, as depicted in Fig. 6-8. This is attributed to decreasing oxygen vacancies and thus the free electron density as the oxygen % is increased [76, 204]. Furthermore, at high oxygen % more intense bombardments on the growing film by energetic oxygen ions would result in inducing compressive stress, re-sputtering the

deposited material, reducing the film density, and creating microstructural defects on the film surface and/or the bulk material. All these reasons would consequently deteriorate the electrical and interface properties of the resulting IGZO material [66, 204]. The EDX analysis for IGZO films of different oxygen ratios confirmed that increasing the oxygen ratio resulted in reducing the indium ratio in the deposited films via re-sputtering and therefore the resistivity would increase. It is worth mentioning that lower than 2% oxygen content was not examined to avoid high oxygen deficiency in deposited films that would lead to high background free carrier density and thus not suitable material for TFTs application. P. Barquinha [200] has shown that IGZO TFTs deposited in pure Ar or at very low oxygen % were always in on-state i.e. do not demonstrate practical active layer conductivity modulation when tested for TFTs due to high free carrier density.

Similar to the AZO results discussed in chapter 4, both the RF power and the sputtering pressure are directly linked to the sputtered species energy and therefore have significant roles on defining the growing film physical characteristics. In regard to the sputtering pressure of IGZO, reducing the sputtering pressure decreases the IGZO resistivity as shown in Fig. 6-9.

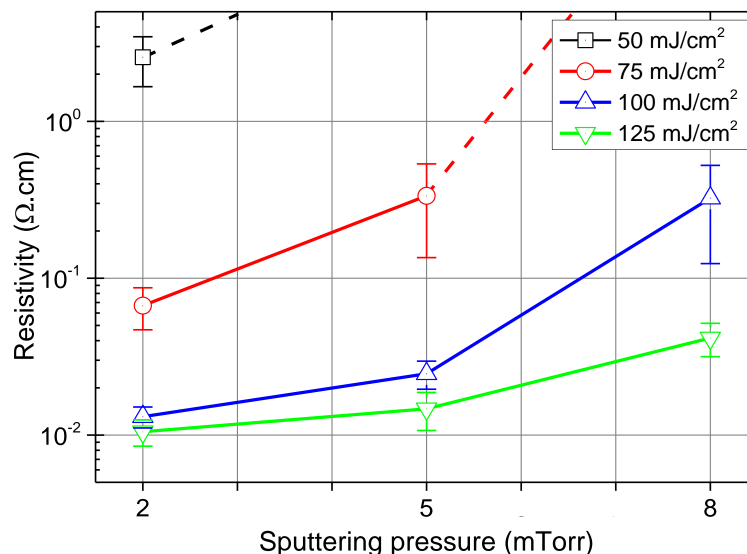

Fig. 6-9. IGZO thin films resistivity vs. sputtering pressure at RT, 50 W, and 2% O_2 in Ar upon ELA with one pulse at different laser energy densities. Dashed lines correspond to unmeasurable values by 4PP.

At lower sputtering pressure, the sputtered species arrive at the substrate with higher kinetic energy and surface mobility on the substrate, because of fewer collisions with the sputtering gases (2% O_2 in Ar) allowing them to form films with better densification and less bulk and/or interface defects [200, 204]. J. H. Jeong et al have reported a material density increase for IGZO thin films from 5.50 g/cm^3 to 6.27 g/cm^3 observed by X-ray reflectivity (XRR)

measurements, when the sputtering pressure reduced from 5 to 1 mTorr [105]. EDX data in Fig. 6-5 demonstrated that there are negligible metallic composition variations among IGZO films compared to the observed resistivity changes when the sputtering pressures increased to 8 mTorr. In other words, the metallic composition changes do not justify the noticed significant resistivity increase with increasing the sputtering pressure, in consistency with J. H. Jeong et al [105] and P. Barquinha [200] results. Besides, S. Yasuno et al have demonstrated via XPS study that increasing the sputtering pressure of IGZO thin films results in increasing the adsorbed defects leading to deteriorating the deposited films electrical properties and thus the fabricated TFT performance [206]. The oxygen related-defects are reported to have a strong impact on TFT performance as well as stability associated with carrier scattering and trapping [207]. It is worth noting that when the pressure is decreased to lower than 2 mTorr, the sputtering process was not stable probably because of inadequate quantity of sputtering gasses to perform stable sputtering.

Although compositional deviations between the IGZO targets and films were observed, the utilised IGZO target composition was found to play a crucial role in defining the resistivity of the deposited IGZO films via varying their metallic composition as shown in Fig. 6-10.

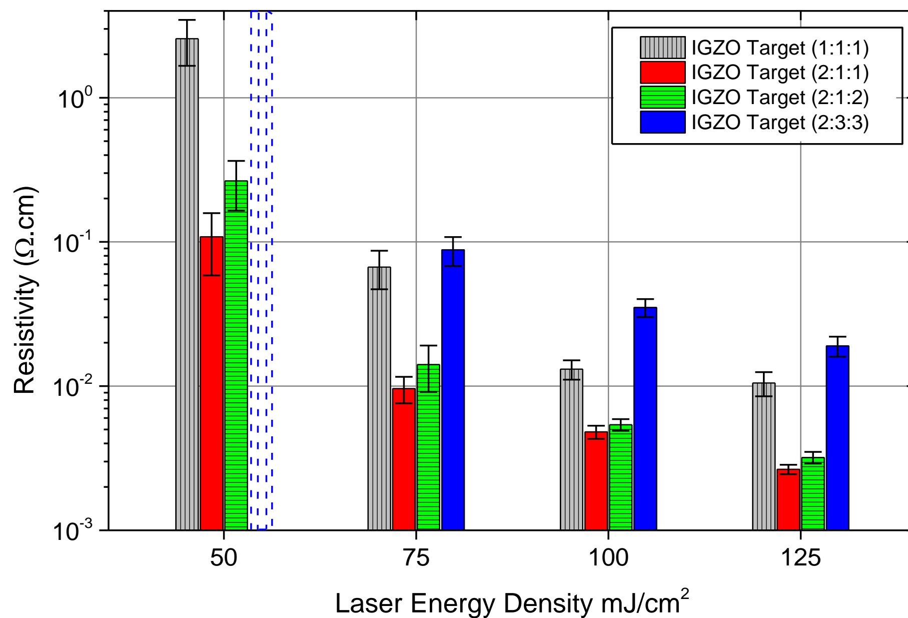

Fig. 6-10. IGZO films resistivity vs. the used IGZO target composition, 200 nm thick IGZO films deposited at RT, 50 W, and 2 mTorr of 2% O_2 in Ar. Dashed bar represents unmeasurable resistivity by 4PP.

It is shown that higher indium contents in IGZO target (like in IGZO 2:1:1 relative to IGZO 1:1:1) and thus in the deposited films, as evidenced by EDX in Fig. 6-6, resulted in lower resistivity owing to larger orbitals (5s) of indium. In contrast, higher gallium contents (like in IGZO 2:3:3

relative to IGZO 1:1:1) resulted in more resistive films which is attributed to the free carrier density reduction via oxygen vacancies suppression due to gallium high ionic potential and small ionic radius leading to strong reactivity with oxygen [66, 208].

6.5.4 The effect of ELA in IGZO thin films electrical characteristics

It was demonstrated in the previous sections that ELA reduces noticeably the resistivity of IGZO samples regardless of the deposition conditions. Theoretically, the resultant resistivity reduction is attributed to the free carrier density (N) and/or mobility (μ) enhancements. The free carrier density and mobility in a TFT active layer are among the essential parameters that strongly control the TFT's performance. The former has a strong impact on the TFTs turn on voltage and off-state current, while the latter is directly linked to the TFTs field effect mobility [7, 48]. To examine the ELA effect on the free carrier density and Hall mobility of IGZO, Hall Effect measurements were performed on 200 nm thick IGZO (1:1:1) and IGZO (2:1:1) samples deposited on glass substrates from two different targets at room temperature, 50 W, and 2 mTorr of 2% O_2 in Ar. For making Ohmic contacts with the samples, titanium/gold (10/60 nm thick) electrodes were deposited through a shadow mask at the samples' corners.

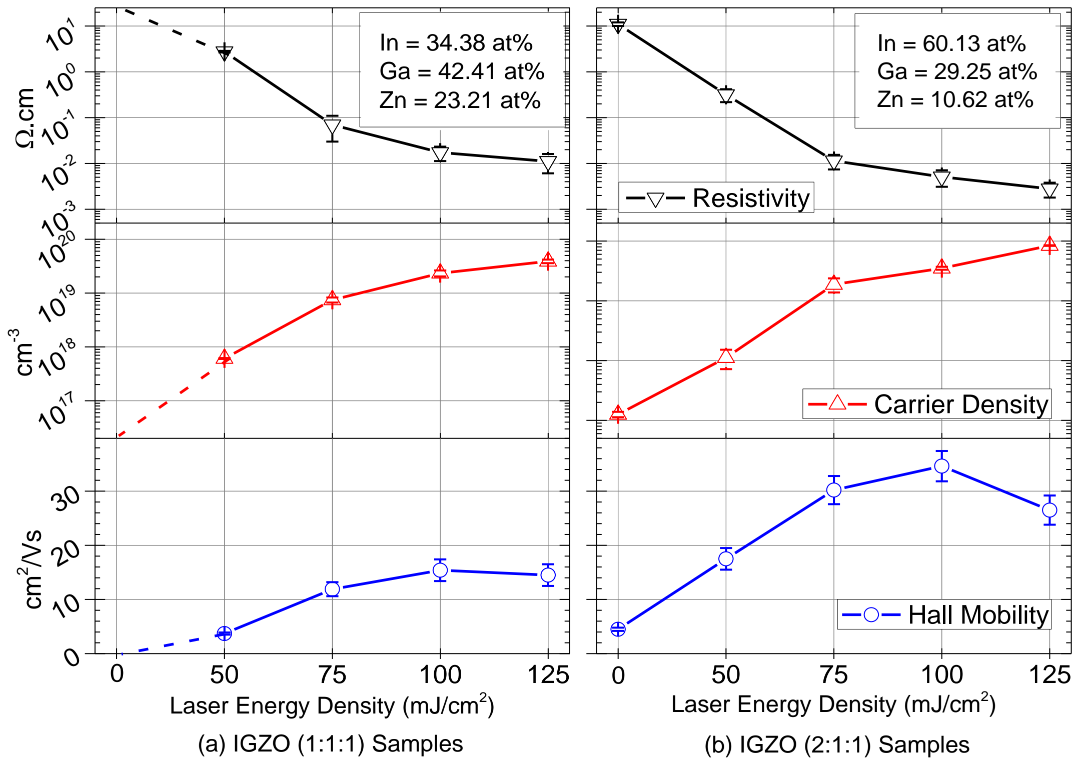

Fig. 6-11. The dependence of the electrical characteristics on ELA laser energy density for 200 nm thick IGZO samples deposited at the optimised condition, (a) from IGZO (1:1:1), and (b) from IGZO (2:1:1). Dashed lines correspond to unmeasurable values.

Considering the electron density and mobility for the IGZO films of different metallic composition, it can be seen from Fig. 6-11 that increasing the indium ratio from IGZO (1:1:1) In=34.38 at% to IGZO (2:1:1) In=60.13 at% results in improving the electron density and mobility. This justifies the observed resistivity trends for IGZO films of different indium ratios deposited at different RF power and oxygen % discussed above and is in agreement with other reports [103, 209]. Hall Effect measurements on the as-deposited IGZO (1:1:1) film were not performed due to difficulty in achieving Ohmic contact with the IGZO films because of their high resistivity [210].

From the AZO samples discussed in the previous chapter we have shown that ELA improves microstructural properties and reduces the adsorbed defects at grain boundaries leading to enhancing the free carrier density and mobility. Amorphous IGZO samples, however, do not exhibit grain boundaries but still interact with the environment via their surfaces leading to oxygen adsorption/desorption which has strong impact on the oxygen vacancies, the trap states densities, and thus the electrical properties [211, 212]. In sputter-deposition of oxide materials, in general, microstructural defects acting as electron scattering or trapping centres are inevitably created due to energetic species bombardments and incorporation of used sputtering gas ions. The generated defects density depends on the deposition parameters and is very critical for semiconducting materials such as a-IGZO [76]. Post-deposition annealing using various techniques including UV photonic processing [79, 108, 111, 123], thermal annealing [77, 205] have been applied to IGZO films leading to improving the structure order, tuning the oxygen vacancies density, removing weakly bonded oxygen species, and reducing adsorbed and microstructural defects. In this work, ELA treatment at moderate laser energy improves both the free electron density and mobility for a-IGZO samples which could be attributed to local atomic rearrangement, the amorphous structure randomness relaxation, and trap states density reduction. The local atomic rearrangement and structure relaxation caused by ELA heating, provided that no crystallisation occurs, would enhance the overlap among ns orbitals of the contained metals leading to better carrier transport [77, 212, 213]. Moreover, the observed free carrier density increase for the ELA-treated IGZO samples associated with trap states reduction, would consequently result in shifting the Fermi level towards the conduction band and thus in overcoming the potential barrier between different sites induced by the amorphous structure randomness. As a result, the free carrier mobility is enhanced [66, 208]. However, when the laser

energy density is increased to 125 mJ/cm^2 the mobility starts degrading which can be attributed to microstructural changes and the onset of IGZO samples crystallisation induced by ELA treatment at higher laser energy densities. [107, 123].

Based on the observed trends for the electrical characteristics of 200 nm thick IGZO films upon ELA treatment, it could be concluded that lower laser energy densities are needed to produce IGZO thin films with electrical properties which are desired for TFT active layer.

6.6 IGZO TFT sputter deposition and ELA results and discussion

6.6.1 Dependence of the IGZO TFT performance on the IGZO layer deposition parameters

In the previous section 6.5.3, it was demonstrated that the IGZO resistivity is strongly controlled by the used set of growth conditions. Building on the observed trends for IGZO thin films resistivity at different growth conditions, IGZO active layer 40 nm thick were deposited for TFTs at a selected set of deposition parameters shown in Table 6-2, and following the process flow illustrated in Fig. 6-1 presented earlier.

TFTs substrate ID	Investigated parameter	RF power (W)	Sputtering Pressure (mTorr)	O_2 in Ar (%)
IGZO 019	Ref. Sample	50	2	2
IGZO 047	RF power	75	2	2
IGZO 020	O_2 in Ar (%)	50	2	5
IGZO 048	Sp. pressure	50	5	2

Table 6-2. Investigated sputter-deposition parameters of IGZO TFTs.

Fig. 6-12 Compares the averaged transfer characteristics curves of IGZO TFTs deposited at different RF power. It should be noted that each curve in the discussed results of TFTs on silicon represents the average of the transfer characteristics curves for five TFTs with the same fabrication conditions. The electrical parameters are extracted from the forward sweep curve at V_D = 1V are shown in Table 6-3. The field effect mobility is estimated from the Eq. 6-1.

$$\mu_{FE} = \frac{L \times g_m}{C_i \times W \times V_D} \quad [48] \qquad 6\text{-}1$$

where (g_m) is the transconductance defined as the slope of the transfer curve in the linear regime of TFTs operation, L and W are the channel length and width respectively, and C_i is the gate dielectric capacitance per unit area. The gate dielectric for the examined TFTs in this work is 50 nm thick Al_2O_3 deposited by ALD. According to [214] the capacitance per unit area for similar thickness of Al_2O_3 deposited by ALD C_i =1.5x10^{-7} F/cm^2.

The TFTs with IGZO active layer deposited at an RF power of 75 W do not demonstrate the active layer conductivity modulation under the gate voltage field-effect, causing the TFTs to be always in the on-state even when negative V_G is applied. This is because of the low resistivity of IGZO samples linked to high free carrier density that cannot be fully depleted from the channel layer-gate dielectric (IGZO-Al_2O_3) interface even when negative gate voltage is applied i.e. a conductive IGZO channel layer connects or shorts the source and drain electrodes. This can be attributed to the effect of oxygen ion bombardments on the growing film resulting in oxygen removal from the growing film, creating oxygen vacancies, and thus introducing higher free electron density [205]. Moreover, indium, which has a strong correlation with the IGZO conductivity, found to increase with the RF power as shown in Fig. 6-3 [66, 209].

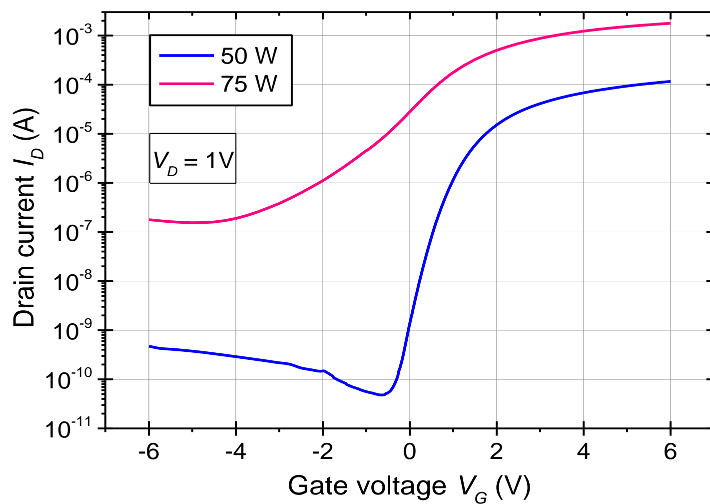

Fig. 6-12. Averaged transfer characteristics curves for as-deposited IGZO TFTs deposited at different RF power, RT, 2 mTorr of 2% O2 in Ar.

RF power (W)	μ_{FE} (cm^2/Vs)	*S* (V/decade)	V_{ON}[vii] (V)	I_{ON}/I_{OFF} (Ratio)	Hysteresis (ΔV_{ON})
50	0.67±0.04	0.28±0.01	- 0.15±0.08	(0.4±0.2) E+06	0.15±0.01
75	4.21±1.0	2.21±0.9	- 6 (always ON)	NA	0

Table 6-3. The extracted electrical parameters for as-deposited IGZO TFTs deposited at different RF power, RT, 2 Torr of 2% O_2 in Ar.

The significant increase in the subthreshold swing S for 75 W IGZO TFTs reveals the IGZO/Al_2O_3 interface is severely degraded due to energetic ions bombardment on the growing film at this RF power leading to creating more interfacial and bulk trap states [76]. High subthreshold swing values generally imply low operating speed and higher power consumption

[vii] The V_{ON} is defined as the gate voltage at which the drain current I_D reaches 1 nA. Also, the TFTs Hysteresis (ΔV_{ON}) was determined as absolute value of V_{ON} for forward sweep - V_{ON} for backward sweep at I_D=1 nA.

[48]. Therefore, for the above stated reasons the fabricated TFTs with IGZO deposited at 75 W are impractical devices. P. Barquinha [200, 205] has already reported similar tendency for IGZO TFTs fabricated at higher RF power. Also, P. Barquinha observed that higher RF power causes more energetic species in the glow discharge that resulted in increasing the IGZO roughness (confirmed by AFM) and thus damaging the IGZO-gate dielectric interface.

The effect of oxygen to argon ratio % on the IGZO TFTs electrical performance is shown in Fig. 6-13, and Table 6-4 for IGZO-TFTs deposited at RT, 50 W, and 2 mTorr.

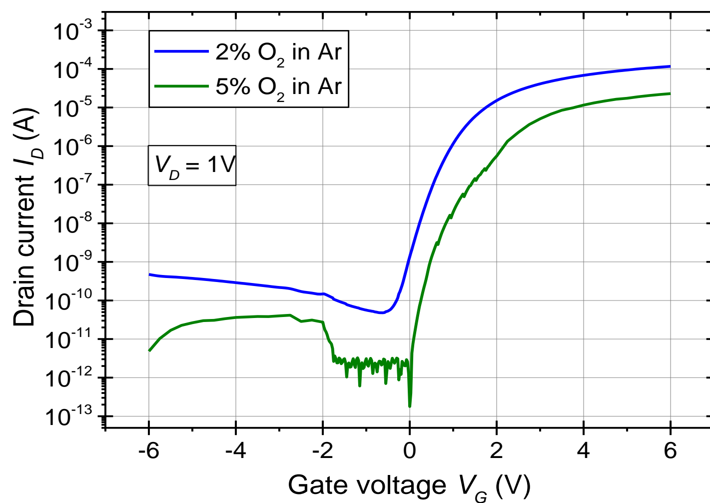

Fig. 6-13. Averaged transfer characteristics curves for as-deposited IGZO TFTs deposited at different O_2 in Ar%, RT, 50 W, and 2 mTorr.

O_2 in Ar (%)	μ_{FE} (cm²/Vs)	*S* (V/decade)	V_{ON} (V)	I_{ON}/I_{OFF} (Ratio)	Hysteresis (ΔV_{ON})
2	0.67±0.04	0.28±0.01	- 0.15±0.08	(0.4±0.2) E+06	0.15±0.01
5	0.11±0.1	0.33±0.3	+ 0.53±0.1	(7.6±0.6) E+06	2.3±.0.3

Table 6-4. The extracted electrical parameters for as-deposited IGZO TFTs at different O_2 in Ar%, RT, 50 W, and 2 mTorr.

At higher oxygen concentration, the TFTs' performance is noticeably degraded which is attributed to the larger density of negative oxygen ions created in the glow discharge and thus more intense bombardments on the growing IGZO film. Consequently, the film compactness and the contained indium ratio are reduced, while the sample roughness and resistivity are increased [215]. It was reported that the effect of oxygen ion bombardments on IGZO-TFTs performance is reinforced at low sputtering pressure [200]. Given that the effect of oxygen % was examined here at a relatively low sputtering pressure of 2 mTorr, the increase of oxygen ratio from 2 to 5 % would increase the impact the energetic oxygen ions on the resulting IGZO thin film and thus the TFT performance via creating higher density of interfacial and bulk defects. This is reflected by the

observed increase in subthreshold swing S from 0.28±0.01 to 0.33 ± 0.3 [105]. Also, irregularity in the TFT transfer characteristics curve in the forms of kinks such as for the 5% oxygen to argon ratio TFTs has been observed for oxide TFTs and attributed to the trap states which hinder the creation of the charge accumulation layer at the active layer/gate insulator interface (IGZO/Al_2O_3) under V_G application [200, 204]. The observed turn on voltage increase to positive V_{ON} values and the off-current reduction by more than an order of magnitude at higher oxygen % indicate that the free carrier density reduction in IGZO samples due to oxygen vacancies suppression assigned to excess oxygen introduction into the sputtering chamber. At lower free carrier density, the impact of the potential barriers associated with the amorphous structure on the carrier mobility would be increased leading to degraded carrier mobility in IGZO and thus the achieved electrical performance when IGZO applied to TFTs [14, 48]. The positive V_{ON} implies the existence of the interface traps and/or bulk traps. Thus, a higher V_G is needed to fill the trap states and create electron accumulation layer close to the IGZO/Al_2O_3 interface to turn the TFT to on-state, when the active layer is deposited at high oxygen % [103, 104].

Higher sputtering pressure results in degrading the TFTs performance as shown in Fig. 6-14 and Table 6-5. This is due to a large microstructural defects density including bulk and/or interface trap states, which is demonstrated by the observed subthreshold swing S increase and field effect mobility μ_{FE} decrease [76, 77]. Also, it was reported that higher sputtering pressure reduced the film compactness and surface smoothness [105, 205].

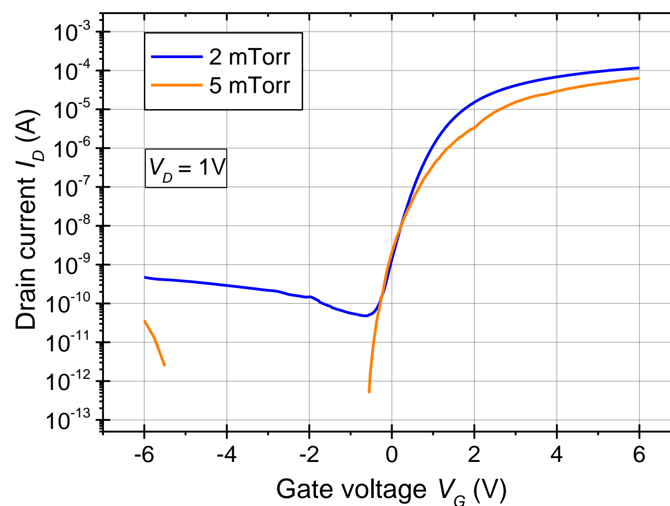

Fig. 6-14. Averaged transfer characteristics curves for as-deposited IGZO TFTs deposited at different sputtering pressure at RT, 50 W, and 2% O_2 in Ar.

Sp. Pressure (mTorr)	μ_{FE} (cm^2/Vs)	S (V/decade)	V_{ON} (V)	I_{ON}/I_{OFF} (Ratio)	Hysteresis (ΔV_{ON})
2	0.67±0.04	0.28±0.01	- 0.15±0.08	(0.4±0.2) E+06	0.15±0.01
5	0.21±0.1	0.33±0.3	+ 0.39±0.1	(5.1±0.7) E+06	1.2±.0.2

Table 6-5. The extracted electrical parameters for as-deposited IGZO TFTs deposited at different sputtering pressure at RT, 50 W, and 2% O_2 in Ar.

All the above observations are associated with reducing the sputtered particles average kinetic energy and surface diffusion length on the substrate surface at higher sputtering pressure for IGZO channel layer due to increasing the collision rates for the sputtered particles. Jeong et al [105] have demonstrated that the TFT performance deterioration at higher sputtering pressure is more associated with the bulk trap states density increase. However, P. Barquinha et al [200, 205] has shown that IGZO thin films sputtered at very low sputtering pressure showed rather poor channel conductivity modulation when applied to TFTs i.e. the TFTs were always in the on-state because of relatively low resistivity.

The IGZO film compactness reduction at higher sputtering pressure or potentially at higher oxygen % due to oxygen ions bombardment could reinforce adsorbing higher defects such oxygen atoms resulting in electron trapping/scattering and TFTs performance degradation. This was demonstrated by the large clockwise hysteresis increase of 2.3±.0.3 V at higher oxygen % and of 1.2±.0.2 V at higher sputtering pressure (taken at I_D=1 nA), associated with trap states filling including interfacial trap states and bulk IGZO trap states under V_G application [216].

To conclude, the optimised IGZO growth parameters at room temperature for better electrical properties required for TSOs application to TFTs are:

1. RF power of 50 W, to avoid increasing the IGZO conductivity to redundant values.
2. Sputtering pressure of 2 mTorr, for dense and reproducible films with less microstructural defects.
3. Oxygen to argon ratio of 2%, to reduce the effect of the energetic oxygen ions created in the glow discharge on the resulting film, as well as to avoid high oxygen vacancies and thus high background free electron density in the resulting IGZO samples.

6.6.2 Effect of ELA on the performance of IGZO TFTs on silicon substrates

Fig. 6-15 shows the effect of ELA with one pulse at different energy density on the averaged transfer characteristic curves for IGZO-TFTs with the optimised IGZO films 40 nm thick deposited at room temperature, 50 W, and 2 mTorr of 2% O_2 in Ar.

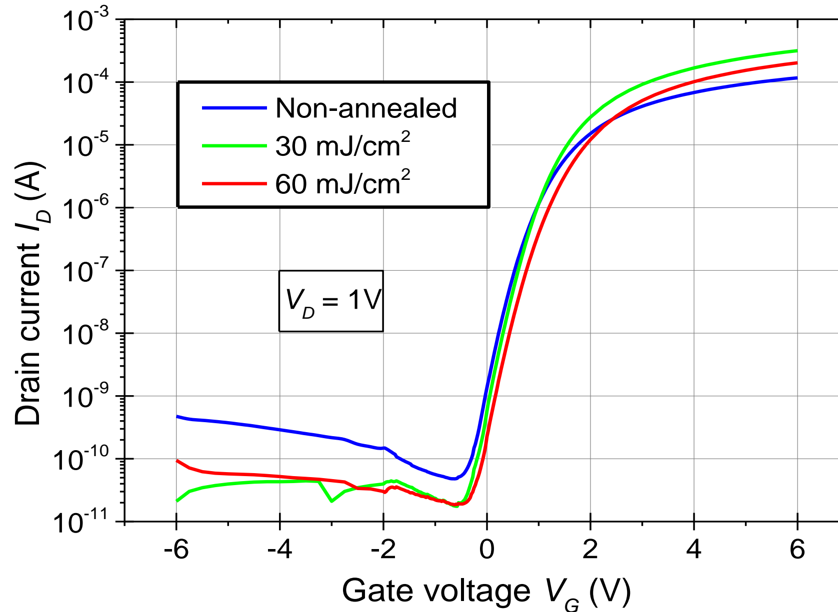

Fig. 6-15. Averaged transfer characteristics curves for the optimised as-deposited IGZO TFTs upon ELA with one pulse at different energy densities.

Laser Energy (mJ/cm²)	μ_{FE} (cm²/Vs)	S (V/decade)	V_{ON} (V)	I_{ON}/I_{OFF} (Ratio)	TFT R_{ON} (K Ω)	Hysteresis (ΔV_{ON})
0	0.67±0.04	0.280±0.01	- 0.15±0.08	(0.4±0.2) E+06	24 ±9	0.14±0.01
15	3.0±0.10	0.277±0.006	+0.18±0.06	(1.6±0.3) E+07	2.8±0.2	0.11±0.01
30	3.33±0.06	0.273±0.002	+ 0.35±0.05	(2.8±0.5) E+07	2.6±0.3	0.13±0.01
45	2.67±0.07	0.292±0.006	+ 0.22±0.09	(1.3±0.9) E+07	6±4	0.11±0.04
60	1.00±0.03	0.29±0.02	+ 0.23±0.09	(1.4±0.3) E+06	11.0±3.0	0.10±0.01

Table 6-6. The extracted electrical parameters for the optimised as-deposited IGZO TFTs upon ELA with one pulse at different energy densities.

The extracted figure-of-merits of the devices are shown in Table 6-6. When the laser energy density is 30 mJ/cm², the drain current for on-state is increased by half an order of magnitude to 4×10^{-4} A, while the off-state current is noticeably decreased by more than an order of magnitude to 4×10^{-11} A. These devices demonstrated an on/off ratio of (2.8±0.5) $\times10^{+07}$, and a negligible hysteresis about 0.13 V. The off state current in TFTs is typically associated with the active layer conductivity and the active layer/gate dielectric interface characteristics [14, 48]. The

off–state current reduction upon ELA could be due to better interface with the gate insulator. In addition, the off-state current reduction after annealing could be assigned to reduction of the trap states such adsorbed oxygen atoms at IGZO surface which trap electrons from IGZO layer creating negatively charged layer acting as a conduction path for electrons between the source and drain electrodes [14]. At higher laser energy density, the trends are reversed for the drain current which is associated to the free electron density and resistivity of the channel layer increased and decreased respectively leading to degrading the channel conductivity modulation under the gate voltage application [108, 112]. The field effect mobility is also increased after ELA treatment at 30 mJ/cm^2. This improvement can be assigned to: (1) Reduction of scattering or trapping defects density on the bulk IGZO or at the interface with Al_2O_3 due to atomic rearrangement. (2) Enhanced local atomic bonding. (3) And, amorphous structure relaxation caused by the generated heat produced by the laser photons absorption [77, 106]. Moreover, as discussed for IGZO thin films before the free carrier density increase caused by ELA treatment would result in enhancing carrier mobility in IGZO channel layer, as shown in Fig. 6-11 and Fig. 6-17, which in turn would result in enhancing the field effect mobility and the on-state current for IGZO TFTs [212].

The electrical contact between TFTs active layer, IGZO in our case, and the source and drain metallic electrodes is one of the essential parameters which are directly related to TFTs performance [48, 202]. The source and drain contact resistance and the active layer resistance are related to the TFTs on-resistance R_{ON} as shown in Eq. 6-2 [48].

$$R_{ON} = \frac{V_D}{I_D} = r_{CH} L + 2R_{SD} \text{ [48]} \qquad (6\text{-}2)$$

where r_{CH} is the IGZO channel resistance for channel length L, and $2R_{SD}$ is the total series contact resistance associated with the source and drain electrodes. Table. 6-6 shows that ELA up to 30 mJ/cm^2 reduces TFTs on-resistance leading to better performance. The TFTs on-resistance reduction is assigned to: (1) Reduction of IGZO channel layer resistivity as demonstrated earlier upon ELA treatment Fig. 6-11. (2) The observed free carrier density increase in the IGZO samples after ELA would move the Fermi level to higher positions towards the conduction band i.e. decreasing IGZO work function leading to better electrical contact between IGZO layer and S/D electrodes [107, 217]. (3) Also, since the whole TFT structure is covered by

the laser beam, the ELA-induced heating would improve the interface between the IGZO channel layer and S/D electrodes and hence reduces the contact resistance [107, 202, 217]. Nevertheless, at higher laser fluences the TFTs on-resistance started to increase again. As demonstrated in Eq. 6-2, the TFTs on-resistance is a function of the source-drain contact resistance with IGZO and the resistance of IGZO. The IGZO resistance/resistivity at higher laser fluences cannot be the origin of the noticed TFTs on-resistance increase since IGZO resistivity demonstrates a declining trend at higher fluences as shown in Fig. 6-11 and Fig. 6-17. Hence, the TFTs on-resistance increase would be attributed to the S/D contact resistance changes at higher laser energy densities. P. Barquinha [200] reported TFTs on-resistance increase when the annealing temperature for IGZO TFTs with titanium-gold electrodes is increased from 150 to 250°C. This was explained by elemental interdiffusion between the titanium-gold electrodes and IGZO caused by the higher annealing temperature and observed by TOF-SIMS. As a result, the contact properties are changed and thus the S/D contact resistance is increased. According to J P Bermundo et al [112], KrF ELA with single pulse at 60 mJ/cm^2 increases the surface temperature of IGZO TFTs to about 1000°C for less than 100 ns. Therefore, it could be considered that when our TFTs were annealed at ≥45 mJ/cm^2 the high temperature generated by ELA causes elemental interdiffusion that changes the interface properties and thus increases the contact resistance between the source-drain electrodes and IGZO channel layer.

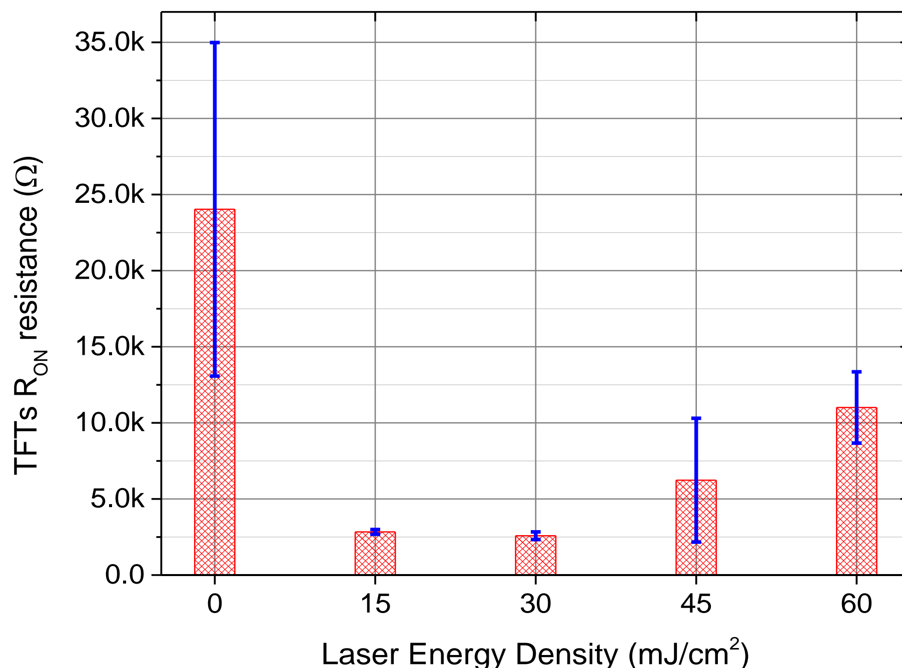

Fig. 6-16 The effect of ELA laser energy density on IGZO TFTs on resistance R_{ON}.

To examine the ELA effect on the electrical and microstructure properties of IGZO channel layer used in the TFTs, IGZO thin films of 40 nm thick were deposited on Al_2O_3-coated silicon substrates and on fused silica glass substrates. Fig. 6-17demonstrates the ELA effect on IGZO electrical characterises for 40 nm-thick IGZO (1:1:1) used for the TFTs, and for IGZO (2:1:1) samples for comparison. As presented earlier for 200 nm thick samples, ELA improves both the free carrier density and mobility leading to lowering the IGZO resistivity.

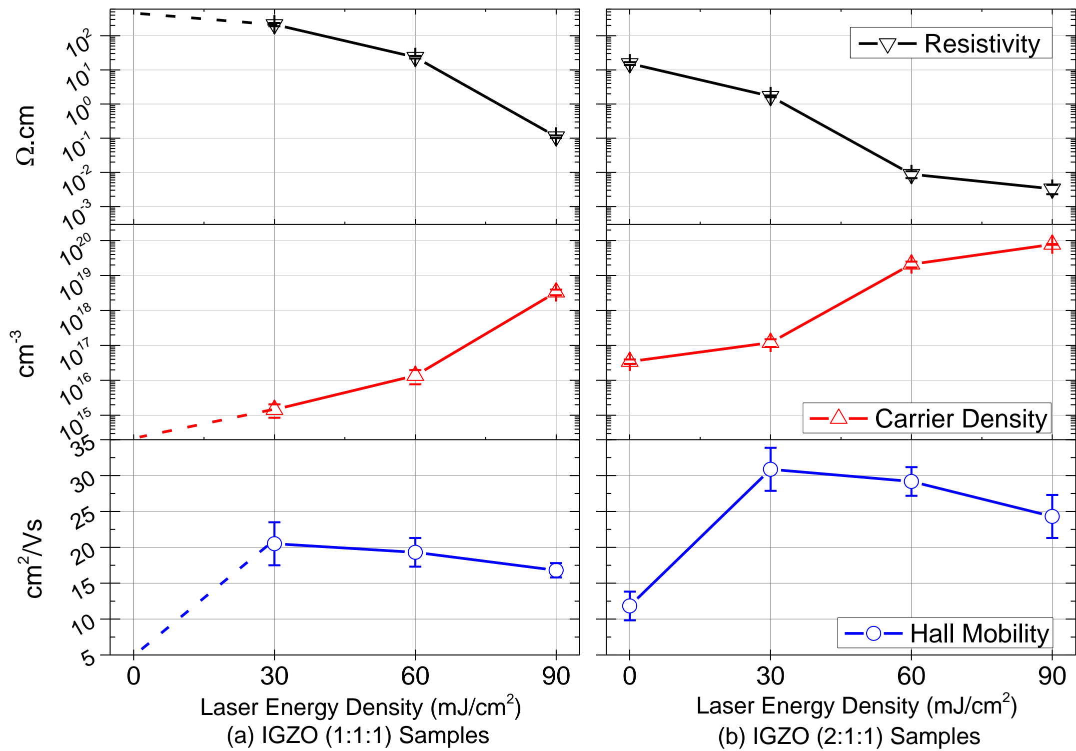

Fig. 6-17. The dependence of the electrical characteristics on ELA laser energy density for 40 nm thick IGZO samples deposited at the optimised condition, (a) from IGZO (1:1:1), and (b) from IGZO (2:1:1). Dashed lines correspond to unmeasurable values.

Comparing Fig. 6-11 and Fig. 6-17, it can be seen that when KrF-ELA is applied to thinner IGZO films 40 nm even at lower energy densities, more pronounceable changes in the electrical characteristics are observed relative to 200 nm thick IGZO samples. This is assigned to the fact that the generated heat under ELA treatment is dependent on both the utilised laser penetration depth through the processed sample as well as the sample thickness. The penetration depth for KrF laser in IGZO samples is 45 nm, hence using 40 nm thick IGZO for TFTs promotes less heat dissipation from the KrF photons penetration depth and thus the sample is uniformly processed at higher temperatures from the surface to the IGZO-Al_2O_3 interface. Unlike for thicker samples, the KrF penetration depth is considered as the heat source for the remaining IGZO thickness via

thermal diffusion and the maximum temperature generated by ELA treatment decreases as the sample thickness is increased due to increasing the heat capacity of IGZO samples. Therefore, the ELA process is less effective on the processed samples electrical properties [123].

In regard to XRD patterns, all the as-deposited IGZO films in this study found to be amorphous, regardless of the growth conditions. XRD patterns for the optimised as-deposited IGZO 40 nm thick samples[viii] upon ELA with one pulse at different energy densities are shown in Fig. 6-18, which matches the most commonly observed patterns for a-IGZO [110, 123, 218].

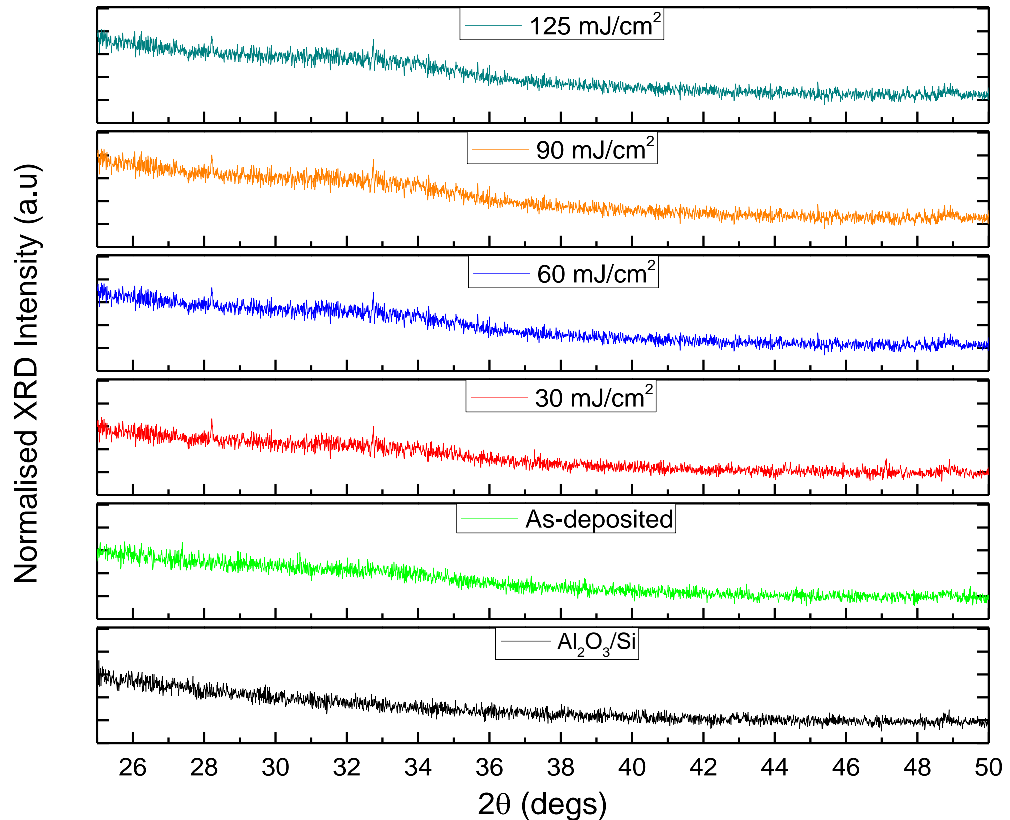

Fig. 6-18. XRD patterns for the optimised IGZO (1:1:1) samples pre and post ELA at different energy densities. The XRD pattern for the used substrates (Al_2O_3/Si) is also included as a reference.

Upon ELA at the examined conditions for TFTs on silicon substrates, IGZO samples maintained the amorphous structure. This can be assigned to the complexity of amorphous IGZO structure, the moderate energy density range applied here, and the mechanism of ELA heating whereby the samples temperature is increased in very short processing times. M. Nakata et al. have observed IGZO samples 20 nm thick crystallisation after furnace annealing at 800°C for 30

[viii] The samples thickness was selected to be 40 nm the same as what is examined for TFTs, in order to evaluate the microstructural changes within the KrF photons penetration depth in IGZO (~45 nm). This also avoids any possible disruption to the obtained XRD patterns caused by different heating throughout the sample thickness under ELA.

min, or upon ELA with single pulse from XeCl excimer laser (λ = 308 nm – pulse duration =25 ns) at high laser energy density of 500 mJ/cm^2 [79]. Maintaining the amorphous structure after ELA for our samples reveals also that the annealed films are still very smooth since crystallisation typically increases the surface roughness due to grain boundaries creation. Although a broad and weak diffraction peak becomes more noticeable at 2θ=33° for the ELA-treated samples at ≥ 60 mJ/cm^2, it does not reveal a strong evidence of clear IGZO crystallisation. The appearance of this peak is due to the ELA induced heating and indicates microstructure changes such as the onset of forming nanocrystals i.e. the films became less amorphous. This could explain the Hall mobility reduction of IGZO thin films processed at ≥ 60 mJ/cm^2 as shown Fig. 6-17.

High-resolution XPS measurements were undertaken on the optimised IGZO samples before and after ELA at 30 mJ/cm^2, which is the optimised laser energy density in terms of TFTs performance. Fig. 6-19 compares the metallic composition for the optimised as deposited IGZO samples deposited from IGZO (1:1:1) target obtained by EDX and XPS pre and post ELA.

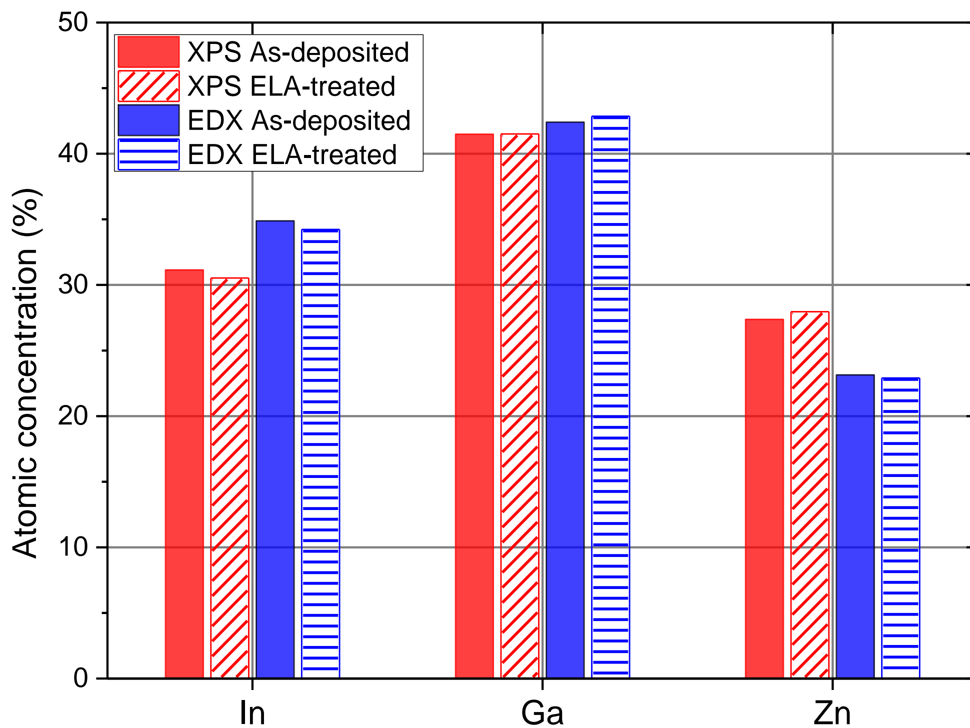

Fig. 6-19. Atomic concentrations of the contained metals in the optimised as-deposited IGZO samples examined for TFTs before and after ELA with one pulse at 30 mJ/cm^2 obtained by XPS vs. EDX.

The observed variations between the two techniques' results are assigned to the surface cleaning procedure performed in XPS measurements with argon ions sputtering in order to remove surface contaminations. This in turn will result in altering the metallic composition of the

examined surface since the contained metals in IGZO samples have different sputtering rates, with that for indium and zinc being the highest and the lowest respectively. This was evidenced for IGZO samples of different sputter deposition conditions as discussed before. Whereas, in EDX no sputtering is involved and the compositional data is gathered throughout the bulk material unlike XPS which is surface analysis technique. Therefore, the XPS results showed lower indium and higher zinc contents compared to EDX results.

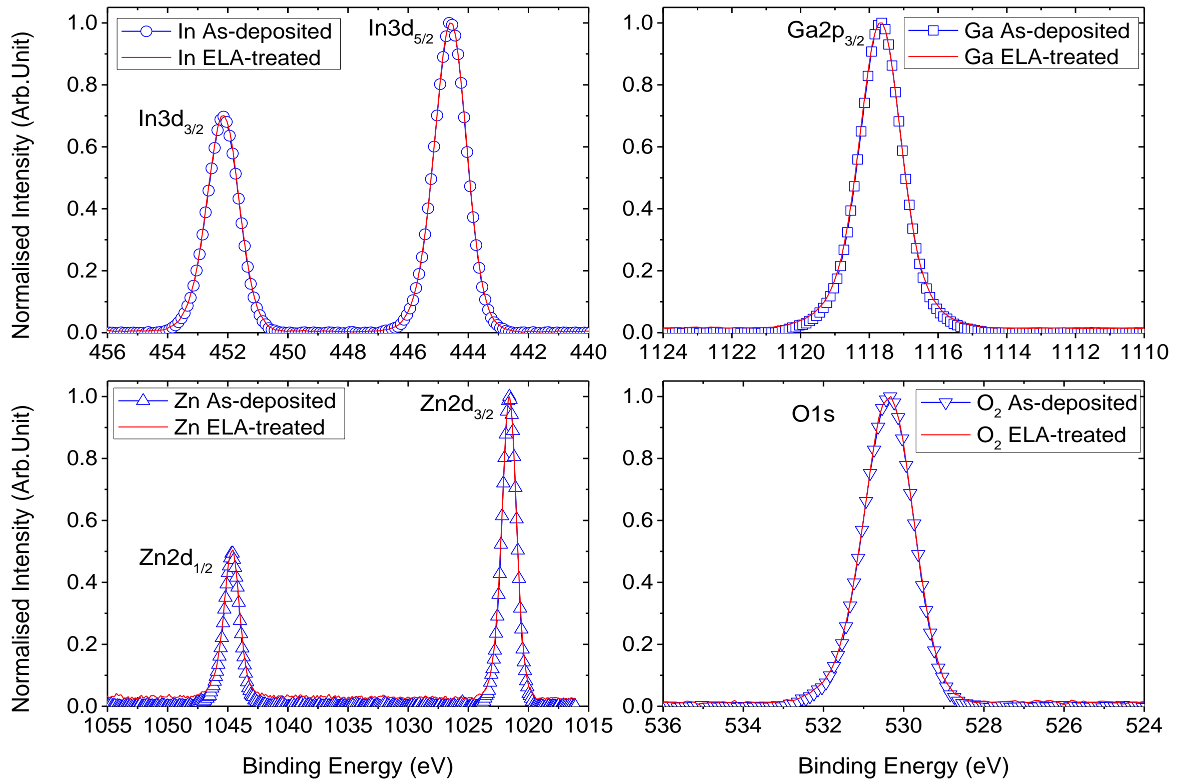

Fig. 6-20. The Effect of ELA with one pulse at 30 mJ/cm² on the photoelectron spectra of the contained elements for the optimised as-deposited IGZO samples examined for TFTs.

As demonstrated in Fig. 6-20, no changes in the XPS spectra for the contained elements In-Ga-Zn-O are detected after ELA treatment with single pulse at 30 mJ/cm^2. This indicates no detectable chemical state changes, which can be assigned to the low laser energy density applied. Also, as shown before the chemical composition obtained by XPS and EDX before and after ELA demonstrated rather small changes. Therefore, the significant electrical properties improvements observed for IGZO thin films upon ELA could be associated with electronic structure improvement and reduction of trap states in the conduction band of IGZO, rather than microstructure and chemical composition changes. For TFT devices, the reduction or trap states density is reflected by the field effect mobility enhancement and the subthreshold swing S rather

small reduction compared to non-treated TFTs. In addition, as stated previously, ELA reduces the active layer resistance as well as the contact resistance between source-drain electrodes and the active layer leading to better TFTs characteristics. The results of XRD and XPS highlight that the TFT performance improvement upon ELA is mostly assigned to reduction of the contact resistance. Further investigations are needed to examine the electronic structure and trap states changes upon ELA at 30 mJ/cm^2 using other techniques such as spectroscopic ellipsometry (SE) [219]. Kimura et al [77] have developed a novel approach to extract the trap states density from the C-V characteristics of TFTs at low frequencies and applied to IGZO TFTs after annealing at 300°C for 1h in air. They have reported annealing caused reducing trap states near the conduction band of IGZO leading to better performance TFTs.

6.6.3 Effect of ELA on the performance of IGZO TFTs on flexible PEN substrates

In the previous section, it was demonstrated the ELA with single pulse at a rather low energy density of 30 mJ/cm^2 is very efficient in enhancing the characteristics of room temperature fabricated IGZO TFTs on silicon substrates. At these conditions the substrate temperature is expected to remain almost unaffected. J P Bermundo et al [112] have used COMSOL Multiphysics simulation to study the temperature changes for IGZO TFTs on silicon substrates upon ELA with single pulse from XeCl laser (308 nm) at 110 mJ/cm^2, and KrF laser (248 nm) at 60 mJ/cm^2. They confirmed that at these ELA conditions, the substrate temperature was kept below 50°C. While the IGZO temperature is extremely increased to more than 1000°C for less than 100 ns during ELA treatments. Fujii et al reported that during ELA of InZnO thin-film transistors with single pulse at 30 mJ/cm^2 from XeCl-laser (308 nm) the substrate and InZnO samples temperature is increased to about 45°C and 220°C respectively, estimated via Multiphysics COMSOL simulation software [220]. Considering the glass transition temperature of plastic substrates such as polyethylene naphthalate (PEN) is about 120°C, the concluded ELA conditions in this research shows promise for application to IGZO TFTs on flexible heat-sensitive plastic substrates. To examine this, commercial IGZO TFTs on 6-inch PEN plastic substrates attached to carrier glass substrates were provided by PragmatIC Printing Ltd. The TFTs geometry is similar to that for IGZO TFTs on silicon substrates discussed above apart from the channel length being 2 μm instead of 5 μm, and the IGZO active layer being grown by pulsed DC magnetron sputtering.

Fig. 6-21compares the averaged transfer characteristic curves for IGZO TFTs on PEN subjected to ELA treatment with one pulse at 15-45 mJ/cm^2. Each curve represents the average of the transfer characteristics curves of 15 TFTs on PEN with the same ELA conditions. The extracted electrical parameters are shown in Table 6-7.

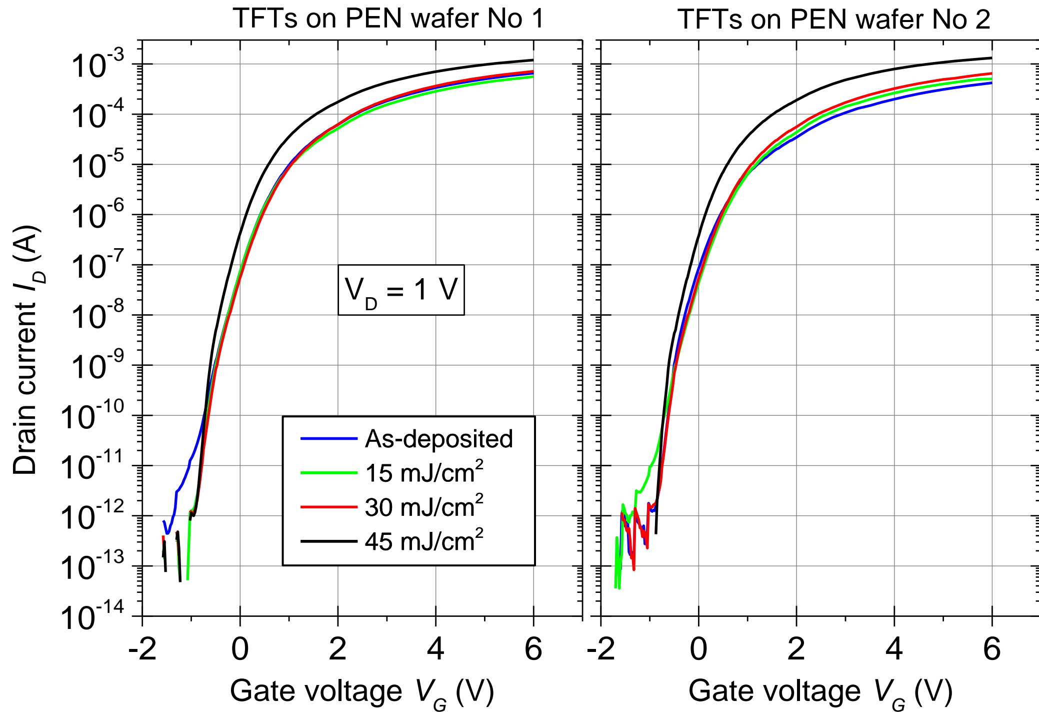

Fig. 6-21. Averaged transfer characteristics curves for IGZO TFTs on PEN upon ELA with one pulse at different energy densities. Two wafers were tested for reproducibility test.

Laser Energy (mJ/cm^2)	μ_{FE} (cm^2/Vs)	*S* (V/decade)	V_{ON} (V)	I_{ON}/I_{OFF} (Ratio)	TFTs R_{ON} (K Ω)	Hysteresis (ΔV_{ON})
0	2.1±0.1	0.28±0.01	-0.46±0.06	(4 ±1) E+07	1.8 ±0.4	0.90±0.09
15	2.1±0.1	0.27±0.02	-0.48±0.05	(5±2) E+07	2.0±0.7	0.90±0.05
30	2.3±0.1	0.27±0.02	-0.46±0.04	(6 ±2) E±07	1.5±0.3	0.85±0.08
45	3.65±0.09	0.24±0.01	- 0.60±0.03	(1.6±0.3) E+08	1±1.0	0.58±0.06

Table 6-7. The extracted electrical parameters for IGZO TFTs on PEN upon ELA with one pulse at different energy densities.

It can be seen that ELA at 45 mJ/cm^2 noticeably enhanced the TFTs electrical characteristics. Namely, the field effect mobility and subthreshold swing S are increased and decreased respectively. The field effect mobility enhancement from 2.13±0.1 to 3.65±0.09 cm^2/Vs reflects a reduction of trap states within IGZO, while the reduction of S values from 0.28±0.01 to 0.24±0.01 V/decade indicates reduction of both interfacial trap sates at IGZO/Al_2O_3 and bulk trap

states in IGZO upon ELA. The trap states reduction is also indicated by the observed V_{ON} hysteresis reduction from 0.9±0.09 to 0.58±0.06 V. [48, 77]. The ELA-treated IGZO TFTs at 45 mJ/cm^2 demonstrate a high on-state current of 10^{-3} A, an off-state current as small as 10^{-13} A, and an I_{ON}/I_{OFF} ratio of (1.6±0.3)×10^8. These features are desired for TFT application as switching elements such as in FPDs [48]. In regard to the TFTs on-resistance (R_{ON}), it was reduced upon ELA as shown in Table 6-7, associated with reducing the active layer IGZO resistivity/ resistance and the contact resistance between the Au/Ti source/drain electrodes and the active layer, resulting in better devices' performance [107, 217]. The achieved electrical properties enhancements for IGZO TFTs by ELA were reproducible when the same processing conditions were applied to a second IGZO TFTs wafer as shown in Fig. 6-21 above.

To highlight, all the optimised TFT devices in this study both on silicon and PEN substrates exhibited turn on voltage V_{ON} values close to zero which is desired for lower power consumption [48].

Based on the findings of the TFTs on silicon substrates, higher laser energy density than 45 mJ/cm^2 was not examined for those on PEN substrates. Nevertheless, it was demonstrated the performance of TFTs on PEN is noticeably enhanced when ELA treated at 45 mJ/cm^2 and hence it is worth examining higher laser energy densities. The difference in the optimum laser energy density for TFTs on silicon and on PEN is assigned to variations in the physical characteristics for as-grown IGZO samples deposited at NTU and those grown at PPL since different deposition methods and conditions were used.

6.7 Concluding remarks

It was explored how different sputter-deposition and ELA parameters impact on IGZO thin films resistivity and IGZO TFTs performance. The used set of deposition conditions (including applied RF power, sputtering gases and pressure, and the target composition) control the deposition rate, the metallic composition, and the electrical resistivity of the resulting IGZO film. ELA at moderate laser energy density remarkably reduces the resistivity of IGZO samples via increasing both the free carrier density and mobility. The observed IGZO TFTs performance dependence on the growth conditions is well justified by the noticed trends for metallic composition and resistivity for IGZO thin films. Moderate RF power (50 W) and low sputtering

pressure (2 mTorr) of low oxygen to argon ratio % (2%) was found to produce suitable thin film material for TFT devices at room temperature. ELA with single pulse at low energy density (30 mJ/cm^2) was very effective in enhancing the performance of IGZO TFTs fabricated on silicon substrates. The concluded ELA treatment process was successfully applied to commercial IGZO TFTs fabricated by PragmatIC Printing Ltd on heat sensitive substrates PEN. Relatively high performance TFTs were obtained by ELA for both sets of TFTs on silicon and PEN plastic substrates via reducing the trap states density and the devices contact resistance. The optimum ELA laser energy density identified in this research to enhance IGZO TFT characteristics is less than 50 mJ/cm^2 which is relatively lower than that typically used LTPS TFTs. Thus, compared to LTPS higher throughput of ELA-treated IGZO-TFTs could be realised at lower processing cost per unit area and on cost-efficient flexible plastic substrates which are essential for flexible electronics. Moreover, the successful transfer of ELA treatment to commercial TFTs deposited at different deposition conditions implies the process reproducibility.

7 Conclusions and Future Perspectives

7.1 Introduction

The research carried out in this PhD was aimed at low thermal-budget fabrication of functional oxide materials including AZO as alternative to ITO for transparent electrode applications, and a-IGZO as a promising material for TFT applications. The materials investigated were fabricated by a combination of room temperature RF magnetron sputtering and excimer laser annealing over a wide range of conditions. Microstructural, compositional, electrical, and optical properties of the fabricated films were systematically investigated as a function of the fabrication (deposition and annealing) conditions. The optimised AZO and IGZO films were examined for application to PV and TFT devices, respectively. This chapter presents the research conclusions, key outcomes, as well as some thoughts for future work.

7.2 Conclusions

The main conclusion of this research is that excimer laser annealing is a very effective annealing approach to further enhance the electrical and optical characteristics of room temperature sputter-deposited oxide thin films via an ultra-rapid and localised heating mechanism. The achieved enhancements in many cases cannot be achieved with conventional annealing techniques. The reported enhancements of AZO and IGZO characteristics present KrF ELA as a promising annealing technique for low temperature fabricated electronics on heat sensitive substrates.

Chapter 4 examined room temperature deposition of AZO thin films on glass substrates by RF magnetron sputtering at a comprehensive range of deposition conditions including the oxygen to argon ratio %, applied RF power, and sputtering pressure. The electrical resistivity evolution of AZO upon different deposition conditions was investigated by studying the electrical, structural, and compositional characteristics. It was demonstrated that the achieved resistivity for AZO is strongly controlled by the average grain size and the oxygen related defects at grain boundaries of the samples. The grain size and oxygen defects are directly linked to the sputtered particles' kinetic energy which in turn is a function of the growth conditions. The particles' energy increases as the applied RF power is increased or the sputtering pressure is decreased, leading to bigger grain sizes, fewer oxygen defects, higher electron density and mobility, and therefore

lower resistivity. Relatively high RF power 180 W (4 W/cm^2), and low pressure (2 mTorr) of low oxygen to argon ratio % (0.2%), were determined as the optimised deposition conditions for good quality AZO transparent electrodes at low substrate temperature demonstrating a resistivity of $1x10^{-3}$ Ω.cm and visible transparency of 82% at λ=550 nm for 180 nm thick AZO samples. The optimised deposition condition resulted in very uniform thickness (<5% thickness variations over 4-inch wafer) and reproducible AZO samples (<3% resistivity variations) at relatively high growth rate (~ 20 nm/min).

In chapter 5, ELA using a KrF (λ=248 nm) excimer laser was applied to AZO samples deposited in the previous chapter. ELA was performed in air at room temperature using different number of pulses and laser energy densities. It was demonstrated that ELA increases both the free carrier density and mobility for AZO samples leading to resistivity reduction that depends on the growth parameters. About 50% resistivity reduction was obtained for the optimised as-deposited AZO samples when processed with 5 pulses at 125 mJ/cm^2 achieving a resistivity of $5x10^{-4}$ Ω.cm. Furthermore, ELA enhances the visible transparency to 86%, and increases the bandgap from 3.69 to 3.80 eV. A detailed analysis to explain the origin of such a resistivity reduction upon ELA was undertaken and presented. Average grain size increase, grain boundaries and oxygen-related defects reduction, and effective Al dopant incorporation into the ZnO lattice were demonstrated as the ELA mechanisms to decrease the room temperature deposited AZO samples' resistivity to values close to that of standard ITO electrodes. It was also demonstrated, via a detailed XRD study, that the ELA effect on AZO samples microstructural properties throughout the samples thickness is dependent on both the samples thickness and the ELA conditions applied. RTA was also examined on the optimised as-deposited AZO samples at different annealing profiles, with RTA at 300°C for 20s in nitrogen resulted in similar resistivity and slightly better visible transmission in relation to the optimised ELA-treated AZO samples. Grain size increase, which is smaller than that achieved by ELA, Al activation into ZnO, and surface roughness reduction were the mechanisms determined to result from RTA to improve the AZO electro-optical characteristics. The optimised ELA and RTA treated samples are ranked as high-quality transparent electrodes and were examined for OPV devices. Devices with the optimised treated (ELA or RTA) AZO samples demonstrated a comparable performance to that of devices with high-quality commercial ITO electrodes. The achieved electrical and optical properties

enhancements upon ELA and RTA were reflected in the OPV device performance, compared to those with the as-deposited AZO samples. The environmental robustness of the fabricated AZO samples was examined under the IEC test 61646 standard conditions (85°C, 85% RH, and for 1000h). The samples' stability was found to be dependent on the fabrication conditions; the smallest degradation rate (20% resistivity increase) was observed for thicker AZO samples (360 nm), while the largest degradation rate (230% resistivity increase) was observed for samples deposited at high sputtering pressure (5 mTorr). In comparison, high-quality reference ITO electrodes showed ~ 10% resistivity increase.

In chapter 6, IGZO thin films were deposited by RF magnetron sputtering at room temperature and different growth conditions (RF power, sputtering pressure, and oxygen to argon ratio %). Then, IGZO samples were subjected to ELA aiming at IGZO thin films as an active layer for TFT devices. It was demonstrated that the metallic composition, which dictates the samples conductivity, is dependent on the used target metallic composition, RF power, and oxygen to argon ratio %. ELA changes the IGZO thin films electrical resistivity across wide range from highly resistive samples to a resistivity close to that of TCOs via increasing both the free carrier density and mobility, while the amorphous microstructure is maintained. A range of IGZO deposition conditions was applied to top-gated-staggered IGZO TFTs on silicon substrates, and the observed TFTs performance at different conditions is justified by the observed metallic composition and resistivity trends for IGZO thin films. Moderate RF power 50 W (1.1 W/cm^2), and low pressure (2 mTorr) of (2% oxygen to argon ratio %) resulted in suitable IGZO thin films for functional TFTs. ELA with single pulse at rather low laser energy density (30 mJ/cm^2) was very effective in improving the performance of IGZO TFTs on silicon substrates. Higher on/off drain current ratios and field effect mobility values were obtained upon ELA, mainly due to decreasing the active layer IGZO resistivity, as well as the contact resistance between IGZO and the source-drain electrodes. Finally, ELA was successfully applied to commercial IGZO TFTs fabricated directly on flexible PEN substrates resulting in enhanced performance (higher on/off drain current ratios and field effect mobility, and lower subthreshold swing and turn on voltage's hysteresis) without damaging the plastic substrates.

7.3 Key outcomes of the research

1. Demonstration, via the performed AZO fabrication and characterisation, of the conduction mechanism in polycrystalline TCOs and how the conductivity is controlled by the structural and compositional properties.
2. Demonstration of the KrF-ELA application to room temperature deposited AZO samples at a moderate laser energy density resulting in electro-optical characteristics close to that of standard ITO transparent electrodes. Compared to the existing reported work on laser annealing of AZO, this research concluded to a set of both deposition and processing conditions that offers reproducible high quality AZO transparent electrodes.
3. Demonstration of RTA, at moderate temperature (300°C) and short processing time (20s), as another processing approach to obtain high quality AZO transparent electrodes when applied to the optimised as-deposited AZO samples reported in this research.
4. Demonstration of the integration of KrF-ELA into IGZO TFTs fabrication achieving valuable performance enhancements, at rather low laser energy densities.
5. Demonstration, for the first time, of the successful application of KrF-ELA to IGZO TFTs on polymer PEN flexible substrates leading to better performance.

Various trends and correlations between the studied materials' physical characteristics were experimentally observed at different fabrication conditions. Optimisation of the growth conditions at room temperature was determined to achieve the best possible quality for as-deposited samples in terms of electrical properties. Post-deposition annealing with ELA and RTA were demonstrated to be a powerful method to further enhance the electrical and optical properties of the optimised as-deposited samples. It was determined that this was the result of process controlled modification of the density and distribution of microstructural defects, as well as of local atomic rearrangements.

7.4 Future perspectives

As in most PhD research programmes, the observed results will always open the door for new research questions and experiments. Some thoughts for future work are presented.

7.4.1 Future work for AZO

1. Based on the XRD findings, XPS depth profile study should be performed on the optimised ELA-treated AZO samples to find out if there are variations in oxygen-related defects concentration and aluminium activation states throughout the sample thickness. Variations are expected due to the stratified nature of the ELA-treated samples.
2. Layer by layer ELA. It was demonstrated that the KrF ELA causes gradient processing over the sample thickness that creates spatial variations in the physical properties over

the samples thickness. Hence, layer by layer ELA could be examined for more uniform properties over the AZO thickness. ELA would be performed on multi-layered AZO samples with each layer being 50 nm thick, i.e. close to KrF photons penetration in AZO samples.

3. Investigation of the mechanical stability of AZO on flexible polymer substrates. AZO thin films would be deposited at room temperature, at the optimised sputtering pressure (2 mTorr) and gases (0.2% oxygen to argon ratio), but at lower RF power than that optimised for growths on glass (<180 W) in order to avoid damaging the polymer substrates by highly energetic particles at high RF power. For comparison with AZO, commercial ITO samples on flexible substrates would be obtained. Then, the AZO and ITO samples conductivity would be tested against the following testing procedures:
   - Bending test, as a measure of the critical radius of curvature at which the examined sample conductivity fails. The test is known as the monotonic bending test method [221].
   - Tensile test, whereby AZO samples are stretched and the conductivity is monitored against the samples strain [221].
   - Wear test that involves moving a polymer ball on the sample surface typically at a frequency of 10 Hz. The test is referred to as high frequency reciprocating rig wear test (HFRR) [222].
4. Examine ELA of AZO thin films on flexible polymer substrates. Processing with multiple pulses at low laser energy densities (e.g. 50 mJ/cm^2) is expected to be highly beneficial.
5. Investigate AZO targets with lower doping levels than 2 wt. %. The achieved free electron density for the optimised as-deposited AZO samples upon ELA ($6.21 \times 10^{20}/cm^3$) revealed that the carrier mobility is dominated by ionised impurity scattering. Moreover, the average transmission in the NIR region was degraded after ELA due to increasing the free electron density which is not desired for some TCO applications, such as silicon based PV devices operating in the wavelength range of 350-1250 nm. Hence, further study could examine using lower doping levels than 2 wt.% in order to obtain lower free electron density which could simultaneously enhance the carrier mobility, leading to similar conductivity to that achieved with 2 wt. %, and enhance NIR transmission.
6. Characterisation after IEC 61646 Test, based on the reported results for AZO samples upon the test, the following tasks are suggested:
   - XPS measurements for AZO samples following the IEC 61646 test that would provide clearer understanding of the AZO conductivity degradation mechanisms and how the degradation is linked to microstructural characteristics.
   - Further investigations on the laser annealed samples to explain the relatively higher conductivity degradation rate after the IEC 61646 test compared to the optimised as-deposited and RTA treated samples. XPS depth profile study on the ELA and RTA treated samples following the test could demonstrate the differences between these samples in terms of the density of the adsorbed

defects from the test environment as well as the penetration depth of these defects.

7. Investigate the use of a protective layer on the AZO samples for better stability against damp heat exposure. EVA (ethylene-vinyl acetate copolymer) is commonly used for CIGS PVs encapsulation and would be a good candidate for this study.
8. Application of AZO to CIGS PV devices, it was reported that high temperature (~ 200°C) fabrication of TCOs on CIGS PV devices damages the interface properties between the CIGS and CdS junction, leading to degrading the PVs' achieved efficiency [25, 223]. The high-quality AZO samples obtained in this research via ELA (i.e. low thermal budget process) are proposed for CIGS PV applications.
9. Investigate the optimised AZO samples as the source, drain, and gate electrodes for TFTs instead of Ti/Au dual layer for fully transparent TFTs. AZO work function is ~ 4.5 eV compared to 4.3 eV for titanium and 5.1 eV for gold.
10. Use simulation software, such as COMSOL, to investigate the laser-induced heating of AZO thin films and the underlying substrates upon ELA. Different ELA conditions and AZO samples thicknesses would be used. This could explain the observed evolution of AZO structural characteristics throughout the sample thickness upon ELA.
11. GZO vs. AZO, gallium doped zinc oxide (GZO) films have been reported as another candidate for ITO replacement [12]. Hence, it is suggested to conduct a study on ELA of room temperature deposited GZO films aiming at low thermal-budget fabrication of high-quality transparent electrodes. The GZO study will be built on the observations and conclusions of the AZO study conducted in this research.

7.4.2 Future work for IGZO

The overall aim of the conducted work on IGZO TFTs was to examine the potential of KrF-ELA as an alternative to thermal annealing. However, there are still various aspects to investigate including

1. Investigate the application of ELA to IGZO TFTs of different geometries in terms of the channel length and width as well as the TFT layers arrangements. For instance, examine KrF-ELA of bottom-gated-staggered IGZO TFTs.
2. Examine the stability of the fabricated TFTs pre and post ELA. There are typical stability tests performed on TFTs for potential applications as switching elements.
    - Examine the TFTs performance stability upon a number of transfer curve measurements over a period of time in air ambient at room temperature.
    - Bias stress measurement whereby a constant gate voltage 20 V is applied typically for a period 10h, while the source and drain electrode are grounded. The transfer curve is constantly measured during this period and the turn on voltage stability is monitored [48, 200].

3. Investigate co-sputtering from IGZO target and ZnO target. It was demonstrated in this research and other reports that sputter-deposited IGZO films always exhibit zinc deficiency compared to the used sputtering target metallic composition. Hence, co-sputtering of IGZO and ZnO targets would examine the zinc deficiency effect on IGZO-TFTs performance.
4. Bilayer IGZO active layer for TFTs. It was demonstrated that the indium ratio in IGZO samples has a strong impact on the electron mobility, with the mobility being enhanced as the indium ratio in IGZO samples is increased. Also, it was observed that the indium ratio increases as the applied RF power is increased. Hence, a 40 nm thick bilayer of (40-x) nm thick IGZO deposited at the optimised RF power 50 W and x nm (x=5, 10, and 15) thick IGZO deposited at higher RF power e.g. 75 or 100 W could be examined. The top layer with higher indium content is anticipated to act as an election mobility booster in the electron accumulation region of TFTs at the gate insulator-IGZO interface leading possibly to better performance. Nevertheless, it should be considered that energetic particles at high RF power may damage the IGZO interface properties.
5. Homojunction IGZO-based TFTs. It was demonstrated that ELA-treated IGZO thin films at relatively higher laser energy density achieve conductivity values which are good enough to be applied as the source and drain electrodes in TFTs. Hence, selective ELA treatment for IGZO thin films at different laser energy densities, i.e. ≥ 100 mJ/cm^2 for the source and drain regions and low energy density for the active layer, could be examined for Homojunction IGZO TFTs.
6. Use simulation software, such as COMSOL, to investigate the laser-induced heating for both the processed IGZO samples and the underlying substrate upon ELA.

8 References

References

[1] J. Jerzy. 2001*"Semiconductor Glossary. Semiconductor OneSource".* [Thermal budget]. Available: http://www.semi1source.com/glossary/default.asp?searchterm=dopant+redistribution [Accessed: 16/05/2016].
[2] D. R. Cairns, R. P. Witte II, D. K. Sparacin, S. M. Sachsman, D. C. Paine, G. P. Crawford and R. Newton, "Strain-dependent electrical resistance of tin-doped indium oxide on polymer substrates," *Appl. Phys. Lett.,* vol. 76, pp. 1425-1427, 2000.
[3] K. Ellmer, "Past achievements and future challenges in the development of optically transparent electrodes," *Nature Photonics,* vol. 6, pp. 809-817, 2012.
[4] M. Choi, Y. Kim and C. Ha, "Polymers for flexible displays: from material selection to device applications," *Progress in Polymer Science,* vol. 33, pp. 581-630, 2008.
[5] KAMIYA, T., NOMURA, K. and HOSONO, H., 2010. Present status of amorphous In–Ga–Zn–O thin-film transistors. *Science and Technology of Advanced Materials,* 11 (4), 044305.
[6] K. Nomura, H. Ohta, A. Takagi, T. Kamiya, M. Hirano and H. Hosono, "Room-temperature fabrication of transparent flexible thin-film transistors using amorphous oxide semiconductors," *Nature,* vol. 432, pp. 488-492, 2004.
[7] E. Fortunato, P. Barquinha and R. Martins, "Oxide Semiconductor Thin-Film Transistors: A Review of Recent Advances," *Adv Mater,* vol. 24, pp. 2945-2986, 2012.
[8] H. Hartnagel, A. Dawar, A. Jain and C. Jagadish, *Semiconducting Transparent Thin Films.* Institute of Physics Pub. Bristol, UK, Philadelphia, PA, 1995.
[9] W. Kern, *Thin Film Processes II.* Academic press, UK, 2012.
[10] D. Basting, *Excimer Laser Technology.* Springer Science & Business Media, Germany, 2005.
[11] M. S. Brown and C. B. Arnold, "Fundamentals of laser-material interaction and application to multiscale surface modification," in *Laser Precision Microfabrication.* Springer, Germany, 2010.
[12] D. Ginley, H. Hosono and D. C. Paine, *Handbook of Transparent Conductors.* Springer Science & Business Media, Germany, 2010.
[13] Ü Özgür, Y. I. Alivov, C. Liu, A. Teke, M. Reshchikov, S. Doğan, V. Avrutin, S. Cho and H. Morkoc, "A comprehensive review of ZnO materials and devices," *J. Appl. Phys.,* vol. 98, pp. 041301, 2005.
[14] P. Barquinha, R. Martins, L. Pereira and E. Fortunato, *Transparent Oxide Electronics: From Materials to Devices.* John Wiley & Sons, UK, 2012.
[15] K. Ellmer, A. Klein and B. Rech, *Transparent Conductive Zinc Oxide: Basics and Applications in Thin Film Solar Cells.* Springer Science & Business Media, Germany, 2007.
[16] S. Calnan and A. Tiwari, "High mobility transparent conducting oxides for thin film solar cells," *Thin Solid Films,* vol. 518, pp. 1839-1849, 2010.
[17] T. Minami, "Transparent conducting oxide semiconductors for transparent electrodes," *Semiconductor Science and Technology,* vol. 20, pp. S35, 2005.
[18] T. Minami, "Present status of transparent conducting oxide thin-film development for Indium-Tin-Oxide (ITO) substitutes," *Thin Solid Films,* vol. 516, pp. 5822-5828, 2008.
[19] I. Espa, *Export Restrictions on Critical Minerals and Metals: Testing the Adequacy of WTO Disciplines.* Cambridge University Press, UK, 2015.
[20] B. Azzopardi, C. J. Emmott, A. Urbina, F. C. Krebs, J. Mutale and J. Nelson, "Economic assessment of solar electricity production from organic-based photovoltaic modules in a domestic environment," *Energy & Environmental Science,* vol. 4, pp. 3741-3753, 2011.
[21] K. Ghaffarzadeh and R. Das, 2012 ."ITO alternatives to gain speed in the $2 billion TCF market" [Transparent Conductive Films (TCF)]. Available at: http://www.idtechex.com/research/articles/ito-alternatives-to-gain-speed-in-the-2-billion-tcf-market-00004561.asp [Accessed:15/05/2016].

[22] K. Ghaffarzadeh and R. Das, 2015. "Transparent Conductive Films (TCF) 2015-2025: Forecasts, Markets, Technologies" [Transparent Conductive Films (TCF)]. Available: http://www.idtechex.com/research/reports/transparent-conductive-films-tcf-2015-2025-forecasts-markets-technologies-000437.asp. [Accessed:20/05/2016].

[23] M. Vosgueritchian, D. J. Lipomi and Z. Bao, "Highly conductive and transparent PEDOT: PSS films with a fluorosurfactant for stretchable and flexible transparent electrodes," *Advanced Functional Materials,* vol. 22, pp. 421-428, 2012.

[24] C. J. Emmott, A. Urbina and J. Nelson, "Environmental and economic assessment of ITO-free electrodes for organic solar cells," *Solar Energy Mater. Solar Cells,* vol. 97, pp. 14-21, 2012.

[25] H. Liu, V. Avrutin, N. Izyumskaya, Ü Özgür and H. Morkoç, "Transparent conducting oxides for electrode applications in light emitting and absorbing devices," *Superlattices and Microstructures,* vol. 48, pp. 458-484, 2010.

[26] S. Major, S. Kumar, M. Bhatnagar and K. Chopra, "Effect of hydrogen plasma treatment on transparent conducting oxides," *Appl. Phys. Lett.,* vol. 49, pp. 394-396, 1986.

[27] A. Van der Drift, "Evolutionary selection, a principle governing growth orientation in vapour-deposited layers," *Philips Res.Rep,* vol. 22, pp. 267-288, 1967.

[28] K. C. Park, D. Y. Ma and K. H. Kim, "The physical properties of Al-doped zinc oxide films prepared by RF magnetron sputtering," *Thin Solid Films,* vol. 305, pp. 201-209, 1997.

[29] H. Hosono, "Recent progress in transparent oxide semiconductors: Materials and device application," *Thin Solid Films,* vol. 515, pp. 6000-6014, 2007.

[30] J. Lu, Z. Ye, Y. Zeng, L. Zhu, L. Wang, J. Yuan, B. Zhao and Q. Liang, "Structural, optical, and electrical properties of (Zn, Al) O films over a wide range of compositions," *J. Appl. Phys.,* vol. 100, pp. 073714, 2006.

[31] J. Lu, S. Fujita, T. Kawaharamura, H. Nishinaka, Y. Kamada, T. Ohshima, Z. Ye, Y. Zeng, Y. Zhang and L. Zhu, "Carrier concentration dependence of band gap shift in n-type ZnO: Al films," *J. Appl. Phys.,* vol. 101, pp. 83705-83705, 2007.

[32] E. Burstein, "Anomalous optical absorption limit in InSb," *Physical Review,* vol. 93, pp. 632, 1954.

[33] B. E. Sernelius, K. Berggren, Z. Jin, I. Hamberg and C. Granqvist, "Band-gap tailoring of ZnO by means of heavy Al doping," *Physical Review B,* vol. 37, pp. 10244, 1988.

[34] Z. Jin, I. Hamberg and C. Granqvist, "Optical properties of sputter-deposited ZnO: Al thin films," *J. Appl. Phys.,* vol. 64, pp. 5117-5131, 1988.

[35] A. Janotti and Van de Walle, Chris G, "Native point defects in ZnO," *Physical Review B,* vol. 76, pp. 165202, 2007.

[36] S. Zhang, S. Wei and A. Zunger, "Intrinsic n-type versus p-type doping asymmetry and the defect physics of ZnO," *Physical Review B,* vol. 63, pp. 075205, 2001.

[37] Van de Walle, Chris G, "Hydrogen as a cause of doping in zinc oxide," *Phys. Rev. Lett.,* vol. 85, pp. 1012, 2000.

[38] T. Minami, H. Sato, H. Nanto and S. Takata, "Group III impurity doped zinc oxide thin films prepared by RF magnetron sputtering," *Japanese Journal of Applied Physics,* vol. 24, pp. L781, 1985.

[39] K. Ellmer, "Resistivity of polycrystalline zinc oxide films: current status and physical limit," *J. Phys. D,* vol. 34, pp. 3097, 2001.

[40] T. Minami, H. Sato, K. Ohashi, T. Tomofuji and S. Takata, "Conduction mechanism of highly conductive and transparent zinc oxide thin films prepared by magnetron sputtering," *J. Cryst. Growth,* vol. 117, pp. 370-374, 1992.

[41] K. Ellmer and R. Mientus, "Carrier transport in polycrystalline transparent conductive oxides: A comparative study of zinc oxide and indium oxide," *Thin Solid Films,* vol. 516, pp. 4620-4627, 2008.

[42] D. Zhang, "Adsorption and photodesorption of oxygen on the surface and crystallite interfaces of sputtered ZnO films," *Mater. Chem. Phys.,* vol. 45, pp. 248-252, 1996.

[43] J. Y. Seto, "The electrical properties of polycrystalline silicon films," *J. Appl. Phys.,* vol. 46, pp. 5247-5254, 1975.
[44] S. Cornelius, M. Vinnichenko, N. Shevchenko, A. Rogozin, A. Kolitsch and W. Möller, "Achieving high free electron mobility in ZnO: Al thin films grown by reactive pulsed magnetron sputtering," *Appl. Phys. Lett.,* vol. 94, pp. 042103, 2009.
[45] I. Hamberg and C. G. Granqvist, "Evaporated Sn-doped In2O3 films: Basic optical properties and applications to energy-efficient windows," *J. Appl. Phys.,* vol. 60, pp. R123-R160, 1986.
[46] E. Denton, H. Rawson and J. Stanworth, "Vanadate glasses," *Nature,* vol. 173, pp. 1030-1032, 1954.
[47] H. Hosono, M. Yasukawa and H. Kawazoe, "Novel oxide amorphous semiconductors: transparent conducting amorphous oxides," *J. Non Cryst. Solids,* vol. 203, pp. 334-344, 1996.
[48] C. R. Kagan and P. Andry, *Thin-Film Transistors.* CRC Press, USA, 2003.
[49] R. Hoffman, B. J. Norris and J. Wager, "ZnO-based transparent thin-film transistors," *Appl. Phys. Lett.,* vol. 82, pp. 733-735, 2003.
[50] W. Shockley, "A unipolar" field-effect" transistor," *Proceedings of the IRE,* vol. 40, pp. 1365-1376, 1952.
[51] J. Lee, D. N. Liu and S. Wu, *Introduction to Flat Panel Displays.* John Wiley & Sons, UK, 2008.
[52] A. C. Tickle, *Thin-Film Transistors: A New Approach to Microelectronics.* John Wiley & Sons, UK, 1969.
[53] P. K. Weimer, "The TFT a new thin-film transistor," *Proceedings of the IRE,* vol. 50, pp. 1462-1469, 1962.
[54] P. Le Comber, W. Spear and A. Ghaith, "Amorphous-silicon field-effect device and possible application," *Electron. Lett.,* vol. 15, pp. 179-181, 1979.
[55] S. Depp, A. Juliana and B. Huth, "Polysilicon FET devices for large area input/output applications," in *Electron Devices Meeting, 1980 International,* 1980, pp. 703-706.
[56] T. Sameshima, S. Usui and M. Sekiya, "XeCl Excimer laser annealing used in the fabrication of poly-Si TFT's," *Electron Device Letters, IEEE,* vol. 7, pp. 276-278, 1986.
[57] H. Klauk, "Organic thin-film transistors," *Chem. Soc. Rev.,* vol. 39, pp. 2643-2666, 2010.
[58] H. Klasens and H. Koelmans, "A tin oxide field-effect transistor," *Solid-State Electronics,* vol. 7, pp. 701-702, 1964.
[59] P. Carcia, R. McLean, M. Reilly and G. Nunes Jr, "Transparent ZnO thin-film transistor fabricated by rf magnetron sputtering," *Appl. Phys. Lett.,* vol. 82, pp. 1117-1119, 2003.
[60] Y. G. Mo, M. Kim, C. K. Kang, J. H. Jeong, Y. S. Park, C. G. Choi, H. D. Kim and S. S. Kim, "Amorphous-oxide TFT backplane for large-sized AMOLED TVs," *Journal of the Society for Information Display,* vol. 19, pp. 16-20, 2011.
[61] M. Ito, C. Miyazaki, M. Ishizaki, M. Kon, N. Ikeda, T. Okubo, R. Matsubara, K. Hatta, Y. Ugajin and N. Sekine, "Application of amorphous oxide TFT to electrophoretic display," *J. Non Cryst. Solids,* vol. 354, pp. 2777-2782, 2008.
[62] T. Kamiya and H. Hosono, "Material characteristics and applications of transparent amorphous oxide semiconductors," *NPG Asia Materials,* vol. 2, pp. 15-22, 2010.
[63] S. R. Thomas, P. Pattanasattayavong and T. D. Anthopoulos, "Solution-processable metal oxide semiconductors for thin-film transistor applications," *Chem. Soc. Rev.,* vol. 42, pp. 6910-6923, 2013.
[64] T. Arai, "Oxide-TFT technologies for next-generation AMOLED displays," *Journal of the Society for Information Display,* vol. 20, pp. 156-161, 2012.
[65] S. Acharya, S. Chouthe, H. Graener, T. Böntgen, C. Sturm, R. Schmidt-Grund, M. Grundmann and G. Seifert, "Ultrafast dynamics of the dielectric functions of ZnO and BaTiO3 thin films after intense femtosecond laser excitation," *J. Appl. Phys.,* vol. 115, pp. 053508, 2014.
[66] H. Hosono, "Ionic amorphous oxide semiconductors: Material design, carrier transport, and device application," *J. Non Cryst. Solids,* vol. 352, pp. 851-858, 2006.

[67] T. Kamiya, K. Nomura and H. Hosono, "Origins of high mobility and low operation voltage of amorphous oxide TFTs: Electronic structure, electron transport, defects and doping," *Display Technology, Journal Of,* vol. 5, pp. 273-288, 2009.
[68] N. Dehuff, E. Kettenring, D. Hong, H. Chiang, J. Wager, R. Hoffman, C. Park and D. Keszler, "Transparent thin-film transistors with zinc indium oxide channel layer," *J. Appl. Phys.,* vol. 97, pp. 64505-64505, 2005.
[69] K. K. Banger, R. L. Peterson, K. Mori, Y. Yamashita, T. Leedham and H. Sirringhaus, "High performance, low temperature solution-processed barium and strontium doped oxide thin film transistors," *Chemistry of Materials,* vol. 26, pp. 1195-1203, 2014.
[70] M. K. Ryu, S. Yang, S. K. Park, C. Hwang and J. K. Jeong, "High performance thin film transistor with cosputtered amorphous Zn–In–Sn–O channel: Combinatorial approach," *Appl. Phys. Lett.,* vol. 95, pp. 072104, 2009.
[71] E. M. Fortunato, L. M. Pereira, P. M. Barquinha, Botelho do Rego, Ana M, G. Gonçalves, A. Vilà, J. R. Morante and R. F. Martins, "High mobility indium free amorphous oxide thin film transistors," *Appl. Phys. Lett.,* vol. 92, pp. 222103, 2008.
[72] H. Chiang, J. Wager, R. Hoffman, J. Jeong and D. A. Keszler, "High mobility transparent thin-film transistors with amorphous zinc tin oxide channel layer," *Appl. Phys. Lett.,* vol. 86, pp. 013503, 2005.
[73] D. Cho, J. Song, Y. C. Shin, C. S. Hwang, W. Choi and J. K. Jeong, "Influence of high temperature postdeposition annealing on the atomic configuration in amorphous In–Ga–Zn–O films," *Electrochemical and Solid-State Letters,* vol. 12, pp. H208-H210, 2009.
[74] R. M. Pasquarelli, D. S. Ginley and R. O'Hayre, "Solution processing of transparent conductors: from flask to film," *Chem. Soc. Rev.,* vol. 40, pp. 5406-5441, 2011.
[75] K. Ellmer, "Magnetron sputtering of transparent conductive zinc oxide: relation between the sputtering parameters and the electronic properties," *J. Phys. D,* vol. 33, pp. R17, 2000.
[76] H. Yabuta, M. Sano, K. Abe, T. Aiba, T. Den, H. Kumomi, K. Nomura, T. Kamiya and H. Hosono, "High-mobility thin-film transistor with amorphous InGaZnO4 channel fabricated by room temperature rf-magnetron sputtering," *Appl. Phys. Lett.,* vol. 89, pp. 2123, 2006.
[77] M. Kimura, T. Nakanishi, K. Nomura, T. Kamiya and H. Hosono, "Trap densities in amorphous-InGaZnO4 thin-film transistors," *Appl. Phys. Lett.,* vol. 92, pp. 133512-133512, 2008.
[78] F. Ruske, M. Roczen, K. Lee, M. Wimmer, S. Gall, J. Hüpkes, D. Hrunski and B. Rech, "Improved electrical transport in Al-doped zinc oxide by thermal treatment," *J. Appl. Phys.,* vol. 107, pp. 013708, 2010.
[79] M. Nakata, K. Takechi, T. Eguchi, E. Tokumitsu, H. Yamaguchi and S. Kaneko, "Flexible high-performance amorphous InGaZnO4 thin-film transistors utilizing excimer laser annealing," *Japanese Journal of Applied Physics,* vol. 48, pp. 081607, 2009.
[80] D. Scorticati, A. Illiberi, T. Bor, S. Eijt, H. Schut, G. Römer, M. K. Gunnewiek, A. Lenferink, B. Kniknie and R. M. Joy, "Thermal annealing using ultra-short laser pulses to improve the electrical properties of Al: ZnO thin films," *Acta Materialia,* vol. 98, pp. 327-335, 2015.
[81] J. Yoo, J. Lee, S. Kim, K. Yoon, I. J. Park, S. Dhungel, B. Karunagaran, D. Mangalaraj and J. Yi, "High transmittance and low resistive ZnO: Al films for thin film solar cells," *Thin Solid Films,* vol. 480, pp. 213-217, 2005.
[82] B. Singh, Z. A. Khan, I. Khan and S. Ghosh, "Highly conducting zinc oxide thin films achieved without postgrowth annealing," *Appl. Phys. Lett.,* vol. 97, pp. 241903, 2010.
[83] A. Singh, R. Mehra, N. Buthrath, A. Wakahara and A. Yoshida, "Highly conductive and transparent aluminum-doped zinc oxide thin films prepared by pulsed laser deposition in oxygen ambient," *J. Appl. Phys.,* vol. 90, pp. 5661-5665, 2001.
[84] W. Yang, Z. Liu, Z. Wu, M. Hong, C. Wang, A. Y. Lee and H. Gong, "Low substrate temperature fabrication of high-performance metal oxide thin-film by magnetron sputtering with target self-heating," *Appl. Phys. Lett.,* vol. 102, pp. 111901, 2013.

[85] W. Yang, Z. Liu, D. Peng, F. Zhang, H. Huang, Y. Xie and Z. Wu, "Room-temperature deposition of transparent conducting Al-doped ZnO films by RF magnetron sputtering method," *Appl. Surf. Sci.,* vol. 255, pp. 5669-5673, 2009.
[86] K. S. Harsha, *Principles of Vapor Deposition of Thin Films.* Elsevier, UK, 2005.
[87] Z. Wang, J. Chu, H. Zhu, Z. Sun, Y. Chen and S. Huang, "Growth of ZnO: Al films by RF sputtering at room temperature for solar cell applications," *Solid-State Electronics,* vol. 53, pp. 1149-1153, 2009.
[88] S. Fernandez and F. Naranjo, "Optimization of aluminum-doped zinc oxide films deposited at low temperature by radio-frequency sputtering on flexible substrates for solar cell applications," *Solar Energy Mater. Solar Cells,* vol. 94, pp. 157-163, 2010.
[89] S. Fernández, A. Martínez-Steele, J. Gandía and F. Naranjo, "Radio frequency sputter deposition of high-quality conductive and transparent ZnO: Al films on polymer substrates for thin film solar cells applications," *Thin Solid Films,* vol. 517, pp. 3152-3156, 2009.
[90] D. K. Kim and H. B. Kim, "Room temperature deposition of Al-doped ZnO thin films on glass by RF magnetron sputtering under different Ar gas pressure," *J. Alloys Compounds,* vol. 509, pp. 421-425, 2011.
[91] R. Wen, L. Wang, X. Wang, G. Yue, Y. Chen and D. Peng, "Influence of substrate temperature on mechanical, optical and electrical properties of ZnO: Al films," *J. Alloys Compounds,* vol. 508, pp. 370-374, 2010.
[92] W. M. Tsang, F. L. Wong, M. K. Fung, J. Chang, C. S. Lee and S. T. Lee, "Transparent conducting aluminum-doped zinc oxide thin film prepared by sol–gel process followed by laser irradiation treatment," *Thin Solid Films,* vol. 517, pp. 891-895, 2008.
[93] M. Y. Zhang and G. J. Cheng, "Highly conductive and transparent alumina-doped ZnO films processed by direct pulsed laser recrystallization at room temperature," *Appl. Phys. Lett.,* vol. 99, pp. 051904, 2011.
[94] Q. Xu, R. Hong, H. Huang, Z. Zhang, M. Zhang, X. Chen and Z. Y. Wu, "Laser annealing effect on optical and electrical properties of Al doped ZnO films," *Optics & Laser Technology,* vol. 45, pp. 513-517, 2013.
[95] W. Hsiao, S. Tseng, K. Huang and D. Chiang, "Electrode patterning and annealing processes of aluminum-doped zinc oxide thin films using a UV laser system," *Optics and Lasers in Engineering,* vol. 51, pp. 15-22, 2013.
[96] V. Schütz, V. Sittinger, S. Götzendörfer, C. Kalmbach, R. Fu, P. von Witzendorff, C. Britze, O. Suttmann and L. Overmeyer, "Nir-cw-laser annealing of room temperature sputtered zno: al," *Physics Procedia,* vol. 56, pp. 1073-1082, 2014.
[97] Q. Nian, M. Y. Zhang, B. D. Schwartz and G. J. Cheng, "Ultraviolet laser crystallized ZnO: Al films on sapphire with high Hall mobility for simultaneous enhancement of conductivity and transparency," *Appl. Phys. Lett.,* vol. 104, pp. 201907, 2014.
[98] W. Hsiao, S. Tseng, C. Chung, D. Chiang, K. Huang, K. Lin, L. Li and M. Chen, "Effect on structural, optical and electrical properties of aluminum-doped zinc oxide films using diode laser annealing," *Optics & Laser Technology,* vol. 68, pp. 41-47, 2015.
[99] R. Boukhicha, C. Charpentier, P. Prod'Homme, P. R. i Cabarrocas, J. Lerat, T. Emeraud and E. Johnson, "Influence of sputtering conditions on the optical and electrical properties of laser-annealed and wet-etched room temperature sputtered ZnO: Al thin films," *Thin Solid Films,* vol. 555, pp. 13-17, 2014.
[100] L. Huang, B. Li and N. Ren, "Enhancing optical and electrical properties of Al-doped ZnO coated polyethylene terephthalate substrates by laser annealing using overlap rate controlling strategy," *Ceram. Int.,* 2016.
[101] S. O. Elhamali, W. Cranton, N. Kalfagiannis, X. Hou, R. Ranson and D. Koutsogeorgis, "Enhanced electrical and optical properties of room temperature deposited Aluminium doped Zinc Oxide (AZO) thin films by excimer laser annealing," *Optics and Lasers in Engineering,* vol. 80, pp. 45-51, 2016.

[102] B. Ayachi, T. Aviles, J. Vilcot and C. Sion, "Rapid thermal annealing effect on the spatial resistivity distribution of AZO thin films deposited by pulsed-direct-current sputtering for solar cells applications," *Appl. Surf. Sci.,* vol. 366, pp. 53-58, 2016.

[103] T. Iwasaki, N. Itagaki, T. Den, H. Kumomi, K. Nomura, T. Kamiya and H. Hosono, "Combinatorial approach to thin-film transistors using multicomponent semiconductor channels: An application to amorphous oxide semiconductors in In–Ga–Zn–O system," *Appl. Phys. Lett.,* vol. 90, pp. 242114, 2007.

[104] H. Q. Chiang, B. R. McFarlane, D. Hong, R. E. Presley and J. F. Wager, "Processing effects on the stability of amorphous indium gallium zinc oxide thin-film transistors," *J. Non Cryst. Solids,* vol. 354, pp. 2826-2830, 2008.

[105] J. H. Jeong, H. W. Yang, J. Park, J. K. Jeong, Y. Mo, H. D. Kim, J. Song and C. S. Hwang, "Origin of subthreshold swing improvement in amorphous indium gallium zinc oxide transistors," *Electrochemical and Solid-State Letters,* vol. 11, pp. H157-H159, 2008.

[106] M. Nakata, K. Takechi, K. Azuma, E. Tokumitsu, H. Yamaguchi and S. Kaneko, "Improvement of InGaZnO4 thin film transistors characteristics utilizing excimer laser annealing," *Applied Physics Express,* vol. 2, pp. 021102, 2009.

[107] B. Du Ahn, W. H. Jeong, H. S. Shin, D. L. Kim, H. J. Kim, J. K. Jeong, S. Choi and M. Han, "Effect of excimer laser annealing on the performance of amorphous indium gallium zinc oxide thin-film transistors," *Electrochemical and Solid-State Letters,* vol. 12, pp. H430-H432, 2009.

[108] H. Zan, W. Chen, C. Chou, C. Tsai, C. Huang and H. Hsueh, "Low temperature annealing with solid-state laser or UV lamp irradiation on amorphous IGZO thin-film transistors," *Electrochemical and Solid-State Letters,* vol. 13, pp. H144-H146, 2010.

[109] M. Nakata, H. Tsuji, Y. Fujisaki, H. Sato, Y. Nakajima, T. Takei, T. Yamamoto and T. Kurita, "Fabrication method for self-aligned bottom-gate oxide thin-film transistors by utilizing backside excimer-laser irradiation through substrate," *Appl. Phys. Lett.,* vol. 103, pp. 142111, 2013.

[110] C. Chung, B. Zhu, D. G. Ast, R. G. Greene and M. O. Thompson, "High mobility amorphous InGaZnO4 thin film transistors formed by CO2 laser spike annealing," *Appl. Phys. Lett.,* vol. 106, pp. 123506, 2015.

[111] S. Cho, M. Choi, K. Chung and J. Park, "Low temperature processed InGaZnO oxide thin film transistor using ultra-violet irradiation," *Electronic Materials Letters,* vol. 11, pp. 360-365, 2015.

[112] J. P. Bermundo, Y. Ishikawa, M. N. Fujii, T. Nonaka, R. Ishihara, H. Ikenoue and Y. Uraoka, "Effect of excimer laser annealing on a-InGaZnO thin-film transistors passivated by solution-processed hybrid passivation layers," *J. Phys. D,* vol. 49, pp. 035102, 2015.

[113] Y. Yang, S. S. Yang and K. Chou, "Characteristic enhancement of solution-processed In–Ga–Zn oxide thin-film transistors by laser annealing," *Electron Device Letters, IEEE,* vol. 31, pp. 969-971, 2010.

[114] C. Tsay and T. Huang, "Improvement of physical properties of IGZO thin films prepared by excimer laser annealing of sol–gel derived precursor films," *Mater. Chem. Phys.,* vol. 140, pp. 365-372, 2013.

[115] J. Kim, B. S. Oh, M. Piao, M. Joo, H. Jang, S. Ahn and G. Kim, "Effects of low-temperature (120 C) annealing on the carrier concentration and trap density in amorphous indium gallium zinc oxide thin film transistors," *J. Appl. Phys.,* vol. 116, pp. 245302, 2014.

[116] S. Yang, J. Y. Bak, S. Yoon, M. K. Ryu, H. Oh, C. Hwang, G. H. Kim, S. K. Park and J. Jang, "Low-temperature processed flexible In–Ga–Zn–O thin-film transistors exhibiting high electrical performance," *Electron Device Letters, IEEE,* vol. 32, pp. 1692-1694, 2011.

[117] D. L. Smith, *Thin-Film Deposition: Principles and Practice.* McGraw-hill New York, USA, 1995.

[118] D. M. Mattox, *Handbook of Physical Vapor Deposition (PVD) Processing.* William Andrew, UK, 2010.

[119] J. A. Thornton, "Magnetron sputtering: basic physics and application to cylindrical magnetrons," *Journal of Vacuum Science & Technology,* vol. 15, pp. 171-177, 1978.

[120] B. Chapman, "Glow discharge processes: sputtering and plasma etching," USA,1980.

[121] S. B. K. Moorthy, *Thin Film Structures in Energy Applications.* Springer, Switzerland, 2015.
[122] C. Tsai, Y. Lee, J. Wang, K. Wei, I. Lee, C. Chen and H. Cheng, "High-performance top and bottom double-gate low-temperature poly-silicon thin film transistors fabricated by excimer laser crystallization," *Solid-State Electronics,* vol. 52, pp. 365-371, 2008.
[123] M. Nakata, K. Takechi, S. Yamaguchi, E. Tokumitsu, H. Yamaguchi and S. Kaneko, "Effects of excimer laser annealing on InGaZnO4 thin-film transistors having different active-layer thicknesses compared with those on polycrystalline silicon," *Japanese Journal of Applied Physics,* vol. 48, pp. 115505, 2009.
[124] M. Kim, K. Yim, J. Son and J. Leem, "Effects of Al concentration on structural and optical properties of Al-doped ZnO thin films," *Bulletin of the Korean Chemical Society,* vol. 33, pp. 1235-1241, 2012.
[125] D. C. Koutsogeorgis, *Investigation of Laser Annealing of Thin Film Phosphors for Potential Luminescent Devices,* PhD. dissertation, The Nottingham Trent University, School of Engineering, 2003.
[126] C. Suryanarayana and M. G. Norton, *X-Ray Diffraction: A Practical Approach.* Springer Science & Business Media, Germany, 2013.
[127] B. D. Cullity and J. W. Weymouth, "Elements of X-ray Diffraction," *American Journal of Physics,* vol. 25, pp. 394-395, 1957.
[128] M. Birkholz, *Thin Film Analysis by X-Ray Scattering.* John Wiley & Sons, Germany, 2006.
[129] B. E. Warren, *X-Ray Diffraction.* Courier Corporation, USA, 1969.
[130] U. Holzwarth and N. Gibson, "The Scherrer equation versus the'Debye-Scherrer equation'," *Nature Nanotechnology,* vol. 6, pp. 534-534, 2011.
[131] R. Hoffman, "Stresses in thin films: The relevance of grain boundaries and impurities," *Thin Solid Films,* vol. 34, pp. 185-190, 1976.
[132] W. Nix and B. Clemens, "Crystallite coalescence: A mechanism for intrinsic tensile stresses in thin films," *J. Mater. Res.,* vol. 14, pp. 3467-3473, 1999.
[133] A. Stokes and A. Wilson, "The diffraction of X rays by distorted crystal aggregates-I," *Proceedings of the Physical Society,* vol. 56, pp. 174, 1944.
[134] R. Cebulla, R. Wendt and K. Ellmer, "Al-doped zinc oxide films deposited by simultaneous rf and dc excitation of a magnetron plasma: relationships between plasma parameters and structural and electrical film properties," *J. Appl. Phys.,* vol. 83, pp. 1087-1095, 1998.
[135] T. H. De Keijser, J. Langford, E. J. Mittemeijer and A. Vogels, "Use of the Voigt function in a single-line method for the analysis of X-ray diffraction line broadening," *Journal of Applied Crystallography,* vol. 15, pp. 308-314, 1982.
[136] E. J. Mittemeijer and U. Welzel, "The “state of the art” of the diffraction analysis of crystallite size and lattice strain," *Zeitschrift Für Kristallographie International Journal for Structural, Physical, and Chemical Aspects of Crystalline Materials,* vol. 223, pp. 552-560, 2008.
[137] G. Friedbacher and H. Bubert, *Surface and Thin Film Analysis: A Compendium of Principles, Instrumentation, and Applications.* John Wiley & Sons, Germany, 2011.
[138] J. F. Watts and J. Wolstenholme, "An introduction to surface analysis by XPS and AES,". Wiley, UK, 2003.
[139] J. C. Vickerman and I. S. Gilmore, *Surface Analysis: The Principal Techniques.* Wiley, UK, 2009.
[140] J. J. Friel, *X-Ray and Image Analysis in Electron Microscopy.* Princeton Gamma-Tech, Incorporated, USA, 1994.
[141] D. K. Schroder, *Semiconductor Material and Device Characterization.* John Wiley & Sons, USA, 2006.
[142] I. Miccoli, F. Edler, H. Pfnür and C. Tegenkamp, "The 100th anniversary of the four-point probe technique: the role of probe geometries in isotropic and anisotropic systems," *Journal of Physics: Condensed Matter,* vol. 27, pp. 223201, 2015.
[143] F. Wenner, "A method for measuring earth resistivity," *Journal of the Franklin Institute,* vol. 180, pp. 373-375, 1915.

[144] F. Smits, "Measurement of sheet resistivities with the four-point probe," *Bell System Technical Journal,* vol. 37, pp. 711-718, 1958.
[145] L. van der Pauw, "A method of measuring specific resistivity and Hall effect of discs of arbitrary shape," *Philips Res.Rep.,* vol. 13, pp. 1-9, 1958.
[146] G. Binnig, C. F. Quate and C. Gerber, "Atomic force microscope," *Phys. Rev. Lett.,* vol. 56, pp. 930, 1986.
[147] J. Tauc, R. Grigorovici and A. Vancu, "Optical properties and electronic structure of amorphous germanium," *Physica Status Solidi (B),* vol. 15, pp. 627-637, 1966.
[148] W. Hume-Rothery and H. M. Powell, "On the theory of super-lattice structures in alloys," *Zeitschrift Für Kristallographie-Crystalline Materials,* vol. 91, pp. 23-47, 1935.
[149] W. Hume-Rothery, R. E. Smallman and C. W. Haworth, "The structure of metals and alloys," *The Institute of Metals,* UK*,* 1988.
[150] V. Lubarda, "On the effective lattice parameter of binary alloys," *Mech. Mater.,* vol. 35, pp. 53-68, 2003.
[151] W. Yang, Z. Wu, Z. Liu, A. Pang, Y. Tu and Z. C. Feng, "Room temperature deposition of Al-doped ZnO films on quartz substrates by radio-frequency magnetron sputtering and effects of thermal annealing," *Thin Solid Films,* vol. 519, pp. 31-36, 2010.
[152] S. Jeong, B. Park, S. Lee and J. Boo, "Metal-doped ZnO thin films: synthesis and characterizations," *Surface and Coatings Technology,* vol. 201, pp. 5318-5322, 2007.
[153] D. Mattox, "Particle bombardment effects on thin-film deposition: A review," *Journal of Vacuum Science & Technology A,* vol. 7, pp. 1105-1114, 1989.
[154] K. Wasa, M. Kitabatake and H. Adachi, *Thin Film Materials Technology: Sputtering of Control Compound Materials.* Springer Science & Business Media, Germany, 2004.
[155] K. Ellmer, F. Kudella, R. Mientus, R. Schieck and S. Fiechter, "Influence of discharge parameters on the layer properties of reactive magnetron sputtered ZnO: Al films," *Thin Solid Films,* vol. 247, pp. 15-23, 1994.
[156] T. Tsuji and M. Hirohashi, "Influence of oxygen partial pressure on transparency and conductivity of RF sputtered Al-doped ZnO thin films," *Appl. Surf. Sci.,* vol. 157, pp. 47-51, 2000.
[157] Z. Zhan, J. Zhang, Q. Zheng, D. Pan, J. Huang, F. Huang and Z. Lin, "Strategy for preparing Al-doped ZnO Thin film with high mobility and high stability," *Crystal Growth & Design,* vol. 11, pp. 21-25, 2010.
[158] Z. Li and S. J. Kwon, "Process optimization of Al-doped zinc oxide films as a window layer for Cu (In, Ga) Se 2 thin film solar cells," *Appl. Surf. Sci.,* vol. 284, pp. 379-385, 2013.
[159] S. Rahmane, M. A. Djouadi, M. S. Aida, N. Barreau, B. Abdallah and N. H. Zoubir, "Power and pressure effects upon magnetron sputtered aluminum doped ZnO films properties," *Thin Solid Films,* vol. 519, pp. 5-10, 2010.
[160] T. Prabhakar, L. Dai, L. Zhang, R. Yang, L. Li, T. Guo and Y. Yan, "Effects of growth process on the optical and electrical properties in Al-doped ZnO thin films," *J. Appl. Phys.,* vol. 115, pp. 083702, 2014.
[161] K. H. Kim, K. C. Park and D. Y. Ma, "Structural, electrical and optical properties of aluminum doped zinc oxide films prepared by radio frequency magnetron sputtering," *J. Appl. Phys.,* vol. 81, pp. 7764-7772, 1997.
[162] K. Tominaga, K. Kuroda and O. Tada, "Radiation effect due to energetic oxygen atoms on conductive Al-doped ZnO films," *Japanese Journal of Applied Physics,* vol. 27, pp. 1176, 1988.
[163] T. Welzel and K. Ellmer, "Comparison of ion energies and fluxes at the substrate during magnetron sputtering of ZnO: Al for dc and rf discharges," *J. Phys. D,* vol. 46, pp. 315202, 2013.
[164] L. W. Rieth and P. H. Holloway, "Influence of negative ion resputtering on ZnO: Al thin films," *Journal of Vacuum Science & Technology A,* vol. 22, pp. 20-29, 2004.
[165] M. Chen, X. Wang, Y. Yu, Z. Pei, X. Bai, C. Sun, R. Huang and L. Wen, "X-ray photoelectron spectroscopy and auger electron spectroscopy studies of Al-doped ZnO films," *Appl. Surf. Sci.,* vol. 158, pp. 134-140, 2000.

[166] M. N. Islam, T. Ghosh, K. Chopra and H. Acharya, "XPS and X-ray diffraction studies of aluminum-doped zinc oxide transparent conducting films," *Thin Solid Films,* vol. 280, pp. 20-25, 1996.
[167] W. Water and S. Chu, "Physical and structural properties of ZnO sputtered films," *Mater Lett,* vol. 55, pp. 67-72, 2002.
[168] Y. Igasaki and H. Kanma, "Argon gas pressure dependence of the properties of transparent conducting ZnO: Al films deposited on glass substrates," *Appl. Surf. Sci.,* vol. 169, pp. 508-511, 2001.
[169] L. Li, L. Fang, X. J. Zhou, Z. Y. Liu, L. Zhao and S. Jiang, "X-ray photoelectron spectroscopy study and thermoelectric properties of Al-doped ZnO thin films," *Journal of Electron Spectroscopy and Related Phenomena,* vol. 173, pp. 7-11, 2009.
[170] J. Hong, K. Katsumata and N. Matsushita, "High-conductivity solution-processed ZnO films realized via UV irradiation and hydrogen treatment," *Acta Materialia,* vol. 103, pp. 844-849, 2016.
[171] M. Tomellini, "X-ray photoelectron spectra of defective nickel oxide," *Journal of the Chemical Society, Faraday Transactions 1: Physical Chemistry in Condensed Phases,* vol. 84, pp. 3501-3510, 1988.
[172] Z. Zhang, C. Bao, S. Ma and S. Hou, "Effect of crystallinity of ZnO buffer layer on the properties of epitaxial (ZnO: Al)/(ZnO: Ga) bi-layer films deposited on c-sapphire substrate," *Appl. Surf. Sci.,* vol. 257, pp. 7893-7899, 2011.
[173] R. C. R. Nagiri, S. D. Yambem, Q. Lin, P. L. Burn and P. Meredith, "Room-temperature tilted-target sputtering deposition of highly transparent and low sheet resistance Al doped ZnO electrodes," *Journal of Materials Chemistry C,* vol. 3, pp. 5322-5331, 2015.
[174] J. A. Thornton, "Influence of apparatus geometry and deposition conditions on the structure and topography of thick sputtered coatings," *Journal of Vacuum Science & Technology,* vol. 11, pp. 666-670, 1974.
[175] A. Spadoni and M. Addonizio, "Effect of the RF sputtering power on microstructural, optical and electrical properties of Al doped ZnO thin films," *Thin Solid Films,* vol. 589, pp. 514-520, 2015.
[176] T. Minami, S. Suzuki and T. Miyata, "Electrical conduction mechanism of highly transparent and conductive ZnO thin films," in *MRS Proceedings,* 2001, pp. F1. 3.
[177] F. Greuter and G. Blatter, "Electrical properties of grain boundaries in polycrystalline compound semiconductors," *Semiconductor Science and Technology,* vol. 5, pp. 111, 1990.
[178] B. Chun, H. Wu, M. Abid, I. Chu, S. Serrano-Guisan, I. Shvets and D. S. Choi, "The effect of deposition power on the electrical properties of Al-doped zinc oxide thin films," *Appl. Phys. Lett.,* vol. 97, pp. 082109, 2010.
[179] K. Ellmer and T. Welzel, "Reactive magnetron sputtering of transparent conductive oxide thin films: Role of energetic particle (ion) bombardment," *J. Mater. Res.,* vol. 27, pp. 765-779, 2012.
[180] T. Minami, T. Miyata, T. Yamamoto and H. Toda, "Origin of electrical property distribution on the surface of ZnO: Al films prepared by magnetron sputtering," *Journal of Vacuum Science & Technology A,* vol. 18, pp. 1584-1589, 2000.
[181] D. Song, P. Widenborg, W. Chin and A. G. Aberle, "Investigation of lateral parameter variations of Al-doped zinc oxide films prepared on glass substrates by rf magnetron sputtering," *Solar Energy Mater. Solar Cells,* vol. 73, pp. 1-20, 2002.
[182] T. Minami, T. Miyata, Y. Ohtani and Y. Mochizuki, "New transparent conducting Al-doped ZnO film preparation techniques for improving resistivity distribution in magnetron sputtering deposition," *Japanese Journal of Applied Physics,* vol. 45, pp. L409, 2006.
[183] D. Dimova-Malinovska, N. Tzenov, M. Tzolov and L. Vassilev, "Optical and electrical properties of RF magnetron sputtered ZnO: Al thin films," *Materials Science and Engineering: B,* vol. 52, pp. 59-62, 1998.
[184] R. Weber, T. Graf, P. Berger, V. Onuseit, M. Wiedenmann, C. Freitag and A. Feuer, "Heat accumulation during pulsed laser materials processing," *Optics Express,* vol. 22, pp. 11312-11324, 2014.

[185] M. Y. Zhang, Q. Nian and G. J. Cheng, "Room temperature deposition of alumina-doped zinc oxide on flexible substrates by direct pulsed laser recrystallization," *Appl. Phys. Lett.,* vol. 100, pp. 151902, 2012.
[186] G. Janssen, "Stress and strain in polycrystalline thin films," *Thin Solid Films,* vol. 515, pp. 6654-6664, 2007.
[187] C. Tsakonas, W. Cranton, F. Li, K. Abusabee, A. Flewitt, D. Koutsogeorgis and R. Ranson, "Intrinsic photoluminescence from low temperature deposited zinc oxide thin films as a function of laser and thermal annealing," *J. Phys. D,* vol. 46, pp. 095305, 2013.
[188] J. Lee and Y. S. Park, "Characteristics of Al-doped ZnO films annealed at various temperatures for InGaZnO-based thin-film transistors," *Thin Solid Films,* vol. 587, pp. 94-99, 2015.
[189] X. Deng, H. Deng, M. Wei and J. Chen, "Preparation of highly transparent conductive Al-doped ZnO thin films and annealing effects on properties," *J. Mater. Sci. : Mater. Electron.,* vol. 23, pp. 413-417, 2012.
[190] H. Hagendorfer, K. Lienau, S. Nishiwaki, C. M. Fella, L. Kranz, A. R. Uhl, D. Jaeger, L. Luo, C. Gretener and S. Buecheler, "Highly transparent and conductive ZnO: Al thin films from a low temperature aqueous solution approach," *Adv Mater,* vol. 26, pp. 632-636, 2014.
[191] L. Ding, S. Nicolay, J. Steinhauser, U. Kroll and C. Ballif, "Relaxing the Conductivity/Transparency Trade-Off in MOCVD ZnO Thin Films by Hydrogen Plasma," *Advanced Functional Materials,* vol. 23, pp. 5177-5182, 2013.
[192] K. Kim, S. Niki, J. Oh, J. Song, T. Seong, S. Park, S. Fujita and S. Kim, "High electron concentration and mobility in Al-doped n-ZnO epilayer achieved via dopant activation using rapid-thermal annealing," 2005.
[193] C. Charpentier, R. Boukhicha, T. Emeraud, J. Lerat, P. R. i Cabarrocas and E. Johnson, "Evolution in morphological, optical, and electronic properties of ZnO: Al thin films undergoing a laser annealing and etching process," *Solar Energy Mater. Solar Cells,* vol. 125, pp. 223-232, 2014.
[194] J. H. Noh, H. S. Jung, J. Lee, J. Y. Kim, C. M. Cho, J. An and K. S. Hong, "Reversible change in electrical and optical properties in epitaxially grown Al-doped ZnO thin films," *J. Appl. Phys.,* vol. 104, pp. 073706, 2008.
[195] J. I. Kim, W. Lee, T. Hwang, J. Kim, S. Lee, S. Kang, H. Choi, S. Hong, H. H. Park and T. Moon, "Quantitative analyses of damp-heat-induced degradation in transparent conducting oxides," *Solar Energy Mater. Solar Cells,* vol. 122, pp. 282-286, 2014.
[196] Y. Liu, C. Hsieh, Y. Wu, Y. Wei, P. Lee, H. Hsieh and C. Liu, "Mechanism of conductivity degradation of AZO thin film in high humidity ambient," *Appl. Surf. Sci.,* vol. 282, pp. 32-37, 2013.
[197] D. Lee, W. Cho, C. Jang, J. Song, C. Park, K. Park, J. Ryu, H. Lee and Y. Kim, "Damp heat and thermal cycling-induced degradation mechanism of AZO and CIGS films in Cu (In, Ga) Se 2 photovoltaic modules," *Current Applied Physics,* vol. 15, pp. 285-291, 2015.
[198] W. Lin, R. Ma, J. Xue and B. Kang, "RF magnetron sputtered ZnO: Al thin films on glass substrates: A study of damp heat stability on their optical and electrical properties," *Solar Energy Mater. Solar Cells,* vol. 91, pp. 1902-1905, 2007.
[199] V. Kumar and H. Wang, "Plasmonic Au nanoparticles for enhanced broadband light absorption in inverted organic photovoltaic devices by plasma assisted physical vapour deposition," *Organic Electronics,* vol. 14, pp. 560-568, 2013.
[200] P. Barquinha, "Transparent oxide thin-film transistors: production, characterization and integration," PhD. dissertation, New University of Lisbon Faculty of Science and Technology, 2010.
[201] K. Ip, G. Thaler, H. Yang, S. Y. Han, Y. Li, D. Norton, S. Pearton, S. Jang and F. Ren, "Contacts to ZnO," *J. Cryst. Growth,* vol. 287, pp. 149-156, 2006.
[202] Y. Shimura, K. Nomura, H. Yanagi, T. Kamiya, M. Hirano and H. Hosono, "Specific contact resistances between amorphous oxide semiconductor In–Ga–Zn–O and metallic electrodes," *Thin Solid Films,* vol. 516, pp. 5899-5902, 2008.

[203] A. Olziersky, P. Barquinha, A. Vila, C. Magana, E. Fortunato, J. Morante and R. Martins, "Role of Ga 2 O 3–In 2 O 3–ZnO channel composition on the electrical performance of thin-film transistors," *Mater. Chem. Phys.,* vol. 131, pp. 512-518, 2011.

[204] P. Barquinha, L. Pereira, G. Goncalves, R. Martins and E. Fortunato, "Toward high-performance amorphous GIZO TFTs," *J. Electrochem. Soc.,* vol. 156, pp. H161-H168, 2009.

[205] P. Barquinha, L. Pereira, G. Goncalves, R. Martins and E. Fortunato, "The effect of deposition conditions and annealing on the performance of high-mobility GIZO TFTs," *Electrochemical and Solid-State Letters,* vol. 11, pp. H248-H251, 2008.

[206] S. Yasuno, T. Kita, A. Hino, S. Morita, K. Hayashi and T. Kugimiya, "Physical Properties of Amorphous In–Ga–Zn–O Films Deposited at Different Sputtering Pressures," *Japanese Journal of Applied Physics,* vol. 52, pp. 03BA01, 2013.

[207] W. Chen, S. Lo, S. Kao, H. Zan, C. Tsai, J. Lin, C. Fang and C. Lee, "Oxygen-dependent instability and annealing/passivation effects in amorphous In–Ga–Zn–O thin-film transistors," *Electron Device Letters, IEEE,* vol. 32, pp. 1552-1554, 2011.

[208] K. Nomura, T. Kamiya, H. Ohta, K. Ueda, M. Hirano and H. Hosono, "Carrier transport in transparent oxide semiconductor with intrinsic structural randomness probed using single-crystalline InGaO3 (ZnO) 5 films," *Appl. Phys. Lett.,* vol. 85, pp. 1993, 2004.

[209] Y. Kim, M. Han, J. Han and S. K. Park, "Effect of metallic composition on electrical properties of solution-processed indium-gallium-zinc-oxide thin-film transistors," *Electron Devices, IEEE Transactions On,* vol. 57, pp. 1009-1014, 2010.

[210] J. K. Jeong, H. Chung, Y. Mo and H. D. Kim, "Comprehensive study on the transport mechanism of amorphous indium-gallium-zinc oxide transistors," *J. Electrochem. Soc.,* vol. 155, pp. H873-H877, 2008.

[211] D. Kang, H. Lim, C. Kim, I. Song, J. Park, Y. Park and J. Chung, "Amorphous gallium indium zinc oxide thin film transistors: Sensitive to oxygen molecules," *Appl. Phys. Lett.,* vol. 90, pp. 192101, 2007.

[212] H. Hosono, K. Nomura, Y. Ogo, T. Uruga and T. Kamiya, "Factors controlling electron transport properties in transparent amorphous oxide semiconductors," *J. Non Cryst. Solids,* vol. 354, pp. 2796-2800, 2008.

[213] K. Nomura, T. Kamiya, H. Yanagi, E. Ikenaga, K. Yang, K. Kobayashi, M. Hirano and H. Hosono, "Subgap states in transparent amorphous oxide semiconductor, In–Ga–Zn–O, observed by bulk sensitive X-ray photoelectron spectroscopy," *Appl. Phys. Lett.,* vol. 92, pp. 202117, 2008.

[214] J. Yota, H. Shen and R. Ramanathan, "Characterization of atomic layer deposition HfO2, Al2O3, and plasma-enhanced chemical vapor deposition Si3N4 as metal–insulator–metal capacitor dielectric for GaAs HBT technology," *Journal of Vacuum Science & Technology A,* vol. 31, pp. 01A134, 2013.

[215] J. Shin and D. Choi, "E ect of Oxygen on the Optical and the Electrical Properties of Amorphous InGaZnO Thin Films Prepared by RF Magnetron Sputtering," *Journal of the Korean Physical Society,* vol. 53, 2008.

[216] C. Chiu, Z. Pei, S. Chang, S. Chang and S. Chang, "Effect of oxygen partial pressure on electrical characteristics of amorphous indium gallium zinc oxide thin-film transistors fabricated by thermal annealing," *Vacuum,* vol. 86, pp. 246-249, 2011.

[217] J. Park, J. K. Jeong, Y. Mo, H. D. Kim and S. Kim, "Improvements in the device characteristics of amorphous indium gallium zinc oxide thin-film transistors by Ar plasma treatment," *Appl. Phys. Lett.,* vol. 90, pp. 262106-262106, 2007.

[218] Y. Yang, S. S. Yang and K. Chou, "Performance improvements of IGZO and ZnO thin-film transistors by laser-irradiation treatment," *Journal of the Society for Information Display,* vol. 19, pp. 247-252, 2011.

[219] H. Park, M. Choi, Y. Jo and K. Chung, "Low temperature processed InGaZnO thin film transistor using the combination of hydrogen irradiation and annealing," *Appl. Surf. Sci.,* vol. 321, pp. 520-524, 2014.

[220] M. Fujii, Y. Ishikawa, R. Ishihara, J. van der Cingel, M. R. Mofrad, M. Horita and Y. Uraoka, "Low temperature high-mobility InZnO thin-film transistors fabricated by excimer laser annealing," *Appl. Phys. Lett.,* vol. 102, pp. 122107, 2013.
[221] D. R. Cairns and G. P. Crawford, "Electromechanical properties of transparent conducting substrates for flexible electronic displays," *Proc IEEE,* vol. 93, pp. 1451-1458, 2005.
[222] U. Mbamara, B. Olofinjana, O. Ajayi, C. Lorenzo-Martin, E. Obiajunwa and E. Ajayi, "Friction and wear behavior of nitrogen-doped ZnO thin films deposited via MOCVD under dry contact," *Engineering Science and Technology, an International Journal,* 2016.
[223] J. Hur, J. Song, J. Kim, D. Byun, C. Son, H. Y. JAE and H. Y. KYUNG, "Efficiencies of CIGS solar cells using transparent conducting Al-doped ZnO window layers as a function of thickness," *Journal of the Korean Physical Society,* vol. 53, pp. 437-441, 2008.

9 Appendices

Appendix A. Reproducibility test of the deposition and annealing parameters for AZO

- Reproducibility test of the optimised deposition parameters for AZO.

The optimised deposition parameters are room temperature, an RF power 180 W, and a sputtering pressure 2 mTorr of 0.2% oxygen to argon ratio.

No	Date	Deposition details and aim	ρ (Ω.cm) across the sample		
			Side 1	Centre	Side 2
1	02/05/2014	Applied RF power investigation. 180 nm AZO on 4-inch glass substrates	1.13×10^{-3}	1.14×10^{-3}	1.13×10^{-3}
2	06/05/2014	Reproducibility test. 180 nm AZO on 4-inch glass substrates	1.13×10^{-3}	1.15×10^{-3}	1.12×10^{-3}
3	09/05/2014	Reproducibility test. 180 nm AZO on 4-inch glass substrates	1.12×10^{-3}	1.13×10^{-3}	1.12×10^{-3}
4	12/05/2014	Reproducibility test. 180 nm AZO on 4-inch glass substrates.	1.11×10^{-3}	1.13×10^{-3}	1.12×10^{-3}
5	27/05/2014	180 nm AZO on fused silica substrates for RTA investigation	1.14×10^{-3}	1.15×10^{-3}	1.13×10^{-3}
6	15/06/2014	180 nm AZO on fused silica substrates for RTA investigation	1.13×10^{-3}	1.14×10^{-3}	1.15×10^{-3}
7	18/06/2014	180 nm AZO on fused silica substrates for RTA investigation	1.14×10^{-3}	1.15×10^{-3}	1.15×10^{-3}
8	20/06/2014	**360 nm** AZO on 4-inch glass substrates.	**6.7×10^{-4}**	**6.8×10^{-4}**	**6.6×10^{-4}**
9	24/06/2014	**360 nm** AZO on 4-inch glass substrates.	**6.8×10^{-4}**	**6.8×10^{-4}**	**6.7×10^{-4}**
10	26/06/2014	180 nm AZO on fused silica substrates for RTA investigation	1.14×10^{-3}	1.14×10^{-3}	1.13×10^{-3}
11	11/07/2014	180 nm AZO on fused silica substrates for RTA investigation	1.15×10^{-3}	1.17×10^{-3}	1.16×10^{-3}
12	14/07/2014	180 nm AZO on microscope slides for OPVs test	1.17×10^{-3}	1.18×10^{-3}	1.17×10^{-3}
13	15/07/2014	180 nm AZO on microscope slides for OPVs test.	1.18×10^{-3}	1.19×10^{-3}	1.18×10^{-3}
14	17/07/2014	180 nm AZO on microscope slides for ELA and OPVs test	1.16×10^{-3}	1.17×10^{-3}	1.16×10^{-3}
15	21/07/2014	180 nm AZO on microscope slides for RTA and OPVs test	1.15×10^{-3}	1.15×10^{-3}	1.16×10^{-3}
16	25/07/2014	Reproducibility test after opening the sputtering camper to air	1.19×10^{-3}	1.2×10^{-3}	1.18×10^{-3}
17	26/08/2014	180 nm AZO on microscope slides for OPVs test	1.14×10^{-3}	1.16×10^{-3}	1.15×10^{-3}
18	12/09/2014	180 nm AZO on fused silica substrates for RTA	1.13×10^{-3}	1.14×10^{-3}	1.13×10^{-3}
19	16/09/2014	180 nm AZO on microscope slides for RTA	1.12×10^{-3}	1.14×10^{-3}	1.13×10^{-3}
20	17/09/2014	180 nm AZO on fused silica substrates for RTA and optical (transmittance and reflectance) measurements	1.14×10^{-3}	1.16×10^{-3}	1.14×10^{-3}
21	18/09/2014	180 nm AZO on fused silica substrates for ELA and optical (transmittance and reflectance) measurements	1.15×10^{-3}	1.16×10^{-3}	1.15×10^{-3}

- Reproducibility test of the optimised ELA and RTA parameters for AZO.

The optimised ELA parameters are 5 pulses at 125 mJ/cm^2 in air.

The optimised RTA parameters are 300°C for 20s in nitrogen.

No	Date	Annealing details and aim	ρ (Ω.cm) changes	
			Pre-annealing	Post-annealing
1	12/05/2014	ELA investigation of AZO on glass substrates (3 samples of 1 cm × cm area)	1.14×10^{-3} 1.18×10^{-3} 1.11×10^{-3}	5.26×10^{-4} 5.27×10^{-4} 5.24×10^{-4}
2	21/07/2014	ELA of AZO for OPVs test (4 samples of 2.5 cm × 7.5 cm area)	1.12×10^{-3} 1.16×10^{-3} 1.14×10^{-3} 1.17×10^{-3}	5.20×10^{-4} 5.21×10^{-4} 5.22×10^{-4} 5.22×10^{-4}
3	28/07/2014	ELA of AZO for Hall Effect measurements (3 samples of 1 cm × cm area)	1.12×10^{-3} 1.16×10^{-3} 1.11×10^{-3}	5.24×10^{-4} 5.27×10^{-4} 5.23×10^{-4}
4	05/08/2014	ELA of AZO in different environments.	1.12×10^{-3}	5.26×10^{-4}
5	03/09/2014	ELA of AZO for OPVs test (4 samples of 2.5 cm × 7.5 cm area)	1.12×10^{-3} 1.18×10^{-3} 1.16×10^{-3} 1.14×10^{-3}	5.22×10^{-4} 5.27×10^{-4} 5.23×10^{-4} 5.22×10^{-4}
6	22/09/2014	ELA of AZO for optical (transmittance and reflectance) measurements	1.13×10^{-3}	5.25×10^{-4}
7	08/08/2014	RTA investigation of AZO on fused silica substrates (3 samples of 1 cm × cm area)	1.11×10^{-3} 1.14×10^{-3} 1.13×10^{-3}	5.21×10^{-4} 5.22×10^{-4} 5.21×10^{-4}
8	24/09/2014	RTA of AZO on fused silica substrates (Reproducibility test, 3 samples of 1 cm × cm area)	1.18×10^{-3} 1.12×10^{-3} 1.14×10^{-3}	5.27×10^{-4} 5.24×10^{-4} 5.24×10^{-4}
9	24/09/2014	RTA of AZO on microscope slides for OPVs test (4 samples of 2.5 cm × 7.5 cm area)	1.16×10^{-3} 1.12×10^{-3} 1.14×10^{-3} 1.11×10^{-3}	5.25×10^{-4} 5.24×10^{-4} 5.25×10^{-4} 5.23×10^{-4}
10	24/09/2014	RTA of AZO for optical (transmittance and reflectance) measurements.	1.15×10^{-3}	5.26×10^{-4}
11	24/09/2014	RTA of AZO for optical (transmittance and reflectance) measurements	1.13×10^{-3}	5.21×10^{-4}
12	24/09/2014	RTA of AZO for combined (RTA-ELA) annealing (5 samples of 1 cm × cm area)	1.12×10^{-3} 1.18×10^{-3} 1.13×10^{-3} 1.14×10^{-3} 1.17×10^{-3}	5.21×10^{-4} 5.26×10^{-4} 5.21×10^{-4} 5.22×10^{-4} 5.26×10^{-4}
13	24/09/2014	RTA of AZO for IEC 61646 test (4 samples of 1.3 cm × 1.3 cm area)	1.12×10^{-3} 1.14×10^{-3} 1.11×10^{-3} 1.18×10^{-3}	5.22×10^{-4} 5.23×10^{-4} 5.22×10^{-4} 5.25×10^{-4}
14	07/10/2015	ELA of AZO for IEC 61646 test (4 samples of 1.3 cm × 1.3 cm area)	1.16×10^{-3} 1.18×10^{-3} 1.11×10^{-3} 1.12×10^{-3}	5.27×10^{-4} 5.28×10^{-4} 5.24×10^{-4} 5.26×10^{-4}
15	07/10/2015	ELA of AZO for combined (ELA-RTA) annealing (5 samples of 1 cm × cm area)	1.11×10^{-3} 1.14×10^{-3} 1.16×10^{-3} 1.18×10^{-3} 1.12×10^{-3}	5.23×10^{-4} 5.25×10^{-4} 5.25×10^{-4} 5.27×10^{-4} 5.25×10^{-4}

Appendix B. ELA parameters effect on the resistivity of AZO of different deposition conditions.

Resistivity changes upon ELA of 180 nm thick AZO thin films deposited at differ applied RF power and sputtering pressure on glass substrates are shown below. Different number of pulses (0-100) from a KrF excimer laser at different laser energy densities (50, 75, 100, 125 mJ/cm^2) were applied in air at ambient temperature.

- AZO samples deposited at room temperature, different RF power, and 2 mTorr of 0.2% oxygen to argon ratio.

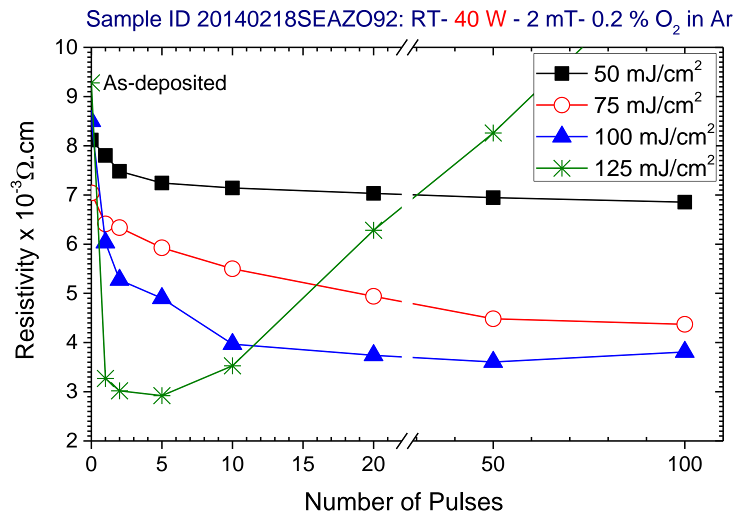

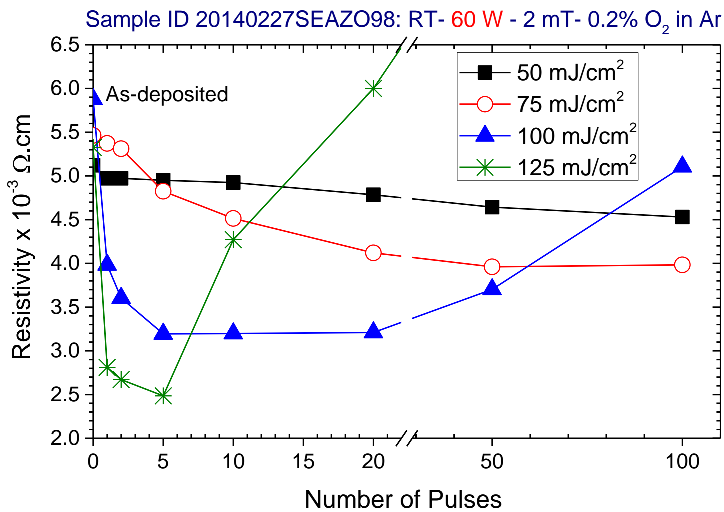

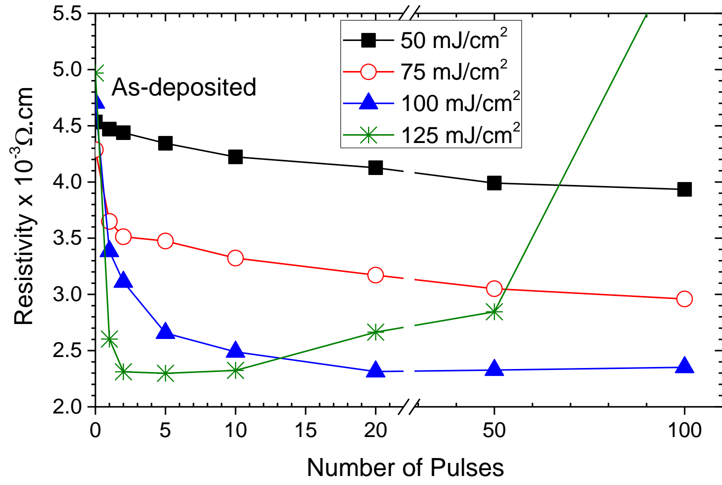

Sample ID 20140221SEAZO94: RT- 80 W - 2 mT- 0.2% O2 in Ar
As-deposited
50 mJ/cm2
75 mJ/cm2
100 mJ/cm2
125 mJ/cm2
Resistivity x 10-3Ω.cm
Number of Pulses

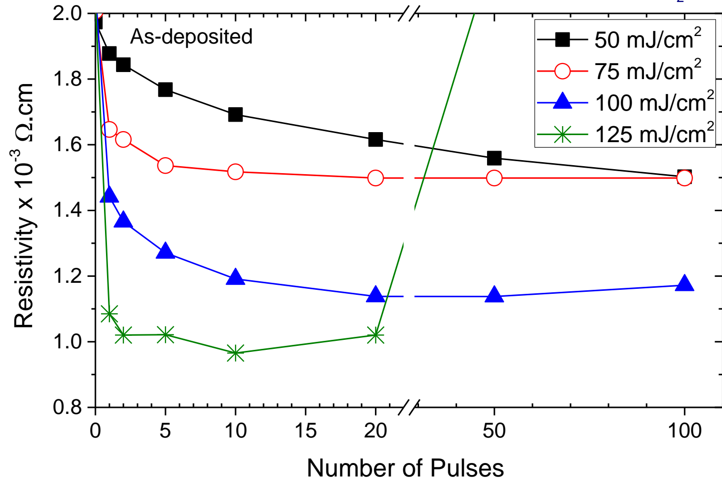

Sample ID 20140224SEAZO95: RT- 100 W - 2 mT- 0.2% O2 in Ar
As-deposited
50 mJ/cm2
75 mJ/cm2
100 mJ/cm2
125 mJ/cm2
Resistivity x 10-3 Ω.cm
Number of Pulses

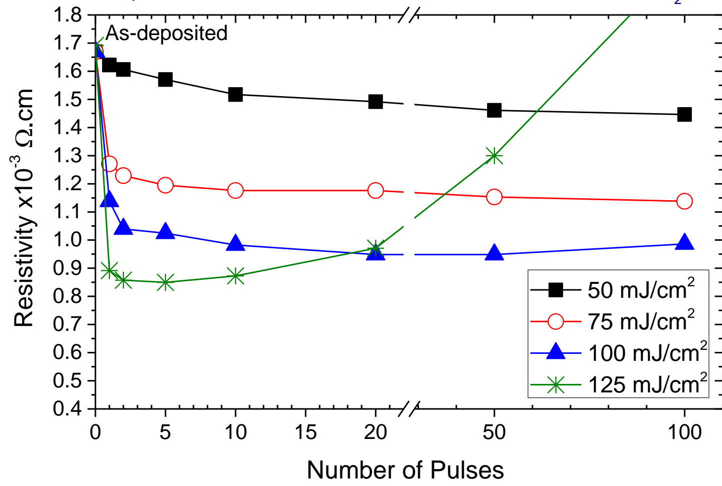

Sample ID 20140225SEAZO96: RT- 120 W - 2 mT- 0.2% O2 in Ar
As-deposited
50 mJ/cm2
75 mJ/cm2
100 mJ/cm2
125 mJ/cm2
Resistivity x10-3 Ω.cm
Number of Pulses

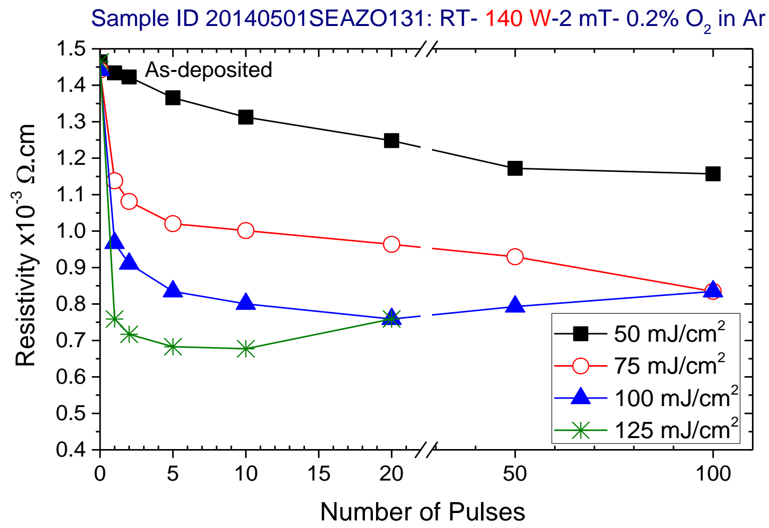
Sample ID 20140501SEAZO131: RT- 140 W-2 mT- 0.2% O2 in Ar
As-deposited
Resistivity x10-3 Ω.cm
Number of Pulses
50 mJ/cm2
75 mJ/cm2
100 mJ/cm2
125 mJ/cm2
1.5
1.4
1.3
1.2
1.1
1.0
0.9
0.8
0.7
0.6
0.5
0.4
0
5
10
15
20
50
100

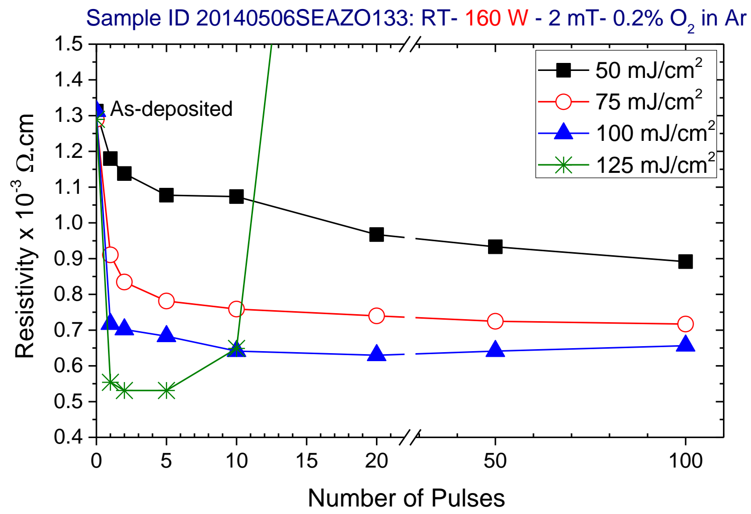
Sample ID 20140506SEAZO133: RT- 160 W - 2 mT- 0.2% O2 in Ar
As-deposited
Resistivity x 10-3 Ω.cm
Number of Pulses
50 mJ/cm2
75 mJ/cm2
100 mJ/cm2
125 mJ/cm2
1.5
1.4
1.3
1.2
1.1
1.0
0.9
0.8
0.7
0.6
0.5
0.4
0
5
10
15
20
50
100

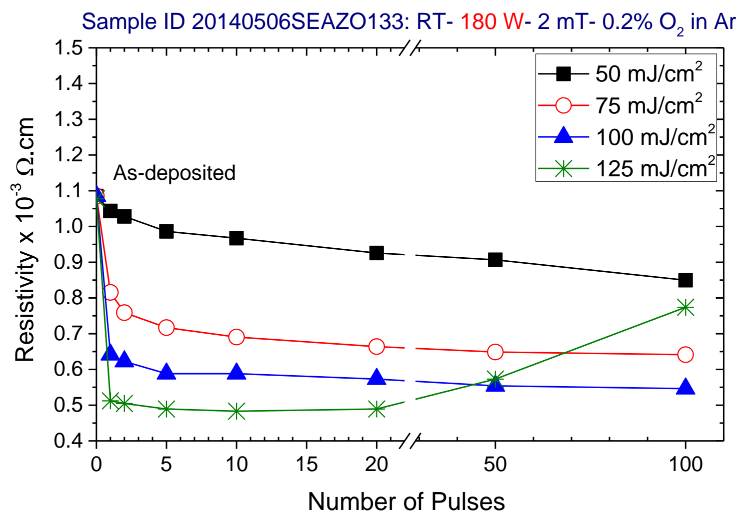
Sample ID 20140506SEAZO133: RT- 180 W- 2 mT- 0.2% O2 in Ar
As-deposited
Resistivity x 10-3 Ω.cm
Number of Pulses
50 mJ/cm2
75 mJ/cm2
100 mJ/cm2
125 mJ/cm2
1.5
1.4
1.3
1.2
1.1
1.0
0.9
0.8
0.7
0.6
0.5
0.4
0
5
10
15
20
50
100

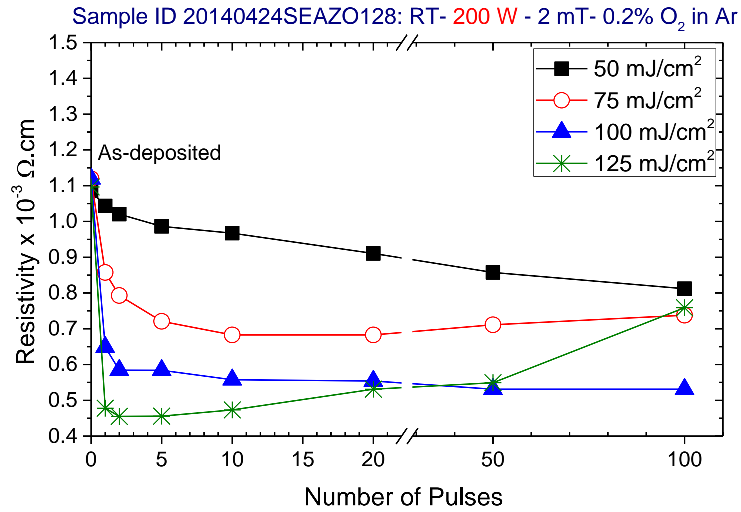

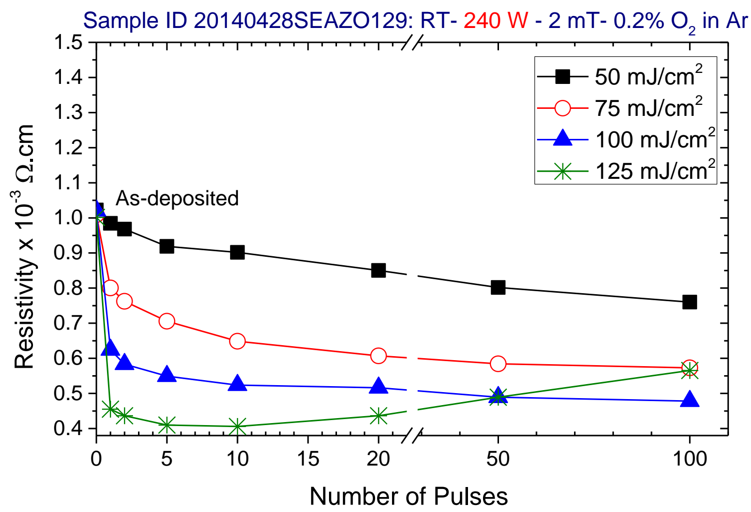

- AZO samples deposited at room temperature, 180 W, and different sputtering pressure of 0.2% oxygen to argon ratio.

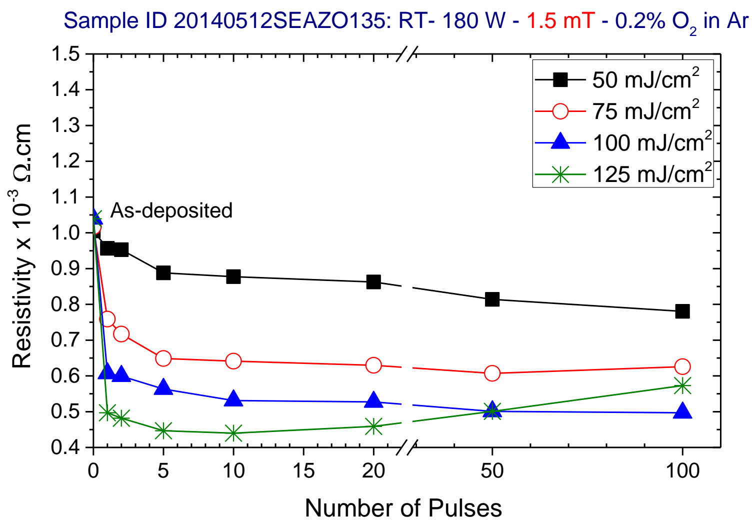

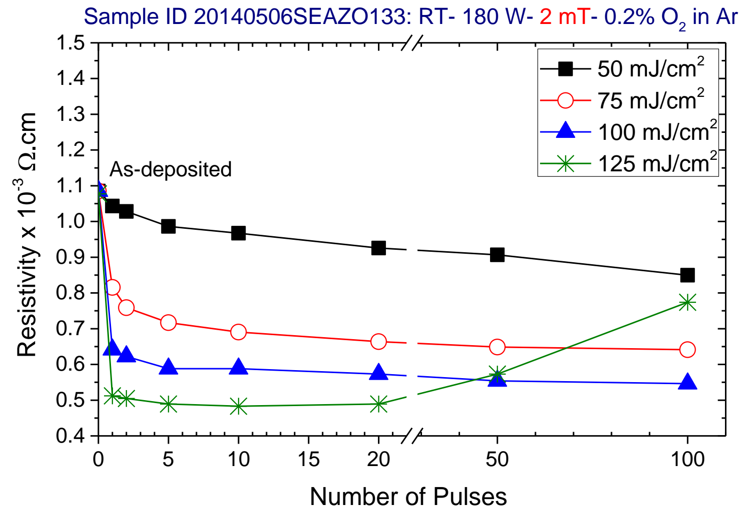
Sample ID 20140506SEAZO133: RT- 180 W- 2 mT- 0.2% O2 in Ar
Resistivity x 10-3 Ω.cm
Number of Pulses
As-deposited
50 mJ/cm2
75 mJ/cm2
100 mJ/cm2
125 mJ/cm2

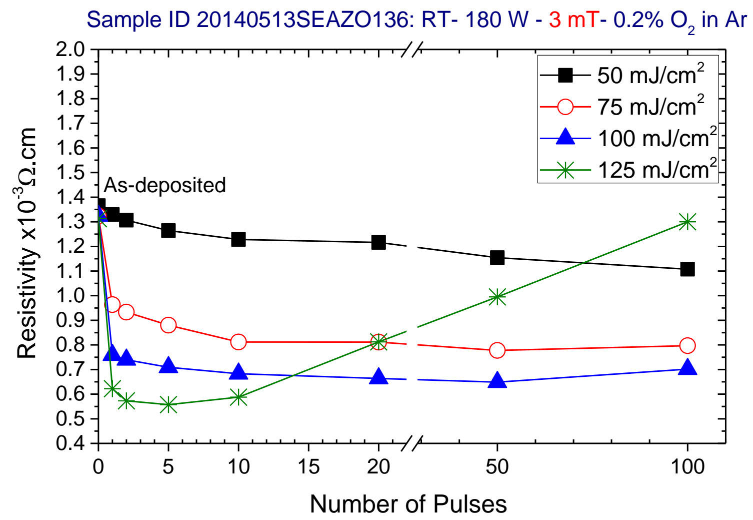
Sample ID 20140513SEAZO136: RT- 180 W - 3 mT- 0.2% O2 in Ar
Resistivity x10-3Ω.cm
Number of Pulses
As-deposited
50 mJ/cm2
75 mJ/cm2
100 mJ/cm2
125 mJ/cm2

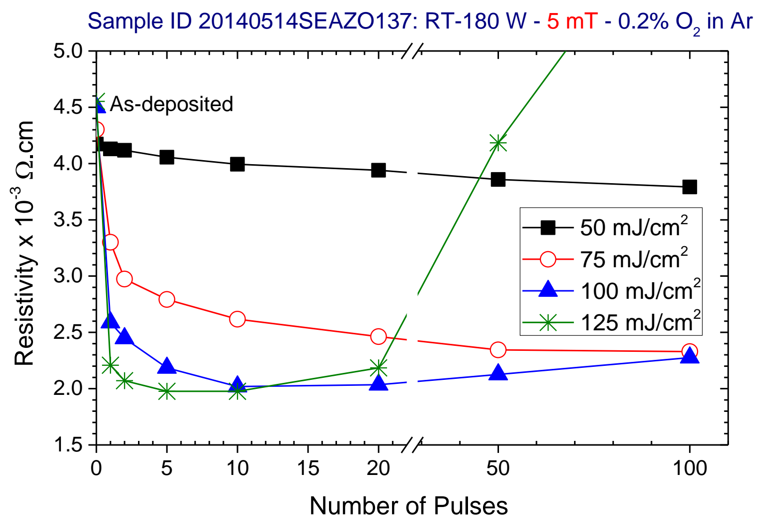
Sample ID 20140514SEAZO137: RT-180 W - 5 mT - 0.2% O2 in Ar
Resistivity x 10-3 Ω.cm
Number of Pulses
As-deposited
50 mJ/cm2
75 mJ/cm2
100 mJ/cm2
125 mJ/cm2

Appendix C. Publications copies

- Enhanced electrical and optical properties of room temperature deposited Aluminium doped Zinc Oxide (AZO) thin films by excimer laser annealing. http://irep.ntu.ac.uk/26767/.
- An Alternative Non by the publisher) -vacuum and Low Cost ESAVD Method for the Deposition of Cu(In,Ga)Se2 Absorber Layers. http://eprints.nottingham.ac.uk/34779/1/An%20Alternative%20Non-vacuum%20and%20Low%20Cost%20ESAVD%20Method%20for%20the%20Deposition%20of%20Cu(In%252cGa)Se2%20Absorber%20Layers%20_Mingqing%20Wang%20et%20al_UCL.pdf